Rubén López Coto

Very-high-energy Gamma-ray Observations of Pulsar Wind Nebulae and Cataclysmic Variable Stars with MAGIC and Development of Trigger Systems for IACTs

Springer

Springer Theses

Recognizing Outstanding Ph.D. Research

Aims and Scope

The series "Springer Theses" brings together a selection of the very best Ph.D. theses from around the world and across the physical sciences. Nominated and endorsed by two recognized specialists, each published volume has been selected for its scientific excellence and the high impact of its contents for the pertinent field of research. For greater accessibility to non-specialists, the published versions include an extended introduction, as well as a foreword by the student's supervisor explaining the special relevance of the work for the field. As a whole, the series will provide a valuable resource both for newcomers to the research fields described, and for other scientists seeking detailed background information on special questions. Finally, it provides an accredited documentation of the valuable contributions made by today's younger generation of scientists.

Theses are accepted into the series by invited nomination only and must fulfill all of the following criteria

- They must be written in good English.
- The topic should fall within the confines of Chemistry, Physics, Earth Sciences, Engineering and related interdisciplinary fields such as Materials, Nanoscience, Chemical Engineering, Complex Systems and Biophysics.
- The work reported in the thesis must represent a significant scientific advance.
- If the thesis includes previously published material, permission to reproduce this must be gained from the respective copyright holder.
- They must have been examined and passed during the 12 months prior to nomination.
- Each thesis should include a foreword by the supervisor outlining the significance of its content.
- The theses should have a clearly defined structure including an introduction accessible to scientists not expert in that particular field.

Rubén López Coto

Very-high-energy Gamma-ray Observations of Pulsar Wind Nebulae and Cataclysmic Variable Stars with MAGIC and Development of Trigger Systems for IACTs

Springer

Author
Dr. Rubén López Coto
Max Planck Institute for Nuclear Physics
Heidelberg
Germany

Supervisors
Prof. Oscar Blanch Bigas
Institut de Física d'Altes Energies (IFAE)
Universitat Autònoma de Barcelona
Barcelona
Spain

Prof. Juan Cortina Blanco
Institut de Física d'Altes Energies (IFAE)
Universitat Autònoma de Barcelona
Barcelona
Spain

Printed on acid-free paper

I wanted to live, but whether I would or not was a mystery, and in the midst of confronting that fact, even at that moment, I was beginning to sense that to stare into the heart of such a fearful mystery wasn't a bad thing. To be afraid is a priceless education. Once you have been that scared, you know more about your frailty than most people, and I think that changes a man. I was brought low, and there was nothing to take refuge in but the philosophical: this disease would force me to ask more of myself as person than I ever had before, and to seek out a different ethic.

—Lance Armstrong,
It's not about the bike: My journey back to life.

A mis padres, porque sin ellos nada habría sido posible

Supervisors' Foreword

Astroparticle physics and especially Very High Energy (VHE) gamma ray astrophysics is at the crossroads of astrophysics and particle physics. It is also a young discipline, hardly going back to the 1990s for the first discoveries.

Both facts are clearly reflected in this thesis. VHE gamma-ray astronomers still roll up their sleeves when they need data for their studies. Running an Imaging Atmospheric Cherenkov Telescope and extracting physics out of its whimsical data is not an easy feat. As common among particle physicists Dr. Rubén López-Coto has become deeply familiar with the hardware of the MAGIC telescopes in La Palma before jumping into the telescope data analysis. He has operated the instrument himself and investigated the trigger response not only of the current MAGIC telescopes, but also proposed a new technical setup and studied the response of the future Cherenkov Telescope Array telescopes. And, as common among astrophysicists, but not much among particle physicists, he has painstakingly identified specific gamma-ray sources in our particular sky, made careful observations and extracted lessons, which can be applied to a whole population.

VHE gamma rays have become a new field of astronomy not only through the consolidation of the imaging atmospheric technique, but also as the discovery of distinct source classes. Fermi-LAT has recently detected emission at MeV energies of novae and in the past, detections of these objects at multi-TeV energies had been claimed. The author of the thesis finds no evidence of VHE emission in a variety of cataclysmic variable stars: a classical nova, a symbiotic nova, a dwarf nova and a nova-like variable.

Conversely, a population of Pulsar Wind Nebulae (PWNe) has been established at VHE during the last decade. The Crab Nebula and 3C 58 are peculiar VHE PWNe. The former has been exhaustively observed at all wavelengths. It is no wonder because it is extremely powerful and one of the brightest objects in our sky. Yet it remains full of surprises, like the recent flares at MeV energies. This study fails to find VHE counterparts for these flares, but adds to our knowledge of the spectrum of the steady emission of the Crab Nebula at multi-TeV energies, thanks to a special set of observations at high zenith angles. 3C 58 on the other hand had

been proposed as a VHE source for a long time, but its discovery had eluded IACTs so far. The author of this thesis had to gather an extremely deep exposure to achieve a significant detection. It was no easy task and one in which only an analyzer with a deep knowledge of the instrument can succeed. 3C 58 has revealed itself as an infra-luminous PWN. It is as much an extreme object at VHE as the Crab Nebula and probably as essential to understand the whole class of PWNe.

Barcelona, Spain   Prof. Oscar Blanch Bigas
May 2016   Prof. Juan Cortina Blanco

Preface

The history of astronomy is as ancient as the reach of our written records. All the human civilizations have been interested in the study and interpretation of the night sky and its objects and phenomena. These observations were performed with the naked eye until the beginning of the seventeenth century, when Galileo Galilei started to use an instrument then developed called telescope. Since then, the range of accessible wavelengths has been increasing, with a burst in the twentieth century with the developing of instruments to observe them: antennas (radio and submillimeter), telescopes (optical, IR) and satellites (UV, X-rays and soft gamma rays). The last wavelength range accessed was the Very High Energy (VHE) gamma rays. At this range fluxes are so low that it is not possible to use space-based instruments with typical collection areas of $\mathcal{O}(1)$ m^2. We must resort to the imaging atmospheric Cherenkov technique, which is based on the detection of the flashes of Cherenkov light that VHE gamma rays produce when they interact with the Earth's atmosphere. The field is very young, with the first source discovered in 1989 by the pioneering Whipple telescope. It is very dynamic with more than 150 sources detected to date, most of them by MAGIC, HESS and VERITAS, that make up the current generation of instruments. Finally, the field is also very promising, with the preparation of a next generation of imaging atmospheric Cherenkov telescopes: CTA, that is expected to start full operation in 2020.

The work presented in this thesis comprises my efforts to take the ground-based γ-ray astronomy one step forward. Part I of the thesis is an introduction to the non-thermal universe and the imaging atmospheric Cherenkov technique. I also give on this part a very detailed description of the hardware, the data taking procedure and the data analysis of the Imaging Atmospheric Cherenkov Telescope (IACT) MAGIC. Finally, I give a glimpse to the future CTA.

Part II deals with several ways to reduce the trigger threshold of IACTs. This includes the simulation, characterization and test of an analog trigger especially designed to achieve the lowest possible energy threshold with the LSTs of CTA. Together with this work, the trigger of the MAGIC telescopes was improved. We have simulated, tested and commissioned a new concept of stereoscopic trigger.

This new system, that uses the information of the position of the showers on each of the MAGIC cameras, is dubbed "Topo-trigger".

The scientific fraction of the thesis deals with galactic sources observed with the MAGIC telescopes. In Part III, I talk about the analysis of the VHE γ-ray emission of Pulsar Wind Nebulae (PWNe). I discovered VHE γ-ray emission from the puzzling PWN 3C 58, the likely remnant of the SN 1181 AD and the weakest PWN detected at VHE to date. I also performed population studies comparing several properties of the central pulsar such as age or spin-down power with the γ-ray luminosity of their surrounding PWNe. In this part, I also characterized the VHE tail of the Crab Nebula by observing it at the highest zenith angles, obtaining that the softening of the spectrum at multi-TeV energies is best represented by a log-parabola function. I also searched for an additional inverse Compton component during the Crab Nebula flares reported by *Fermi*-LAT in the synchrotron regime, not observing a significant enhance of the spectrum at TeV energies with respect to the one measured during non-flaring episodes.

Part IV is concerned with searches for VHE γ-ray emission of cataclysmic variable stars. I studied, on a multiwavelength context, the VHE γ-ray nature of the previously claimed pulsed γ-ray emission of the cataclysmic variable AE Aqr. The result of this search is that we could not confirm the previous claims of VHE γ-ray emission from this object. I also performed observations of novae and a dwarf nova to pinpoint the acceleration mechanisms taking place in this kind of objects and to discover a putative hadronic component of the soft γ-ray emission. With these observations, I obtained upper limits on the amount of accelerated hadrons on this type of objects.

The conclusion chapter summarizes all the work performed and lists prospects related with the topics treated in this thesis.

Barcelona, Spain   Dr. Rubén López Coto
May 2016

Acknowledgements

Una tesis no es cuestión de un puñado de páginas llenas de ecuaciones, resultados y conclusiones. Investigar es una forma de vivir que ciertos individuos hemos elegido, y que probablemente el resto de gente normal no comprenda ni comparta. La *tesis* no empieza el día que te dan una beca, ni el que te aceptan en la escuela de doctorado, ni siquiera el día que inscribes la tesis. Ese sentimiento interior empieza el día en el que lees algo maravilloso, increíble, mágico, pero que es real, y entonces te dices, yo quiero contribuir a eso. En mi caso, eso fue hace ya casi trece años, cuando me enteré que el universo podía caber en una cáscara de nuez…

Para mi, los agradecimientos son las únicas páginas en las que puedes tener la libertad suficiente para sincerarte y mencionar a toda la gente que, de una manera u otra, han contribuido a que todo lo demás sea posible. Es por esto que estas líneas quizás las deba empezar en Madrid, donde junto con Guille, Darío, Kike, Mario y Juan Carlos aprendí que la universidad iba más allá de la facultad de Física y "la resi" un sitio increíble que compartir con ellos.

Un autobús me llevó al calor sevillano en el que viví algunos de los mejores años de mi vida. A los compañeros que pasaron conmigo aquellos años les quiero dar las gracias por haberlo hecho todo tan divertido: estudiar así hace que te entren ganas de quedarte muchos más años en la Facultad. Quiero mencionar especialmente a algunos: Pikiki, amigo y compañero de fechorías, Carlos que me apoyó con su amistad durante mucho tiempo, y sobre todo estaba conmigo aquella mañana (y todo aquel año) en la que nos bajamos de un coche y nos encontramos a un señor con la mano gigante que gritaba *Sprechenstude!!*. A Chema quiero decirle que nunca me olvidaré de los Cancún sin pasar por la ducha y que espero que siga por donde siga no se olvide de sus amigos de aquí. Y Dani y Juanito, un poco de lo mismo, nunca me olvidaré del que sigue siendo uno de los mejores viajes ever, aunque después lo tuviésemos que complementar con clases particulares en la calle Betis.

Three days and half Europe away was Münster, where I did my Erasmus-master. To everybody I met there, *ich mochte euch alles bedanken* for the great time we spent together during "the best year of our lives". I want to let you know that you all

contributed to make me a different, richer and, I want to believe, better person. Un recuerdo especial va, como no podía ser de otra forma, para Clara y Marta. Estos cuatro años en Barcelona habrían sido mucho más intensos con vosotras por aquí. De cualquier forma, quiero que sepáis que ya nada es tan divertido y el Erasmus eterno se quedó, como tantas otras cosas, en aquella camiseta verde. Así que en cierto sentido, sólo os estáis perdiendo la parte aburrida de esta historia.

De vuelta a España mis pasos me llevaron a Granada, donde por fin aprendí qué era la astrofísica y por qué iba a dedicar una parte considerable de mi vida a ella. A toda la gente que conocí allí les quiero decir que me encantó pasar allí aquel año. En especial quería agradecerle a Miguel la oportunidad de empezar a trabajar seriamente en el mundo de la investigación y todas las cosas que aprendí con él durante ese período. A Antxon también le debo no sólo lecciones sobre astrofísica sino también consejos sobre la vida.

Llegados a este punto, tengo que dedicarles un párrafo a los tíos más feos que he conocido desde que empecé esta locura que me ha llevado a tener la oportunidad de escribir estas palabras, y es probable que los más feos a los que conozca nunca. Moi, Fran y Rubén "el guapo", sois unos grandes que hicisteis que el año que pasé en Granada me supiese a muy poco. Para compensar eso, espero seguir conservando vuestra amistad siempre. Esté donde esté, quiero que sepáis que siempre que lo necesitéis puedo ser el Tantra de vuestro jueves, el Labrador de vuestro viernes, los cien eslotis de vuestro sábado o el café del lunes en el que tenga que haber un orden del día para hablar de tantas cosas.

Al final la suerte de la tesis cayó del lado de Barcelona, y digo la suerte porque al empezar me encontré con que tenía no uno, sino dos supervisores a los que no habría podido pedir más - ni mejor - de lo que me han dado. A Juan quiero agradecerle que haya endurecido mi carácter, que me haya dicho sin adornos lo que no quería oír y que me haya enseñado en esa pizarra todas esas cosas de las que no tenía ni idea. A l'Oscar li vull agrair tot el temps que vam passar junts aquests anys, que s'assegués amb mi i es preocupés de la meva feina i d'altres tantes coses. També li vull agrair per deixar-me la llibertat suficient per que m'equivoqués i aprengués d'això. I, és clar, pel català, perquè sense ell mai ho hauria fet servir de la manera que ho faig.

Al Manel li vull agrair que em donés l'oportunitat de fer la tesi a IFAE, em donés suport amb el català i es preocupés des del principi que tot m'anés bé. A Javi le quiero pedir que cuando explote y se haga famoso, se acuerde del Ballbreaker en el que empezó su carrera futbolística. Yo por mi parte, le agradezco que siempre haya tenido un momento para ayudarme en lo que fuese necesario. A Abelardo no me puedo olvidar agradecerle que con su pesimismo le diera un toque mucho más realista a cualquier estimación de la vida cotidiana. I cannot forget here all the postdocs that were at IFAE all these years: thanks to Stefan for teaching me some statistics and for being a great galactic convener, to Victor for the bit of CTA work we shared and John E. "Curie" Ward for sharing with me life and working lessons. I need to specially thank Daniel Mazin and Julian Sitarek. With Daniel, either in Barcelona or in Munich, I shared the obsession for always improving the telescope

he taught me so much about. To Julian I cannot thank him enough all the help he gave me in the programming and physics.

Una parte muy importante de esta tesis es la gente que me ha rodeado en el despacho tanto tiempo mientras miraba una pantalla. Con Roberta sólo lo compartí unos días, pero no se mudó muy lejos y hemos compartido la misma obsesión astrofísica durante estos años. Jeza fue la primera en irse, pero afortunadamente su dulzura de madre me ha estado acompañando todos estos años. A Ignasi le tengo que agradecer que me iniciase en este mundo y me enseñase todo lo que estuvo en su mano. Con Gianluca compartí mi afición a la bicicleta y un viaje inolvidable. Jelena, a pesar de habernos abandonado, sigue en el despacho de al lado con la cualidad de ser tan auténtica como siempre. A Alicia quiero agradecerle que me haya enseñado muchas cosas, sobre todo a que en la vida hay veces en las que te entran ganas de vomitar arcoíris y otras en las que hay que guardárselos. Adiv ha estado ahí todos estos años y quiero decirle que ha sido un gran compañero de viajes recorriendo media Europa. A Dani le quiero agradecer su humor sarcástico y sus comentarios ácidos que siempre nos sacan una sonrisa. A Quim no se si decirle nada porque no se si vendrá a ver la tesis, pero si tengo que agradecerle algo es su visión particular e inocente del mundo, que hace que los demás nos planteemos la nuestra. Pero para inocencia pura Leyre, tanto que a veces hasta me sabe un poco mal que se crea todas las cosas que le cuento, pero se me pasa pronto. Tarek quiero que sepa que me lo pasé muy bien en los meetings de CTA y es un gran fichaje para el equipo del IFAE en todos los aspectos. Tito ha pasado demasiado poco tiempo como para que le pueda contagiar mi realismo, pero estoy seguro de que he dejado una buena semilla. Aunque no sea en el despacho, Carlos nos ha amenizado los almuerzos y otras muchas cosas, por eso quería agradecerle el tener siempre la razón con tanto suaj. No me puedo olvidar de Pol, Pauline, Carlitos, Raúl… a los que no conozco hace tanto pero también me han acompaãdo estos últimos meses. Y por último y aunque no esté en IFAE, Dani Garrido ha estado conmigo desde aquel frío Enero en Zeuthen, y por lo que parece también vamos a llegar juntos a la meta. A él le quiero dar las gracias por haber sido siempre tan sincero.

No puedo olvidarme de dar las gracias al resto de la gente que ha estado conmigo en IFAE o Barcelona estos años. Los ingenieros que tantos problemas han resuelto con LabView, un soldador o simplemente un trozo de cinta aislante: Juan, Pepe y Oscar. A Cristina, por siempre cuidar de sus niños. Al resto de gente de IFAE, en especial a Enrique Fernández por ser mi tutor, y a los directores Matteo y Ramón por haberme ayudado cuando les fue posible. A la gente del ICE, en especial Nataly, Jonatan y Daniela. A los de la UB: Josep Maria, Marc, Pere, Benito y Xavi. Y a los médicos, porque ellos también han formado parte de esta historia.

Munich was my second house during long periods of time, that is why I want to thank the people I have not mentioned yet: Masahiro, Razmik, Thomas, David, Koji, Pierre, Susumu, Francesco D., Miquel, Priya, Wojtek, Francesco B., Christian, Uta, Marcel, Takeshi and Sybille. You are a great group and made me feel part of it since the first day.

Declaration

I herewith declare that I have produced this thesis without the prohibited assistance of third parties and without making use of aid other than those specified; notions taken over directly or indirectly from other sources have been identified as such. This paper has not previously been presented in identical or similar form to any other Spanish or foreign examination board.

The thesis work was conducted from September 2011 to July 2015 under the supervision of Juan Cortina Blanco and Oscar Blanch Bigas at Barcelona.

Barcelona, Spain   Rubén López Coto
July 2015

Contents

Units and Prefixes

Units

Abbreviature	Name	Equivalence
m	meter	
s	second	
V	volt	
kg	kilogram	
eV	electronvolt	1.60×10^{-19} kg m^2 s^{-2}
erg	ergio	624.15 GeV
Hz	hertz	1 s^{-1}
Jy	jansky	10^{-26} erg s^{-1} cm^{-2} Hz^{-1}
pc	parsec	3.086×10^{16} m
d	day	8.64×10^4 s
yr	year	3.154×10^7 s

Prefixes

Abbreviature	Prefix	Equivalence
E	Exa	10^{18}
P	Peta	10^{15}
T	Tera	10^{12}
G	Giga	10^{9}
M	Mega	10^{6}
k	kilo	10^{3}
-	-	10^{0}
c	centi	10^{-2}
m	mili	10^{-3}
μ	micro	10^{-6}
n	nano	10^{-9}
p	pico	10^{-12}

Acronyms and Abbreviations

1FHL	First *Fermi*-LAT high-energy catalog
2FGL	Second *Fermi*-LAT catalog
2PC	Second *Fermi*-LAT pulsar catalog
a.s.l.	Above sea level
AAVSO	American Association of Variable Star Observers
ACTA	Amplifier for the Cherenkov Telescope Array
AD	Anno Domini
ADC	Analog-to-Digital Converter
AE Aqr	AE Aquarii
AGASA	Akeno Giant Air Shower Array
AGILE	Astrorivelatore Gamma ad Imagini Leggero
AGN	Active Galactic Nuclei
Al	Aluminum
AMC	Active Mirror Control
AP	After Pulse
APNS	Accretion-Powered Neutron Star
Ar	Argon
ARGO-YBJ	Astrophysical Radiation with Ground-based Observatory at YangBaJing
ASCA	Advanced Satellite for Cosmology and Astrophysics
ASDC	ASI Science Data Center
ASIC	Application-Specific Integrated Circuit
ASTRI	Astrofisica con Specchi a Tecnologia Replicante Italiana
Az	Azimuth
BAT	Burst Alert Telescope
BC	Before Christ
BH	Black Hole
BJD	Barycentric Julian Date
C	Carbon
C.L.	Confidence Level

C.U.	Crab Units
Cas A	Cassiopeia A
CC	Central Control
CCD	Charge-Coupled Device
CCO	Compact Central Object
CH	Counting House
CIEMAT	Centro de Investigaciones Energéticas Medioambientales y Tecnológicas
CMB	Cosmic Microwave Background
CN	Classical Nova
CoG	Center of Gravity
CORSIKA	COsmic Ray SImulations for KAscade
CR	Cosmic Ray
CTA	Cherenkov Telescope Array
CV	Cataclysmic Variable
DAQ	Data AcQuisition
DC	Direct Current
DEC	Declination
DESY	Deutsches Elektronen SYnchrotron
DN	Dwarf Nova
DRS	Domino Ring Sampler
DT	Discriminator Threshold
EAS	Extended Air Shower
EM	Electromagnetic
EUVE	Extreme Ultraviolet Explorer
EWD	Ejector White Dwarf
FADC	Flash Analog-to-Digital Converter
Fe	Iron
FILAR	Four Input Links for ATLAS Readout
FIR	Far Infrared
FoV	Field of View
FWHM	Full Width Half Maximum
GCN	GRB Coordinate Network
GPS	Global Positioning System
GRB	Gamma-Ray Burst
GZK	Greisen–Zatsepin–Kuzmin
H	Hydrogen
HE	High Energy
He	Helium
HEASARC	High Energy Astrophysics Science Archive Research Center
HEGRA	High Energy Gamma-Ray Astronomy
HESS	High Energy Stereoscopic System
HiRes	High Resolution Fly's Eye Experiment
HOLA	High Optical Link ATLAS
HPD	Hybrid Photo Detector

HV	High Voltage
IACT	Imaging Atmospheric Cherenkov Telescope
IC	Inverse Compton
IDL	Interface Description Language
IFAE	Institut de Física d'Altes Energies
INAF	Istituto Nazionale di AstroFisica
INS	Isolated Neutron Star
IPRC	Individual Pixel Rate Control
IR	Infrared
IRAF	Image Reduction and Analysis Facility
IRF	Instrument Response Function
ISM	Interstellar Medium
IUE	International Ultraviolet Explorer
KVA	Kungliga Vetenskapsakademien telescope
L0	Level 0
L1	Level 1
L3	Level 3
LAT	Large Area Telescope
LED	Light-Emitting Diode
LIDAR	LIght Detection And Ranging
LST	Large Size Telescope
LUT	Look-Up Table
LVDS	Low-Voltage Differential Signaling
LWP	Long Wavelength Primary
MAGIC	Major Atmospheric Gamma-ray Imaging Cherenkov
MARS	MAGIC Analysis and Reconstruction Software
MC	Monte Carlo
MHD	Magnetohydrodynamic
MJD	Modified Julian Day
MOLA	MAGIC OnLine Analysis
MST	Medium Size Telescope
N	Nitrogen
Ne	Neon
NECTAr	New Electronics for the Cherenkov Telescope Array
NN	Next Neighbor
NOT	Nordic Optical Telescope
NS	Neutron Star
NSB	Night Sky Background
O	Oxygen
OG	Outer Gap
PACTA	Pre-Amplifier for the Cherenkov Telescope Array
PC	Polar Cap
PCI	Peripheral Component Interconnect
phe	Photoelectrons
PMT	Photomultiplier Tubes

PSF	Point Spread Function
PULSAR	PULSer And Recorder
PWN	Pulsar Wind Nebula
QE	Quantum Efficiency
QED	Quantum Electrodynamics
RA	Right Ascension
RD	Red Dwarf
RF	Random Forest
RMS	Root Mean Square
RN	Recurrent Nova
RoI	Region of Interest
ROSAT	ROentgen SATellite
RPP	Rotation-Powered Pulsar
RRAT	Rotating Radio Transient
SAO	Smithsonian Astrophysical Observatory
SBIG	Santa Barbara Instrument Group
SCT	Schwarzschild-Couder Telescope
SED	Spectral Energy Distribution
SG	Slot Gap
Si	Silicon
SiPM	Silicon PhotoMultiplier
SN	Supernova
SNR	Supernova Remnant
SSC	Synchrotron Self Compton
SST	Small Size Telescope
STIS	Space Telescope Imaging Spectrograph
SWP	Short Wavelength Primary
TA	Telescope Array
TED	Test Experimental Device
TIB	Trigger Interface Board
ToO	Target of Opportunity
ToT	Time over Threshold
TPU	Trigger Processing Unit
TS	Test Statistics
UB	Universitat de Barcelona
UHECR	Ultra High Energy Cosmic Ray
UL	Upper Limit
UT	Universal Time
UV	Ultraviolet
UVOT	Ultraviolet/Optical Telescope
V_{in}	Input Voltage
V_{out}	Output Voltage
VCSEL	Vertical Cavity Surface Emitting Laser
VERITAS	Very Energetic Radiation Imaging Telescope Array System
VHE	Very High Energy

VLA	Very Large Array
VME	Virtual Mobile Engine
WD	White Dwarf
WP	Working Package
XMM-Newton	X-ray Multi-Mirror Mission-Newton
XRT	X-ray Telescope
XRTDAS	XRT Data Analysis Software
Zd	Zenith distance

List of Figures

List of Tables

Part I
Introduction

Fig. 1 Air shower. Credit: Fabian Schmidt

Chapter 1
Short Introduction to Cosmic Ray and γ-Ray Astronomy

Astronomy can be described as the science that allows us to understand the physics of the phenomena that occur outside our atmosphere. Until the beginning of the 20th century, astronomical studies only dealt with thermal phenomena. This changed when Viktor Hess, after a series of balloon flights, measured an increase of the density of ionized particles with altitude (Hess 1912), and attributed it to a radiation source outside the Earth's atmosphere, later called Cosmic Rays (CRs). This kind of radiation, that reaches energies up to 10^{20} eV, is so energetic that cannot be produced in a thermal processes. Otherwise, the temperature of the body producing it would have to be close to that existing in the early stages of the Big Bang. Apart from CRs, one can observe the products of non-thermal processes along the whole Electromagnetic (EM) spectrum, from radio to VHE gamma rays.

CRs are the particles with the highest energies known and their study allows to understand the composition and evolution of the universe. However, since they are charged particles, they are deflected by the randomly oriented magnetic fields they find in their travel to the Earth. This implies that their arrival directions are almost randomly distributed in the Earth's atmosphere and their origin cannot be traced back, unless their energy exceeds the ∼EeV, at which energy their trajectories are not bent for distances of ∼tens of Mpc. Therefore, the study of CRs only produce results about their composition, energy spectrum and possible anisotropies of the ones with energies above EeV. To study sources accelerating them, one has to observe neutral particles not deflected by magnetic fields, such as photons or neutrinos. The latter are very difficult to be detected because they only interact with other particles by weak interaction, their cross-sections are very small. Since the topic of this work is the VHE γ-ray astrophysics, in this chapter I will first give a glimpse to the CR astrophysics, historically closely related to the study of gamma rays. Later, a more detailed description of the processes generating gamma rays and the γ-ray astrophysics will be described.

1.1   Cosmic Rays

The study of CRs started with Viktor Hess' discovery. At the beginning, it was thought that CRs were a new type of energetic radiation and that is why the term coined by Robert Millikan in 1926 is misleading (Millikan and Cameron 1926). It was some years later when it was discovered that CRs had a corpuscular nature (Bothe and Kolhörster 1929). The term is now used to designate particles coming from the outer atmosphere. In 1938 Pierre Auger showed that CRs could initiate Extended Air Showers (EASs) extending hundreds of meters on the ground and producing millions of secondary particles. He calculated that the primary particles generating the shower should have ∼PeV energies. The early study of CRs was very productive to discover new particles such as the positron, muon, kaon and pion. CRs are currently studied using balloon experiments, detectors placed at satellites and extended ground installations to detect the particles produced in air showers. There are several open questions regarding CRs such as how and where they are originated, their composition at the highest energies and the maximum energy they can reach.

1.1.1   Spectrum and Chemical Composition

The all-particle spectrum of CR radiation as seen from the Earth is shown in Fig. 1.1. It peaks at energies of ∼100 MeV and extends up to ∼10^{20} eV. The solar magnetic field blocks most of the particles coming from outside the solar system below 1 GeV, therefore CRs below this energy are of solar origin. Between 100 GeV and 5 PeV the CR spectrum follows a power-law with photon spectral index $\Gamma \sim 2.7$. The transition region is known as the knee and is charge dependent (particles with higher charge peak at higher energies). Particles with energies below the knee are thought to be of galactic origin and those above the knee are probably extragalactic. Between 5 PeV and 3 EeV, the spectrum follows a power-law with photon spectral index $\Gamma \sim 3.0$. Between 3 EeV up to 30 EeV the spectrum hardens to a $\Gamma \sim 2.6$ spectral index. Above 30 EeV, the spectrum undergoes a severe cut-off limit due to the interaction of cosmic rays with CMB, the so-called "GZK cut-off". Figure 1.2 shows recent results of the Auger and TA collaborations in the region where the GZK cut-off is expected. CRs are mainly composed by protons and helium nuclei (99 %), but a minority are heavier nuclei, electrons, positrons, antiprotons and neutrinos. Gamma rays, usually classified as CRs as well, represent a tiny fraction of the CRs arriving to the atmosphere.

1.1.1.1   The GZK Cut-Off

The interaction between the cosmic rays and the CMBs radiation sets the highest energy up to which CRs can be observed. When a CR with energy $\gtrsim 10^{20}$ eV interacts with the CMB, they produce hadrons through Δ resonance:

Fig. 1.1 Cosmic-ray
spectrum observed from the
Earth. From Hanlon (2010)

Cosmic Ray Spectra of Various Experiments
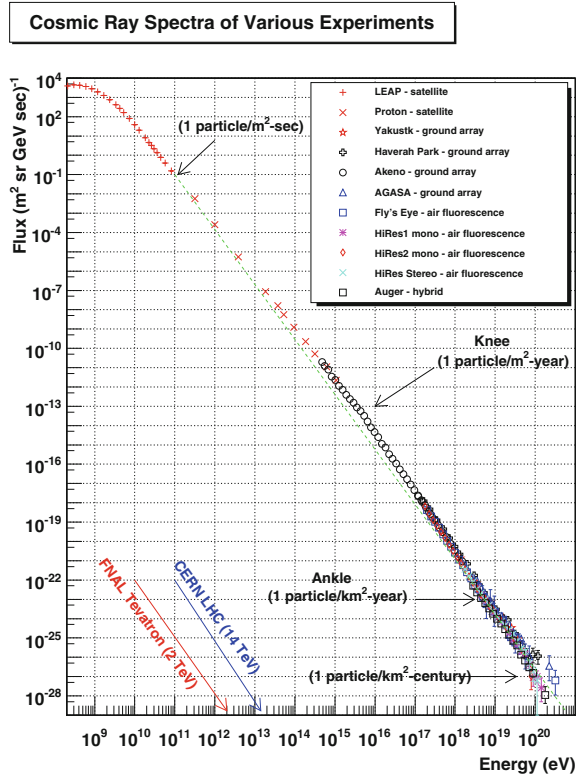
Fig. 1.2 Auger and
Telescope Array results for
the CR flux at the highest
energies measured. From
Matthews (2014)

$$p + \gamma_{\text{CMB}} \rightarrow \Delta^+ \rightarrow p + \pi^0$$
$$p + \gamma_{\text{CMB}} \rightarrow \Delta^+ \rightarrow n + \pi^+ \tag{1.1}$$
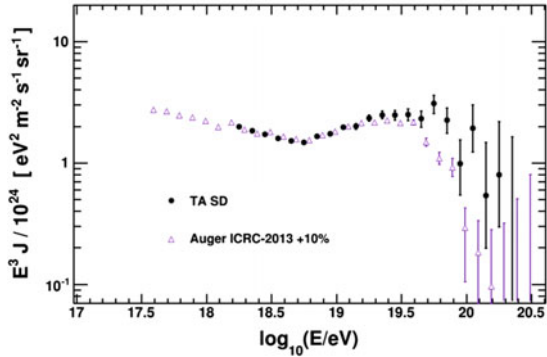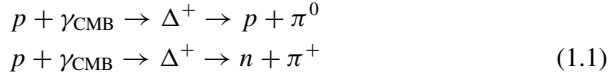
This limits the maximum distance that CRs of energies $>10^{20}$ eV can travel to 50 Mpc. It was computed simultaneously by Kenneth Greisen, Vadim Kuzmin and Georgiy Zatsepin in 1966 (Greisen 1966; Zatsepin and Kuzmin 1966). The existence of the GZK cut-off was a matter of debate due to the AGASA measurement of several events above the GZK limit (Takeda 1998; Hayashida 1998). These results, however, have not been confirmed by subsequent measurements by the HiRes, Auger and TA collaborations.

1.1.2   Cosmic Ray Production

Only a few features are present in the CR spectrum. This makes plausible that the acceleration mechanism for the bulk of CRs is the same. It is generally believed that CRs get accelerated as they repeatedly cross the same astronomical shock. This mechanism was proposed by Fermi (Fermi 1949). Depending on the characteristics of the moving plasma we can differentiate between *first* and *second order* Fermi acceleration.

The first order Fermi acceleration occurs when particles moving through a shock wave encounter magnetic field inhomogeneities. The particle might be reflected back through the shock and gain energy. The energy gained every time the particle crosses the shock is proportional to the velocity of the shock. The number of times the particle crosses the shock is proportional to its magnetic field.

The second order Fermi acceleration occurs when a charged particle interacts with a moving magnetized cloud. The energy gained by the particle per interaction is proportional to the square of the speed of the moving cloud.

Considering that CRs are accelerated by the Fermi mechanism, the particle's gyroradius cannot exceed the size of the acceleration region, otherwise it would not be confined to this region anymore. The maximum energy E_{max} reached by a particle with charge Z accelerated in a region with radius R where a magnetic field B is present is given by:

$$E_{\text{max}} \approx 10^{18} \text{ eV } Z \left(\frac{R}{\text{kpc}} \right) \left(\frac{B}{\mu\text{G}} \right) \tag{1.2}$$

Figure 1.3 shows the so-called "Hillas plot", which displays the magnetic field of a source as a function of its physical size for possible candidates to accelerate CRs. The straight lines list the space available for sources capable to reach a certain CR energy. Possible sources of CRs are:

Fig. 1.3 Magnetic field and typical size of several potential sources of UHECRs. The *lines* indicate that the confinement radius requirement for a particular particle with the indicated energy does not exceed the source size. Sources below each line cannot produce CRs with an energy larger than the indicated value. From Hillas (1984)
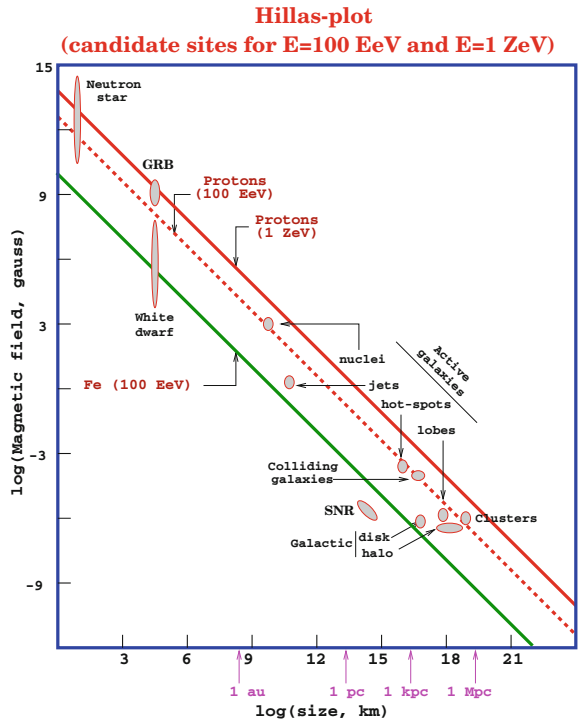
Galactic sources

- Pulsars
- Supernova Remnants (SNRs)
- PWNe
- Binary systems
- Young stars

Extragalactic sources

- Active Galactic Nuclei (AGN)
- Gamma-Ray Bursts (GRBs)
- Starburst galaxies
- Clusters of galaxies

1.2 γ-Ray Astrophysics

In the most violent non-thermal processes, photons of the highest possible energies, the gamma rays, are produced. γ-ray astrophysics studies the EM spectrum beyond energies of $\sim$1 MeV and it is divided into several energy domains, all of them shown in Table 1.1.

Table 1.1 Energy domains of the γ-ray astrophysics

Name	Abbreviation	Energy range
Low energy	LE	1 MeV–30 MeV
High energy	HE	30 MeV–50 GeV
Very-high energy	VHE	50 GeV–100 TeV
Ultra-high energy	UHE	100 TeV–100 PeV
Extremely-high energy	EHE	>100 PeV

1.2.1 Detection Techniques

The atmosphere is not transparent to this radiation, therefore it must be detected from satellites or indirectly using ground-based telescopes. The study performed in this thesis in centered on the VHE γ-ray domain.

- **Satellites**

  Detectors on-board satellites are typically used to detect gamma rays with energies below few hundred GeV. They detect photons using different techniques, depending on their energy: the dominant interaction process is Compton scattering below 30 MeV and pair production above 30 MeV. Satellite detectors have a very good γ/hadron separation, although their angular resolution below GeV energies is very poor (above 0.5°). An additional advantage is that they can be calibrated before launch, a fact that results in a smaller systematic error in the energy determination. In addition, they have a high duty cycle, being able to observe almost all the time.

- **Imaging Atmospheric Cherenkov Telescopes (IACTs)**

  The flux of VHE sources is so low that the maximum area available on-board satellites ($\sim$1 m^2) does not allow to collect sufficient number of photons. To detect such low fluxes, a technique based in the detection of the Cherenkov light emitted by these gamma rays when they interact with the molecules in the atmosphere is used. It is known as the imaging atmospheric Cherenkov technique and will be described in detail in Sect. 2.1.3. Using arrays of telescopes, one achieves collection areas of the order of $\sim$km^2, several orders of magnitude larger than satellites. They are sensitive to the background of the light of night sky, so they can only observe during dark time.

- **Air shower arrays**

  Gamma rays with energies in excess of $\sim$100 GeV produce particle cascades that reach the ground where they can be detected using different techniques. The most successful one is the water Cherenkov technique. This technique measures

the Cherenkov light produced by the cascade particles as they cross water tanks equipped with photomultipliers. They have higher energy threshold, worst angular ($>1°$) and worse energy resolution than the IACTs, but their collection areas are larger, therefore they are able to detect the low fluxes at multi-TeV energies. These arrays have also large duty cycles since they can also work during daytime.

1.2.2 Mechanisms for γ-Ray Production

There are several processes that involve the production of VHE gamma rays. They are schematically depicted in Fig. 1.4. We will briefly describe them in the following. For more information, please refer to Longair (1992), Aharonian (2004).

(a) Pion decay.

(c) Bremsstrahlung.

(b) Synchrotron radiation.

(d) Inverse Compton.
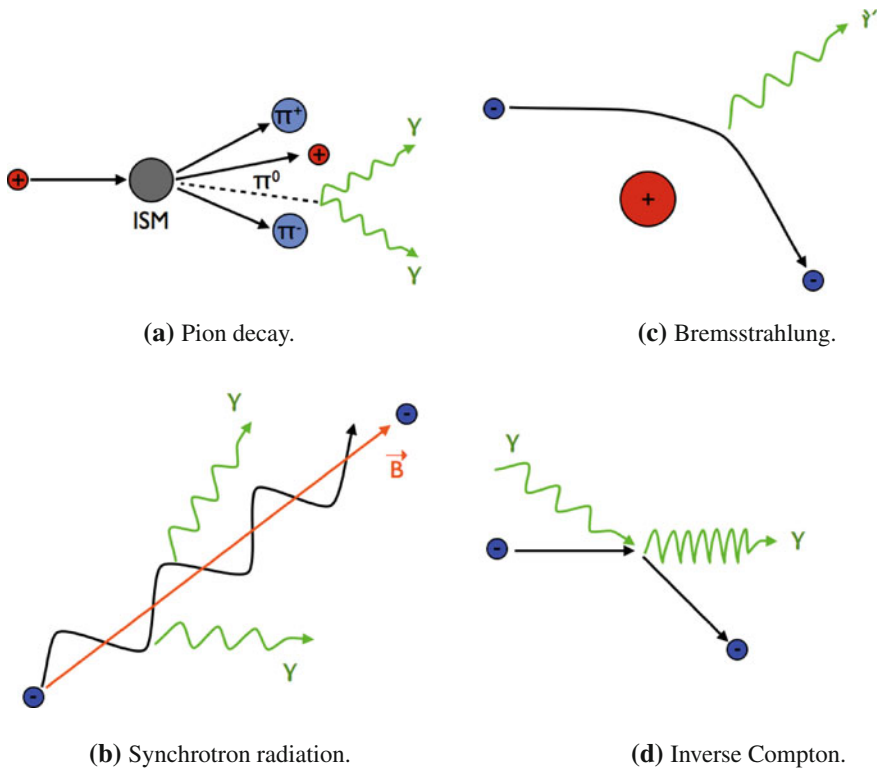
Fig. 1.4 VHE γ-ray production mechanisms

1.2.2.1 Pion Decay

It is the main mechanism of γ-ray production from hadron interactions. When CRs interact with matter in the acceleration region or the Interstellar Medium (ISM) producing pions kaons and hyperons in their decay. Charged (π^+, π^-) and neutral (π^0) pions are produced with the same probability. Neutral pions decay producing two photons in most of the cases:

$$\pi^0 \rightarrow \gamma + \gamma \qquad (99\,\%)$$
$$\pi^0 \rightarrow \gamma + e^- + e^+ \quad (1\,\%)$$

and if the kinetic energy of the original hadron is high enough, the photons emitted are of γ-ray nature.

1.2.2.2 Inverse Compton Scattering

Most of the VHE γ-ray photons we detect are produced by Inverse Compton (IC). Relativistic leptons up-scatter photons and transfer them part of their energy, converting them in higher energy photons. To calculate the interaction cross-section between electrons and photons, one has to take into account the energy of the primary photon and electron. If the energy is low enough, we can ignore relativistic effects. We distinguish three regimes:

$$E_\gamma E_e \ll m_e^2 c^4; \ \sigma = \tfrac{8}{3}\pi r_e^2 \qquad\qquad\qquad \text{(Thomson cross-section)}$$
$$E_\gamma E_e \approx m_e^2 c^4; \ \sigma = 2\pi r_e^2 \left\{ \tfrac{1+\epsilon}{\epsilon} \left[\tfrac{2+2\epsilon}{1+2\epsilon} - \tfrac{\ln(1+2\epsilon)}{\epsilon} \right] + \tfrac{\ln(1+2\epsilon)}{2\epsilon} - \tfrac{1+3\epsilon}{(1+2\epsilon)^2} \right\} \ \text{(Klein$-$Nishina cross-section)}$$
$$E_\gamma E_e \gg m_e^2 c^4; \ \sigma = \pi \tfrac{1}{\epsilon} r_e^2 \left[\ln(2\epsilon) + \tfrac{1}{2} \right] \qquad\qquad \text{(Klein$-$Nishina approximation)}$$

where E_γ is the energy of the photon, E_e the energy of the lepton, r_e is the classical electron radius and $\epsilon = E_\gamma / m_e c^2$. It can be shown that in the latter case, the maximum energy reached by the photons is given by:

$$E_{max} \approx 4\gamma^2 E_\gamma \qquad\qquad\qquad (1.3)$$

where γ is the Lorentz factor of the leptons. Photons emitted in the Thomson regime follow the spectral shape of the seed photons, whereas those in the Klein–Nishina regime suffer a very sharp cut-off due to relativistic effects.

1.2.2.3 Synchrotron Radiation

It is produced when ultrarelativistic electrons are accelerated in a magnetic field. The electrons trace spirals around the magnetic field lines. The emitted photons peak at an energy $E_{max} = 5 \times 10^{-9} B_\perp \gamma^2$, where $B_\perp$ is the magnetic field perpendicular to the electrons movement and γ is the Lorentz factor of the electrons. Synchrotron

photons do not usually achieve VHE, although they are of special interest for VHE gamma rays because they serve as targets for IC up-scattering.

Curvature Radiation It is similar to synchrotron radiation, although instead of moving around the magnetic field lines, the electrons emit radiation when they move following the curved magnetic field lines.

1.2.2.4 Electron Bremsstrahlung

It is produced when a charged particle is deflected by the presence of an electric field. Gamma rays produced by bremsstrahlung usually have energies of MeV, although the deflection of UHECRs may produce VHE gamma rays.

1.2.3 Sources of VHE Gamma Rays

At the time of writing this thesis, there are more than 150 established VHE γ-ray sources.[1] I will give a brief description of all the types:

Galactic sources

- Pulsars:

  Pulsars are rotating magnetized Neutron Stars (NSs) (we will give more details in Sect. 5.2). Particles get accelerated in specific regions of the NS magnetosphere. Photons are produced in a narrow emission beam. Since the rotation and the magnetic axes are usually not aligned, we observe EM emission only when the beam crosses the line of sight. The first pulsed VHE gamma rays were discovered by MAGIC in 2008 (Aliu et al. 2008). The spectrum was extended above 100 GeV by VERITAS (Aliu et al. 2011), up to 400 GeV by MAGIC (Aleksić et al. 2012) and very recently up to TeV energies (Zanin 2014). Pulsed VHE gamma rays may be due to IC scattering. Recently, also pulsed emission from the Vela pulsar was reported by HESS (Brun 2014), although the emission mechanism remains unclear.

- SNRs

  SNRs are the leftovers of Supernova (SN) explosions. CRs get accelerated through the Fermi mechanism in the shock that develops when the SN ejecta interact with the ISM. VHE gamma rays are thought to be of hadronic origin, although it remains to be confirmed (Gabici and Aharonian 2015). An example of a classical SNR where the origin of the emission could not be determined can be found in Aharonian et al. (2004). A more detailed description is given in Sect. 5.1.2.

---

[1]http://tevcat.uchicago.edu/.

- PWNe

  Pulsars lose their rotational energy mainly through an $e^{\pm}$ wind that interacts with the ISM and the SNR where it is contained. Some leptons are eventually accelerated and emit EM radiation from radio up to gamma rays via synchrotron emission and VHE gamma rays via IC scattering of ambient photons. They are described in detailed in Chap. 5. There are currently 22 PWNe and PWN candidates detected at VHE gamma rays (all of them can be found in Table B.9 in Appendix B.5), the latest of which is 3C 58, described in Chap. 7.

- γ-ray binaries

  They consist of a compact object (a NS or a Black Hole (BH)) that is orbiting a massive star. Five such objects are known to emit VHE gamma rays to date: LS I +61 303, HESS J0632+057, HESS J1018-589, PSR B1259-63 and LS 5039. There are several explanations for the observed VHE γ-ray emission. In the microquasar scenario, accretion into the compact object produces a jet where particles get accelerated. In the pulsar wind scenario, a pulsar orbits the massive star, the pulsar wind interacts with the companion wind, and a shock develops, where particles get accelerated.

Extragalactic sources

- AGN

  They are galaxies hosting a supermassive BH in their center. Two plasma jets carrying part of the object's angular momentum are emitted perpendicular to the accretion disk. The jet extends for several kpc distance. Particles get accelerated in shocks traveling along the jet. The behavior of the AGN seems to strongly depend on the viewing angle of the jet from the Earth.

- Starburst galaxies

  They are galaxies with a high star formation rate. As a consequence, the SN explosion rate and the CR density are larger than usual, providing shocks strong enough to accelerate particles that emit VHE gamma rays. Two starburst galaxies have been detected at VHE: NGC 253 and M82.

- GRBs

  They are the most energetic γ-ray outbursts known. No GRBs have been detected by IACTs so far, but *Fermi*-LAT has detected photons at 95 GeV from GRB 130427A (Ackermann et al. 2014). Their origin is still under debate, although the main accepted mechanisms are to be either hypernova explosions or the merger of two compact objects.

References

Ackermann M et al (2014) Science 343:42

Aharonian F (2004) Very high energy cosmic gamma radiation: a crucial window on the extreme Universe. World Scientific

Aharonian F et al (2004) Nature 432:75

Aleksić J et al (2012) A&A 540:A69

Aliu E et al (2008) Science 322:1221

Aliu E et al (2011) Science 334:69

Bothe W et al (1929) Zeitschrift fur Physik 56:751

Brun P (2014) In: Very high energy phenomena in the universe

Fermi E (1949) Phys Rev 75:1169

Gabici S et al (2015). arXiv:1502.00644

Greisen K (1966) Phys Rev Lett 16:748

Hanlon WF (2010) http://www.physics.utah.edu/~whanlon/spectrum.html

Hayashida N et al (1998) apjl 504:0

Hess VF (1912) Z Phys 13:1084

Hillas AM (1984) Ann Rev Astron Astrophys 22:425

Longair MS (1992) High energy astrophysics. Cambridge University Press, Cambridge

Matthews J (2014) In: Very high energy phenomena in the universe

Millikan RA et al (1926) Phys Rev 28:851

Takeda M et al (1998) Phys Rev Lett 81:1163

Zanin R (2014) V Fermi symposium proceedings

Zatsepin GT et al (1966) J Exp Theor Phys Lett 4

Chapter 2
The Imaging Atmospheric Cherenkov Technique and the IACTs MAGIC and CTA

In this chapter we will describe the concept behind the detection of gamma rays through the imaging atmospheric Cherenkov technique. We will also describe the IACT arrays on which this thesis focuses: the Major Atmospheric Gamma-ray Imaging Cherenkov (MAGIC) telescopes and the Cherenkov Telescope Array (CTA). The hardware and techniques used to analyze the data of MAGIC will be described in detail. We will give an overview of the CTA project, together with a brief description of the telescope types involved in the project.

2.1 The Imaging Atmospheric Cherenkov Technique

The EM spectrum spans more than 20 orders of magnitude in energy from radio to TeV gamma rays. The atmosphere is transparent to most of the radiation up to the UV, but higher energy photons do not penetrate into the atmosphere due to their interaction with the air molecules. A picture showing the bounds of the EM spectrum and the transparency of the atmosphere to all of them is shown in Fig. 2.1. To detect those photons, one has to use satellites where they have not been blocked yet. Unfortunately, due to the low fluxes, the collection area offered by satellites is not large enough at energies exceeding 100 GeV.

Due to the interaction with the atmospheric nuclei, VHE particles produce cascades, also known as EASs. As the relativistic charged particles produced in the cascade move faster than the speed of light in the atmosphere, they produce Cherenkov light at wavelengths ranging from IR to UV. In the following, we will give a more detailed description of the shower development in the atmosphere and the way we can detect the Cherenkov light using optical telescopes. For a more detailed review, see Engel et al. (2011).
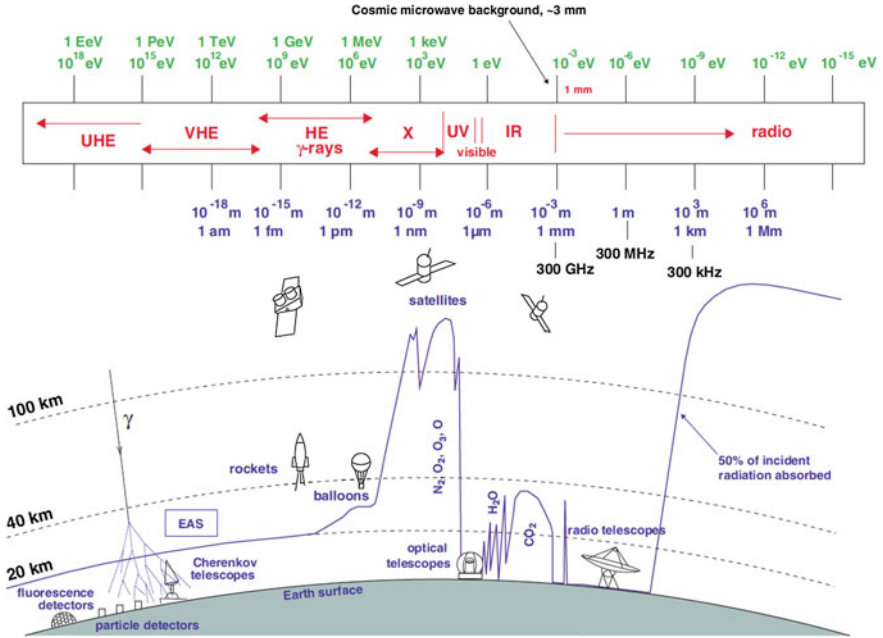
Fig. 2.1 The bounds of the EM spectrum (*above*) as seen from the altitude where photons are fully absorbed in the atmosphere (*below*). From Longair (1992), Moralejo (2000), Wagner (2006)

2.1.1 Types of Showers

To describe the particle interaction with the air nuclei it is better to describe the atmosphere in terms of the so-called *atmospheric depth X*, which is the product of particle density and distance or the amount of mass per unit of area that an incident particle encounters on its path. For vertical incidence, the atmospheric depth at sea level is $X_{air} \sim 1013\,\mathrm{g\ cm^{-2}}$. We will describe the characteristics of the particle cascades produced depending on the primary particle initiating the shower.

2.1.1.1 EM Showers

When a gamma ray enters into the atmosphere, if its energy is $E \gtrsim 20\,\mathrm{MeV}$, it undergoes $e^{\pm}$ pair creation in the presence of an air nucleus. These e^- and e^+ suffer bremsstrahlung if their energy exceeds the critical energy $E_C = 86\,\mathrm{MeV}$, which is the energy for which energy losses by bremsstrahlung and ionization are equal. The bremsstrahlung process produces photons that are still very energetic, undergoing further pair production. Eventually, a so-called EM shower of e^-, e^+ and gamma rays develops (see left panel of Fig. 2.2). The energy loss dE of an e^- with path dx due to bremsstrahlung can be written as:
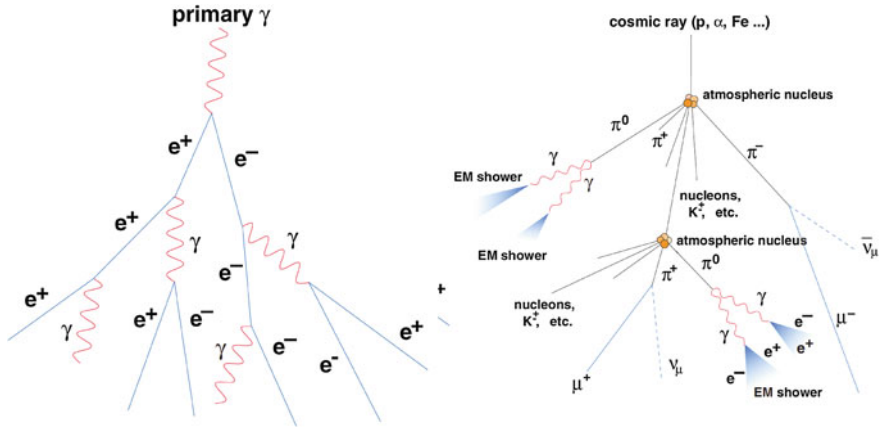
Fig. 2.2 Scheme of an EM (*left panel*) and hadronic (*right panel*) initiated showers. Taken from Wagner (2006)

$$\frac{dE}{dx} = -\frac{E}{X_0^e} \tag{2.1}$$

where $X_0^e = 37.2\,\mathrm{g\,cm^{-2}}$ is the radiation length for an $\mathrm{e^-}$ (or $\mathrm{e^+}$) in air. The radiation length of a γ-ray photon X_0^γ can be written as a function of that of the electron: $X_0^\gamma = 7/9 X_0^e$. An EM shower is roughly symmetric with respect to the shower axis. The first interaction point is not very dependent on the γ-ray energy and is situated at a height of about 20–30 km above sea level (a.s.l.) for a vertically incident particle. Roughly speaking, the number of particles is doubled each step of the cascade, and the energy of the particles halved. When the energy of $\mathrm{e^\pm}$ reaches E_C, the cascading stops and the number of particles is maximum. The height a.s.l. at which this condition is fulfilled is known as *height* of the shower maximum (H_{max}). This height is inversely proportional to the logarithm of the energy $H_{\mathrm{max}} \propto 1/\ln(E)$ of the primary gamma ray.

2.1.1.2 Hadronic Showers

When the primary particle generating the EAS is a hadron, the first interaction with an atmospheric nucleus is governed by the strong force. In this process, mostly pions are created (90 %, in roughly equal proportions $\pi^0 : \pi^+ : \pi^- \to 1 : 1 : 1$) as well as kaons (10 %) and light baryons (p, $\bar{\mathrm{p}}$, n, $\bar{\mathrm{n}}$) in a much smaller proportion. Hadrons and pions undergo further collisions. The shower grows until the energy per nucleon reaches the minimum energy required for pion production decay ($\sim$1 GeV). In addition pions decay into photons, $\mathrm{e^-}$, $\mathrm{e^+}$ and muons, generating secondary EM and muon-initiated showers. The pionic and muonic decays involved in a hadronic shower are the following:

$$\pi^0 \longrightarrow \gamma\gamma \quad ; \pi^+ \longrightarrow \mu^+\nu_\mu \quad ; \pi^- \longrightarrow \mu^-\bar{\nu}_\mu$$
$$\mu^+ \longrightarrow e^+\nu_e\bar{\nu}_\mu \ ; \ \mu^- \longrightarrow e^-\bar{\nu}_e\nu_\mu$$

As illustrated in the right panel of Fig. 2.2, several EM subcascades are generated. Apart from that, due to the strong interaction, the transverse momentum of secondary hadrons is larger than that of leptons in EM showers, therefore hadronic showers are wider.

The timing of the showers is also important to differentiate them. γ-ray initiated showers develop in less than 3 ns for impact parameters smaller than the hump (the region where the Cherenkov photon density is highest), while hadron-initiated ones take more than 10 ns to develop. Figure 2.3 shows MC simulations of two EASs produced by a gamma ray and a proton of the same energy. One can clearly see the γ-ray showers are more "beamed" than proton showers.

2.1.2 Cherenkov Light

The existence of Cherenkov light was first proposed by Pavel Cherenkov (1934). It is an effect produced by ultrarelativistic charged particles moving at a speed faster than the speed of light in the medium. A charged particle moving at a speed v in a medium with refraction index n, the medium polarizes along its track. If the speed of the particle is $v < c/n$, where c is the speed of light in vacuum, the polarization is symmetrical and no electric field is produced at long distances (see Fig. 2.4a). On the other hand, if the speed of the particle is $v > c/n$ it moves faster than the EM radiation that induces the polarization, which is not symmetric anymore as shown in Fig. 2.4b. To compensate the effect of a non-symmetric dipole medium, an EM shock wave called Cherenkov radiation is produced. This radiation is emitted in the form of a cone at an angle θ (see Fig. 2.4c) such as:

$$\cos\theta = \frac{c}{v\,n(\lambda)} \tag{2.2}$$

where $n(\lambda)$ is the spectral index of the medium, which depends on the wavelength of the Cherenkov light. The number of Cherenkov photons produced by an ultrarelativistic particle as a function of the length and wavelength is given by (Yao et al. 2006):

$$\frac{d^2N}{dx\,d\lambda} = \frac{2\pi\alpha}{\lambda^2}\left(1 - \frac{c^2}{v^2\,n^2(\lambda)}\right) \approx 370\sin^2\theta(\lambda)\ [\text{eV}^{-1}\text{cm}^{-1}] \tag{2.3}$$

where $\alpha \approx 1/137$ is the fine structure constant and λ the wavelength.

Cherenkov light produced in the atmosphere The cascades originated in the atmosphere contain several relativistic particles that travel faster than the speed of light in the atmosphere. The fact that showers should produce Cherenkov light was
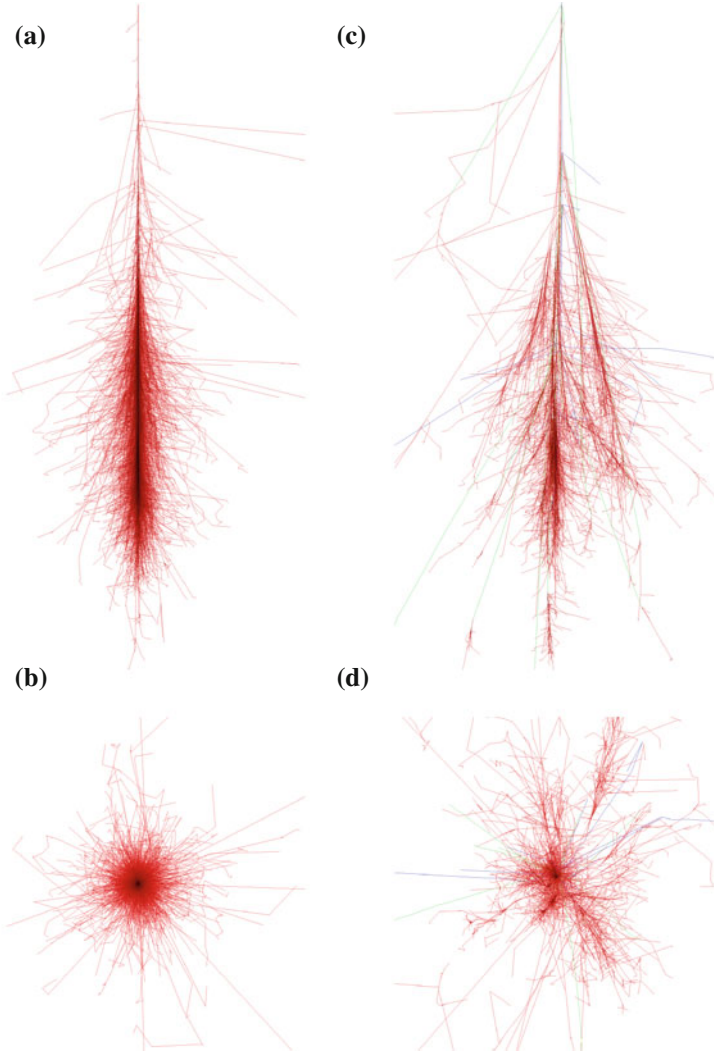
Fig. 2.3 *Upper left panel* 100 GeV γ-ray shower particle track. *Lower left panel* The same γ-ray shower seen on the transversal plane. *Upper right panel* 100 GeV proton shower particle track. *Lower right panel* The same proton shower seen on the transversal plane. *Red lines* correspond to e⁻, e⁺ and γ-ray tracks, green for muons and blue for hadrons. From Schmidt (2015)

pointed out by Blackett (1948) and later measured by Jelley and Porter (1963). According to the Cherenkov light propagation shown in Fig. 2.4c, a vertical incident ultrarelativistic particle illuminates a doughnut ring on the ground. The superposition of the rings generated by all the particles emitting Cherenkov light form a circle on the ground. Since $(n - 1) \sim \mathcal{O}(10^{-4})$ in the air, the maximum angle from Eq. 2.2 is $\theta \lesssim 1°$.

(a)   **(b)**   **(c)**
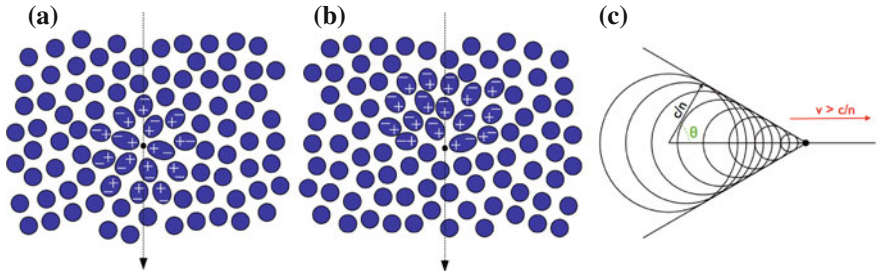
Fig. 2.4 *Left panel* Polarization of a medium when a charge particle crosses it moving at a speed $v < c/n$. *Middle panel* Polarization of a medium when a charge particle crosses it moving at a speed $v > c/n$. *Right panel* Schematic view of the Cherenkov radiation emitted by the particle shown in the middle figure
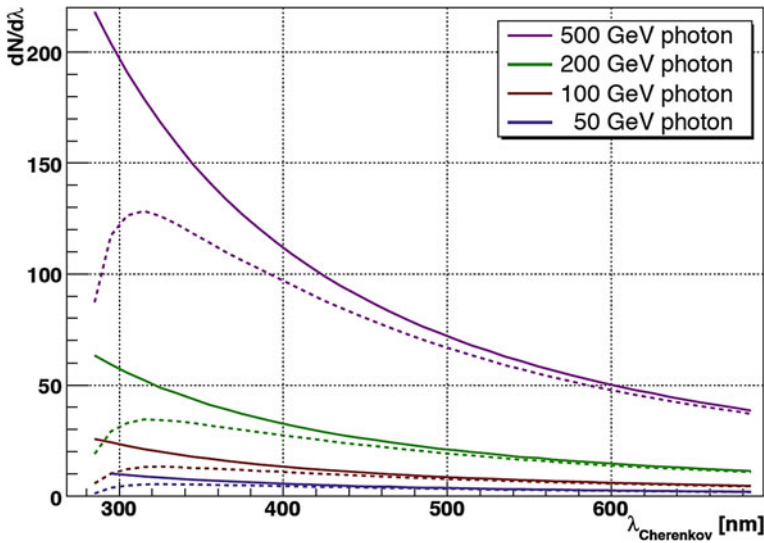
Fig. 2.5 Cherenkov light spectrum emitted for γ-ray showers of different energies. The *solid lines* correspond to the emitted spectrum at 10 km height and the *dashed ones* to that detected at 2200 m a.s.l.

From Eq. 2.3 we see that the number of Cherenkov photons is inversely proportional to the square of their wavelength. From here it derives that most of the photons are emitted in the UV, as can be seen in Fig. 2.5. The observed spectrum is different from the emitted one due to several attenuation processes that occur in the particles track: Rayleigh scattering off air molecules ($\propto \lambda^{-4}$), that mainly affects the UV photons; Mie scattering off aerosols, water droplets and dust; UV absorption by ozone molecules; and infrared absorption due to H_2O and CO_2. Due to all these processes, the maximum of Cherenkov light observed at 2200 m a.s.l. in a shower peaks at around 330 nm, independent on the energy of the incident particle (see Fig. 2.5).

Fig. 2.6 Lateral Cherenkov distribution density for a shower produced by a gamma ray of 100 GeV and a proton of 400 GeV. Taken from (Barrio et al. 1998)
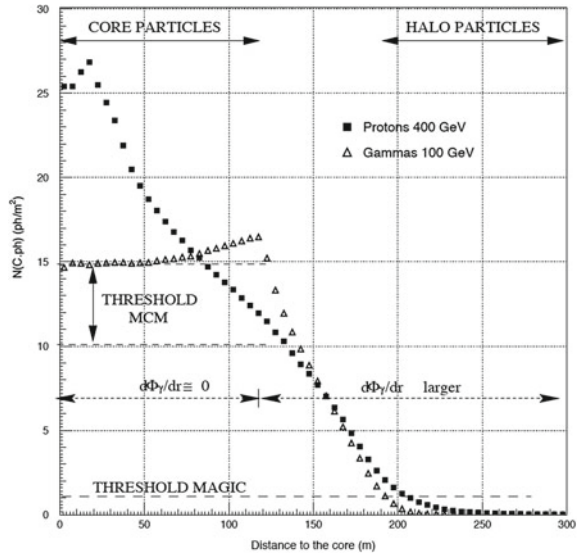
For vertical incident gamma rays, the Cherenkov photon density is almost constant in a ring with radius $\lesssim 120$ m centered in the core of the shower as it is shown in Fig. 2.6. It is higher in the region known as the *hump* and then it fades away. The *hump* is produced by the increase in the angle θ due to a change in the refracting index of the atmosphere at different heights. The energy of an incident γ-ray photon is proportional to the Cherenkov photon density detected on the ground, fact used to reconstruct their energy. In the case of hadrons, this relation is not fulfilled, as can be seen in Fig. 2.7.

Fig. 2.7 Cherenkov photon density as a function of the energy for different incident particles (Wagner 2006; Oser et al. 2001)
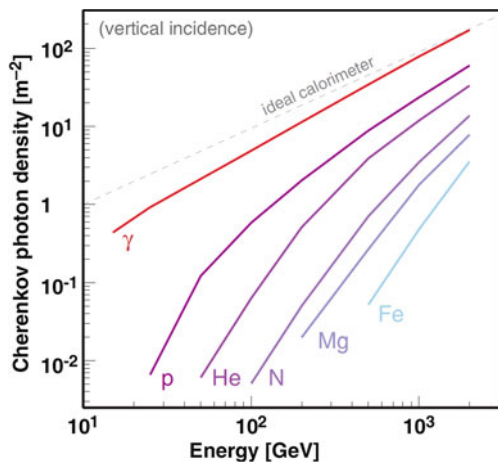
2.1.3 The Imaging Technique

The main purpose of the imaging atmospheric Cherenkov technique is to combine the spatial and temporal information of the measured light to produce images of the showers and differentiate between hadron and γ-initiated showers. To achieve this, IACTs have large reflectors that collect the maximum amount of Cherenkov light from a single shower possible and pixelized cameras equipped with very fast response pixels. The events are triggered by systems that record them only when several pixels are above a certain threshold for a short time (the shorter the time, the less Night Sky Background (NSB) that is integrated). They are also equipped with fast readout systems to record and reconstruct the narrow signals the photodetectors issue when they are excited by photons.

The reflectors used are usually Davies-Cotton, that have a good off-axis performance, but are not isochronous. When the reflector size increases, the arrival timing difference to the camera plane of light reflected by different segments of the mirror becomes important and parabolic reflectors are used because they are isochronous, although they have large coma aberration for off-axis angles. The pixels are usually fast, high-Quantum Efficiency (QE) Photomultiplier Tubess (PMTs), although there have been recent developments on cameras using Silicon PhotoMultiplier (SiPM) showing a good performance (Bretz et al. 2014).

An scheme of how the technique works is shown in Fig. 2.8. The reason of using more than one telescope is to proper reconstruct the direction of the incident γ-ray and
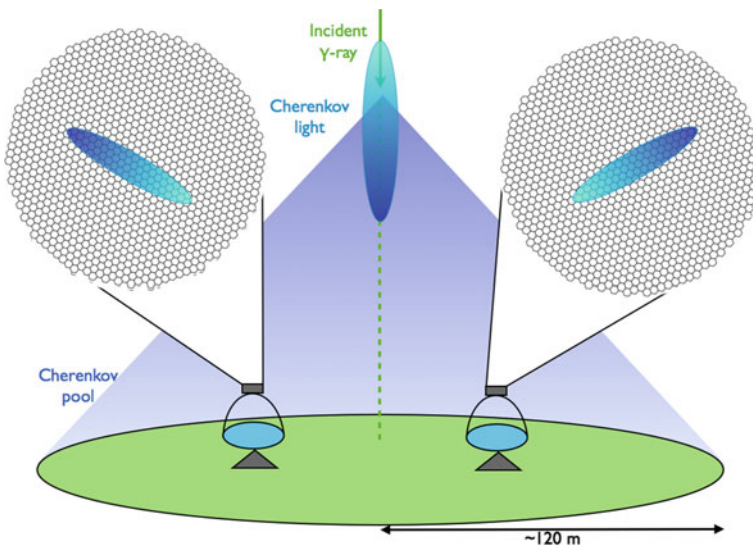
Fig. 2.8 Scheme of the imaging atmospheric Cherenkov technique

have a better background suppression. IACT systems usually work in stereoscopic mode, recording only the events triggered by more than two telescopes in a given time window.

Sources of background: Hadrons are arriving almost isotropically to the atmosphere, therefore the background contribution will come from everywhere. In fact, most of the events recorded by IACTs have hadronic origin (the proportion with respect gamma rays is $\sim 1000 : 1$ at 1 TeV for a strong source as Crab). The energy distribution of the hadronic background follows a power-law distribution $dN/dE \propto E^{-2.7}$. As it was described in the previous sections, the showers produced by primary particles of different origin have different shapes when projected in the camera (see Fig. 2.9). γ-ray showers produce elliptical images on the ground, while hadron-like cascades produce more irregular images. This fact is used at the analysis level to distinguish between EM showers and hadronic ones (see Sect. 2.2.3.3).

There are other sources of background, such as muons, that usually form ring-like images on the camera plane and can also be rejected because of their shape. On the other hand, there are also irreducible sources of isotropic background, such as cosmic $e^{\pm}$, that produce EM cascades identical to those produce by gamma rays, or diffuse gamma rays coming from the galactic plane as they were measured by Abramowski et al. (2014a).

Apart from Cherenkov photons, one has the contribution of the Night Sky Background (NSB), that are background photons propagating isotropically in the night sky. The NSB contribution in la Palma was measured to be $(1.75 \pm 0.4)10^{12}$ ph m^{-2} sr^{-1} s^{-1} between 300 and 600 nm (Mirzoyan and Lorenz 1994).

Differences between observations at large Zenith distance (Zd): As some of the observations of this thesis were performed at high Zd (up to Zd = 70°), we will give a brief description of the differences between the shower development and their
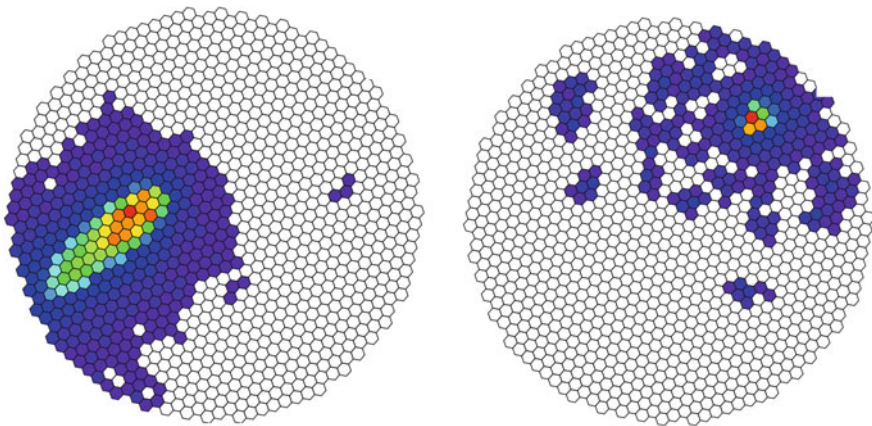
Fig. 2.9 Example of an image of a γ-ray (*left panel*) and hadron (*right panel*) showers

imaging at different Zd. When observing at high Zd, the shower development takes place in the uppest layers of the atmosphere. This implies a larger path for the shower to go through the atmosphere, being approximately $L' \simeq L/\cos(Zd)$. The diameter of the plane perpendicular to the reflector follows the same relation $l' \simeq l/\cos(Zd)$. Since the amount of light reflected by the mirrors is proportional to the amount of light arriving to the plane perpendicular to the reflector, the photon density ρ arriving to the camera is proportional to the diameter square of the plane perpendicular to the reflector $\rho \propto l^2$ and the relation between the light density at high Zd ρ' and the one at $Zd = 0\rho$ is:

$$\rho' \propto l'^2 \propto \frac{\rho}{\cos^2(Zd)} \tag{2.4}$$

therefore larger attenuation and lower Cherenkov photon density at the observation level (see Fig. 2.10).

The reduction of Cherenkov light on the ground causes an increase in the energy threshold. It should theoretically increase with the Zd as $E_{\text{threshold}} \propto \cos^{-2}(Zd)$ due to the decrease in Cherenkov photon density, but is measured to increase faster with increasing Zd due to the worst imaging of the showers and the loss of discrimination power between the hadronic and EM ones. The worsening of the energy threshold is on the other hand compensated by an increase in the collection area of the telescope. As the Cherenkov light pool is larger when observing showers at high Zd, the collection area increases.
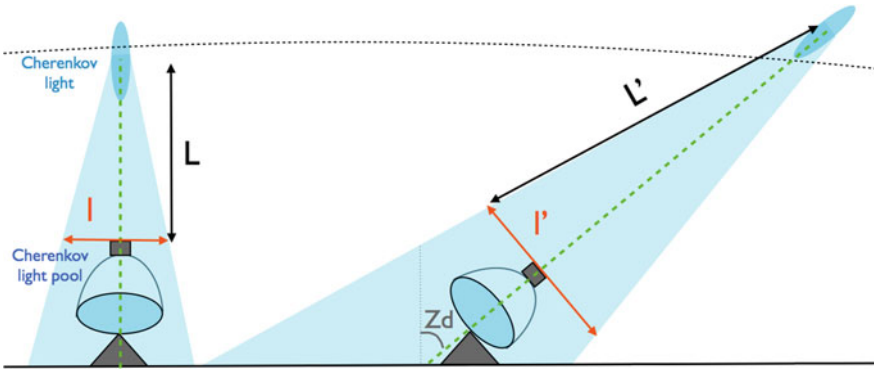
Fig. 2.10 Difference in the shower development between low Zd (*left* telescope) and high Zd (*right* telescope) observations. We can see that the distance from the camera to the point in the atmosphere where the showers start to develop is smaller for low Zd observation (L) than for high Zd observations (L'). The diameter of the Cherenkov light pool in the plane perpendicular to the reflector is also larger for high Zd observations ($l' \simeq l/\cos(Zd)$)

2.2 MAGIC

The Florian Goebel Major Atmospheric Gamma-ray Imaging Cherenkov (MAGIC) telescopes are a stereoscopic system of two 17 m diameter IACTs located on the Canary island of La Palma, Spain (28.8°N, 17.9° W at 2225 m a.s.l). The system is specially designed to achieved the lowest possible energy threshold and a fast response to transient phenomena. MAGIC I started to take scientific data in 2004 and MAGIC II in 2009 (see Fig. 2.11). During the summers of 2011 and 2012 the system underwent a major upgrade of the digital trigger, readout systems, and one of the cameras (Aleksić et al. 2014f) to make it homogenous and improve its performance. The MAGIC data analyzed in this thesis were taken both in stand-alone (only with MAGIC II) and stereo modes, hence both observation modes will be described.

2.2.1 Hardware Description

We will describe in the following the main components of the MAGIC telescopes. We will give a detailed description of the data acquisition and the electronic chain components relevant for data taking.

Fig. 2.11 Picture of the two MAGIC telescopes on the island of la Palma

2.2.1.1 Structure and Drive

The telescope mount is alt-azimuthal. The dish, moving in zenith and supporting the mirrors is identical in both telescopes and consists of a frame of octagonal shape made of carbon fibre-epoxy tubes joined by aluminum knots (see Fig. 2.12). The structure is rigid and light-weight (less than 20 tons including mirrors and camera support). The lower structure moving in Azimuth (Az) is made of steel tubes and weighs a total of 65 tons including the undercarriage (Fig. 2.12). To hold the camera, there is a aluminum circular tube anchored to the main structure by ten pairs of steel cables. The deformation of the structure is less than 3.5 mm for any of the telescope orientations (Bretz et al. 2009), which is corrected using the Active Mirror Control (AMC) described in Sect. 2.2.1.2.

The range of movement spans from −90 to 318° in Az and from −70 to 105° in Zd. There are two 11 kW motors in two of the six bogies composing the Az undercarriage and one motor of the same power for the zenith axis (see Fig. 2.12). The telescope's GRB mode allows to move 180° in 20 s. The telescope position is measured by three 14-bit shaft encoders, one of them in the Az axis and two in the zenith one. The telescope can track sources with an accuracy of 0.02°. To account of the deformation of the telescope structure, the pointing of the telescope is calibrated taking pictures of stars at different Zd and Az using a CCD camera installed in the middle of the reflector dish (*T-point* camera). In addition to the information given by the shaft encoders, the telescope pointing is constantly monitored by another CCD camera (*Starguider* camera), mounted in the center of the mirror dish as well. It measures the position of the telescope camera (with a ring of LEDs placed at the camera edge) respect to background stars and compares it to the latest available bending model (Fig. 2.13).
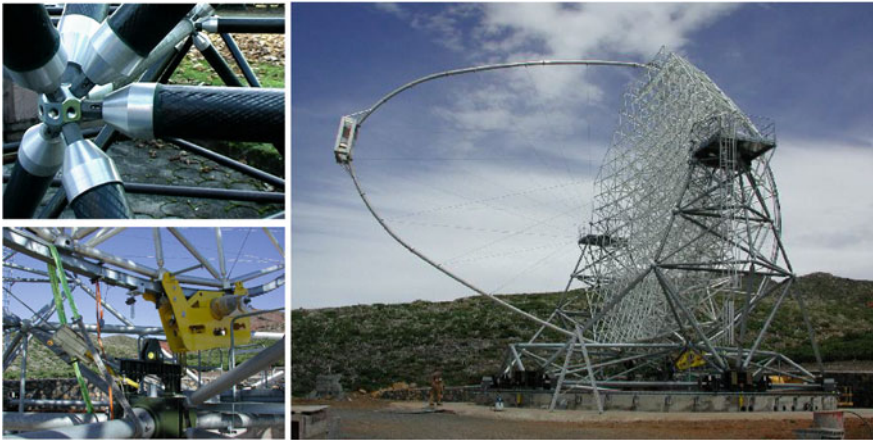
Fig. 2.12 *Top left* Aluminum knot where several carbon fibre-epoxy tubes join. *Bottom left* Zenith motor. *Right* Telescope mount without mirrors
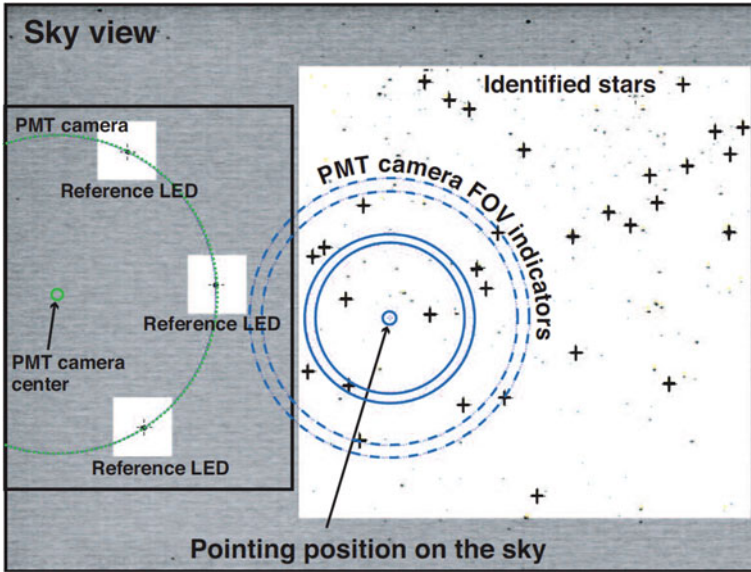
Fig. 2.13 Picture of the starguider camera installed in the central part of the MAGIC telescope. Taken from Wagner (2006)

2.2.1.2 Reflector and Mirrors

The reflector has $f = D = 17\,\mathrm{m}$, being f and D the focal length and diameter of the parabolic reflector dish. Parabolic mirrors are isochronous. As the time spread of Cherenkov signals is 1–2 ns, Cherenkov pulses are not significantly broadened, the signal extraction time is reduced and less noise is integrated. The Point Spread Function (PSF) for each of the mirrors r_{39}, defined as the diameter of the camera that contains 39 % of the light of a point-like source, is $r_{39} \sim 10\,\mathrm{mm}$ wide at the camera on-axis plane. Each of the mirrors has a spherical shape with radii ranging from 34 to 36.7 m to match the parabolic shape of the reflector. The total mirror surface of both telescopes is $\sim 236\,\mathrm{m}^2$. The reflective surface is tessellated with $1 \times 1\,\mathrm{m}$ facets (see Fig. 2.14a). In MAGIC I, each of the 247 facets contains four $0.5 \times 0.5\,\mathrm{m}$ aluminum honeycomb mirrors. In MAGIC II, there are 143 facets with single $1 \times 1\,\mathrm{m}$ all-aluminum mirrors on a honeycomb structure and 104 facets with single $1 \times 1\,\mathrm{m}$ glass-honeycomb-glass mirrors (see Fig. 2.14b). Each of the facets is controlled by the AMC software described in the following.

Active Mirror Control The AMC is the part of the hardware in charge of correcting mirror focusing depending on the Zd for correcting for the deformations of the telescope. The system consists of two actuators per mirror panel. Each actuator can move the mirror with a precision of less than $20\,\mu\mathrm{m}$ corresponding to a shift in the camera plane of the light spot of less than 1 mm (Biland et al. 2008). The system adjusts the focusing of the mirror using Look–Up Tables (LUTs) binned in Zd and

(a) Mirrors of MAGIC I   **(b)** Mirrors of MAGIC II
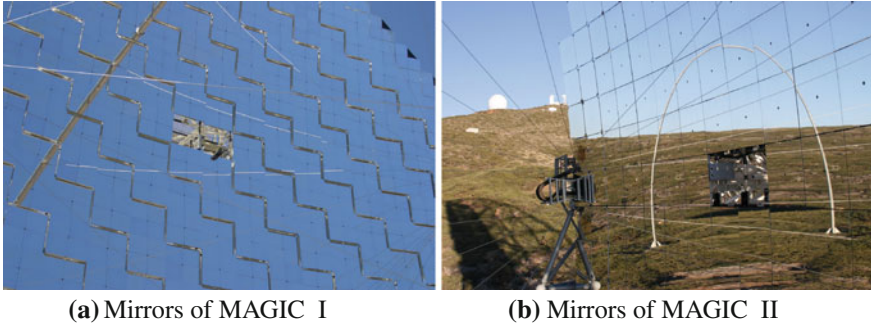
Fig. 2.14 MAGIC mirrors

Az. An optical PSF of r_{39} $\sim$11 mm can be reached, very close to the theoretical minimum, which is the PSF of a single mirror. The AMC system also contains a high-sensitivity CCD camera called SBIG camera, used for measurements of the PSF of single and multiple-mirrors.

2.2.1.3 Camera

Each camera is one of the most important parts of the telescope. The cameras are made of high-QE PMTs (also known as pixels) to collect as much Cherenkov light as possible, fast response to integrate the minimum NSB possible and low gain to allow observing during moonlight conditions. Each of the PMTs is coupled to a light collector called *Winston cone* that increases the light collection efficiency and prevents the collection of photons coming with large angles with respect to the reflector, avoiding the collection of some light reflected by the ground and part of the isotropically distributed NSB. The first camera of MAGIC I had a different design as the current one, which is a clone of that installed in MAGIC II when it started operation. Since there were not data analyzed in this thesis with the old MAGIC I camera, we will only describe the current one.

The camera has a circular shape with $\sim$1.2 m diameter and a weight of $\sim$850 kg (see Fig. 2.15a). It has a Field of View (FoV) of 3.5° diameter and is composed of 1039 uniformly distributed PMTs. The camera also contains the power and cooling system, optical fibers and the electronics necessary to transmit signals to the *Counting House (CH)* where they are digitized. In front of the Winston cones there is a plexiglass window to protect the camera from the environment. To protect the camera from sun light and other external agents, it is equipped with movable lids.

PMTs PMTs are grouped in 169 clusters of 7 pixels, 127 of the clusters fully equipped and 42 (the outer ones) only partially. Each of the clusters is easily accessible from the back side of the camera for pixel exchanging (see Fig. 2.15b). Each PMT has a 0.1° FoV. The PMTs are Hamamatsu R10408 6-dynode photo-tubes with spherical photocathode and $\sim$32–34 % QE at 350 nm wavelength (Nakajima et al. 2013). Each

(a) Front view of the MAGIC II camera.   **(b)** Back view of the MAGIC II camera.
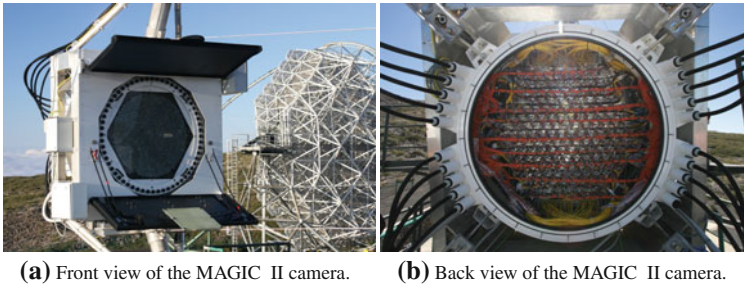
Fig. 2.15 MAGIC Camera

of the clusters is equipped with a slow control processor which controls several parameters of the PMT, as setting High Voltage (HV) or reading Direct Current (DC) currents. The HV is produced by a Cockroft-Walton type DC-DC converter. The PMT gain is $\sim 3 \times 10^4$ and the typical HV set is ~ 1250 V. After the PMT, the signal is further amplified by a low-noise pre-amplifier to account for the low gain of the PMT. The clusters are also equipped with a pulse generator that allows injecting signals to the pre-amplifier for testing purposes.

The analogue electronic signals are converted into optical signals by Vertical Cavity Surface Emitting Lasers (VCSELs) after the pre-amplifier stage. They are transmitted to the CH by 162 m long optical fibers.

2.2.1.4 Calibration System

To flat field the PMT gain, obtain the conversion factor between the counts of the digitizers to number of photoelectrons (phe) and the conversion between Flash Analog-to-Digital Converter (FADC) timing into an absolute timing, the MAGIC telescope needs a calibration system. It consists of a Nd-YAG laser, operating at 355 nm with 0.7 ns pulse width. To obtain a dynamic range, two rotating filter wheels can attenuate the laser beam, so that the signal produced in a PMT ranges between 1 and 1000 phe. To achieve an homogenous distribution of the calibration light at the camera plane, the laser beam is diffused using an integrating (Ulbricht) sphere. The system is placed in the center of the reflector dish.

2.2.1.5 Receivers

Trigger, readout electronics and Data AcQuisition (DAQ) are placed in a CH. We will describe the electronic chain that is followed by the signals coming from the telescope. The optical signals coming from the telescope through the optical fibers enter the so-called receiver boards where they are converted back to electric ones by photodiodes. The electric signals are then split into a trigger and a readout branch.

2.2.1.6   Trigger System

Digital trigger The current trigger system installed in the MAGIC telescopes for normal operation is a digital trigger composed of three stages (Paoletti et al. 2007):

- *Level 0 (L0)* trigger: Signals in the individual pixels go through discriminators with a given threshold. It is installed in the receiver boards and it issues a square signal of adjustable width every time the analog input of the telescope is over the Discriminator Threshold (DT).
- *Level 1 (L1)* trigger: It is a digital filter that searches for spatial and time coincidence of pixels that pass the L0 trigger. Pixels are grouped in 19 hexagonal overlapping cells called *macrocells*. Each hexagon is composed by 37 pixels, one of which is blind (see Fig. 2.16, left panel). When a pixel is above the threshold, an LVDS signal of 5.5 ns phe is sent to the L1 board. If n Next Neighbour (NN) pixel signals overlap, the L1 issues a valid trigger. There are different NN multiplicities implemented in the L1 trigger (n = 2, 3, 4 or 5). The one currently used for stereo observations is n = 3, having an effective overlapping trigger gate of 8–9 ns. The NN configuration implies that the pixels above the threshold must be in a close compact configuration, being every pixel in the group in contact with at least other two (except for the 2NN configuration). The output signal of each of the 19 macrocells is processed by a Trigger Processing Unit (TPU) that merges them into an OR gate. The macrocells cover a region of ∼2.5° diameter (Fig. 2.16, right panel).
- *Level 3 (L3)* trigger: It receives the output of the TPU from both telescopes and stretches it to achieve 100 ns width. It searches for an overlapping between the stretched signals of both telescopes in an effective time window of ∼180 ns.
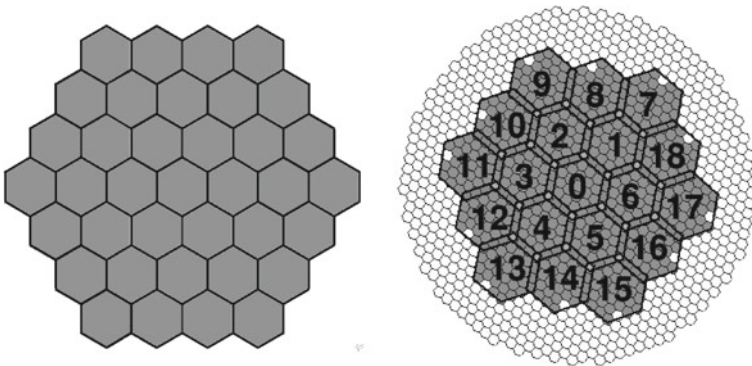
Fig. 2.16   The *left* figure is a picture of a single L1 macrocell, each of the hexagons corresponding to one pixel. The *right* one is the distribution of the L1 trigger macrocells in the MAGIC camera. The numbers are the ones used in the hardware identification of the macrocells. The lines are imaginary hexagons limiting each of the macrocells

Other trigger options MAGIC was designed to achieve the lowest possible energies. At the lowest energies, cosmic events are similar to "accidental" ones produced by noise. Several trigger options have been installed to discriminate accidentals from showers.

Sum trigger-II The Sum trigger-II is a trigger system based on the same concept as the Sum trigger designed for MAGIC I (Rissi et al. 2009), which allowed the discovery of VHE pulsed emission from the Crab pulsar above 25 GeV (Aliu et al. 2008). It adds up the analog signals from several pixels in 19-pixel macrocells. To minimize the effect of signals produced by After Pulses (APs) in the PMTs, the signal of every pixel is "clipped" before the analogue sum: if it exceeds a certain value, the analogue clipped signal that is sent to the adder is ideally constant. With the clipping of the signals, we avoid issuing valid triggers due to the signal coming from one or two pixels in the whole macrocell. The output of the adder enters a DT. The DT that is currently set in the MAGICtelescopes is of the order of several tens of phe to achieve the lowest possible energy threshold without exceeding the recording limit of the DAQ. For further information about Sum trigger-II, see (García et al. 2014).

Topo-trigger Special trigger option developed during this thesis that makes use of the digital macrocell information of both telescopes to record more low energy events. It has been simulated, tested and is currently under commissioning. A detailed description can be found in Chap. 4.

2.2.1.7   Readout

The readout is the part of the electronic chain that digitizes and temporarily stores the analogue signals from the telescope. We will briefly describe the history of the readouts used in MAGIC and then give a deeper explanation of the readout currently used, the Domino Ring Sampler (DRS) version 4.

Glimpse to the previous readouts used in MAGIC

Siegen: Between the beginning of MAGIC (∼2003) and February 2007, MAGIC operated with a readout known as *Siegen*. The readout consisted of a dual gain 300 MSample/s system. Using this option, the readout system was too slow to handle the ∼2 ns signals coming from the PMTs and they had to be stretched to 6–7 ns. Due to the stretching of the signals, the differences between signals produced by gamma rays, cosmic events or NSB were smoothed and the performance worse than with a faster readout. The dead time of the system was 25 μs.

MUX: In February 2007, the MAGIC I readout was upgraded to a 2 GSample/s system which made use of a fiber-optic multiplexing technique (MUX). Multiplexing was possible thanks to the low duration of the signals (∼few ns) and the trigger rate (it was typically ∼1 kHz), resulting in a low duty-cycle for the digitizer. The system

was custom-made in order to reduce the cost and consumption and instead of using a FADC for each readout channel, a single FADC could handle 16 channels (Mirzoyan et al. 2002; Bartko et al. 2005). The dead time of the system was $25\,\mu s$.

DRS2 When MAGIC II was constructed, it was equipped with a readout based on the DRS2 analog memory chip. The working principle of the DRS is the following (see Fig. 2.17): the signal coming from the receiver board is sequentially connected to an array of 1024 capacitors by fast switches synchronized to an external clock. Each of the capacitors is charged by the analogue signal of the corresponding pixel for a time that is proportional to the period of the clock controlling the switching (the so-called Domino wave). The capacitors are overwritten after 1024 clock cycles. When a trigger is received, the Domino wave stops and the charge stored in the 1024 capacitors is digitized by an Analog-to-Digital Converter (ADC). Later on, only 80 capacitors are stored by the DAQ, but as the whole buffer needs to be read, the dead time of the system is $500\,\mu s$. This means that for a stereo trigger rate of $\sim 300\,Hz$, the dead time is 15 %. DRS2 chips are highly non-linear and temperature dependent devices that need to be constantly calibrated. A complete description of the DRS2 chips can be found in (Bitossi 2009).

DRS4 To reduce the non-negligible dead time of the telescope using the DRS2 chip and to converge to one single readout in both telescopes, in December 2011 the MUX readout in MAGIC I and the DRS2 readout in MAGIC II were replaced by a readout based on the DRS4 chip. The DRS4 chip works basically like a DRS2 chip. They are still temperature dependent, so they still have to be calibrated on a regular basis, but they are linear and when a trigger is issued, only a Region of Interest (RoI) of 60 capacitors is read at 33 MHz, reducing the dead time to $27\,\mu s$. Additional
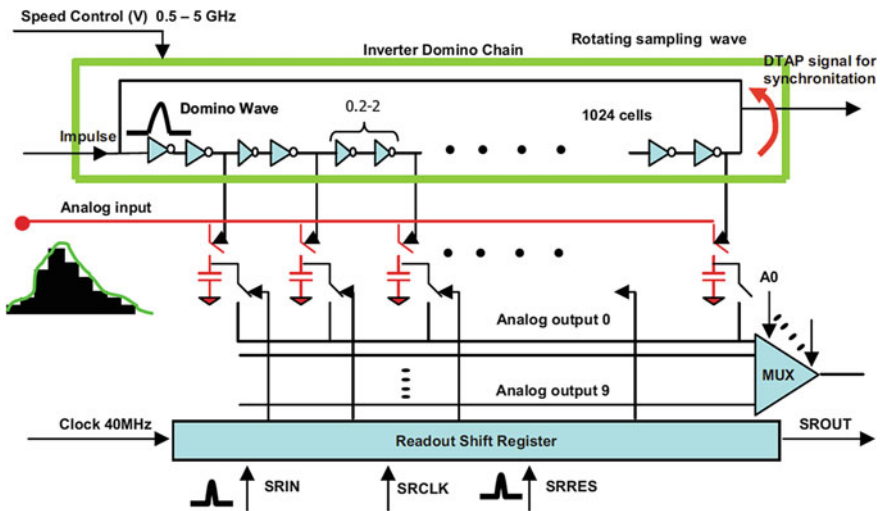
Fig. 2.17 Schematic view of the DRS chip. Taken from Bitossi (2009)

Fig. 2.18 Picture of the DRS4 chip currently used in the MAGIC telescopes
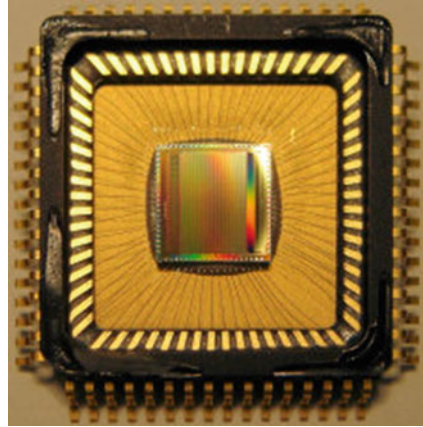
advantages with respect to the DRS2 chip are a larger bandwidth (700 MHz instead of 200 MHz) and a lower pedestal noise (0.7 phe per cell, a factor 2 lower). For a detailed characterization, see Sitarek et al. (2013) and for a picture of a DRS4 chip, see Fig. 2.18.

DRS chips are installed in especially designed boards called PULSer And Recorder (PULSAR). PULSAR boards are general purpose VME interface boards used in high energy physics. Each PULSAR board hosts 4 mezzanines, each mezzanine contains 3 chips and a single DRS4 chip has 8 channels, so every PULSAR board can digitize 96 pixels.

The data from the RoI of the DRS4 chip are read by the DAQ program. It interfaces with the PULSAR boards through FILAR cards and HOLA boards, which are respectively PCI cards installed in the DAQ computer and mezzanines installed in the PULSAR boards. The signal is transmitted from the HOLA to the FILAR boards via optical S-Link. The DAQ program then runs three threads in parallel: reading, analyzing and storing. There are 14 PULSAR boards to digitize all the pixels in a telescope, and there are two additional PULSAR boards with special functionalities: the "digital PULSAR" that adds digital information to the data such as trigger number and absolute time, and the "busy PULSAR", which stops the triggers when the system is processing an event or an error occurs (Tescaro et al. 2009, 2013).

Rate limiter: The current DAQ can handle a short-term event rate up to 3 kHz. When the telescope was illuminated by car flashes, or what is more important, when bright stars suddenly entered in the FoV while repositioning to a GRB, the DAQ crashed due to the very high stereo rate. It takes several minutes to recover from such a crash. A "rate limiter" was installed to momentarily block triggers when the rate exceeds 1 kHz.

2.2.1.8   Other Subsystems

Timing system The absolute time is generated by a Rubidium clock with a precision of 3×10^{-11} in 1 second. The Rubidium clock is a high-precision system, however it drifts over long time scales. To correct it, the device is synchronized every second to a GPS signal with a precision of the order of nanoseconds. The absolute time enters the data stream through the PULSAR.

Central pixel The central pixel of both MAGIC cameras is a modified PMT designed to detect variations of the optical flux of rapid-variability sources such as pulsars (Lucarelli et al. 2008). The pixel has a modified DC branch and a dedicated readout. The whole central cluster of the MAGIC camera was modified to host the necessary additional electronics, so it can be used for regular and optical observations.

Weather station A Reinhardt MWS 5 MW weather station is installed on the roof of the CH of the MAGIC telescope. It measures the temperature, pressure, humidity and wind speed and direction every second to determine if atmospheric conditions allow observations. For the atmospheric safety limits see Sect. 2.2.2.2.

LIght Detection And Ranging (LIDAR) An elastic single-wavelength LIDAR is installed in the dome of the CH (Fruck et al. 2014). The LIDAR is equipped with a 5 mW Q-switched, pulsed Nd:YAG laser with a 532 nm wavelength, a 60 cm diameter, 1.5 m focal length Al mirror, a robotic equatorial mount, an Hybrid Photo Detector (HPD) capable of single photon counting and a computer equipped with an FADC card which digitizes the output of the HPD. The LIDAR operates as follows: it sends light pulses up to the atmosphere and they are backscattered by clouds or aerosols. The arrival time distribution of the backscattered photons registered at the HPD can be used to measure the transparency of the atmosphere.

Pyrometer The pyrometer is a device that computes the transparency of the atmosphere by measuring the temperature of the sky. It is installed in the MAGIC I reflector and points parallel to the telescope. It measures IR radiation in the 8–14 μm range and fits it to a blackbody spectrum. If the sky is cloudy, it reflects thermal radiation from the Earth and the sky temperature is higher. This temperature is used to determine a parameter known as *cloudiness*, that gives an estimate of the transparency of the atmosphere. It is defined as:

$$\frac{T_{\text{low}} - T_{\text{meas.}}}{T_{\text{low}} - T_{\text{up}}} \tag{2.5}$$

where $T_{\text{meas.}}$ is the measured temperature of the sky, $T_{\text{up}} = 200$ K corresponds to the best condition of the sky and $T_{\text{low}} = 250$ K to the worst.

AllSky camera The AllSky camera is a monochrome AllSky-340 camera manufactured by SBIG. It points to the zenith and has a FoV of 360° in Az and almost 90° in Zd. It takes an image of the sky every 2 min, with an automatically adjusted exposure time. The images taken by the camera are automatically uploaded to a server and can be monitored online.

MAGIC OnLine Analysis (MOLA) MOLA is a multithreaded C++ program used to obtain on-the-flight estimations on the γ-ray emission from sources in the FoV observed by MAGIC (Tescaro et al. 2013). It runs three parallel threads: two reading threads used to gather the single-telescope charge and arrival time of the events and an analysis thread that matches and reconstruct the events from the two telescopes. It computes the θ^2 plot with respect to the candidate source position and it also produces light curves of the measured γ-ray flux and skymaps. The program is specially used for nightly estimations on the flux of variable γ-ray sources such as blazars. Its most remarkable achievement was the discovery of a very rapid flare on the IC 310 galaxy while observing NGC 1275 and the extension of those observations (Aleksić et al. 2014a).

GRB monitoring alert system A GRB monitoring program runs in the background of one of the CH computers. It receives information of the GRB from the GRB Coordinate Network (GCN) and evaluates the observability of the received alerts following several criteria (distance to the Sun and to the Moon, Zd, uncertainty on the position). If the alert fulfills all the criteria, the Central Control (CC) takes control of the observation and automatically points the telescope to the GRB location.

2.2.2 Data Taking

MAGIC standard operation and under which it achieves its best performance is under so-called "*dark* conditions" (i.e. when the moon absent from the sky). The total amount of available *dark* time amounts to $\sim$1600 h/yr. About $\sim$65 % of the available dark time is observed and the rest is loss due to bad weather or technical problems. Thanks to the low gain of the PMTs, MAGIC can also observe during moonlight conditions up to 75 % of the moon phase and only has to stop observations on the 3 to 4 full-moon nights. Filters for moonlight observations (see Fig. 2.19) similar to those currently being used by VERITAS (Staszak 2014), are currently being commissioned and will allow the extension of the observations to any moon phase.

The default data taking mode of MAGIC is the stereo mode. The mean L0 DT is set to $\sim$4.5 phe in both telescopes (slightly higher in MAGIC II due to the higher mirror reflectivity), although the individual pixel DT is controlled by means of an Individual Pixel Rate Control (IPRC). It sets the DT of individual pixels and controls that the L0 rate is contained within the limits established. Currently, for *dark* observations, the usual L0 rate is $\sim$800 kHz. The IPRC decreases the L0 DT when the rate is lower than 250 kHz and increases it when the rate is larger than 1.2 MHz. For *moon* observations, the usual L0 rate is $\sim$500 kHz, the DTs are decreased when the L0 rate is lower than 150 kHz and they are increased when the L0 rate is larger than 700 kHz. The L1 rates for standard operation are $\sim$15 kHz in both telescopes, leading to an accidental stereo rate of 40 Hz (the calculation of the stereo accidental rate is explained in Sect. 4.1). During the operation and to ensure a correct calibration of the readout, there are

Fig. 2.19 Filter for
moonlight observations

also 25 Hz of interleaved calibration events and 25 Hz of interleaved pedestal events recorded. The L3 stereo rate recorded by the DAQ is 250–350 Hz, so the current cosmic rate recorded is between 200–300 Hz.

The CC of the telescope, called SuperArehucas, takes care of all the subsystems of the telescope. It sends and receives reports with the state of all the hardware subsystems every second and allows the observers to control their most important functionalities. A detailed description of the CC program can be found in Zanin (2011).

2.2.2.1 Pointing Modes

The MAGIC telescope takes data in two different pointing modes: the *ON/OFF* and the *wobble* modes:

- *ON/OFF:* In the ON/OFF mode, the position of the target is tracked at the center of the camera. Two different types of observations have to be performed: *ON* observations with the source in the center of the camera, and *OFF* observations, preferably under similar Zd/Az conditions on a region where no γ-ray emission is expected.
- *Wobble:* This pointing mode was first proposed by Fomin et al. (1994) and it consists on tracking alternative positions in the sky that are at a slight offset from the center of the camera. For MAGIC the usual offset is 0.4° and each position is observed during 20 min. It has the advantage that no dedicated OFF observations have to be performed because the OFF is taken simultaneously. If only one OFF position is selected, it is taken in the opposite position of the camera with respect to the camera center as it is shown in Fig. 2.20a. More than one simultaneous OFF positions are possible, as can be seen in Fig. 2.20b. The collection of more

background events allows increasing the significance due to the more precise background determination. In addition, the background is evaluated from the same data sample as the signal, hence it matches its Zd/Az distribution and background light conditions. The main drawbacks from this observation mode are: a loss on γ-ray efficiency of the order of 15–20% because the source is 0.4° from the center of the camera and a systematic uncertainty in the background determination due to the camera inhomogeneities. These inhomogeneities are caused by dead pixels in the camera, non-flat trigger efficiency in the whole camera and insufficient flat fielding of the camera due to the gain differences between PMTs.

Independent of the pointing mode, working in stereoscopic mode makes the telescope acceptance dependent on the relative pointing of the telescopes. Only the events triggering both telescopes are recorded, therefore there will be more recorded events from the showers developed between the two telescopes and this is what is called the *stereo blob*. This problem was partially solved after the upgrade, when the system was homogenized and the trigger regions made equivalent. Currently, most of the observations carried out with MAGIC are in *wobble* mode.

(a) (b)

Wobble mode with 1 OFF. Wobble mode with 3 OFFs.
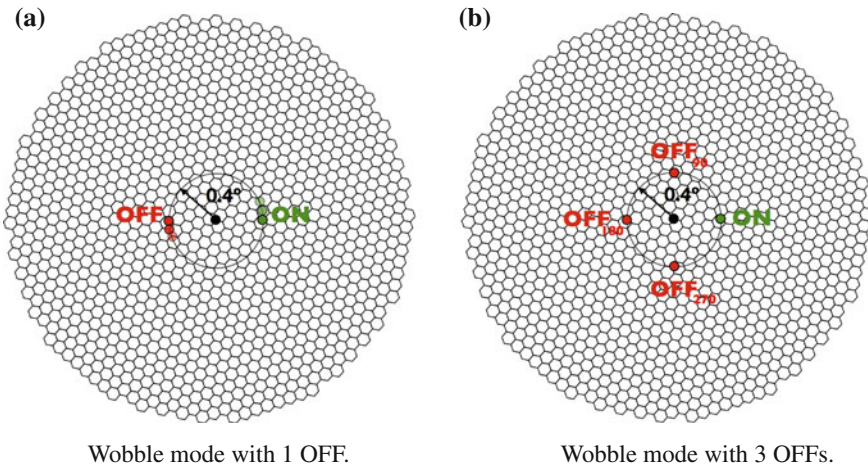
Fig. 2.20 Schematic view of the *wobble* pointing mode. The *black circle* marks the center of the camera. A region placed 0.4° from the source is tracked, being the source all the time situated at this distance from the center of the camera (*green circle*). The simultaneous background is taken all the moment from a region situated in the opposite side of the circle with center in the center of the camera and radius 0.4° (*red circle* in the *left* figure) in the case of 1 OFF region. In the case of 3 or more OFF regions, the background is taken from regions separated the same distance from one another in the aforementioned circle as it is shown in the *right* figure. The subindex of the OFF regions determine the angle turned in the circle counted counterclockwise from the ON region

2.2.2.2 Safety Limits

There are several atmospheric or technical conditions under which the telescope cannot be operated without taking the risk of seriously damage it. Here are the safety limits that should be fulfilled:

- Wind gusts $< 40\,\mathrm{km/h}$
- Wind mean speed $< 50\,\mathrm{km/h}$
- Humidity $< 90\,\%$
- Average PMT current $< 30\,\mu\mathrm{A}$
- Individual PMT current $< 47\,\mu\mathrm{A}$
- Zd $> 1.5°$

2.2.2.3 Data Types

There are different data types that can be taken with MAGIC. In the following, we find a summary of the most common ones that have to be taken every night:

- **Pedestal subtraction run (B)**: Taken at the beginning of the night to calibrate the baseline of the DRS capacitors and set the zero level to 10000 counts to avoid problems with negative values due to the noise fluctuations. It has to be taken at least one hour after the electronic was switched on because of the temperature dependency of the DRS chips.
- **Pedestal run (P)**: It records randomly triggered events (usually 2000 per run) which contain only noise. It has to be taken with the camera open to evaluate the effect of the NSB and readout noise to calculate the pedestal offset to be subtracted in the calibration of the data.
- **Calibration run (C)**: It contains events triggered by the calibration system. They are later used in the analysis to calibrate the data.
- **Data run (D)**: It contains all the events that issued valid triggers from the telescopes. They are mainly cosmic events, although it also contains interleaved calibration and pedestal events, together with accidental events triggered by noise. They correspond to approximately 20 min of data taking, the time that one wobble lasts. Data runs are divided into subruns which contain $\sim$1 Gb of data, corresponding to $\sim$2 min of data.

2.2.3 Data Analysis

The standard software for MAGIC data analysis is called MAGIC Analysis and Reconstruction Software (MARS) (Zanin et al. 2013). It converts the raw ADC counts recorded by the DAQ into high-level products using a collection of programs

written in C++ language that makes use of ROOT[1] libraries. The final purpose of the software is to reconstruct the primary particle generating the cascade and determine the direction and energy of the γ-ray candidates. In the following there is a summary of the processes performed by MARS:

- *Calibrate* the digital signals contained in the raw data and convert the information to phe (Sect. 2.2.3.2).
- *Image cleaning* and calculation of the *image parameters* for single-telescope (Sect. 2.2.3.3).
- *Merge* the data from both telescopes and calculate the *stereo image parameters* (Sect. 2.2.3.5).
- *Train* Random Forest (RF) for γ/hadron separation, fill LUTs for energy reconstruction and reconstruct the shower direction (Sect. 2.2.3.6).
- *Apply* RFs and LUTs to the data to calculate the *hadronness*, reconstructed energy and arrival direction of each event (Sect. 2.2.3.6).
- Calculate *signal significance* (Sect. 2.2.3.7), *skymaps* (Sect. 2.2.3.8), *spectra* and *light curves* (Sect. 2.2.3.9).

A scheme of the aforementioned process followed by the data is shown in Fig. 2.21. We will give a detailed description of the programs in the following sections.

2.2.3.1 Monte Carlo Simulation

As IACTs cannot be calibrated with a source of gamma rays, one has to trust on simulations to reconstruct the energy and incoming direction of the events. The Monte Carlo (MC) simulation is performed outside the MARS framework and is composed of three stages (for further information, see Majumdar et al. (2005)):

- The *atmospheric simulation* is performed using the `Corsika` 6.019 program (Heck et al. 1998), which simulates air showers. As an atmospheric model, we have used the so-called "MagicWinter" containing a mixture of N_2 (78.1 %), O_2 (21.0 %) and Ar (0.9 %). The model to describe hadronic interactions is FLUKA, together with the QGSJet-II model for high-energy interactions. Electromagnetic interactions are simulated using the EGS4 model. MAGIC simulations work with a modified version of CORSIKA that stores the information of the direction and position in the ground of the Cherenkov photons produced in the shower.
- The simulation of the telescope's *mirror response* to the incoming Cherenkov light and its absorption in the atmosphere, is done by the `reflector` program. It uses the Elterman model for the aerosol distribution in the atmosphere (Elterman 1964). It simulates the absorption of Cherenkov photons in the atmosphere and their reflection in the telescope's dish and calculates their position and arrival time at the camera plane.

---

[1]http://root.cern.ch/drupal/.
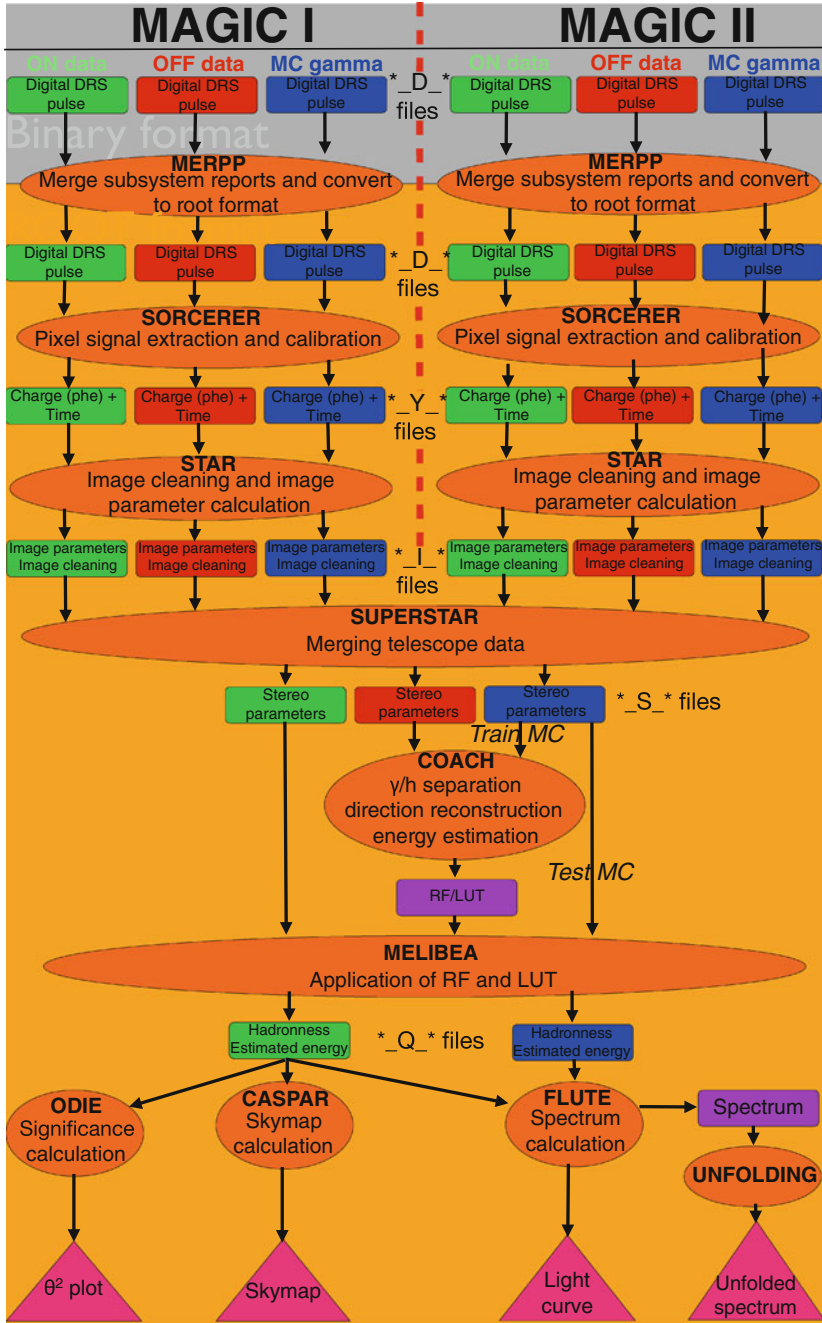
Fig. 2.21 Scheme of the MAGIC analysis chain

- The response of the PMTs and the readout electronics are simulated using the `camera` program. The measured QE of the PMTs is taken into account to simulate the pixel response, the trigger is simulated and the measured readout noise is also included in the simulation. The program also simulates the effect of the measured PSF of the individual mirror facets and their error in the alignment.

Recently, a new simulation program integrated in the MARS framework that simulates the reflector and camera response called `matelsim` has been developed (López 2013). However this program is still under testing and the official MAGIC simulation programs are still `reflector` and `camera`.

The output of the `camera` program has the same format as the raw data after converting it to ROOT data format, so it can be analyzed using the same software. For data analysis, only simulations of gamma rays are necessary, however one can also simulate with CORSIKA several types of particles and in MAGIC also $e^{\pm}$, p and He^{++} are used for performance studies. For most of the sources, gamma rays are simulated in a ring of 0.4° radius centered in the camera center (known as *ringwobble* MC, see Fig. 2.22a). However, for the analysis of extended sources or sources situated at different off-axis angles, *diffuse* gamma rays are simulated in a circle with radius 1.5° centered in the center of the camera (see Fig. 2.22b). MC gamma rays are produced in ranges of Zd: low (5–35°), medium (35–50°), high (50–62°) and very-high (62–70°) Zd. The distribution of generated MC gamma rays is flat in cos(Zd) in each of the ranges. The ranges are selected to have similar coverage in cos(Zd) in all bins.

(a)   **(b)**
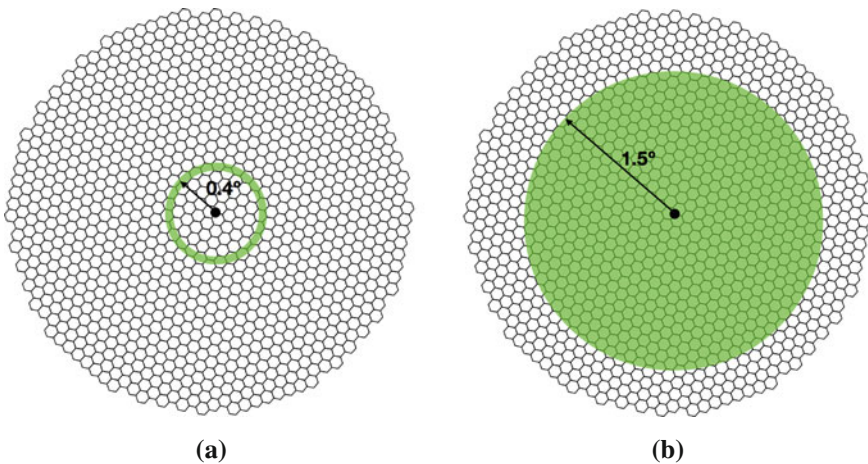
Fig. 2.22 Ringwobble (*left panel*) and diffuse (*right panel*) MC schemes. The *green* shaded area is the one where the MC gamma rays are simulated

2.2.3.2   Signal Extraction and Calibration

The raw data, with the output of the digitizers in counts vs time is converted to ROOT format by a program called `merpp` (MERging and Preprocessing Program) which also merges the data file and the subsystem reports.

Once the data is in ROOT format, it can be calibrated to convert ADC counts into number of phe. The old calibration program was called `callisto` (CALibrate LIght Signals and Time Offsets), but after the installation of the DRS4 readout in both telescopes, a new program called `sorcerer` (Simple, Outright Raw Calibration; Easy, Reliable Extraction Routines) was developed to handle DRS-related problems. 60 "time slices" are stored for each pixel, corresponding to 60 capacitors, each of them containing the number of ADC counts in 0.5 ns). The pedestal subtracted from each time slice depends not only on the capacitor that is read, but also on the last time it was read. After the pedestal is subtracted, the *sliding window* algorithm is used to extract the signal. It takes the maximum resulting from integrating 6 consecutive slices. The signal arrival time is the average position of the selected 6 slices weighed with the ADC counts contained in each of them.

The conversion from ADC counts to number of phe is performed using the *F-factor* method (Mirzoyan 1997). For calibration pulses it is assumed that the number of phe follows a Poissonian distribution with mean N and standard deviation $\sqrt{N}$. The distribution of measured charge in ADC counts Q has a mean $\langle Q \rangle$ and a deviation σ_Q which is wider than pure Poissonian expectations due to noise in the PMT e$^-$ multiplication process. The relative amplitude of both distributions can be written as follows:

$$F\frac{\sqrt{N}}{N} = \frac{\sigma_Q}{\langle Q \rangle} \tag{2.6}$$

where F is the so-called *F-factor*, which is different for each PMT and must be measured in the laboratory. The electronic chain also contributes to the broadening of the peaks, but this contribution is negligible with respect to the effect of the PMT. Since the spread of *F-factor* for the PMTs of each telescope is small, one can take one single *F-factor* for each of the telescopes. The conversion factor m between ADC counts and phe is then given by:

$$m = \frac{N}{\langle Q \rangle} = F^2 \frac{\langle Q \rangle}{\sigma_Q^2} \tag{2.7}$$

As the gain of the VCSELs is not constant in time, m must be updated using calibration events interleaved with cosmic events at a rate of 25 Hz.

2.2.3.3   Image Parameter Calculation and Image Cleaning

From this step on, the shower images are parametrized and the pixel information is lost. The program performing all these computations is called `star`. The charge and

arrival time information are used for the analysis and only pixels that contain useful information about the shower are kept for the shower parametrization (see Fig. 2.23). The algorithm to remove the noisy pixels is called *image cleaning* (Aliu et al. 2009; Lombardi 2011).

In the *absolute* image cleaning method, a pixel is considered a "core pixel" if its charge is above a certain threshold Q_c, if it is adjacent to another core pixel and if its arrival time does not differ from the mean arrival time of the core of the image by more than Δt_c. Boundary pixels are defined as the ones above a threshold Q_b, that are adjacent to at least one *core* pixel and if their arrival time does not differ from the arrival time of that *core* pixel a time larger than Δt_b.

For the single-telescope data used in the analysis of Chap. 9, the values used to define *core* and *boundary* pixels are the following:

$$Q_c = 8 \, \text{phe}; \quad Q_b = 4 \, \text{phe}$$

$$\Delta t_c = 4.5 \, \text{ns}; \quad \Delta t_b = 1.5 \, \text{ns}$$

In the *sum* image cleaning method, the algorithm searches for 2, 3 or 4 neighboring pixels (2NN, 3NN, 4NN) with a summed charge above a certain threshold Q_c in a time window t_c. To prevent from large signals due to APs, each pixel's signal is clipped before the sum. The threshold values and the time windows applied to search for *core* pixels with the *sum* algorithm can be found in Table 2.1. Once the *core* pixels are selected, the *boundary* ones are the ones at least neighbour to one *core* pixel, their charge is larger than 3.5 phe and their arrival time difference with respect to their *core* neighbour pixel is smaller than 1.5 ns.
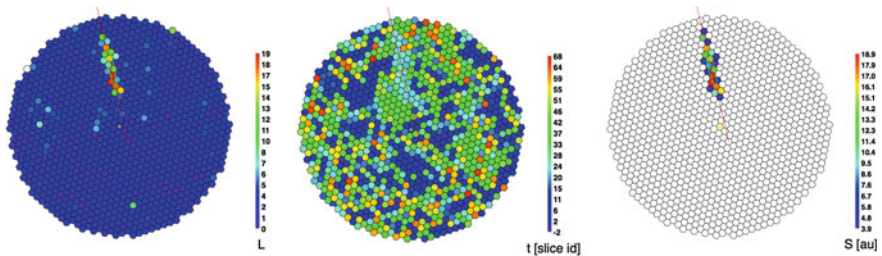
Fig. 2.23 Signal charge (*left panel*), arrival times (*middle panel*) and cleaned image (*right panel*)

Table 2.1 *Sum* cleaning charge and time parameters

Topology	Q_c [phe]	t_c [ns]
2NN	2×10.8	0.5
3NN	3×7.8	0.7
4NN	4×6	1.1

Once the *core* and boundary pixels are selected, the resulting images are parametrized and this is the information that is stored in the data. The image parameters used in the MAGIC analysis are the following:

Hillas parameters An ellipse is fit to the pixels after cleaning. The momenta of this fit up to second order are used to parametrize the image (Hillas 1985):

- **Size**: Total charge (in phe) contained in the image. It is related to the energy of the primary γ-ray if the shower falls close to the telescope (usually $\lesssim 120$ m).
- **Width**: RMS spread along the minor axis of the ellipse fitting the image. It is a measurement of the lateral development of the shower.
- **Length**: RMS spread along the major axis of the ellipse fitting the image. It is a measurement of the longitudinal development of the shower.
- **Center of Gravity (CoG)**: Center of gravity of the image. It is computed as the mean of the X and Y weighted mean signal along the camera coordinates.
- **Conc(N)**: Fraction of the image concentrated in the N brightest pixels. It measures how compact the shower is and tends to be larger in gamma rays.

A shower image with some of the *Hillas parameters* can be seen in Fig. 2.24.

Source-dependent parameters: They are still related to the physical properties of the shower, but they depend on the expected position of the source.

- **Dist**: Angular distance from the source expected position in the camera to the CoG of the shower image. This parameter is larger for the showers with larger impact parameter.
- **Alpha**: Angle between the ellipse major axis and the line connecting the expected source position to the CoG of the shower image. As the showers produced by gamma rays coming from the shower should point to the source position in the camera, this angle is small for γ-like showers.

Fig. 2.24 Picture showing some of the *Hillas parameters*
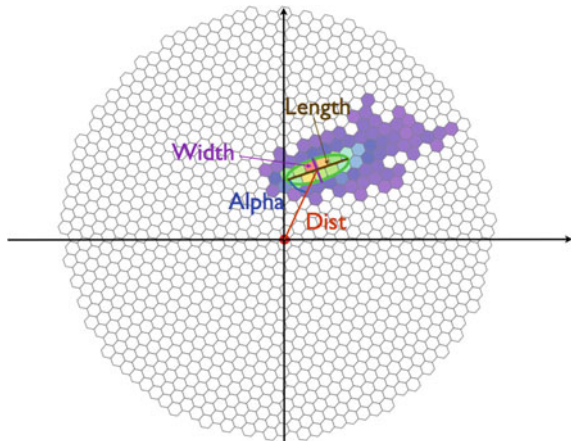
Time parameters: Since γ-like events are shorter in time than hadron-like events, time information is also useful to discriminate between hadron and γ-induced showers.

- **Time RMS**: RMS of the arrival times of the pixel that survived the *image cleaning*. It is smaller for γ-like showers.
- **Time gradient**: Slope of the linear fit to the arrival time projection along the major axis of the ellipse. It measures the direction of the shower development, positive if coming to the expected source position and negative otherwise.

Image quality parameters: They are used to evaluate if the image is very noisy or if it is well contained in the camera.

- **LeakageN**: Fraction of the size of the source contained in the N outermost rings of the camera.
- **Number of islands**: Number of non-connected pixels that survived the image cleaning.

Directional parameters: They discriminate between the head (top part of the shower) and tail (bottom part of the shower). Typical showers have higher charge concentration in the head than in the tail.

- **Asymmetry**: Signed distance between the shower's CoG and the pixel with the highest charge. It is positive when the pixel with the highest charge is closer to the camera center than the CoG.
- **M3Long**: Third moment of the shower image along its major axis. It follows the same sign criterium as the Asymmetry parameter.

2.2.3.4   Data Quality Selection

Data affected by technical problems, bad weather or different light conditions (e.g. data taken under moonlight conditions) should be separated from the "good" dataset. Some of this data could be recovered, follow a parallel analysis and their final products merged with those of the "good" dataset, although most of the times they are rejected.

To distinguish between good and bad quality data, we use several indicators. We plot the number of visible stars the starguider detect and the average *cloudiness* for every subrun. If the *cloudiness* is above 40, the data is considered of bad quality. We also plot the *rate* above a low *size* cut (usually 50 phe). This allows to reject accidental events and plot the real cosmic rate. This rate is different depending on the Zd. We can empirically correct the rate multiplying it by $\cos^{-1}(Zd)$. For a dark night with good weather conditions, the cosmic rate corrected by the Zd is constant. This empirical correction is valid up to Zd$\sim$50°. For the same observation period and for each telescope, where we expect a similar rate for good quality nights, we calculate the average cosmic rate and we accept data with a rate within 15 % of the average rate. The subruns outside this range might be affected by atmospheric extinction or technical problems and are rejected. The average rate is different for
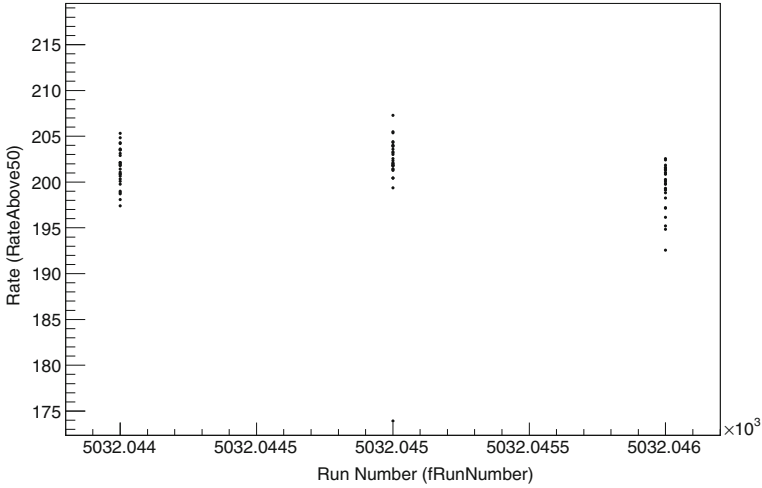
Fig. 2.25 Rate plot for the data quality selection for MAGIC I rate (for *size* >50 phe) is plotted as a function of run number. Each of the points corresponds to the rate of a 2-min subrun

each of the telescopes: MAGIC II rate is usually higher than MAGIC I due to the higher reflectivity of the mirrors installed in MAGIC II. A plot where a typical data quality rate plot is shown in Fig. 2.25.

2.2.3.5   Stereo Image Parameter Calculation

Once good-quality data have been selected, the `superstar` program merges the two telescopes data. One can now reconstruct the three-dimensional shower development and determine several parameters useful for the energy and direction reconstruction. Some of them are shown in Fig. 2.26a.

- **Impact point**: The impact point on the ground is calculated using the crossing point of the major axis of the two shower images and the position of each telescope (see Fig. 2.26b).
- **Shower axis**: The shower axis is given by the crossing point of the major axis of the two superimposed shower images in the camera plane, as can be seen in Fig. 2.26c. This is the so-called *crossing point* method to calculate the shower direction (Aharonian et al. 1997b; Hofmann et al. 1999). The more powerful *disp* method will be described in Sect. 2.2.3.6.
- **Height of shower maximum**: Using the shower axis, together with the angle at which the CoG of the image is measured with respect to each telescope, one can estimate the height of the shower maximum (H_{max}). The H_{max} is in inverse proportion to the energy, as it was shown in Sect. 2.1.1.1. This parameter is strongly correlated with the shower energy and is a powerful γ/hadron discriminator.
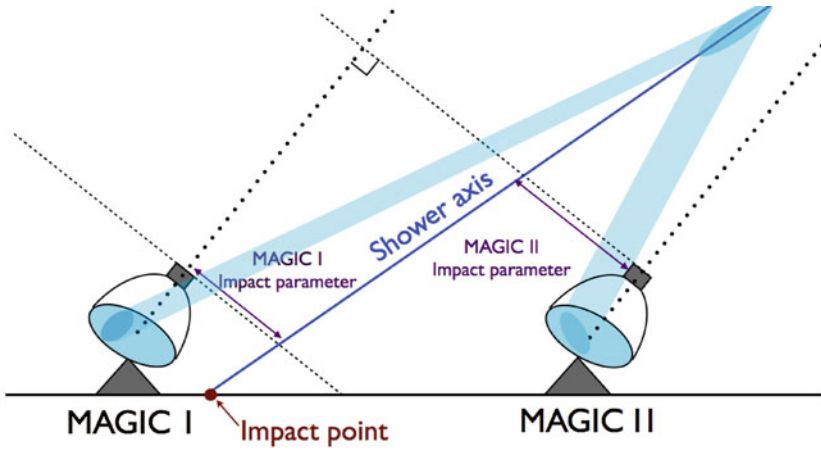
(a) Stereo event shower geometry.
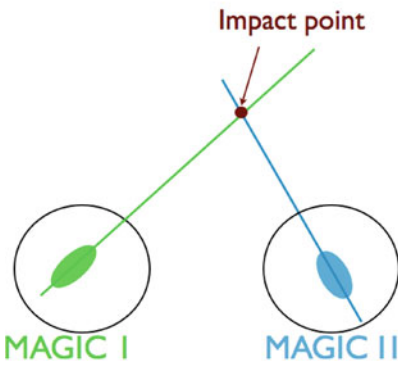
(b) Calculation scheme of the impact point on the ground.
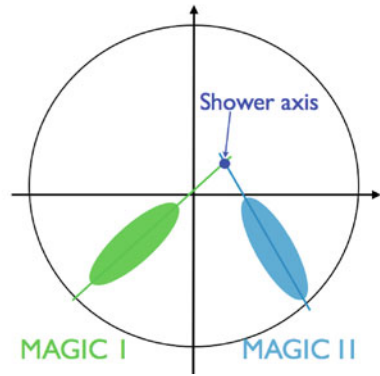
(c) Scheme of the shower direction determination.

Fig. 2.26 Different views of the shower geometry

- **Impact parameter**: Calculated as the perpendicular distance between the shower axis and the pointing direction of each telescope.
- **Cherenkov radius**: It is computed as the radius of the ring of Cherenkov light pool produced by an e$^-$ with the critical energy of 86 MeV at the height of shower maximum.
- **Cherenkov photon density**: Cherenkov photon density on the ground of a shower produced by an e$^-$ with an energy of 86 MeV at the height of the shower maximum.

2.2.3.6   Event Separation and Characterization

Even for a strong γ-ray source as the Crab Nebula, the number of hadron events that survive image cleaning is $\sim$3 orders of magnitude larger than the one of gamma rays. The purpose of the single-telescope and stereo image parametrization is to separate γ-like showers from the rest.

For stereo observations we use RFs for γ/hadron separation and direction reconstruction, and LUTs for the energy estimation. To create the RFs and LUTs, we use a program called `coach`. For single-telescope, we use RFs for γ/hadron separation, direction reconstruction and energy estimation and all of them are produced by a program called `osteria`.

γ/**hadron separation** To evaluate how similar to a γ-ray shower an event is, we use a multi-variate algorithm based on decision trees called *Random Forest (RF)* (Albert et al. 2008). It uses training samples representing γ-ray showers and hadronic showers. As it is shown in Fig. 2.21, at this stage the MC sample is split in two subsamples: the *train* subsample, used to teach the RF how γ-like events look like, and the *test* subsample, that is used later in the analysis to calculate the collection area and migration matrix and has to be different from the *train* sample not to have a biased result. A sample of real hadron data is also needed here to train the RF on what are the parameters of hadron-like events. The hadron sample must match the Zd conditions at which the RF needs to be trained. As the hadron to γ-ray rate is large, any sample of a non-detected source or a weak one is suitable to train the RF.

The algorithm works as follows: we select P parameters to discriminate between gamma rays and hadrons, then the training RF grows a number n (by default $n = 100$) of decisional trees. The growing works as follows: One of the P parameters is randomly selected, and the data sample (containing gamma and hadron events) is separated in two subsamples (branches) based on this parameter. The cut of the parameter that better separates the sample is found by the RF by minimizing the Gini index (Gini 1921):

$$Q_{\text{Gini}} = 4 \frac{N_\gamma}{N} \frac{N_{\text{h}}}{N} \tag{2.8}$$

where N_γ is the number of gammas, N_{h} the number of hadrons and N the total number of events. The procedure is repeated by randomly selecting another parameter and further separating the subsample until the final branch only contains events of one of the populations. This branch is assigned a 1 (or 0) depending if the events are hadrons (or gammas).

We apply the RF to the data sample using the program `melibea`. Every event has to pass through all the n decisional trees previously grown. The event is then assigned a *hadronness* value 0 or 1 depending if it ends up in a γ-branch or a hadron-branch. The final *hadronness* value of the event is given by the mean value of the hadronness of all the trees:

$$h = \sum_{i=1}^{n} \frac{h_i}{n} \tag{2.9}$$

where h_i is the *hadronness* resulting from passing the event through the i-th branch and h is the final *hadronness* assigned to the event.

Arrival direction reconstruction The determination of the arrival direction of the incoming γ-ray is easy for stereo observations (using the *crossing method* introduced in Sect. 2.2.3.5). For single-telescope observations we need to resort to the so-called "Disp" method (Fomin et al. 1994; Lessard et al. 2001). The Disp method has also proven to improve the arrival direction reconstruction for stereo observations, therefore it is used in stereo analysis as well.

The source position in a γ-ray shower produces an elliptical image at the camera. The distance from the image CoG to the source position is known as *disp* and can be determined using the following formula:

$$disp = A(size) + B(size)\frac{width}{length + \eta(size)leakage2} \tag{2.10}$$

where $A(size)$, $B(size)$ and $\eta(size)$ are second order polynomials of $\log(size)$ whose coefficients are determined using MC gamma rays. As illustrated in the left panel of Fig. 2.27, the source may be at two different positions for the same *disp*. The directional parameters introduced in Sect. 2.2.3.3 can be used to break this degeneracy.

This parametrization is not very efficient at high energies because many images are truncated. The method used for single-telescope direction reconstruction is a method based on the RF algorithm trained with MC gamma rays whose *disp* parameters are known. The RF is grown on a similar way as that explained for the γ/hadron separation, but the minimized parameter is the *disp* variance of each of the branches.

For stereo analysis, the *crossing method* gives a good estimate of the γ-ray arrival direction, but this method fails for parallel showers and very small reconstructed images. An improved method uses the *disp* information of both reconstructed
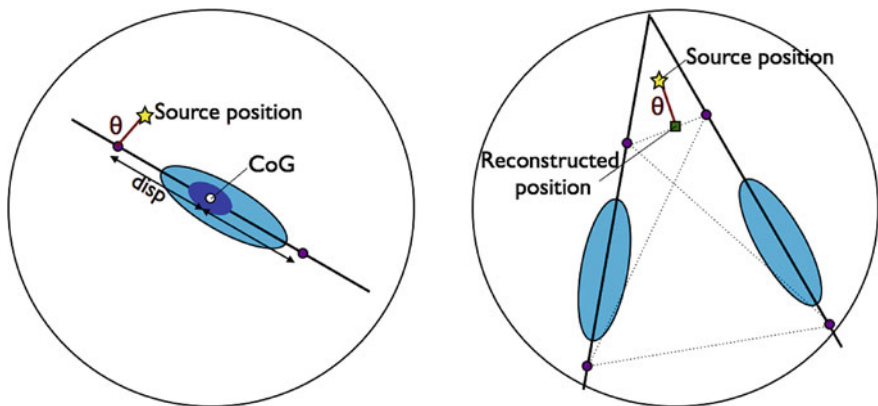
Fig. 2.27 *Disp* reconstruction method for single-telescope (*left panel*) and stereo (*right panel*)

showers. Figure 2.27 (right panel) illustrates this method. First, we calculate the four estimates of the source position (*disp*) for the shower images (two per image). Secondly, we calculate the distance between each pair of source position estimates from different images (the dotted lines in the right panel of Fig. 2.27). Thirdly, we select the pair at the smallest distance which is the one taken for calculating the reconstructed direction of the shower. If this distance is larger than 0.22°, the reconstruction is not valid. Finally, the reconstructed direction is the average between the chosen pair of positions weighted with the number of pixels in each image. The θ distance shown in Fig. 2.27 (right panel) is the angular distance between the reconstructed and the true position of the source. Its distribution can be used to extract the γ-ray signal as it will be shown in Sect. 2.2.3.7.

The *disp* method helps in the reconstruction of events with large impact parameter. Considering the 2-dimensional distribution of reconstructed arrival directions, we define the **angular resolution** as the angle that encloses 68 % of the events. The left panel of Fig. 2.28 shows the angular resolution of MAGIC as a function of the energy obtained using MC γ-ray events. It reaches a value of 0.11° at 250 GeV and it is as good as 0.06° above a few TeV.

Energy estimation For single-telescope observations, the energy estimation is performed by means of a RF. The RF is grown in a similar way as previously mentioned, but in this case we select different parameters and aim at minimizing not the Gini index, but the variance of E_{true} of the events in each of the subsamples.

In the stereo analysis instead we use LUTs. LUTs are filled with the true energy (E_{true}) and the RMS of MC simulated gamma rays. They are binned in *size* and *impact parameter/r_C*, where r_C is the Cherenkov radius defined in Sect. 2.2.3.5. The estimated energy (E_{est}) of each event is the weighted average of both telescopes where the weight is given by the RMS of the bin. Finally, we apply an empirical correction proportional to the $\cos(Zd)$.
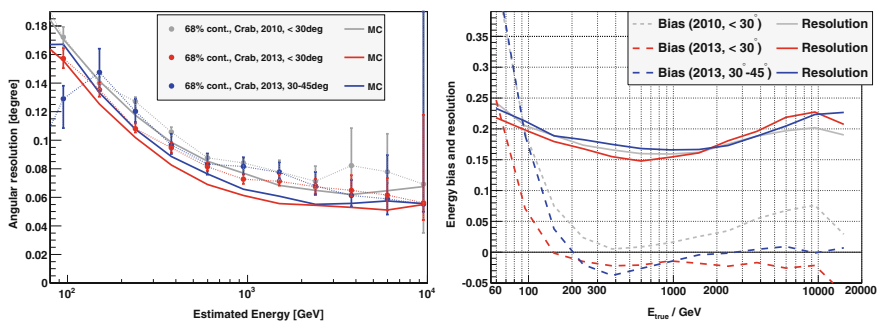
Fig. 2.28 MAGIC angular resolution (*left panel*), energy resolution and energy bias (*right panel*). 2010 refers to the period before the readout upgrade to DRS4 and 2013 to the period after. Plots taken from Aleksić et al. (2014g)

The **energy bias** is defined as:

$$E_{\text{bias}} = \frac{E_{\text{est}} - E_{\text{true}}}{E_{\text{true}}} \tag{2.11}$$

to compute the energy bias for a given energy bin, we fit a gaussian to the energy biases of the individual events. The energy bias of the system is the mean of that gaussian. The **energy resolution** is defined as the σ of the gaussian. A plot comparing the current MAGIC energy resolution and bias at low and medium Zd and the resolution and bias previous to the upgrade are shown in the right panel of Fig. 2.28. We can see that the energy resolution is as good as 15 % at few hundred GeV. It worsens for higher energies because the impact parameter grows and truncated images become more frequent. For low energies it also gets worse due to misreconstructed images. The energy bias is close to 0 for energies $>100\,\text{GeV}$, however it rapidly increases below these energies due to threshold effects.

Finally, the **energy threshold** of the telescope is defined as the peak of the simulated energy distribution for a source with photon spectral index 2.6. It can be evaluated at several stages of the analysis, but most relevant is the threshold obtained after applying analysis cuts because it corresponds to the energy at which most of the events used for analysis are recorded. Events with energies below the threshold can be reconstructed as well, but the spectral points have significant errors. After applying a cut of 50 phe, *hadronness* and θ^2 cuts, the current energy threshold of the MAGIC telescope is $\sim 75\,\text{GeV}$ for low Zd observations. A plot showing the energy distribution of gamma rays after analysis cuts of MAGIC for two Zd ranges is shown in Fig. 2.29.
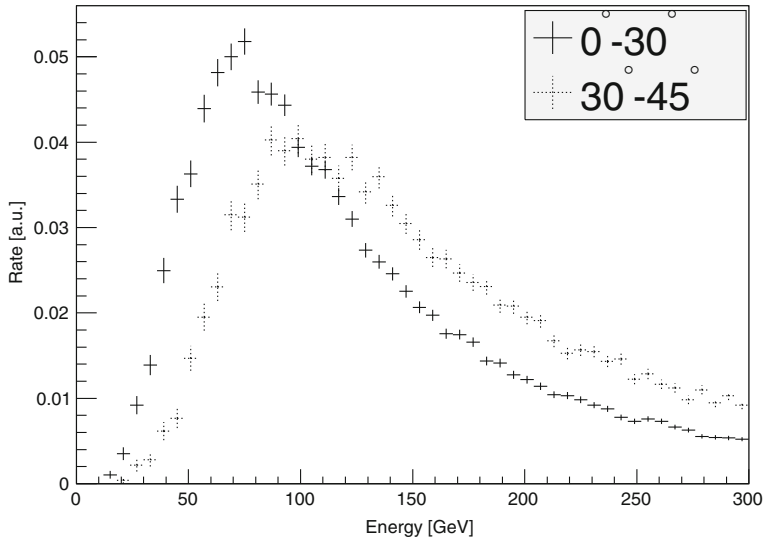
Fig. 2.29 Rate of γ-ray events surviving analysis cuts for a Zd range between 0–30° (*solid lines*) and between 30–45° (*dashed lines*). Plot taken from Aleksić et al. (2014g)

2.2.3.7   Signal Extraction and Sensitivity

Once we have evaluated *hadronness*, reconstructed energy and direction of the events, we can evaluate if the data sample contains a signal. For stereo analysis, a program called `odie` computes the angular distance θ between the reconstructed and the expected source position for every event and fills the so-called *signal histogram*, binned in θ^2. Assuming that the acceptance of the camera is the same for regions close to the center, the background would be flat over the whole histogram, while the γ-like events would accumulate at small values of θ^2. Only events that survive some other previously defined cuts in *hadronness, size*... are included in the signal histogram. These cuts can be optimized on an independent data sample (usually Crab Nebula data). The current standard set of cuts used for the detection in several energy ranges can be found in Table 2.2.

Once we have filled the signal histogram with the events surviving all the cuts and the signal region has been defined, we count the number of events in the signal region, N_{on}. These events are not only gamma rays coming from the source, but also γ-like hadrons, $e^{\pm}$ and diffuse gammas. In order to estimate how many hadron events are inside the signal region, we fill a different θ^2 histogram, the *background histogram*, where θ is now the distance from the reconstructed position to the "off position", which is the position that is situated at the same distance as the source from the center of the camera, but on a different region (see Fig. 2.20). The γ-ray events having small θ^2 with respect to the source position, are also included in the background histogram as it can be seen in Fig. 2.30. As it was shown in Fig. 2.20b, we can take more than one equivalent region to calculate the number of number of hadrons that there is in the signal region. Finally, the number of excess N_{ex} is given by:

$$N_{\text{ex}} = N_{\text{on}} - \alpha N_{\text{off}} \tag{2.12}$$

where α is 1/(number of OFF regions). An example of a θ^2 histogram is shown in Fig. 2.31.

The significance of the signal is usually calculated using Eq. 2.17 from Li and Ma (1983):

$$\sigma_{\text{LiMa}} = \sqrt{2 \left(N_{\text{on}} \ln \left[\frac{1+\alpha}{\alpha} \left(\frac{N_{\text{on}}}{N_{\text{on}} - N_{\text{off}}} \right) \right] + N_{\text{off}} \ln \left[(1+\alpha) \left(\frac{N_{\text{off}}}{N_{\text{on}} - N_{\text{off}}} \right) \right] \right)} \tag{2.13}$$

Table 2.2   Standard cuts for the different energy ranges in the MAGIC analysis

Energy range	Hadronness	θ^2	Size [M1]	Size [M2]	E_{est}
Low energies	<0.28	<0.02	>60	>60	–
Medium-to-high energies	<0.16	<0.009	>300	>300	–
High energies	<0.1	<0.007	>400	>400	>1000

Fig. 2.30 Sketch illustrating how θ is calculated respect to the source and off positions
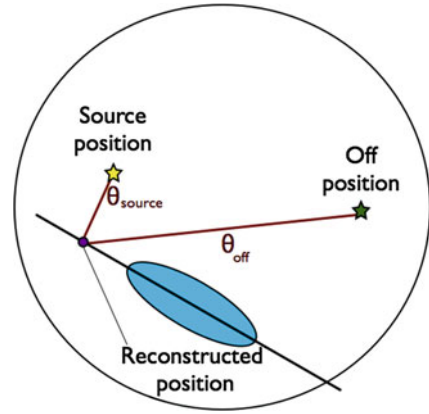
Fig. 2.31 θ^2 distribution obtained for the Crab Nebula after medium-to-high hadronness and size cuts (Table 2.2). The grey histogram is filled with a θ^2 calculated with respect to the off position. The points correspond to an histogram filled with a θ^2 calculated with respect to the source position
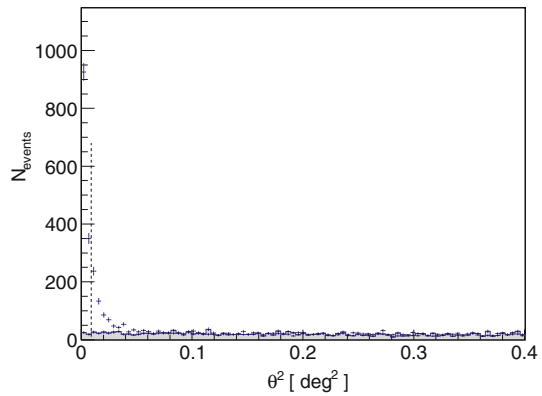
but it can also be given as:

$$\sigma_{Nex/\sqrt{Noff}} = \frac{N_{\text{ex}}}{\sqrt{N_{\text{off}}}} \tag{2.14}$$

which is a Gaussian approximation of (2.13).

Sensitivity The sensitivity of the instrument is calculated as the minimum signal that can be detected in 50 h with 5σ using the significance $\sigma_{Nex/\sqrt{Noff}}$. It is usually expressed in units of the Crab Nebula flux.

Given an observation of the Crab Nebula where a number of observed excesses N_{ex}, background events in the signal region N_{off} in a time t are observed, the significance in a time $t_0 = 50$ h is given by:

$$\sigma_{Nex/\sqrt{Noff}}(t_0) = \sqrt{\frac{t_0}{t}} \frac{N_{\text{ex}}}{\sqrt{N_{\text{off}}}} \tag{2.15}$$
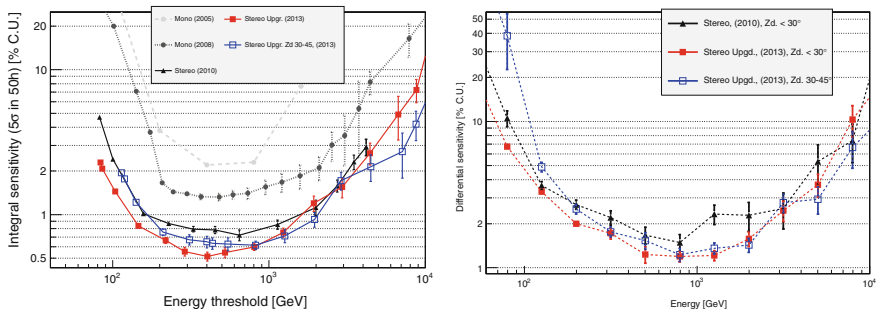
Fig. 2.32 MAGIC integral (*left panel*) and differential (*right panel*) sensitivity as a function of energy. *Red curves* correspond to the current MAGIC sensitivity for low Zd observations (between 0°–30°) and the *blue* one represents the current MAGIC sensitivity for the Zd range between 30°–45°. For comparison, the *black curve* represents MAGIC sensitivity before the installation of the DRS4 readout and the *grey dotted* and the *grey dashed curves* the sensitivity of MAGIC in single-telescope mode, for MUX and Siegen readouts respectively. Plots taken from Aleksić et al. (2014g)

And the sensitivity, given as the minimum flux that can be detected in 50 h with a significance 5σ in Crab units is:

$$Sensitivity = \frac{5\sigma}{\sigma_{Nex/\sqrt{Noff}}(t_0)} \tag{2.16}$$

The sensitivity is useful to compare the performance of different instruments and to estimate the flux that can be detected for a given amount of observation time.

There are two ways to give the sensitivity of an experiment: we can search for a set of cuts (*hadronness, size, θ^2 ...*) that give the best sensitivity above a given energy threshold. This is the so-called **integral sensitivity**. We can also search for the set of cuts that give the best sensitivity in a given energy range and compute the **differential sensitivity** in that range. The current MAGIC integral and differential sensitivities are shown in Fig. 2.32.

2.2.3.8   Skymaps

Skymaps are two-dimensional histograms containing the arrival direction of all the γ-ray candidates. To select the events going to the histogram, the standard cuts applied to the data are the same as those shown in Table 2.2. They are produced using the source-independent information provided by the *disp* method. The program producing the skymaps in MAGIC is called caspar.

The most difficult task to produce a reliable skymap is the background estimation. Due to the inhomogeneities in the pixel response, stars in the FoV and observations at different Zd and Az, the background estimation is affected. An advantage of *wobble* observations is that background can be extracted from the same data sample

Fig. 2.33 TS skymap of the Crab Nebula
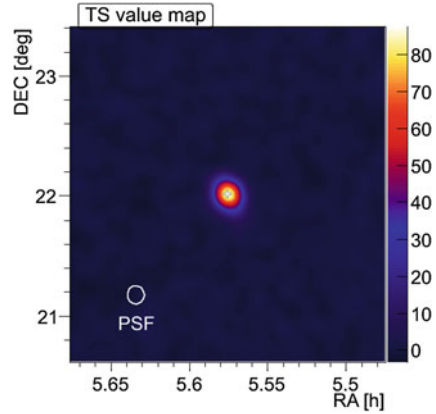
as the signal. To avoid contamination from the signal region and correct the camera inhomogeneities, for each wobble position the camera is divided in two halves and the γ-ray candidates from the half that does not contain the source are accepted for the background skymap. For calculating the significance of a signal in a skymap, we use the Test Statistics (TS) significance, which is the LiMa significance applied on a smoothed and modeled background estimate.

An example of a TS skymap can be seen in Fig. 2.33. When we have the signal and background skymaps, we subtract them to obtain the excesses histogram. This histogram is smoothed using the instrument's PSF added in quadrature with a Gaussian kernel to smear the number of excesses obtained. Finally, the σ_{smooth} used to smear the excesses histogram is given by:

$$\sigma_{\text{smooth}} = \sqrt{\sigma_{\text{PSF}}^2 + \sigma_{\text{Kernel}}^2} \tag{2.17}$$

The Gaussian kernel is usually taken equal to the PSF, so finally $\sigma_{\text{smooth}} = \sqrt{2}\sigma_{\text{PSF}}$.

2.2.3.9 Spectrum and Light Curve

Spectrum The γ-ray differential spectrum of a given source is the number of photons per unit of energy, time and area. It can be written as:

$$\frac{d\phi}{dE} = \frac{dN_\gamma(E)}{dE\, dA(E)\, dt} \tag{2.18}$$

To calculate it we need to compute the number of gammas in a given energy range, the collection area of the instrument and the effective observation time we spend on a given source. In MAGIC we use two dedicated programs to calculate the spectrum: the first one is called `flulxlc` (FLUX and Light Curve) and is used for

single-telescope data, the second one is called `flute` (FLUx vs. Time and Energy) and is a simplified and advanced version of the first one that works for stereo data only. These programs use the `melibea` output of the data to calculate the *number of gammas* in each energy bin and the *effective time*. It also uses the `melibea` output of the MC gamma rays to calculate the *collection area* and the best cuts to extract the number of excesses in each energy bin (the scheme of this process is shown in Fig. 2.21).

Number of gammas: $N_\gamma(E)$ is the number of excess events $N_{ex} = N_{on} - N_{off}$ in the energy range E. It is calculated in a similar way as it is done for the signal detection described in Sect. 2.2.3.7. A set of cuts (*hadronness*, θ^2) is selected in each energy bin, and the number of excess computed. The set of cuts is determined using MC in the following way: an efficiency is defined, and we change *hadronness* and θ^2 cuts until the number of surviving events exceeds this efficiency for each energy bin. These cuts are usually looser than the ones used to detect a signal, because that generally results in a better agreement of real and MC data and assures a better estimate of the *collection area*.

Effective time: It is the effective time of observation of a source. If we assume that the arrival time distribution of cosmic events follows a Poissonian distribution, the time difference between the arrival time of an event and the next one Δt, behaves exponentially. Given the Poissonian probability of observing n events in a time t for the event rate λ:

$$P(n, t) = \frac{(\lambda t)^n e^{-\lambda t}}{n!} \tag{2.19}$$

The probability that an event comes after a time t' is equal to the probability of observing 0 events in a time $t < t'$:

$$P(t' > t) = P(0, t) = e^{-\lambda t} \tag{2.20}$$

Since this probability can also be written as:

$$P(t' > t) = \int_t^\infty \frac{dP(t' = t)}{dt} dt \tag{2.21}$$

Therefore, the time evolution of the probability is given by:

$$\frac{dP(t' = t)}{dt} = \lambda e^{-\lambda t} \tag{2.22}$$

The event rate is given by the product of the time evolution probability times the number of recorded events N_0:

$$\frac{dN}{dt} = N_0 \lambda e^{-\lambda t} \tag{2.23}$$

being λ the rate of events recorded by the telescope that can be obtained from fitting to an exponential function the distribution of difference on arrival times between events Δt. An example of the distribution of Δt for a typical observation can be seen in Fig. 2.34. Finally, the effective time can be written as the total number of events divided by the event rate:

$$t_{\text{eff}} = \frac{N_0}{\lambda} \tag{2.24}$$

The reason that the effective time is not coincident with the time elapsed between the beginning and the end of the observation is that there might be gaps in data taking (between runs) and that the data taking has a certain dead time after each event (as it was explained in Sect. 2.2.1.7).

Collection area: It is the geometrical area around the instrument where the gamma rays are detected. It is calculated using MC gamma rays and results from dividing the number of detected gamma rays surviving analysis cuts by the number of simulated gamma rays in a given energy range multiplied by the simulated area, or the area of an ideal telescope that would detect all the simulated gamma rays. Its mathematical expression is:

$$A_{\text{eff}}(E) = A_{\text{sim}} \frac{N_{\text{sel}}(E)}{N_{\text{sim}}(E)} \tag{2.25}$$

where A_{sim} is the simulated area, $N_{\text{sim}}(E)$ the number of simulated events in a given energy range and $N_{\text{sel}}(E)$ the number of events surviving cuts in the mentioned energy range. Equation 2.25 is only true if the MC gamma rays are simulated with the spectrum of the γ-ray source. Otherwise each event has to be weighted as it is explained in Appendix A.1.

The effective area depends on the Zd of the observations, being larger for larger Zd because the shower is produced further away in the atmosphere, as it was explained in Sect. 2.1.3. An example of the effective area covered by MAGIC at the trigger and analysis level is shown in Fig. 2.35. The simulated area in MAGIC is currently a

Fig. 2.34 Distribution of time differences between events
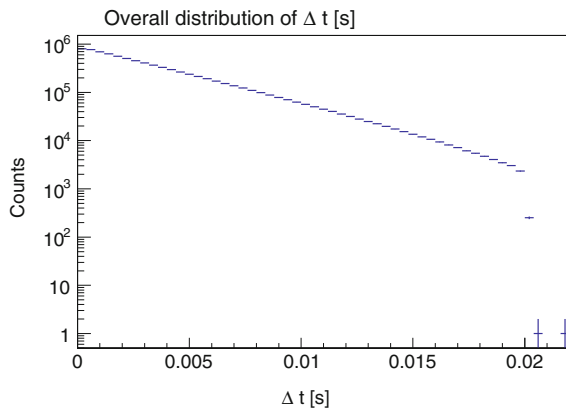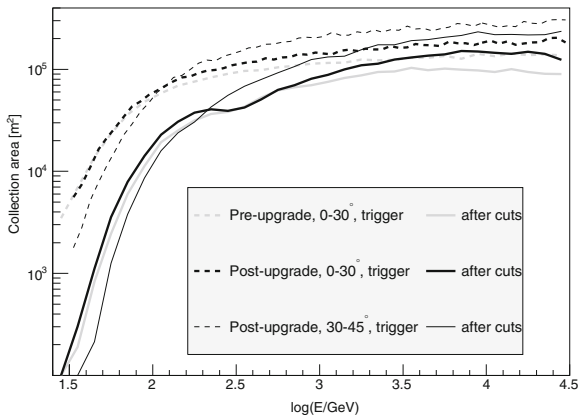
Fig. 2.35 Collection area before (*dashed lines*) and after (*solid lines*) applying analysis cuts. The collection area for the telescope equipped with the DRS4 readout and Zd range between 0–30° is represented with a thick black line and for the range between 30–45° with a thin *black line*. For comparison, the collection area for the period before the MAGIC upgrade is also included in *grey*. Plots taken from Aleksić et al. (2014g)

circle whose maximum radius, for each of the Zd ranges where the MC gamma rays are simulated can be found in Table 2.3.

Light curve: Light curves show integral fluxes in a given energy range and in bins of time. The differential energy spectrum (Eq. 2.18) is calculated for each of the time intervals, and then integrated over the energy range:

$$\phi = \int_{E0}^{E1} \frac{d\phi}{dE} \quad [\text{cm}^{-2}\text{s}^{-1}] \tag{2.26}$$

Upper limits: Upper Limits (ULs) on the flux are computed when no significant γ-ray signal is found. Using the number of measured excess events N_{ex}, the number of off events N_{off} and selecting a Confidence Level (C.L.) and systematic error, we can calculate an U.L. to the number of expected signal events N_{ul} using the method described in Rolke et al. (2005). The C.L. usually used to calculate MAGIC ULs is 95 % and the systematic error assumed is 30 %. N_{ul} is the UL on the maximum number of expected events according to the measurements performed and the confidence level

Table 2.3 Maximum impact parameters simulated for each Zd range

Zd range [°]	Maximum impact [m]
05–35	350
35–50	500
50–62	700
62–70	1000

defined. As we do not have any information about the source, we also have to assume a spectral shape, usually a power-law with spectral index $\Gamma = 2.6$.

$$\phi(E) = K S(E) = \left(\frac{E}{E_0}\right)^{-\Gamma} \tag{2.27}$$

The integral flux above an energy $E_{\min}$ can be written as:

$$\int_{E\min}^{\infty} \phi(E)\, dE = K \int_{Ec}^{\infty} S(E)\, dE = \frac{N_{\text{ul}}}{\int_{E\min}^{\infty} \int_{0}^{t_{obs}} A(E)\, dE\, dt} \tag{2.28}$$

where t_{obs} is the observation time. Finally, the UL on the integral flux K_{ul} can be written as:

$$K_{\text{ul}} < \frac{N_{\text{ul}}}{T \int_{E\min}^{\infty} S(E)\, A(E)\, dE} \quad [\text{TeV}^{-1}\text{cm}^{-2}\text{s}^{-1}]. \tag{2.29}$$

2.2.3.10 Unfolding

Due to the non-idealities of the detectors, experimental results get usually distorted. To correct for the finite resolution of our telescope, we apply an unfolding procedure. In IACTs, events have an estimated energy, but their true energy is not known. Defining the detector response function to a measured quantity y (E_{est}) from a true quantity x (E_{true}) as $M(x, y)$, the measured distribution $g(y)$ can be written as a function of the true distribution $f(x)$:

$$g(y) = \int M(x, y)\, f(x)\, dx + b(y) \tag{2.30}$$

where $b(y)$ accounts for a possible background contribution in the measurement. Since the data is binned in bins of E_{true} and E_{est}, the equation can also be written:

$$g_i = \int M_{ij}\, f_j + b_i \tag{2.31}$$

In the case of MAGIC, the tensor M_{ij} is given by the *migration matrix* of the detector and can be calculated from simulated γ-ray MC. It basically represents the probability that an event with E_{true} belonging to bin j ends up in bin i of the E_{est} distribution. The easier way to solve this problem would be to invert M_{ij}, but this is sometimes not possible. In this case, the best way to solve this problem is the least square minimization method, finding the value that minimizes the χ_0^2. This, however, gives unstable results, so a regularization term is added:

$$\chi^2 = \chi_0^2 + \frac{\omega}{2}\chi_0^2 + Reg(f) \tag{2.32}$$

where $Reg(f)$ is the regularization and ω is the inverse of the regularization strength, which is a way to adjust the weight given to the regularization within the χ^2 equation. Large values of ω imply less regularization and usually produce spectra with fluctuations, but small values of ω produce too smooth unfolded distributions that can deviate from the data. The determination of an appropriate value for the regularization is very important when producing an unfolded spectrum. There are several methods to compute the regularization in MAGIC, they are described in Schmelling (1994), Bertero (1989), Tikhonov & Arsenin (1977)

There is another way of unfolding the data, the so-called *forward unfolding* method. It assumes a-priori the spectral shape that will be followed by the measurement, and minimizes the χ_0^2 with respect to these parameters. This is generally done analytically, forcing the solution to be continuous. The result is the best fit to the a-priori defined parameters, therefore no spectral points are available. Since no regularization is used, the result from the forward unfolding only depends on the assumed spectral shape.

The convergence on the result of all the unfolding methods has to be carefully checked. The spectra results shown by MAGIC are usually given using the *forward unfolding* method, although to produce the spectral points one of the other methods is used.

2.3   CTA

The Cherenkov Telescope Array (CTA) is an initiative to build a next generation ground-based VHE γ-ray instrument. It is proposed as an open observatory and it currently (May 2015) gathers about 1300 scientists from 29 countries worldwide. It is planned to have two sites, one in the southern hemisphere focused on galactic physics and another one in the northern hemisphere, mainly focused on extragalactic physics and transient events. The final site selection for both sites is expected to take place during the year 2015. An artist view of the CTA array is shown in Fig. 2.36. The technical objectives of the future-generation CTA can be summarized as:

- Achieve the lowest possible energy threshold by an IACT to be sensitive to transient phenomena such as blazars, GRBs, novae and any other phenomena that emits photons in the $\mathcal{O}(10$–$100)$ GeV band and lasts for days to weeks. This purpose will be achieved by the use of LSTs with their large reflectors able to collect the few photons produced by $\mathcal{O}(10)$ GeV cascades. LSTs are designed to work in stereo, which translates in an increase in the collection area of the array and a more powerful gamma/hadron separation. The latter is especially important at the lowest energies where γ-like showers are similar to cascades generated by hadrons or accidental triggers.
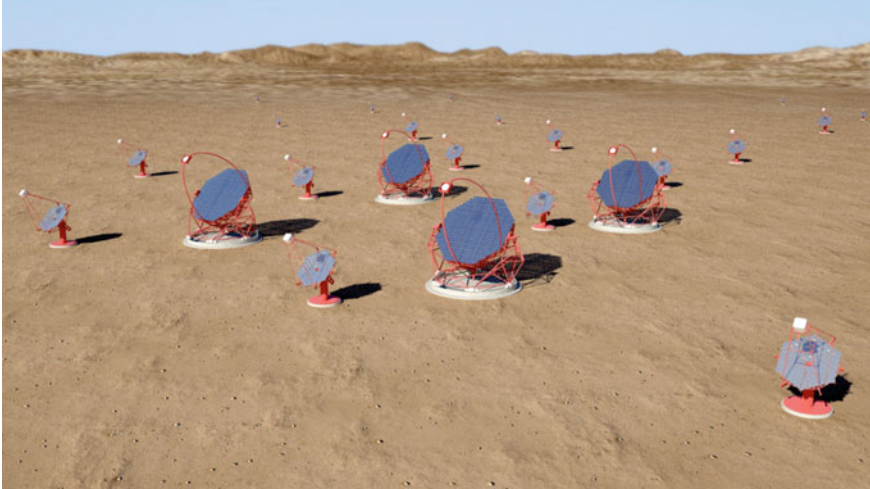
Fig. 2.36 CTA design concept. One can see four LSTs in the center of the array and they are surrounded by MSTs. SSTs are placed farther away from the center of the array to extend the overall collection area. Image courtesy G. Perez, SMM, IAC

- Improve the sensitivity at the medium energy band $\mathcal{O}$(0.1-1) TeV down to a few mCrab. This is achieved by collecting more photons and improving the angular and energy resolution for a better background rejection. The improved cameras and the increased number of MSTs with respect to the current arrays using similar telescopes (HESS, VERITAS) will make it possible.
- As the flux of γ-ray photons at $\mathcal{O}$(10) TeV is very small, to significantly detect them at these energies one has to increase the collection area. Background suppression at these energies is not a problem because of the steepness (power-law with a 2.7 photon spectral index) of the hadron spectrum. Several SSTs will be located in the outer parts of the array. They have high energy threshold ($\mathcal{O}$(1) TeV), but their only purpose is to extend the collection area of the array to collect the maximum number of VHE photons at energies >10 TeV.

There are mainly three telescope types:

- **Large Size Telescope (LST)**: They are designed to be light-weighted to achieve fast repositioning to catch GRBs. The structure is made of carbon-fiber tubes holding a tessellated parabolic reflector of 23 m diameter. The current design has a 27.8 m focal length, 4.5° FoV and 0.1° PMTs as pixels (Acharya et al. 2013). A maximum of four telescopes will be placed in the center of the array of each observatory. A drawing of the LST design can be seen in Fig. 2.37a.
- **Medium Size Telescope (MST)**: They are designed to have 12 m Davies-Cotton reflectors. The current design is to have 17 m focal length, 7–8° FoV and 0.18° PMT pixels. In the order of thirty MSTs will surround the LSTs in each site. A picture of the MST prototype constructed in DESY Berlin is shown in Fig. 2.37b
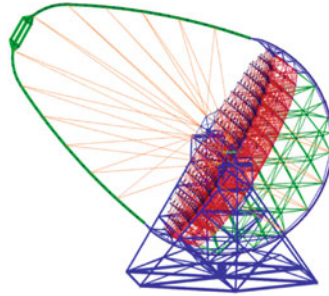
(a) LST drawing.

(b) Single-mirror MST prototype in DESY Berlin.
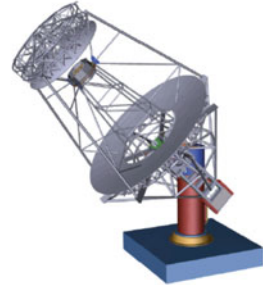
(c) Dual-mirror MST SCT prototype design.

(d) Single-mirror SST prototype in Krakow.´

(e) Dual-mirror SST prototype on Mount Etna.

Fig. 2.37 Prototypes and designs of the different telescope types for CTA

There is also a plan to construct a double mirror SCT to extend the southern array with a maximum of 36 telescopes of this type (Vassiliev & Fegan 2008). They are currently planned to have a 10° FoV allowing a small plate scale that can be filled with smaller pixels such as SiPM. A drawing of the SCT telescope design is shown in Fig. 2.37c.

- **Small Size Telescope (SST)**: A variable number between 35–70 SSTs will be placed in principle only in the southern observatory, focused on galactic physics and interested in the highest γ-ray energies. Several solutions have been designed to reduce the cost and be able to construct such a large number of telescopes. A prototype using the traditional Davies-Cotton optics with a 1 m reflector was built in Kraków and is shown in Fig. 2.37e. The usage of the Schwarzschild-Couder optics has also been developed for this type of telescopes and a picture of the 2 m primary reflector ASTRI SST prototype constructed by INAF is shown in Fig. 2.37d.

The physic cases are several (Acharya et al. 2013) and can be summarized as:

1. Study the origin and propagation of cosmic rays
2. Understand particle acceleration in several objects such as pulsars, PWNe, SNRs, novae, black holes and any other object where extreme acceleration takes place.
3. Search for new physics beyond the Standard Model and study the nature of dark matter.

The duration of this thesis took place during the Design and Prototyping phases of the CTA schedule, therefore all the contribution to the CTA project is technical. CTA is expected to start scientific operation in 2018, although the full array is not expected to be completed before 2020.

References

Abramowski A et al (2014a). arXiv:1411.7568
Acharya BS et al (2013) Astropart Phys 43:3
Aharonian F et al (1997b) Astropart Phys 6:343
Albert J et al (2008) Nucl Instrum Methods Phys Res A 588:424
Aleksić J et al (2014f). arXiv:1409.6073
Aleksić J et al (2014g). arXiv:1409.5594
Aleksić J et al (2014a) Science 346:1080
Aliu E et al (2008) Science 322:1221
Aliu E et al (2009) Astropart Phys 30:293
Barrio JA, et al (1998) MPI-PhE 98–05
Bartko H et al (2005) Nucl Instrum Methods Phys Res A 548:464
Bertero M (1989) Linear inverse and ill-posed problems, vol 75. Academic Press, New York, pp 1–120
Biland A et al (2008) Int Cosmic Ray Conf 3:1353
Bitossi M (2009) Ultra-fast sampling and readout for the MAGIC-II telescope data acquisition system, Ph.D. thesis
Blackett PMS (1948) The emission spectra of the night sky and aurorae, 34
Bretz T et al (2014). arXiv:1403.3573
Bretz T et al (2009) Astropart Phys 31:92
Cherenkov P, Doklady CR (1934) Akad. Sci. URSS 2:451
Elterman L (1964) Appl Opt 3:745
Engel R et al (2011) Annu Rev Nucl Part Sci 61:467
Fomin VP et al (1994) Astropart Phys 2:137

Fruck C et al (2014). arXiv:1403.3591

García JR, et al (2014). arXiv:1404.4219

Gini C (1921) Econ J 31:22

Heck D et al (1998) CORSIKA: a Monte Carlo code to simulate extensive air showers. (Forschungszentrum Karlsruhe GmbH)

Hillas AM (1985) Int Cosm Ray Conf 3:445

Hofmann W et al (1999) Astropart Phys 12:135

Jelley JV et al (1963) QJRAS 4:275

Lessard RW et al (2001) Astropart Phys 15:1

Li T-P et al (1983) ApJ 272:317

Lombardi S (2011) Int Cosm Ray Conf 3:266

Longair MS (1992) High energy astrophysics. Cambridge University Press, Cambridge

López M (2013) Proc ICRC, vol 692

Lucarelli F et al (2008) Nucl Instrum Methods Phys Res A 589:415

Majumdar P et al (2005) Int Cosm Ray Conf 5:203

Mirzoyan R et al (1994) MPI-PhE/94-35

Mirzoyan R (1997) Int Cosm Ray Conf 7:265

Mirzoyan R et al (2002) IEEE Trans Nucl Sci 49:2473

Moralejo A (2000) Búsqueda de fuentes cósmicas de radiación gamma de muy alta energía con el detector AIROBICC, Ph.D. thesis

Nakajima D et al (2013) Proc ICRC, vol 787

Oser S et al (2001) ApJ 547:949

Paoletti R et al (2007) IEEE Trans Nucl Sci 54:404

Rissi M et al (2009) IEEE Trans Nucl Sci 56:3840

Rolke WA et al (2005) Nucl Instrum Methods Phys Res A 551:493

Schmelling M (1994) Nucl Instrum Methods Phys Res A 340:400

Schmidt F (2015) CORSIKA shower images. http://www.ast.leeds.ac.uk/fs/showerimages.html

Sitarek J et al (2013) Nucl Instrum Methods Phys Res A 723:109

Staszak D (2014) Nucl Instrum Methods Phys Res A 742:212

Tescaro D et al (2009). arXiv:0907.0466

Tescaro D et al (2013). arXiv:1310.1565

Tikhonov A et al (1977) Solutions of ill-posed problems., Scripta series in mathematicsWinston, Great Falls

Vassiliev VV et al (2008) Int Cosm Ray Conf 3:1445

Wagner R (2006) Measurement of VHE γ-ray emission from four blazars using the MAGIC telescope and a comparative blazar study, Ph.D. thesis

Yao W-M et al (2006) J Phys G Nucl Phys 33:1

Zanin R (2011) Observation of the Crab pulsar wind nebula and micro quasar candidates with MAGIC, Ph.D. thesis

Zanin R et al (2013) Proc ICRC, vol 773

Part II
Contributions to the Lowering of the Threshold of Imaging Atmospheric Cherenkov Telescopes

Fig. 1 Artist view of four LSTs. Credit: IFAE, CTA consortium

Chapter 3
Single Telescope Trigger for CTA

The goal of the LSTs for CTA, as it was described in Sect. 2.3, is to achieve the lowest possible energy threshold. To push the threshold down in energy, one of the most important systems is the camera trigger, that selects the events that are recorded. Since most of the problems when lowering the energy threshold of the system is that the accidental triggers increase, the trigger system needs to powerfully distinguish between the events containing cosmic showers and the ones containing only noise. Arrays of Cherenkov telescopes typically use multi-level trigger schemes to keep the rate of accidental triggers produced by direct NSB and PMT APs low. At a first stage, individual telescopes produce a trigger signal from the pixel signals in the telescope camera. The final event trigger is then formed by combining trigger signals from several telescopes. We will present in this chapter the work performed to develop, test and characterize an analog trigger system for the analog cameras of LSTs and MSTs.

3.1 Description of the Analog Trigger Concept

We designed a trigger system completely based on the analog treatment of the signals coming from the camera pixels (Barcelo et al. 2013; Tejedor et al. 2013). A schematic of the whole trigger system is shown in Fig. 3.1. The photosensors are grouped in clusters of 7 pixels and their signals are first handled by a *L0 decision* trigger that has two trigger strategies implemented. The *majority* trigger option issues a rectangular pulse for the pixels that are above a certain DT and then makes an analog sum of all the rectangular pulses in the cluster. The *sum* trigger option issues the analog sum of the signals from a group of pixels. The signals coming from several clusters, with either of the two L0 options, go to an *L0 fan-out* board that copies and distributes them to the *L1 decision* trigger installed in each cluster. It adds up the signals coming from
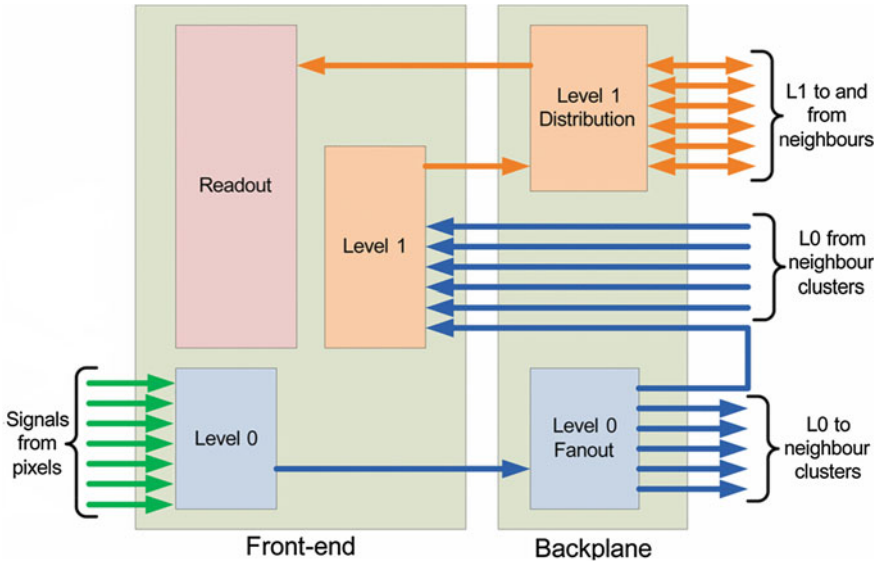
Fig. 3.1 Trigger scheme for analog cameras for CTA. From Tejedor et al. (2013)

neighboring clusters and issues a rectangular signal if the addition is above a certain threshold. The signals issued by the L1 are then distributed by the *L1 distribution* that collects the signals generated by the L1 decision boards and provide them to the Trigger Interface Board (TIB) and the readout.

The work performed on the trigger system for CTA presented in this thesis was twofold: on one hand, we performed simulations to evaluate the difference in performance between using the different trigger options implemented in the analog trigger developed for the analog readouts of the MSTs (NECTAr, Vorobiov et al. 2011) and LSTs (*Dragon,* Kubo and Paoletti 2011). We also used simulations to investigate the effect of non-idealities such as wider PMT pulses in the LST performance. On the other hand, we characterized the test modules for the L0 trigger, first on its discrete component form, and later the L0 ASICs that will finally be used for the analog camera of the LST prototype.

3.2   Optimal Design Based on Simulations

The simulation of the different trigger options is necessary to compare their performance. In this section we describe the results of comparing the performance of the sum trigger and the majority trigger. Furthermore, we have studied for the sum trigger option the gain between single-telescope and stereo observations and also the effect of non-idealities such as wider pulse amplitude of the PMTs.

3.2.1 Simulation Characteristics

3.2.1.1 Software

The *Production-I* of MC simulations for CTA only implemented one trigger scheme. Most of the simulations summarized here were performed with the trigsim package (Wischnewski 2011). This package was meant to be later implemented in the standard CTA MC simulation package `Sim_telarray` (Bernlöhr 2008). It actually uses a special option of Sim_telarray that generates files with the arrival time of each phe produced in each pixel. Some results also come from the new implementation of other trigger schemes in `Sim_telarray`.

In *Production-II*, several trigger schemes are implemented and run. It also stores by default the information of arrival time for each phe produced in each pixel, if the shower generates more than a pretty low value of phe. Some results regarding different trigger options were also drawn that are in concordance with those presented in this section (Bernlöhr 2013).

3.2.1.2 Input Parameters

It is important to clarify the input parameters of the simulation to understand the possible differences between the results of different simulations. When we do not state the contrary, these are the parameters used for the simulations:

- Pulse shape: Gaussian with FWHM = 2.6 ns;
- APs distribution: Used the complete distribution of AP provided by Hamamatsu in April 2010. See Fig. 3.2.

Fig. 3.2 APs Distribution
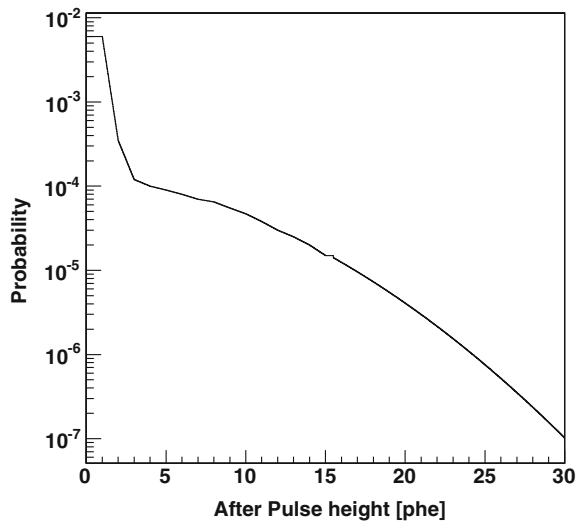
- Cells = 21 pixels patch with overlapping.
- Clipping levels [for sum trigger]: Clip = 6 and 8 phe.
- Simulation time 50 ns.
- Different gate widths used (2, 4, 6 ns) + Time over Threshold (ToT).
- Different cuts in the minimum number of phe (no cuts, 25 phe, 50 phe).

3.2.1.3 Showers

We used proton and gamma showers for the simulations. To calculate the cosmic ray rate we use files with a spectrum of energies simulated with a power-law with photon spectral index $\Gamma = 2$ for energies in a range 0.005 TeV < E < 500 TeV. To calculate *collection areas*, we used gammas with single-energies (0.01, 0.03, 0.1, 1, 10, 100 TeV) and to calculate the *energy threshold*, we used files with a spectrum of energies simulated with a power-law with photon spectral index $\Gamma = 2$ for energies in a range 0.01 TeV < E < 100 TeV. The spectrum was re-weighted to a power-law with photon spectral index $\Gamma = 2.6$ to calculate the energy threshold, as it is explained in the Appendix A.1.

3.2.1.4 NSB Simulation

The first step was to check how the camera trigger rate induced by the NSB changes as a function of several parameters that could be tuned in the trigger. The expected rates of phe per pixel from the NSB depend on the site conditions, the QE of the photo-detector to be used as well as the pixels size and the dimension of the reflector surface. Different scenarios are simulated for the amount of NSB that is accepted in the triggers of each telescope (see Sect. 3.2.2.1). The NSB simulations were run for one single trigger cell and the results extrapolated to the whole telescope, taking into account the overlap between cells.

3.2.1.5 Telescopes

The characteristics of the different telescopes were selected according to the latest specifications accepted by the MC group for *Prod-I*. It is also important to know for each telescope the NSB levels we are working with. As the PMTs used are the same for each of them, the only difference comes from the different FoV of each pixel, dependent of the mirror area and focal length. For the considered two type of telescopes we have the following characteristics:

- **LST**: Mirror area = 381.9 m^2; Focal length = 28.0 m; Number of pixels = 1813; Extragalactic NSB = 208 MHz per pixel.
- **MST**: Mirror area = 103.9 m^2; Focal length = 15.6 m; Number of pixels = 1765; Extragalactic NSB = 173 MHz per pixel.

3.2.1.6 Camera Trigger

The camera trigger simulation performs the combinations of analog signals of pixels in a trigger region. Two possible combinations have been studied: in the first one, the so-called *analog sum trigger*, all the analog signals of the trigger regions are analogically added; in the second one, the so-called *analog majority trigger*, the analog signals of the pixels in one cluster are first compared with a threshold and the corresponding digital signals are then analogically added for all the clusters in the trigger region, and the resulting sum compared with another threshold.We will present results comparing these two options.

3.2.2 Comparison Between Different Trigger Options

It was agreed between the MC Working Package (WP) that two different scenarios will be considered for the simulations (Hinton 2012). Those options are presented and the determination of the operation point for each of them described.

3.2.2.1 Different Scenarios Proposed

1. *Safe*: DTs are fixed so that the single-telescope accidental rates due a NSB double as high as the extragalactic NSB are equal to the cosmic ray rate.
2. *Aggressive*: DTs are fixed so that the stereo accidental rates due a NSB at double as high as the extragalactic NSB are equal to 10 % the cosmic ray stereo rate. This scenario would allow to lower the energy threshold and increase the collection area at the lowest energies.

3.2.2.2 Determination of the Operation Point

We computed the operation point where we would work in the different scenarios considered for the simulations.

1. *Safe*: For the safe scenario we performed the following steps: First of all, we run the single-telescope simulations for $1.5 \times$ proton rate (to account for the presence of nuclei heavier than protons) and NSB. We run the NSB simulations for a single cell and multiply the single-cell rate by a factor κ, given by:

$$\kappa = \frac{p \times n}{N_c}$$

where p = number of pixels in the telescope, n the number of times each pixel appears in the overlapping clusters (for our clusters $n = 3$, except for the outer cells) and N_c the number of pixels in each cluster (for the analog clusters $N_c = 21$).
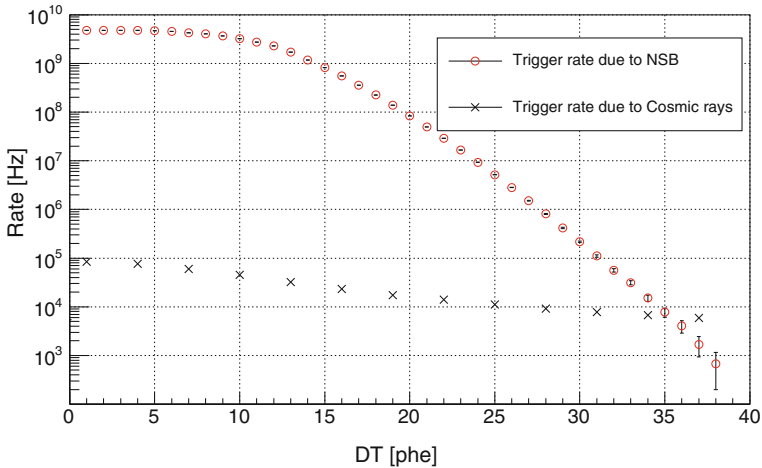
Fig. 3.3 Trigger rate due to NSB (*red circles*) and due to cosmic rays (*Black crosses*) for an LST working in single-telescope mode. The crossing point gives the DT where we will operate

Table 3.1 DTs, single-telescope and stereo rates for the different simulated scenarios considered

			Sum trigger		Majority trigger	
			Safe	Aggressive	Safe	Aggressive
LST	DT [phe]		35	34	10	9
	Rate [kHz]	Single-telescope	6.5	6.7	3.4	4.0
		Stereo	2.4	2.5	0.35	0.39
MST	DT [phe]		34	31.5	10	9
	Rate [kHz]	Single-telescope	1.5	1.8	1.4	1.6
		Stereo	1.2	1.3	0.24	0.25

We plot both rates and the point where both curves intersect gives the DT to be used for this scenario. An example of the method used can be found in Fig. 3.3.

2. *Aggressive*: To evaluate the operation point of this option, we simulated $1.5 \times$ proton rate and calculated the stereo NSB rate (see details in Appendix A.2). The crossing point between the $1.5 \times 0.1 \times$ proton stereo rate and the NSB stereo one gives the DT at which both are equal (Table 3.1).

3.2.2.3 Results for the Optimization of Trigger Options

The comparison between the performance of the sum and majority trigger is done using the *collection area* and *energy threshold* given by each trigger option for each telescope and for each DT scenario.

For any trigger strategy, one can reduce the trigger rate induced by the NSB as much as desired, but this will also mean a reduction of the collection area and increase in the energy threshold (defined in Sects. 2.2.3.9 and 2.2.3.6 respectively). Hence, a sensible criteria to choose one trigger strategy would be checking the collection area and energy threshold one could get as a function of the trigger rate induced by the NSB.

Triggers still have to be reconstructed and classified as hadrons or photons. Therefore, one might expect that the best figure of merit would be the final sensitivity of the telescope (i.e., gamma efficiency over the square root of hadron efficiency). However, one has to keep in mind that a basic trigger scheme does not differentiate between real gamma and background events, but between NSB-induced events and γ-like events (either from gamma or hadron origin). So at the end, the trigger scheme which provides the largest collection area for γ-like events, while keeping the NSB-induced events under control, will very likely be the best trigger scheme, from the simulation point of view.

Finally, one still has to keep in mind that we have been so far only considering single-telescope trigger and CTA will work in stereo mode asking for two or more telescopes in coincidence. The assumption is that although the stereo requirement will change the effective collection area for CTA, the change will be quite independent on the single telescope trigger strategy. This should be true if the dependence of trigger probability on distance between the shower core and the telescope axis is similar for the different trigger strategies. This condition was checked for gamma-ray induced showers.

Collection Area The collection area has been computed for each of the simulated energies, for the different scenarios considered and for both the LST and MST telescopes.

LST We start with the comparison between different options for the LST. Apart from testing different trigger options, we also checked the effect of applying a cut in the minimum number of phe in each event. The cut is meant to check that the results do not change by eliminating the events producing the smallest images that will probably not be used for the analysis. The cut selected is 25 phe. The plots of the collection area and the ratio between the collection area of a given option divided by the collection area applying sum trigger with a clipping of 6 phe are shown in Fig. 3.4.

It is shown that in general the *sum* trigger gives larger collection areas than *majority* for low energies. Between the two clipping options, the one using a higher value of clipping (8 phe) is a slightly better option to obtain larger collection areas at low energies (the ones relevant for the LSTs). This effect could be explained because of the lower energy showers triggering the system. They will produce one pixel with a very high charge and some pixels surrounding it with a lower one. Since the larger signal is cut due to the clipping, the option using a higher clipping value let lower energy showers trigger the system. We have also checked that the ratios hardly change when applying a cut in phe. Conclusions at very low energies (10 GeV) cannot be obtained, because of the very large uncertainties due to the low statistics with the
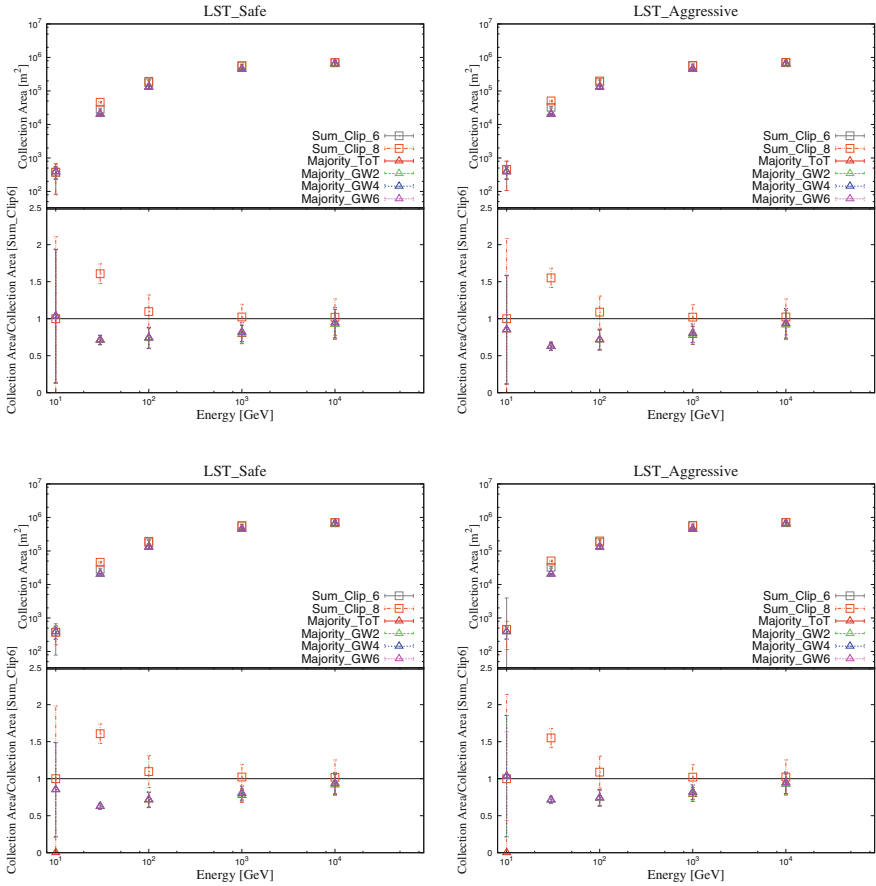
Fig. 3.4 LST collection area for the safe (*top left*) and aggressive (*top right*) trigger scenarios with no cut in the minimum number of phe, and safe (*bottom left*) and aggressive (*bottom right*) scenarios with a cut of 25 phe. Sum_Clip_6 corresponds to the sum trigger with a clipping = 6 phe, Sum_Clip_8 to the sum trigger with a clipping = 8 phe, Majority_ToT to majority time over threshold, and Majority_GWN to the majority opening a trigger gate of width N ns

used DTs. For energies larger than 1 TeV, the majority and sum trigger options are equivalent. This would be in principle expected, as the performance of the sum trigger is known to exceed the one of the majority trigger at low energies (<100 GeV), but not necessarily at higher ones.

Let us now compare the aggressive and safe scenarios. As the aggressive scenario allows to lower the DT more than the safe one (not with the majority trigger), it triggers more showers, therefore the collection areas are slightly larger. In Fig. 3.5 we show the ratio between the collection area of the safe aggressive and safe scenarios.

Due to the large errors in the extrapolation of collection areas for both scenarios, we find that, although a bit higher for the lowest energies with the aggressive option, both of them are, within errors, equivalent.
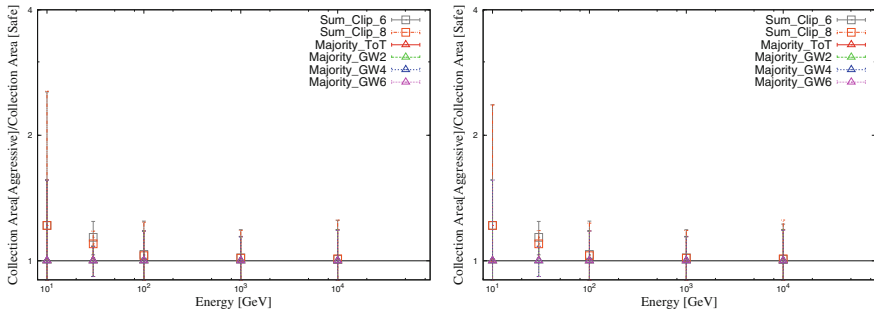
Fig. 3.5 Comparison between safe and aggressive trigger scenarios for the LST with no cut in the minimum number of phe (*left*) and with a cut of 25 phe (*right*). The options plotted are the same as in Fig. 3.4

MST We also studied the performance of the analog trigger to be used with the analog cameras of the MSTs. The trigger options studied are the same as those investigated for the LSTs, also studying the effect of a minimum cut of 25 phe in the events accepted (Fig. 3.6).

The sum trigger option gives slightly larger collection areas for energies >1 TeV, but within the errors, all trigger options are equivalent. As it was already mentioned, the sum trigger is expected to show a better performance at the lowest energies, however for high energies both options are expected to perform similarly, as it is shown.

Figure 3.7 shows a comparison between the aggressive and safe scenarios for the MST. The DTs are again lower for the aggressive scenario, although the performance is equivalent within the errors as it was the case for the LSTs.

Energy Threshold To compute the energy threshold we simulate a power-law spectrum with $\Gamma = 2.6$ spectral index for energies between 0.01 and 100 TeV. The energy threshold is the mean of a gaussian fit around the maximum of the histogram containing the energy of the triggered energy distribution, as it is explained in Sect. 2.2.3.6. We can find in Table 3.2 the thresholds for the different options.

We see that in every case, sum trigger provides lower energy threshold than majority trigger. This is a direct consequence of having a larger collection area at low energies. The cut in phe does not affect the energy threshold of any of the options. The aggressive strategy improves the trigger energy threshold of the telescope slightly.

3.2.3 Gain Between Single-Telescope and Stereo Observation for the LSTs

According to the CTA requirements for the LST, the LST DAQ should be able to record events with a rate up to 7.5 kHz. The goal of the LST project is to be able to handle a recording rate of 15 kHz. To evaluate the gain obtained going from
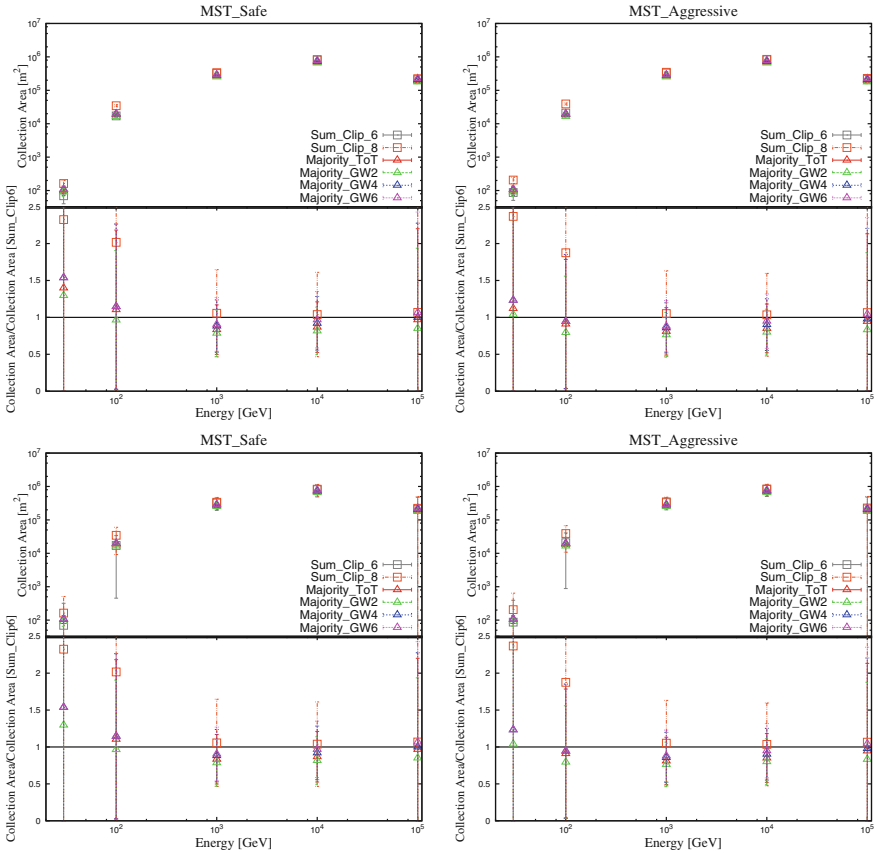
Fig. 3.6 MST collection area for the safe (*top left*) and aggressive (*top right*) trigger scenarios with no cut in the minimum number of phe, and safe (*bottom left*) and aggressive (*bottom right*) scenarios with a cut of 25 phe. The options plotted are the same as in Fig. 3.4
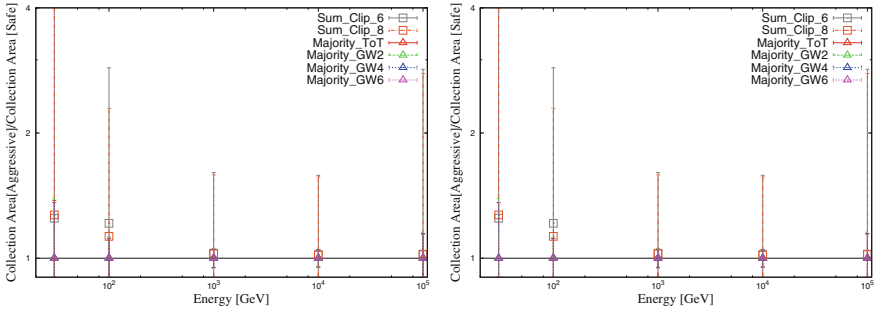
Fig. 3.7 Comparison between safe and aggressive trigger scenarios for the MST with no cut in minimum number of phe (*left*) and with a cut of 25 phe (*right*). The options plotted are the same as in Fig. 3.4

Table 3.2 Energy thresholds for the different trigger options and scenarios

	Trigger type	Energy threshold [GeV]			
		Cut = 0 phe		Cut = 25 phe	
		LST	MST	LST	MST
Safe	Sum Clip [6 phe]	43.0 ± 0.2	138 ± 11	43.0 ± 0.2	138 ± 11
	Sum Clip [8 phe]	32.9 ± 0.2	126.5 ± 1.5	32.9 ± 0.2	126.5 ± 1.5
	Majority	52.0 ± 0.3	146 ± 7	52.0 ± 0.3	146 ± 7
Aggressive	Sum Clip [6 phe]	37.4 ± 0.2	136 ± 4	41.4 ± 0.2	136 ± 4
	Sum Clip [8 phe]	29.6 ± 0.2	120.0 ± 1.4	29.6 ± 0.2	120.0 ± 1.4
	Majority	38.3 ± 0.4	137 ± 5	38.3 ± 0.4	137 ± 5

Table 3.3 Energy thresholds and rates for different DTs for single-telescope and stereo LSTs

Operation point selection criterium	DT [phe]	Single-telescope rate [kHz]	Stereo rate [kHz]	Energy threshold [GeV]
Single-telescope 7.5 kHz	26.9	7.5	2.7	20.6 ± 0.2
Single-telescope 15 kHz	26.0	15.3	3.0	19.4 ± 0.2
Single-telescope crossing point	27.0	6.6	2.7	20.7 ± 0.2
Stereo 7.5 kHz	23.8	82.2	7.5	13.9 ± 0.2
Stereo 15 kHz	23.0	151.0	15.5	13.7 ± 0.2
Stereo crossing point	23.8	84.1	7.8	13.9 ± 0.2

7.5 to 15 kHz recording rate, we computed the energy threshold for these trigger rates. We also evaluated the gain of moving from the requirement and goal single-telescope recording rate to the same rate in stereo. Since the sum trigger with a clipping of 8 phe produced the best performance according to the results obtained in Sect. 3.2.2.3 performed these simulations using these settings. To achieve the lowest possible energy threshold, we considered for the simulations an extragalactic NSB of 208 MHz per pixel, instead of the galactic NSB considered to compare the performance of the majority and sum triggers. We computed the single-telescope and stereo rates, and the energy threshold for 3 different scenarios in each of the observation modes:

- Single-telescope (stereo) rate of 7.5 kHz
- Single-telescope (stereo) rate of 15 kHz
- Crossing point between the NSB trigger curve and the cosmic-ray trigger curve.

The energy threshold for all the different configurations can be found in Table 3.3. Figure 3.8 shows how the single-telescope and stereo trigger rates depend on the DT.

From these results we conclude that we gain less than 6 % in threshold when going from the required rate of 7.5 kHz to the goal rate of 15 kHz. On the other hand, going from single-telescope to stereo observations decreases the energy threshold by ∼30 %.
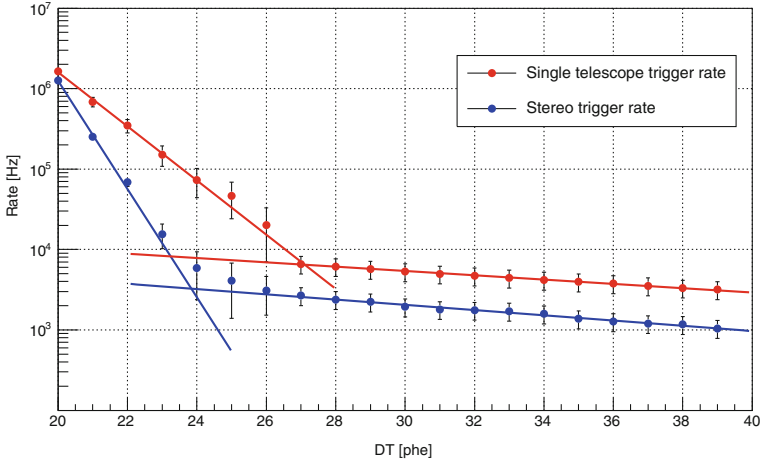
Fig. 3.8 Single-telescope and stereo trigger rates for extragalactic NSB
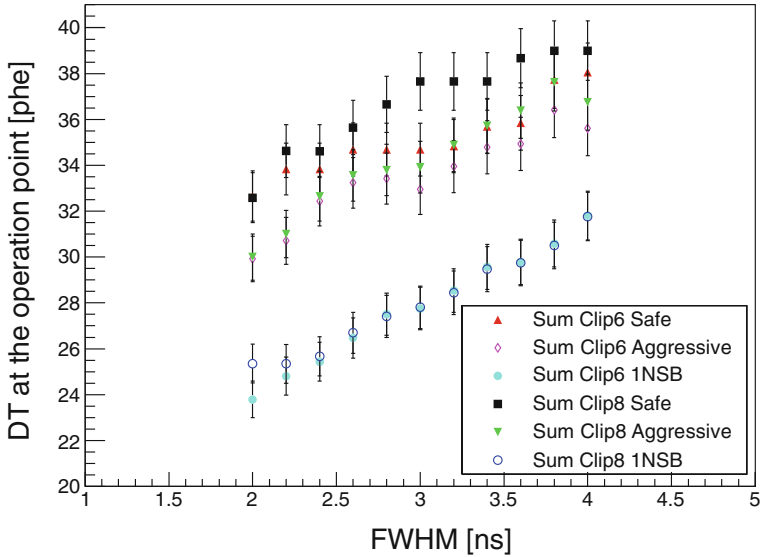
Fig. 3.9 DT at the operation point as a function of the FWHM

3.2.4 Impact of the PMT Pulse Width on the Trigger Collection Area

As it was described in Sect. 2.1.3, the faster the integration time of the signal, the less background light is integrated. The photosensors developed for the LST are last generation PMTs with peak QE exceeding 40 % and designed to achieve the lowest possible AP rate. The AP rate is dependent on the materials used for the photocathode

and also on the voltage applied between dynodes. If this voltage is reduced, the PMT signals get broader.

To evaluate the effect of pulse widening, we calculated the performance of the trigger for different pulse widths, ranging from 2.0 to 4.0 ns in steps of 0.2 ns. The goal for the LST PMTs is 2.6 ns, but we considered a broad range of pulse widths to ascertain the tendency in trigger threshold. We performed these simulations for the sum trigger with different clippings (6 and 8 phe) and three different trigger scenarios: safe and aggressive with galactic NSB and safe with extragalactic NSB. To compute the operation points, we used the method described in Sect. 3.2.2.2. The resulting DTs for each of the configurations and each of the FWHMs can be found in Table B.2 in Appendix B.2. The increase of DT to work at the same operation point as a function of the FWHM is shown in Fig. 3.9.

The DT at the operation point increases almost linearly with the FWHM, implying also an increase in the energy threshold of the telescope. To compare the performance of the different options, we calculated the collection area achieved at different energies for the different options. Figure 3.10 collects the results for the ratio between
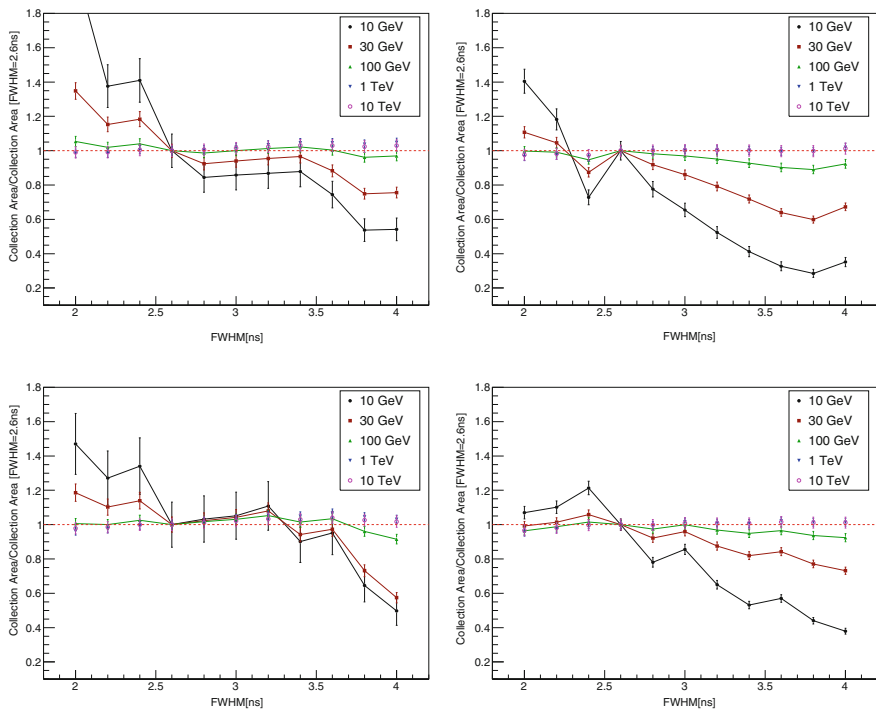
Fig. 3.10 Ratios between the collection area for a given FWHM and that for FWHM = 2.6 ns for different energies. On the *top left* we have the plot using sum trigger, a clipping of 8 phe and the safe scenario. On the *top right*, the same plot using a clipping of 6 phe. On the *bottom left* one can see the same plot as in the *top left* but considering the aggressive scenario and on the *bottom right* the same as in the *top left* but considering extragalactic background. The *red dashed line* indicates ratio = 1
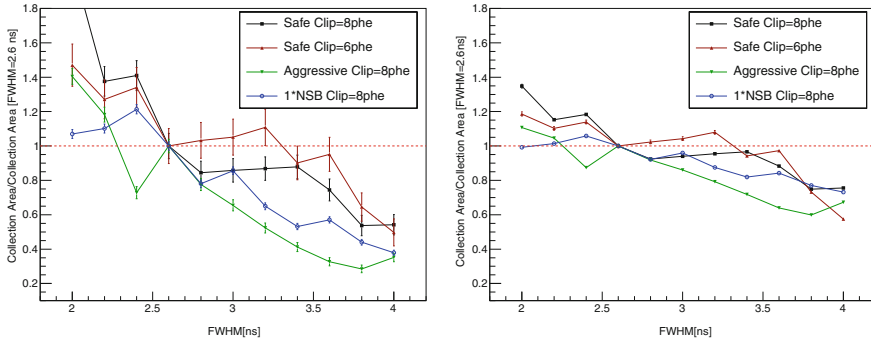
Fig. 3.11 Ratios between the collection area for a given FWHM and that for FWHM = 2.6 ns for 10 and 30 GeV for all the scenarios considered. The *red dashed line* indicates ratio = 1

the collection area reached by a given configuration divided by that corresponding to FWHM = 2.6 ns for a given energy.

As expected, the widening of the PMT pulse only affects the lowest energies, as the variation due to the increase in the operation point affects the lowest energy showers triggered by the telescope. If we compare the performance between all the options simulated for the lowest energies, as it is shown in Fig. 3.11, we can check the tendency of the performance when increasing the PMT width.

From the results shown in Figs. 3.10 and 3.11, we derive that for energies lower than 30 GeV, the trigger collection area shrinks by 5–8 % every 0.2 ns for FWHM > 2.6 ns. For the safe scenario, this effect is <20 % for FWHM <3.4 ns. This worsening is larger when the applied DTs are lower, as happens in the aggressive scenario or the one with extragalactic NSB (1*NSB). If we trigger deep in the NSB by lowering the DTs using these options, even a pulse width >3 ns reduces the collection area by >20 %.

3.3 Characterization of Trigger Hardware

The hardware for the L0 decision trigger was developed at IFAE and the definition of its requirements, test and characterization were performed as part of this thesis. We will first briefly describe the results for the discrete component trigger, as it was the first option developed. We will give a more detailed description of the L0 ASIC trigger that is the option that will finally be installed in the analog cameras of CTA.

3.3.1 Discrete Component Trigger

The first option to implement the analog trigger into mezzanines connected to the analog readouts for CTA was to use discrete components (resistors, capacitors...).

They met the cost, weight and power consumption specifications, although the performance was not optimal due to non-idealities in the circuits.

More concretely, the clipping was not constraining the signal height to a certain value as it was expected, but just producing an attenuation. To illustrate this effect, we show in Fig. 3.12 a plot of the transfer function that produces an ideal clipping. In Fig. 3.13 we show the transfer function for the discrete component L0 board when applying a given clipping. The difference between an ideal clipping and the one provided by the discrete component boards is that for larger signals we do not get a linear response, but the output voltage still increases with the input. This has an unknown effect on the trigger performance that was not evaluated. As the performance of the discrete component trigger was not optimal, we decided to move to the ASIC trigger option that provided a better performance with a reduction in weight and power consumption and what is more important, also a reduction in cost.

Fig. 3.12 Transfer function of a system where an ideal clipping is applied. The *black line* represents the signal without any clipping, the *magenta* one the signal clipped at 400 mV, the *cyan* one the signal clipped at 300 mV and the *red* one the signal clipped at 200 mV
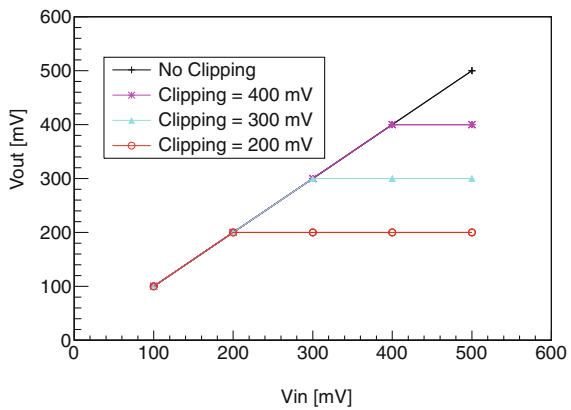
Fig. 3.13 Transfer function of the analog discrete component trigger where the clipping is applied. In *red* we show the non-clipped signal and in *green* the clipped one
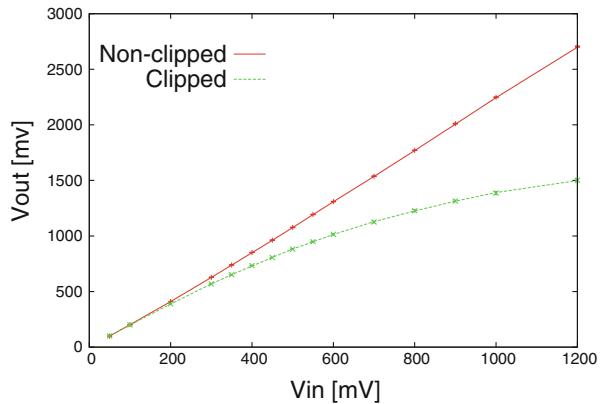
3.3.2 L0 ASIC Trigger

Application-Specific Integrated Circuits (ASICs) are integrated circuits, developed and designed to satisfy a specific application requirement. The work on the discrete components trigger, that produced a working and fully tested board, made possible the design of an ASIC with all the functionalities of the discrete components trigger. Moreover, the ASIC trigger reduces weight, space and cost, so all the groups designing the analog trigger for CTA decided to move from a discrete components trigger to a full trigger system made by ASICs (Barrio et al. 2014a, b).

The full analog trigger chain will finally be composed by an L0 decision ASIC, an L0 distribution ASIC and an L1 decision ASIC, all of them mounted on their corresponding mezzanines. The L0 mezzanines include, before the L0 ASIC, adjustable delay lines to compensate the differences in transit time between PMTs to achieve a better synchronization of the individual signals at the trigger level. The L0 distribution ASIC is under test, the L1 decision was designed, tested and characterized at CIEMAT and the L0 decision ASIC was designed by UB and fully characterized and tested at IFAE.

The L0 decision ASIC uses an AMS $0.35\,\mu m$ SiGe BiCMOS technology, having an area of $\sim 11\,mm^2$. The technology is common to that used for PACTA, ACTA and NECTAr chips, fact that reduces the cost of producing all of them in the same run. It processes analog signals of individual pixels in a cluster of 7 pixels. As it was mentioned, each ASIC contains two different L0 approaches, the *majority* trigger and the *sum* trigger. Both of them were designed by using full differential circuits to minimize the effect of long distances in the connection with other subsystems. As the trigger clusters are defined as groups of 7 pixels, the ASIC input signals are 7 differential analog inputs. Each differential pair goes through an attenuator circuit to the two L0 trigger options in order to equalize all pixel gains with a better precision. This attenuator lets adjust the gain of the signal from $1.35 \times$ Input Voltage (V_{in}) to $0.6 \times V_{in}$ in steps of $0.05\,mV$. The majority trigger concept compares the signal from each pixel to a voltage threshold by using a discriminator circuit. If the signal overcomes the threshold, a $100\,mV$ signal is issued at the output of the channel. Each differential pair output of the discriminator is available as an LVDS output. The discriminator outputs are internally added and are also available as an analog differential output voltage (V_{out}). The sum trigger concept cuts the signals greater than a given value by using a clipping circuit, as it was explained in Sect. 2.2.1.6. There are 3 different clipping options that clip the signal at different ranges, and for each of those options there are 63 different *fine clipping* options. Afterwards, the signals from all the pixels in the cluster are added and the resulting signal sent to the L0 distribution subsystem by an analog differential output. The input for these trigger boards has an equivalence of $20\,mV/phe$. A block diagram of the L0 ASIC is shown in Fig. 3.14.

Requirements: Following CTA internal requirements on durability, reliability and cost, we defined requirements for the L0 ASICs. These requirements and the results are collected in Table B.1 in Appendix B.1.
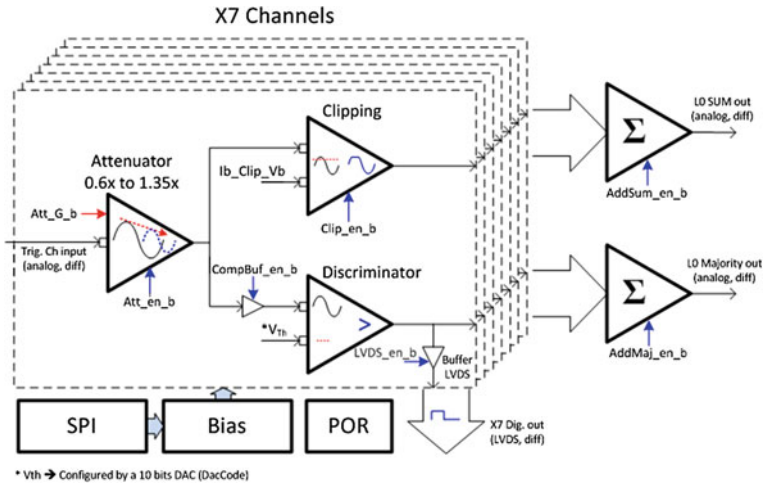
Fig. 3.14 L0 ASIC block diagram. From Sanuy et al. (2013)

Characterization measurements: We measure the output voltage of the ASIC for different conditions and check the functionality of all the channels and functions. All the measurements are performed for 10 input voltages:

V_{in} = 0.05, 0.06, 0.07, 0.08, 0.09, 0.1, 0.2, 0.3, 0.4, 0.5, 0.6, 0.7, 0.8, 1 V

We performed the characterization measurements for the 30 chips that were available after the first production.

Sum trigger: For the sum trigger part of the ASIC, we first checked the clipping functionality. Figure 3.12 illustrates how an ideal clipping works. All the possible settings for the sum part of every chip were tested. We measured for every input (14), channel (7), attenuation (16) and clipping options (only half of the fine clippings for each of the clipping options, i.e. 3 × 32), the corresponding output of the chip. The final measurement recorded is the mean of 10 measurements of this output. Figure 3.15 shows an example, for a given attenuation, of the sum output measured for all the input voltages aforementioned.

To characterize the clipping, we measured the evolution of the *Saturation output voltage* ($Vout_{sat}$), which is the output voltage limited by the clipping, as a function of the clipping value. For this measurement, we selected a value of high attenuation, plotted the V_{in} versus V_{out} for different inputs and fit the output voltage of the clipped part to a straight line, as it is shown in Fig. 3.15. The value that is finally plotted as a function of the clipping will be the mean between the saturation output voltage for every channel of the chip $<Vout_{sat}>$ and also its dispersion ($RMS(<Vout_{sat}>)$) for each of the fine clippings. We differentiate three curves corresponding to each of the clipping options (Fig. 3.16).
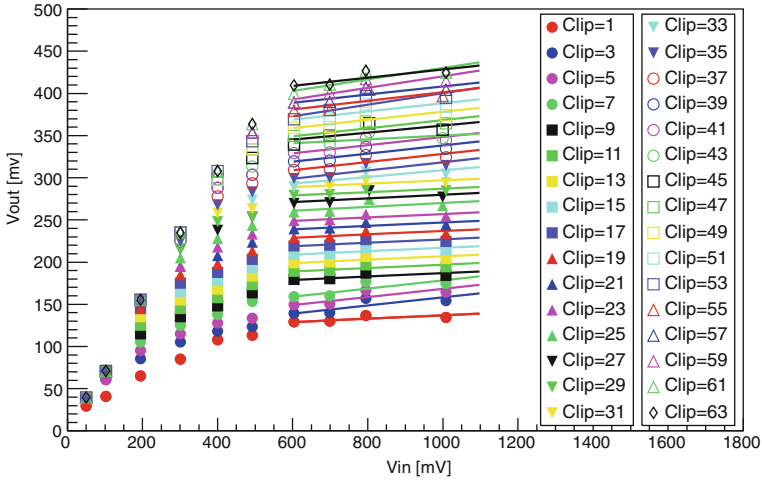
Fig. 3.15 Sum trigger V_{out} versus ASIC V_{in} for a given attenuation and different values of fine clipping. The output signals are fit in the range between 600 mV and 1 V to calculate the saturation output voltage
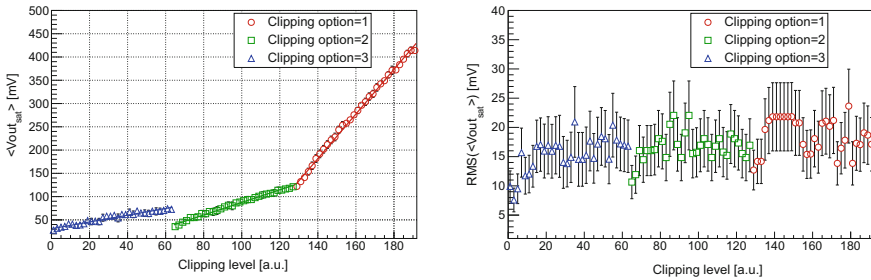
Fig. 3.16 Mean saturation output voltage as a function of the clipping (*left panel*) and its RMS(*right panel*) for one chip. Three sets of points are shown in different *colors*, each one corresponding to each of the clipping options. Each of them is adjusted by a first order polynomial in the region between 600 mV and 1 V, also drawn

To check that the clipping is not affected by the attenuation, for a given clipping value we measured the $Vout_{sat}$ for all attenuations. We repeated this measurement for 2 of the clipping options. For clipping option 1 we could not perform this measurement because the signals were too attenuated for large attenuation values and they were not reaching the level to be clipped. As the clipping should not depend on the attenuation selected, the $Vout_{sat}$ should be the same for the different attenuations. These measurements for one of the chips can be seen in Fig. 3.17. The sets of points for each of the clipping options are fit with a first degree polynomial $f(x) = p_1 x + p_0$. All of them are compatible with p1 = 0, i.e. a $Vout_{sat}$ non dependent on the attenuation.

Finally, we measured that the adder of the sum output was working correctly. For a given attenuation and clipping we measured the output of the adder. We used an
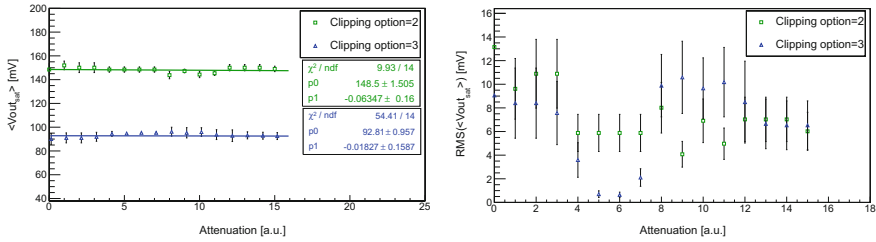
Fig. 3.17 Mean saturation output voltage as a function of the attenuation (*left panel*) and its RMS (*right panel*) for one chip. Two sets of points are shown in different *colors*, each one corresponding to each of the clipping options. Results from the fit for the different clipping options are shown in the same color as the points for the corresponding option. The sets of points for each of the clipping options are fit with a first degree polynomial $f(x) = p_1 x + p_0$

input signal of 50 mV and a high clipping value not to have clipped signals at the output. We measured the output of the adder for all the possible combinations of channels added. The measured output is divided by the number of channels added, therefore the final result should be the same for all the measurements. We plot the histograms of the output of the adder measured divided by the number of channels added for every number of channels added. The histograms are fit with a gaussian with parameters:

$$f(x) = A \exp\left(-\frac{x - \mu}{\sqrt{2}\sigma}\right)^2 \tag{3.1}$$

whose standard deviation σ is at the level of 1–2 % of the mean. The results of this check are shown in Fig. 3.18.

Majority trigger: We define the DT for a given input signal with a given attenuation as the discriminator voltage at which the output signal goes to 0. For the majority option it is important that the DT goes linearly with the input voltage. This linearity was determined by measuring the DT of all the channels for a given input and attenuation. We plotted the mean of all the channels. We fit the mean DT for several inputs and found that the mean DT as a function of the input is linear at a level ∼5 % for any input. An example of the mean DT of one chip as a function of the input voltage, for a given attenuation, is shown in Fig. 3.19.

Finally, the majority adder was also checked using the same procedure as for the sum adder, as it is shown in Fig. 3.20. For a given attenuation we measured the addition of all the possible combinations of channels. The final output was divided by the number of channels added to fill different histograms, depending on the number of channels added. The histograms were fitted with the gaussian described in Eq. 3.1, whose standard deviations were at a level <1 %.
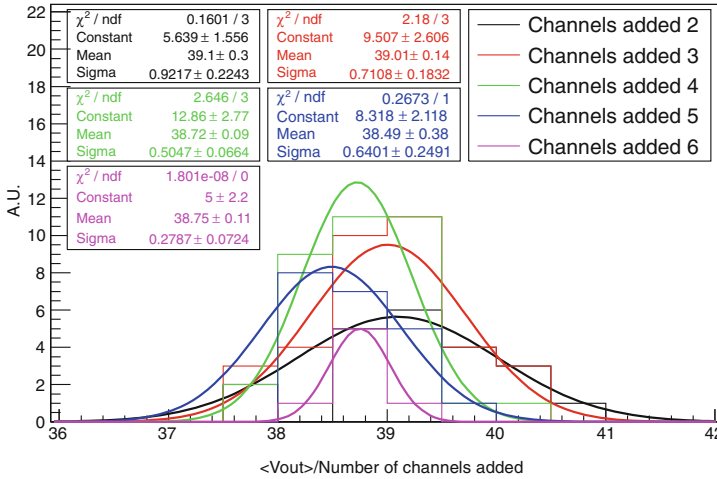
Fig. 3.18 Output of the *sum adder* divided by the number of channels added for an input signal of 50 mV. Histograms for the different number of channels added are shown in different *colors* (2 channels in *black*; 3 channels in *red*; 4 channels in *green*; 5 channels in *blue*; 6 channels in *magenta*) and fit with a gaussian, represented by a *line* of the same color as the histogram. The results of the fit are shown in the plot with the same color as the fit. Constant corresponds to A, Mean to μ and Sigma to σ as they are expressed in Eq. 3.1
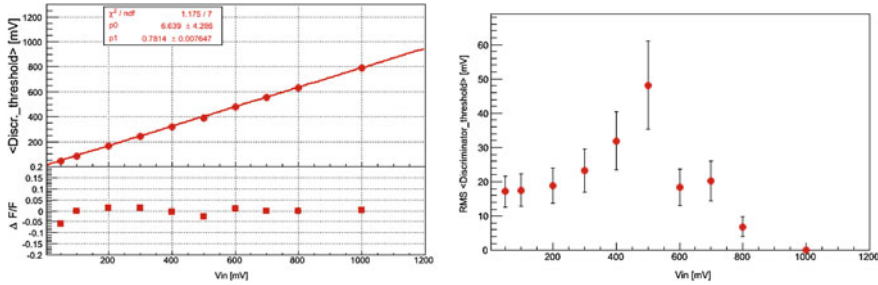
Fig. 3.19 Mean DT as a function of the input voltage for one chip (*left*) and its RMS (*right*). The mean DT is fit with a first degree polynomial $f(x) = p_1 x + p_0$. The results of the fit are shown in the left figure. The errors are very small and fall within the points. The relative residuals of the fit are also shown in the *bottom* panel of the *left* figure

3.3.3 Conclusions

The test and characterization of the L0 trigger was presented in this section. For the L0 trigger using ASICs, we find that for the *sum* option the saturation output voltage grows linearly with the clipping level and it does not depend on the attenuation used. For the *majority* option, we find that the comparator is linear at a level <5 %. The adders of analogue signals for both options work linearly.
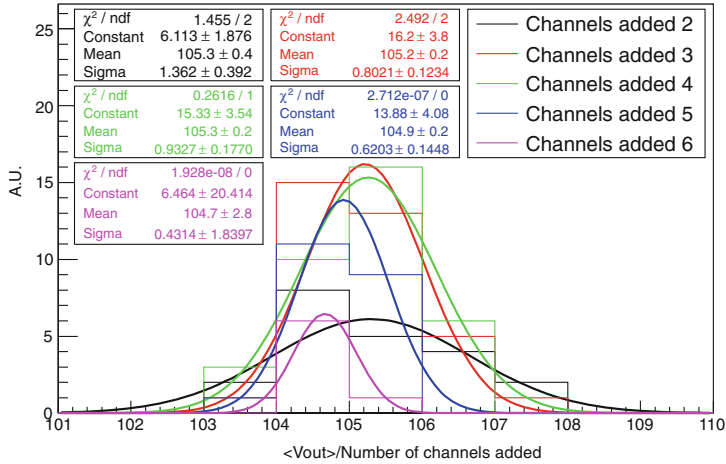
Fig. 3.20 Output of the *majority adder* divided by the number of channels added. Histograms for the different number of channels added are shown in different *colors* (2 channels in *black*; 3 channels in *red*; 4 channels in *green*; 5 channels in *blue*; 6 channels in *magenta*) and fit with a gaussian, represented by a *line* of the same color as the histogram. The results of the fit are shown in the plot with the same color as the fit. Constant corresponds to A, Mean to μ and Sigma to σ as they are expressed in Eq. 3.1

We find that the option of using ASICs performs better than that using discrete components. Moreover, using this option, we reduce cost, weight and power consumption, so we conclude that this is the final option that should be used for the LST and MST analog cameras. As of March 2015, we have already completely characterized a test sample of 30 L0 ASICs. The failure rate for this sample is $\sim 7\%$. For the final quality control, we have reduced the number of measurements to the minimum necessary to reliably perform all the characterization measurements and fully automatized the process to take 15 minutes/chip. We are currently testing and characterizing 250 additional L0 ASICs to be part of the LST prototype that will be installed in La Palma, Spain in 2016.

3.4 Concluding Remarks

Using simulations, we found that for the LSTs, which are built to collect more light and have a lower energy threshold, the performance of the sum trigger is better than that of the majority trigger at energies below 100 GeV. Among the sum trigger options under consideration, the best compromise between the cut given by the clipping and the suppression of the after pulses is given by a clipping level = 8 phe, although it is worth pointing out that there was no real optimization of the clipping value. We simply selected a few clipping values (6 phe, 8 phe) and the performance was checked among

them. Moreover these clipping values were obtained before the change in geometry of the telescopes and QE of the PMTs. For the new configuration larger clipping values may even improve the performance. The MSTs are not designed to have good sensitivity at low energies (<100 GeV). Hence, the performance of majority and sum triggers have large uncertainties in this energy region because of the low number of triggers. The results for both triggers at higher energies are compatible within the errors. A comparison between the aggressive and safe scenarios shows an improvement of the collection area for the aggressive scenario at the lowest energies, although within the errors. The energy threshold is also slightly improved by the use of the aggressive option. We also found that for both trigger options, a cut in the minimum number of phe of 25 phe in the events recorded does not affect the results obtained. It is therefore safe for further simulations to apply this cut and eliminate events with less than 25 phe without changing the results.

Nevertheless, as we are only considering galactic NSB, the DTs used to reproduce the safe and aggressive trigger scenarios considered are high, the collection area at low energies decreases and the energy threshold stays at a level >20 GeV in every case. If we considered lower extragalactic NSB, those DTs would be reduced, and therefore the energy threshold of the telescope would be lower as well.

Regarding CTA requirements and LST goals, the gain in energy threshold is small when moving from the 7.5 kHz requirement to the 15 kHz goal. The gain of moving from single-telescope to stereo observations is ~30 % in energy threshold. We also evaluated the impact of having PMTs with pulse widths wider than the goal of 2.6 ns. In general, we find that the worsening of the collection area is between 5–8 % every 0.2 ns with respect to that achieved with a pulse width of 2.6 ns. To be on the safe side and keep the worsening of the performance at a level $\lesssim$20 %, the pulse width of the PMTs should be smaller than 3.0 ns.

All these results should be confirmed and optimized when the telescope parameters are fixed and the final site for the telescopes decided. This will be done in the *Production-III* MC run, focused on the selection of the final telescope layout and the optimization of the system.

On the hardware side, we studied the response of L0 boards containing discrete components and an ASIC to produce the L0 trigger of the system. We found that, although the discrete component trigger meets the requirements of the L0 trigger, the response obtained with the ASIC trigger is much more satisfactory in terms of linearity of the attenuator, clipping and DT. Besides that, the ASIC trigger provides lower weight, consumption and cost. This is the option that is currently being fully characterized to be installed in the first LST prototype.

References

Barcelo M et al (2013) arXiv:1307.3169
Barrio JA et al (2014a) In TWEPP 2014 workshop
Barrio, JA et al (2014b) arXiv:1410.8526

Bernlöhr K (2008) Astropart Phys 30:149
Bernlöhr K (2013) CTA Trigger telecon slides
Hinton JA (2012) CTA Trigger telecon slides
Kubo H et al (2011) Proceedings of the international cosmic ray conference, vol 9, p 178
Sanuy A et al (2013) Analog trigger L0 ASIC Package and Pin out
Tejedor L et al (2013) IEEE Trans Nucl Sci 60:2367
Vorobiov S et al (2011) Nucl Instrum Methods Phys Res A 639:62
Wischnewski R (2011) Proceedings of the international cosmic ray conference, vol 9, p 63

Chapter 4
The Topo-Trigger: A New Stereo Trigger for Lowering the Energy Threshold of IACTs

The purpose of the hardware presented in this chapter is to decrease the energy threshold of the MAGIC telescopes without significantly increasing the data acquisition rate. To achieve this purpose, we developed an additional level of trigger that relies on the location in both MAGIC cameras where the trigger is issued to rule out accidental events. This allows to decrease the DT, which results in a reduction of the energy threshold of the instrument. We simulated the Topo-trigger concept using the standard MAGIC MC and tested it with real telescope data. In this chapter we show the concept and results of these tests.

4.1 Limitations of the Trigger System in the MAGIC Telescope

The trigger system in the MAGIC telescope is hardware limited at several stages. Every time an L1 trigger is issued, the L1 trigger system is busy for 100 ns, not accepting any other trigger in this time. This L1 trigger dead time is given by:

$$\text{Dead time} = \text{L1 rate} \times 100 \, \text{ns}$$

In order not to lose >2% of the cosmic ray events, we cannot accept L1 trigger rates larger than 200 kHz.

The rate of stereo accidental triggers is given by:

$$\text{Stereo accidental trigger rate} = \text{L1 rate [M1]} \times \text{L1 rate [M2]} \times \text{L3 Coincidence window}$$
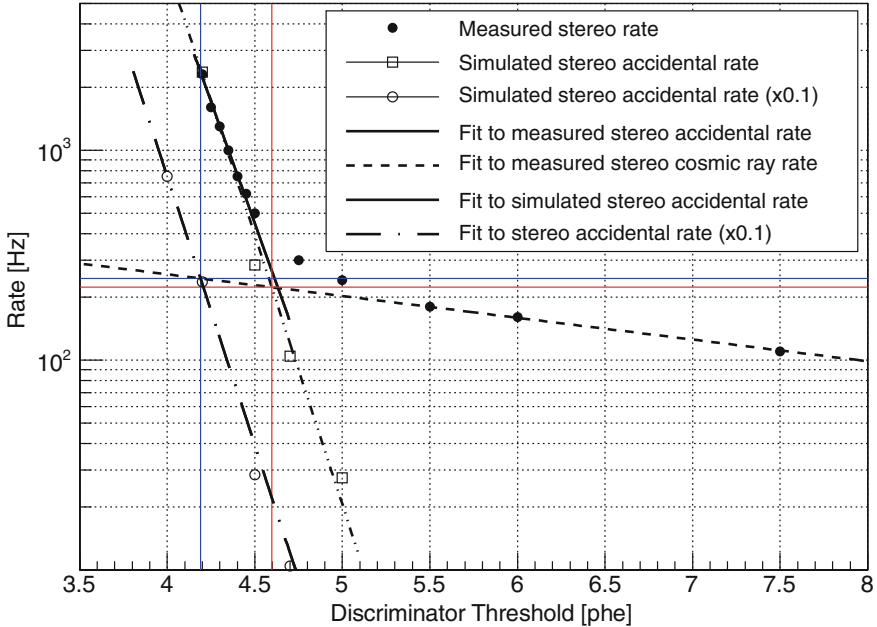
Fig. 4.1 Measured and simulated stereo trigger rate for the MAGIC telescopes. The crossing point of the *red lines* determines the current operation point in the MAGIC telescope. The crossing point of the *blue lines* marks the operation point where we would go by decreasing the accidental rate to 10 % of its value and maintaining the same rate recorded (color figure online)

where L3 Coincidence window = 180 ns. The maximum stereo rate the current DAQ can record is ∼3 kHz (Tescaro et al. 2013). The simulated stereo accidental trigger rate (open squares) and measured stereo accidental trigger rate (filled circles) of MAGIC are shown in Fig. 4.1. We are currently working at the crossing point between the extrapolation of the stereo cosmic ray trigger rate and the stereo accidental trigger rate (shown as the crossing point between the two red lines). What we aim to do with the algorithm we are presenting in this work is to reduce the accidental stereo trigger rate to 10 % of its value (open circles). We would then move to operate to the crossing point between the extrapolation of the stereo cosmic ray rate and the 10 % of the accidental stereo trigger rate (the crossing point between the two blue lines).

4.2   The Topo-Trigger

The trigger logic implemented at this moment in the MAGIC telescope discriminate between showers and NSB using the spatial and time information of the pixels' signals for the single-telescope trigger level and the time information at the stereo level (for more information about MAGIC trigger, see Sect. 2.2.1.6). To get rid of additional accidental triggers, we could also use the spatial information at the stereo level.

4.2.1 Setup of MC Simulations

For the simulation of gamma rays we used CORSIKA (Heck et al. 1998) software. The particles simulated are γ-ray photons with energies ranging between 10 GeV and 30 TeV, simulated with a power-law function with $\Gamma = 1.6$ photon spectral index. For all the calculations, the spectrum was re-weighted to a Crab-like spectrum with photon spectral index $\Gamma = 2.6$, as it is explained in the Appendix A.1. The events are simulated at a $0.4\,^\circ$ distance from the center of the camera, as it is the standard in MAGIC observations. We also simulated a sample of events at a distance ranging from $0.6\,^\circ$ to $1.4\,^\circ$ from the center of the camera to study the performance for off-axis events. The Zd ranges from 5 to $35\,^\circ$, the Az angle ranges from 0 to $360\,^\circ$ and the maximum impact parameter simulated is 350 m. We used 3×10^6 showers. The simulation performed is similar to that described in Sect. 2.2.3.1.

The current DT applied in the L0 individual pixel trigger currently used for the MAGIC simulations (*Nominal* DT) is 4.5 phe for MAGIC I (M I) and 4.7 phe for MAGIC II (M II). The different DTs used for the two telescopes are due to the differences in reflectivity of the mirrors and QE of the PMTs. The L1 trigger logic is 3NN and the L3 gate used is 180 ns. The DTs used to test the Topo-trigger are chosen such that if we manage to reduce the stereo trigger rate due to accidentals one order of magnitude, the stereo trigger rate is the same as for the Nominal DT. We reduced the DT to 4.2 phe in M I and 4.3 phe in M II (*Reduced* DT). The results for the stereo accidental trigger rates for *Reduced* and *Nominal* DTs can be found on Table 4.1. The differences between the accidental rates of M I and M II lies on the better reflectivity of M II mirrors and is also reproduced in the data. To partially compensate this difference, M II DTs are ∼5 % higher than M I ones.

4.2.2 Spatial Information Available at Trigger Level

The basic idea is to implement online cuts on the spatial information available at the trigger level. In particular, we can use the 19 L1 trigger macrocell bits from the two telescopes to obtain information about the location of the image in the camera.

Table 4.1 L1 trigger rates for different NSB, DTs and for the two MAGIC telescopes. The Nominal DT corresponds to 4.5 phe for M I and 4.7 phe for M II, while the Reduced one corresponds to 4.2 phe for M I and 4.3 phe for M II. Credit: López-Coto et al. (2016), ⓒ SISSA Medialab Srl. Reproduced by permission of IOP Publishing. All rights reserved

	Accidental trigger rate [kHz]		
DT	M I	M II	Stereo
Nominal	25 ± 4	39 ± 5	0.18 ± 0.04
Reduced	78 ± 7	125 ± 9	1.8 ± 0.2
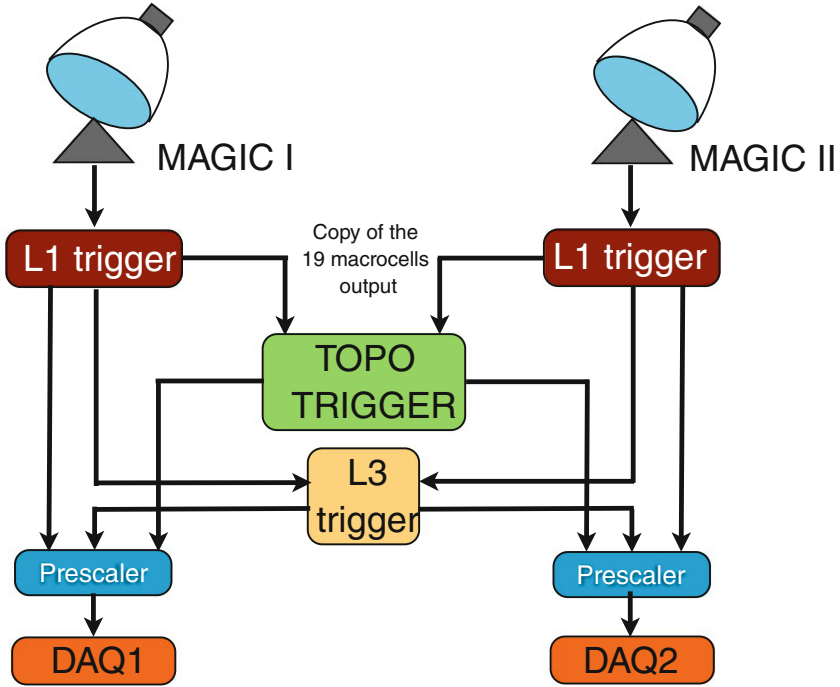
Fig. 4.2 Scheme of the MAGIC trigger system including the implementation of the Topo-trigger.
Credit: López-Coto et al. (2016), © SISSA Medialab Srl. Reproduced by permission of IOP Publishing. All rights reserved

A scheme of the MAGIC trigger system including the future Topo-trigger is shown in
Fig. 4.2. When a L1 trigger is issued in each telescope, a copy of the signal goes to the
prescaler and another one to the L3 trigger. We intend to deliver another copy to the
Topo-trigger. The Topo-trigger compares the macrocells triggered in each telescope
every time a L1 trigger is issued and sends a veto signal to the prescaler when the
combination of macrocells does not correspond to that triggered by a gamma ray.

4.2.3   Macrocell Selection

Let us discuss the separation angle under which the shower is seen from the two
MAGIC telescopes. We denote this angle alpha as is shown in Fig. 4.3. The angle is
maximum when the shower develops in between the two telescopes. The distance
between M I and M II is 85 m and the assumed distance at which the shower is produced is 10 km a.s.l. ($\sim$7.8 km above the telescopes). The maximum angle separation
between a point-like shower between the two telescopes is $\alpha \simeq 0.6°$. Taking into
account the macrocell distribution shown in Fig. 2.16 and that every pixel covers 0.1°,
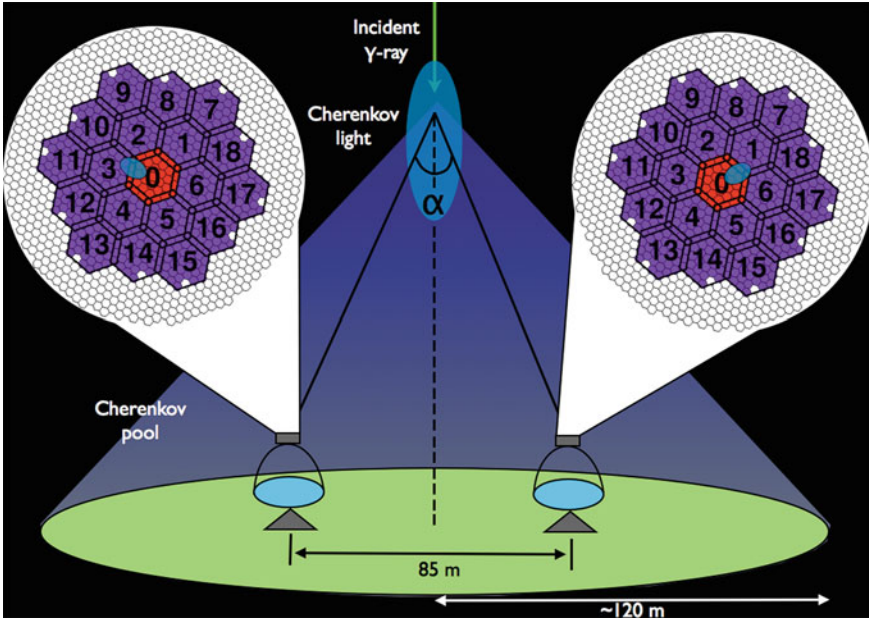
Fig. 4.3 Scheme of the detection of Cherenkov light produced by a low energy γ-ray shower by the MAGIC telescopes. The angle α between the light arriving to both telescopes is smaller than $0.6\,^{\circ}$ for all the showers produced at a height of $\sim 10\,$km. Credit: López-Coto et al. (2016), © SISSA Medialab Srl. Reproduced by permission of IOP Publishing. All rights reserved

we conclude that the maximum separation of the showers seen in the two MAGIC cameras is 1 macrocell. We have to point out that the angle α calculated depends on the height at which the shower interacts with the atmosphere (high energy showers go deeper into the atmosphere, therefore produce larger α angles). This means that most of the showers trigger the same macrocell at both telescopes or neighboring macrocells. This is the essence of our new trigger level.

In the simulations, we record the macrocell digital output for 10 ns after the L1 trigger is issued. This digital output of each macrocell is 0 if the macrocell was not triggered during those 10 ns and 1 if it was triggered. As the events triggered by NSB are accidentals, we expect them to trigger only one macrocell. Using MC simulations, we calculated that the probability that an accidental event is triggered by more than one macrocell is $P_{2M} = 0.4\,\% \cdot P_{1M}$, where P_{2M} is the probability of triggering 2 macrocells due to an accidental and P_{1M} the probability of triggering 1. As the fraction of events triggering more than one macrocell is much smaller than the one triggering only one, we selected the events that triggered only one macrocell in each telescope and studied them. In order to illustrate possible macrocell 1–1 combinations for gamma rays, we select showers that gave triggers in a given macrocell in M I and look at the macrocell distribution for these showers in M II. In Fig. 4.4 we have two examples: in the top panel we have selected events for which only macrocell 0 (the
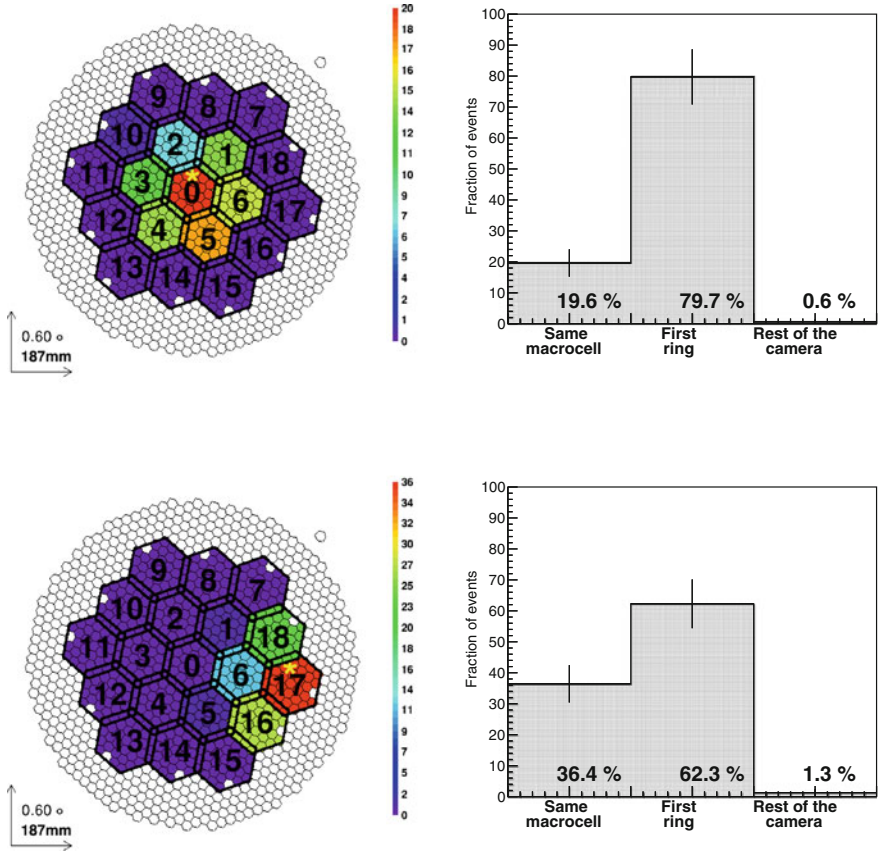
Fig. 4.4 Macrocells triggered in M II when selecting one macrocell in M I for events triggering only one macrocell in each telescope for simulated gamma rays after analysis cuts (*left panels*) and the histograms of the distributions (*right panels*) (color figure online)

central one, marked with an asterisk) is triggered in M I. On the bottom panel, we have selected events for which only macrocell 17 (one of the border ones) is triggered. The color of the left panel plots represents the fraction of events that triggered a given macrocell in M II. In the right panel plots we show how the events distribute in M II. Events in the first bin triggered the same macrocell in M I and M II (macrocell 0 (17) in the upper (lower) plot). Events in the second bin triggered in M II one of the macrocells of the first ring surrounding macrocell 0 (17), in this case, macrocells 1, 2, 3, 4, 5 and 6 (6, 16 and 18). The third bin corresponds to the rest of the macrocells.

From the events triggering only one macrocell in each telescope, we will accept only events triggering the same macrocell in both telescopes or the neighboring ones. We will keep most of the events triggered by gamma rays, while getting rid of a large fraction of the accidental stereo triggers. Each telescope has $N = 19$ macrocells, so there are $N^2 = 361$ possible different combinations of one-to-one macrocell.

The Topo-trigger, in first approximation, accepts 103 of them. Showers are mainly distributed according to the distribution we have obtained with the simulations, but the triggers due to accidentals will be randomly distributed in the whole camera, and most of them will be triggering only one macrocell each time. It becomes clear that if we reject the triggers produced in the macrocell combinations that are not fulfilling the condition of being the same macrocell or the surrounding ones in both telescopes, we would reject:

$$\begin{array}{c} \% \text{ Fraction of} \\ \text{rejected accidentals} \end{array} = \frac{361 - 103}{361} \times 100 = 72\,\%$$

We will apply further cuts based on the position of the macrocells respect to the source. Following the geometry shown in Fig. 4.3, if the source is at a certain direction in the sky, we do not only know that the shower should fall in the same macrocell or the surrounding ones, but also which of the surrounding macrocells will be hit in the other telescope. If we divide the data in bins of Az, we can further select the macrocells that are accepted and increase our rejection power. We could make Az bins as fine as desired, but at some point there is no improvement. As the finer possible binning would be given by the size of the macrocells, since we have 12 outer macrocells we cannot improve further than establishing 12 bins in Az.

The tables with the macrocells selected in one telescope depending on the one triggering the other and the Az angle at which the telescopes are pointing can be found in Appendix B.3. By applying the macrocell selection to each Az bin, we obtain:

$$\begin{array}{c} \% \text{ Fraction of} \\ \text{rejected accidentals} \end{array} = \frac{361 - 53}{361} \times 100 = 85\,\%$$

Let us now evaluate the impact of the cuts on the γ-ray events. We have applied the Topo-trigger macrocell selection to MC γ-ray events triggering with the Reduced DT configuration. The fraction of simulated gamma rays rejected by the algorithm is $\sim$2.4%. As we will show in Sect. 4.2.4, the fraction of events rejected at the analysis level is significantly lower than this. In summary, according to MC, by applying the Topo-trigger macrocell selection cuts, we reject 85% of the accidental events but only 2.4% of the γ-ray events at the trigger level.

Off-Axis Simulations

In the previous sections we have verified that the selection algorithm works applying it to the standard MC simulations with the source located at a $0.4°$ distance from the center of the camera. Now we want to check that the algorithm does not depend on the source position of the camera, but on the relative position of the telescopes with respect to each other. We simulated γ-ray events at distances from the center of the camera ranging from $0.6°$ to $1.4°$. We did not include NSB in our simulations to study the effect in events triggered by a γ-ray shower. We examined the triggered macrocell distribution and applied the Topo-trigger macrocell selection mentioned

in Sect. 4.2.3. The distribution of triggered macrocells is similar to the one obtained using the standard MC with the source at $0.4°$ from the camera center.

4.2.4 Expected Performance

We will now calculate the collection area and energy threshold of the instrument after applying the Topo-trigger selection. We will proceed as it was explained in Sects. 2.2.3.9 and 2.2.3.6. For the analysis of the MC gamma rays, we calibrate the data, clean the images applying the image cleaning method and apply a gamma/hadron separation with the so-called random forest algorithm as in the standard MAGIC analysis Zanin et al. (2013). We ran MC simulations for 2 cases, and for the second case we apply two different image cleanings:

(a) Nominal DT with standard image cleaning.

    (b.1) Reduced DT with the standard image cleaning (6 phe for core pixels and 3.5 phe for the neighbour ones).

    (b.2) Reduced DT with an image cleaning with charge parameters reduced by 7 % (which is the mean DT reduction applied from Nominal to Reduced DT).

Figure 4.5 shows the true energy distribution of MC γ-ray events for the different trigger configurations. The black histogram represents the rate for the current trigger configuration of MAGIC (Nominal DT). The green histogram represents the rate for the Reduced DT configuration with DT = 4.2 phe for M I and DT = 4.3 phe for M II applying Topo-trigger macrocell selection with the standard image cleaning. The blue line represents the rate for the Reduced DT configuration with a 7 % reduced image cleaning. We can see that the energy threshold goes down by up to 8 % at the analysis level.

The collection area in each energy bin is calculated as explained in Sect. 2.2.3.9. The collection area for both the Nominal DT and the Reduced one is shown in the top panel of Fig. 4.6, and the ratio between the collection area obtained using the current MAGIC trigger configuration and the collection area obtained with the Reduced DT applying the Topo-trigger macrocell selection in the bottom panel of the same figure. The black points correspond to the collection area obtained with the current trigger configuration of MAGIC. The green points correspond to the collection area obtained reducing the DT to 4.2 phe in M I and 4.3 phe in M II and applying the Topo-trigger macrocell selection. The blue points represent the rate for the Reduced DT configuration with a 7 % reduced image cleaning. The red line in the bottom panel delimits the region where the Reduced DT option performs better than the Nominal DT (ratio > 1). We can see that the improvement in collection area using the Topo-trigger at the lowest energies is ∼60 %, although the errors are very large due to the low statistics at those energies. At the energy threshold, where we have a peak in the number of events triggered, the improvement using the Topo-trigger is
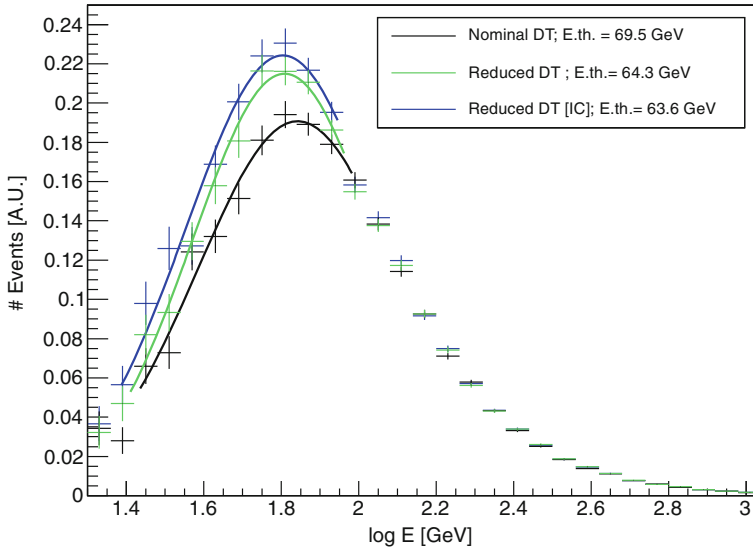
Fig. 4.5 True energy distribution of MC gamma rays (in arbitrary units) for a source with a 2.6 spectral index for different trigger configurations (color figure online)

between 10–20 % with respect to the current MAGIC configuration. Moreover, this gain in events is still ∼5 % for showers with energies between 70 GeV to 100 GeV. As expected, there is no effect for higher energies. At the highest energies (the last point in energy of Fig. 4.6), there are only a few events that give trigger, therefore the fluctuations are large. We would like to stress that all these improvements are at the analysis level, i.e. for the events that are used to derive spectra, light curves and skymaps.

After applying the Topo-trigger cuts at the analysis level, we keep 98.8 % of the total events that survived the analysis cuts. At the trigger level we were keeping only 97.6 % of those events, meaning that most of the events that were rejected when applying the macrocell algorithm, are not used for analysis either.

4.3 Piggy-Back Measurements

We installed a system to record the macrocell pattern for every event at the trigger system in La Palma. As the trigger DT was not lowered, we do not expect any improvement by applying the algorithm to the data. We only intend to verify that no gamma rays are lost at the analysis level due to the Topo-trigger macrocell selection applied in the software and hardware.
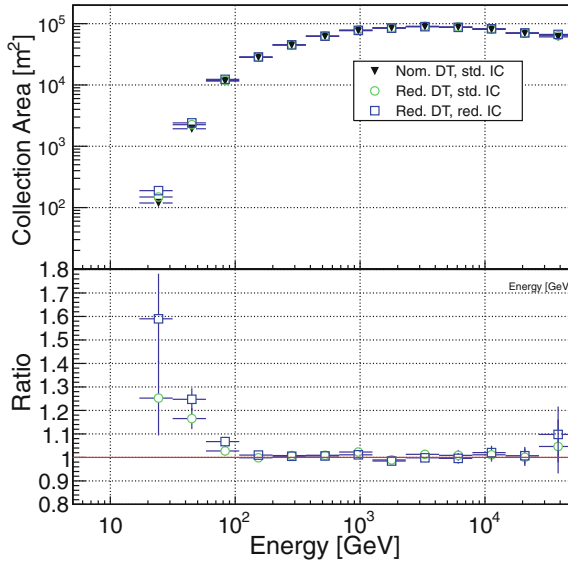
Fig. 4.6 Collection area using the Nominal DT and the Reduced one applying cuts (*top*) and the ratio between the Reduced DT configurations and the Nominal DT one (*bottom*)

4.3.1   Description of the Setup

We prepared a setup that records the digital output of the macrocells for every event recorded by the DAQ system Tescaro et al. (2013). A scheme of the setup used for recording the macrocell information is shown in Fig. 4.7.

The signals of the camera go to the receiver boards where the first stage of the discriminator process (L0) is done. Once they have passed through the receivers, the NN logic is applied in each macrocell, as explained in Sect. 2.2.1.6. The output of each of the 19 L1 trigger macrocells goes to the TPU. It sends a square signal every time the L1 trigger condition is fulfilled in any of the 19 macrocells. The TPU has 5 outputs: one that goes to the L3 trigger with no delay, the second one to monitor L1 rate, the third is a sync signal that goes to the prescaler and is used to synchronize L3 output, the fourth is a delayed signal for the L1 and the fifth one, that is usually unused, latch the macrocell information. We send the output of the TPU to a patch board + Test Experimental Device (TED), which handles the digital signal coming from the 19 macrocells, stretches it and sends it to a pulsar board. The pulsar board stops and writes the information of the macrocells when it receives a trigger from the prescaler issued by the L3 trigger: we record the macrocell information of the events that triggered the stereo system.
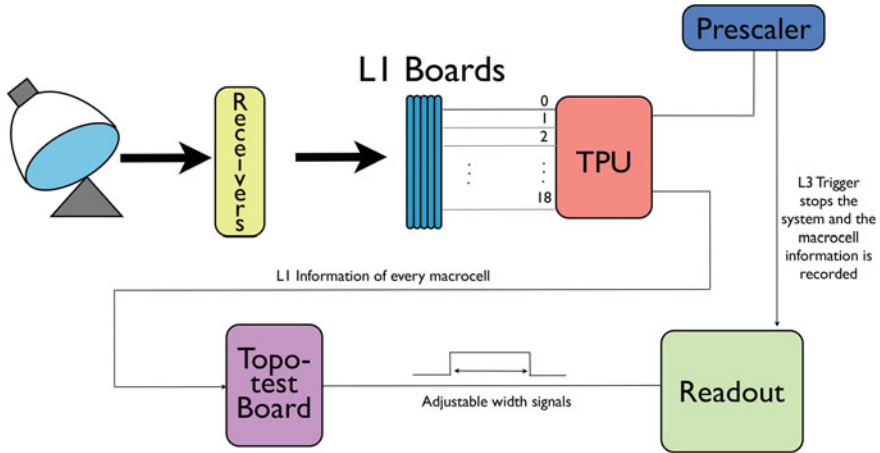
Fig. 4.7 Scheme of the recording system installed at the MAGIC telescopes for the Topo-trigger piggy-back measurements. Credit: López-Coto et al. (2016), © SISSA Medialab Srl. Reproduced by permission of IOP Publishing. All rights reserved

4.3.2 Sensitivity and γ-ray Rate Comparison

We took Crab Nebula data at Az angles ranging from $100°$ to $175°$ and Zd between $6°$ and $22°$. We analyzed these data using the standard analysis in MAGIC and applied the standard hadron/gamma separation and event reconstruction cuts for two energy ranges: medium-to-high energies and low energies.

Medium-to-high energies We applied the standard γ/hadron separation, reconstructed energy and θ^2 cuts used for medium energies (described in Sect. 2.2.3.7), leading to an energy threshold of ~250 GeV. We calculated the sensitivity of the telescope and the γ-ray rate for the sample without applying any cut in macrocells and applying the Topo-trigger macrocell cuts. The result was that we have exactly the same number of background and gamma events after applying the Topo-trigger macrocell selection cuts, so the sensitivity and γ-ray rate are kept constant.

Low energies We also made an analysis applying the standard cuts for low energies. We computed the ratio between the sensitivity with and without macrocell cuts:

$$\frac{\text{Sensitivity}}{\text{ratio}} = \frac{\text{Sensitivity[macrocell cuts]}}{\text{Sensitivity[no cuts]}} = 1.005 \pm 0.007$$

And the ratio of γ-ray rate with and without macrocell cuts:

$$\frac{\gamma\text{-ray rate}}{\text{ratio}} = \frac{\gamma\text{-ray rate[macrocell cuts]}}{\gamma\text{-ray rate[no cuts]}} = 0.997 \pm 0.001$$
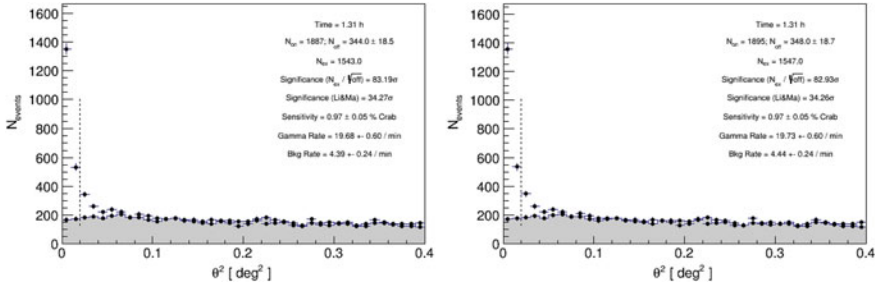
Fig. 4.8 θ^2 plots applying (*left panel*) and without applying (*right panel*) the macrocell selection cuts to a Crab Nebula dataset

Table 4.2 Summary of the results for the sensitivity ratio and γ-ray rate ratio between the analysis applying the Topo-trigger macrocell cuts and without applying them for medium and low energies. Credit: López-Coto et al. (2016), © SISSA Medialab Srl. Reproduced by permission of IOP Publishing. All rights reserved

	Sensitivity ratio	γ-ray rate ratio
Medium E	1	1
Low E	1.005 ± 0.007	0.997 ± 0.001

As we can see, there is a small loss in γ-ray rate (0.3 %). The sensitivity does not change within the errors. The loss in γ-ray rate is compatible with the expectations from the simulations shown in Sect. 4.2.4 (Fig. 4.8).

The results for the sensitivity and γ-ray rate ratio between the data to which we applied the macrocell selection and the data without applying any macrocell selection are summarized in Table 4.2. These results confirm what we expected from the simulations: if we apply the macrocell selection to the events used for analysis, we keep basically the same detection efficiency.

4.4   Discussion and Conclusions

We developed a novel stereo trigger system for IACTs which make use of the topological information of the showers in the camera. Combining the information of the Az angle at which the telescope is pointing and the L1 trigger macrocell hit in each telescope we can reject 85 % of the accidental stereo trigger rate, which is the dominant at the lowest energies, without losing gamma rays. By studying the effect of applying the selection algorithm to off-axis data, we find that the discrimination power of the algorithm does not depend on the source position in the camera. We run simulations reducing the DT used for triggering the telescopes and applying this algorithm and we found that implementing this trigger translates into a decrease of up to 8 % in the energy threshold and an increment of ~60 % in the collection area

at the lowest energies and from 10–20 % at the energy threshold, where most of the events are triggered. The algorithm developed allows to lower DT without increasing the accidental rate. We installed a device to record the triggered macrocells of the events recorded by the MAGIC telescope. Without reducing the DT applied at the L0 trigger, we verified that the Topo-trigger macrocell selection tested in the MC does not lead to any loss in the sensitivity or in the γ-ray rate. The potential of this easy to implement algorithm is that it could also be used for any other system with a similar trigger based on macrocell or clusters that give you the information of the topological distribution of a trigger in the camera.

The board that will be used to veto signals from the L3 trigger is already installed in the MAGIC telescope and is currently under commissioning.

References

Heck D et al (1998) CORSIKA: a Monte Carlo code to simulate extensive air showers. Forschungszentrum Karlsruhe GmbH)
López-Coto R et al (2016) J Instrum 11:P04005
Tescaro D et al (2013), arXiv:1310.1565
Zanin R et al (2013) Proceedings of the ICRC 2013, id 773

Part III
Pulsar Wind Nebulae
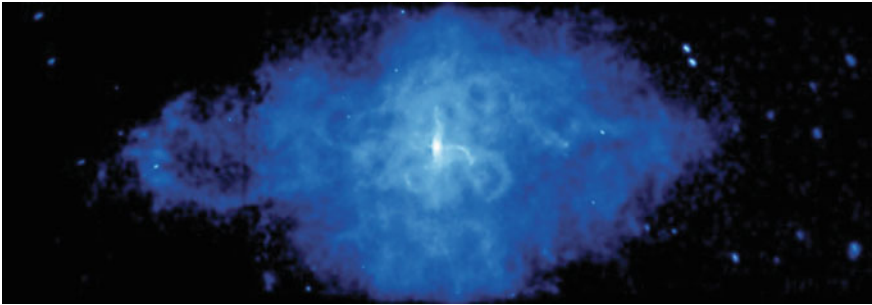
Fig. 1 Chandra image of 3C 58. Credit: NASA/CXC/SAO/P.Slane et al.

Chapter 5
Introduction to Pulsar Wind Nebulae

5.1 Star Fate

Main sequence stars are self-luminous celestial objects held together by their own gravity. They are constantly producing energy by nuclear fusion. The fate they suffer at the end of their lives depends on the mass of their helium cores and hydrogen envelopes at death (Heger et al. 2003). For a complete description of the final state of a star as a function of the initial mass and metallicity, see Fig. 5.1. In the following, we present a breakdown of the objects that are formed at the end of the lives of stars, depending on their mass M.

- $M < 9$–$10\ M_\odot$: After the fusion of Hydrogen (H) and Helium (He), if the core of the star does not reach the temperature required to fuse Carbon (C) or Neon (Ne), the fusion reactions stop and the star can no longer be supported by fusion reactions against the gravitational collapse, then the star starts to contract. According to the Pauli exclusion principle, two electrons cannot occupy the same state, so the star stops collapsing when it reaches a degeneracy state and is sustained by electron degeneracy. This is possible if the mass of the star is smaller than the Chandrasekhar limit of $1.4\ M_\odot$ (Chandrasekhar 1931), beyond which the gravitational force cannot be supported by the electron degeneracy. This remnant is known as White Dwarf (WD).
- 9–$10\ M_\odot < M < 40\ M_\odot$: After the fusion of all the heavy elements (C, Ne, Oxygen (O), Silicon (Si), Iron (Fe)), if the mass of the stellar remnant is larger than the Chandrasekhar limit, the electron degeneracy pressure cannot hold the core against the gravitational force. The star undergoes a collapse and releases some of its gravitational energy in a SN explosion (see Sect. 5.1.1). Depending on the initial mass of the object, it becomes a NS or a BH.
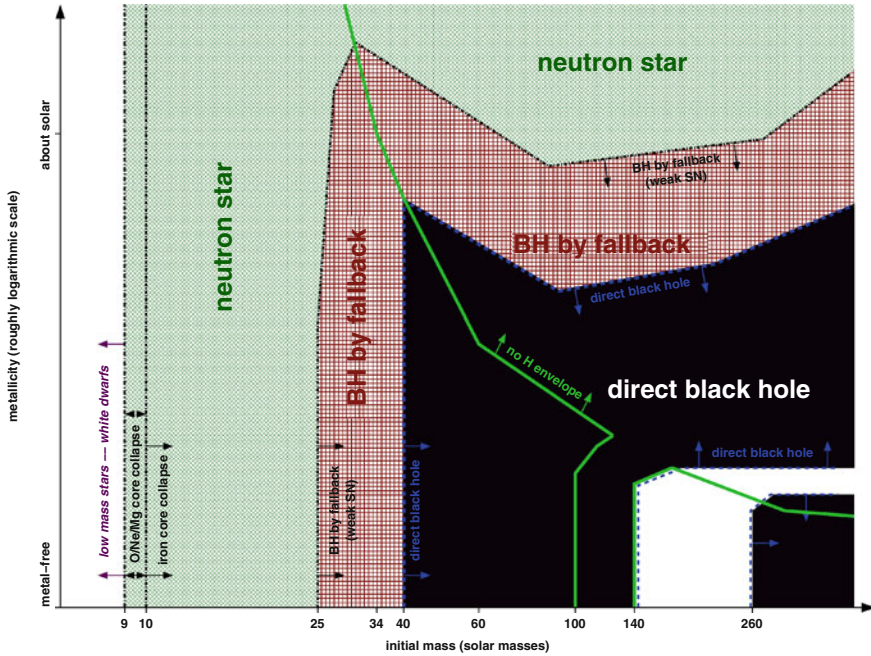
Fig. 5.1 Diagram showing the fate of the stars depending on their initial mass and their metallicity. Plot from Heger et al. (2003)

(a) $9\text{--}10\,M_{\odot} < M < 25\,M_{\odot}$: Once the electron degeneracy is overcome and the core collapses, the temperature increases and free electrons and protons combine to form neutrons and neutrinos $p^{+} + e^{-} \rightarrow n + \nu$. The object formed is called NS because it is mainly formed by neutrons (Grupen 2005). We will extend their description in Sect. 5.2.

(b) $25\,M_{\odot} < M < 40\,M_{\odot}$: If the mass of the remnant of the stellar object is sufficiently high to overcome the neutron degeneracy pressure by its gravitational force, a BH is generated after the SN explosion.

- $40\,M_{\odot} < M < 140\,M_{\odot}$ or $M > 260\,M_{\odot}$: If the star was initially much more massive, there is no visible SN explosion and a BH is directly formed.
- $140\,M_{\odot} < M < 260\,M_{\odot}$: Nuclear reactions inside the star generate gamma rays which in turn produce $e^{\pm}$ pairs. This pair creation produces a thermal pressure drop that leads to a partial collapse. For massive stars with a mass in this range, the partial collapse is followed by a thermonuclear explosion that rips the star apart and leaves no remnant.

If the star's metallicity is larger than $M_{\odot}$, they typically end their lives as a NS, independent of their mass.

5.1.1 Supernovae

From the observational point of view, SNe are divided into two types, including several subclasses into each of them (Reynolds 2008).

- **Type I**: They do not present H lines

  - *Type Ia*: They show a strong ionized Si II (6150 Å) absorption line.
  - *Type Ib*: They lack a spectral feature of Si II (6150 Å).
  - *Type Ic*: Apart from H, they also lack He.

- **Type II**: They present H lines

  - *Type IIP*: They show a plateau in the light curve after reaching the maximum.
  - *Type IIL*: They show a linear decline in the light curve after reaching the maximum.
  - *Type IIn*: They show a spectrum with narrow emission lines.

All the SNe, except Type Ia, are produced by a explosion of the star driven by gravitational core-collapse. Type Ia has a thermonuclear origin and is thought to be generated by the nuclear burning of a carbon-oxygen WD. We will center the discussion of this part of the thesis in the study of the evolution of SNe that left after their explosion NSs that rotate very rapidly, also known as pulsars.

5.1.2 Supernova Remnants

Apart from the stellar remnants mentioned in Sect. 5.1, the material ejected by the SN explosion interacts with the ISM forming a SNR. There are three types of SNRs: if they have shell-like structure, then they are *shell-like SNRs*; if they are filled at the center at all wavelength and have a central object that constantly injects particles and energy to the remnant, they are known as *plerions* or *PWNe*; and if the PWN is surrounded by a shell-like SNR, the system is called *composite*. We will describe in Sect. 5.4 in more detail the SNR type where this part of the thesis focuses: the PWN. For a general review of SNRs at high energies, we refer the reader to (Reynolds 2008). Figure 5.2 is an image of the youngest SNR known in the galaxy, Cassiopeia A (Cas A).

5.2 Neutron Stars

As it was briefly described in Sect. 5.1, NSs are formed in the gravitational collapse of a massive star. When the core of the star reaches a density of the order of the nuclear density, the collapse stops leaving as a remnant the most dense stellar object known so far, a sphere of radius ~ 10 km, density $\rho \sim 10^{17}$ kg m^{-3} and mass between
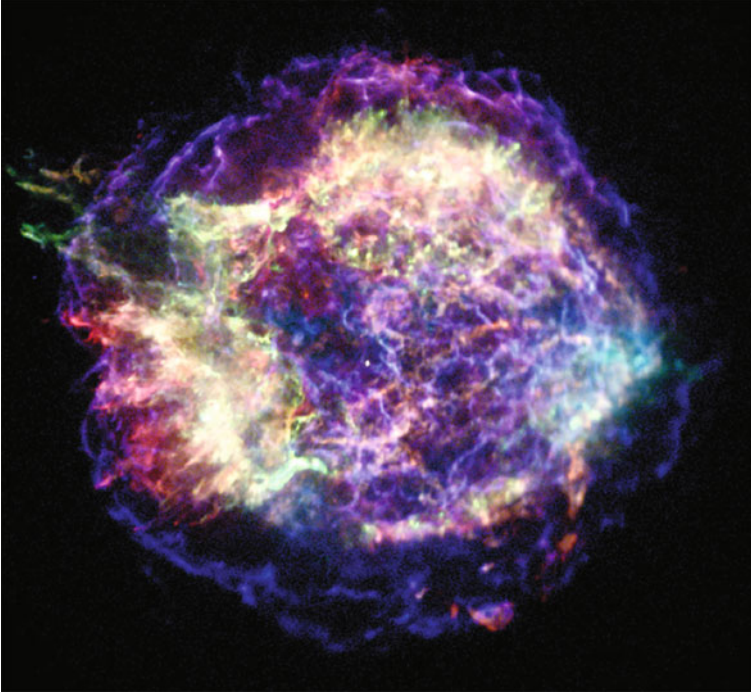
Fig. 5.2 X-ray image of the SNR Cas A taken with *Chandra*. The color code is: *red*: 0.5–1.5 keV, *green*: 1.5–2.5 keV and *blue* 4.0–6.0 keV). The central white point corresponds to the central compact object. Credit: NASA/CXC/MIT/UMass Amherst/M.D.Stage et al. (color figure online)

1.4 and 3 $M_\odot$. During the collapse, the star dramatically reduces its size, but as the angular momentum and magnetic flux are conserved, a high-magnetic field rapidly-spinning (with a period varying from 1 ms to 10 s) NS is created. They were first postulated by Baade and Zwicky (1934) (Fig. 5.3).

5.2.1 Inner Structure of an NS

A sketch of the inner structure of a NS can be seen in Fig. 5.4. A very thin atmosphere is believed to surround an extremely hard crust made of ions and electrons. Under this outer crust there is an inner one made of nuclei mixed with electrons and neutrons. Around 9 Km from the center of the NS, an outer core made of superfluid neutrons with some superconducting protons lies under the inner crust. The composition of the inner core is completely unknown, but some exotic kind of matter such a quark-gluon plasma or strange matter might be present.

Fig. 5.3 Artist view of a pulsar. Credit: Christian Joore
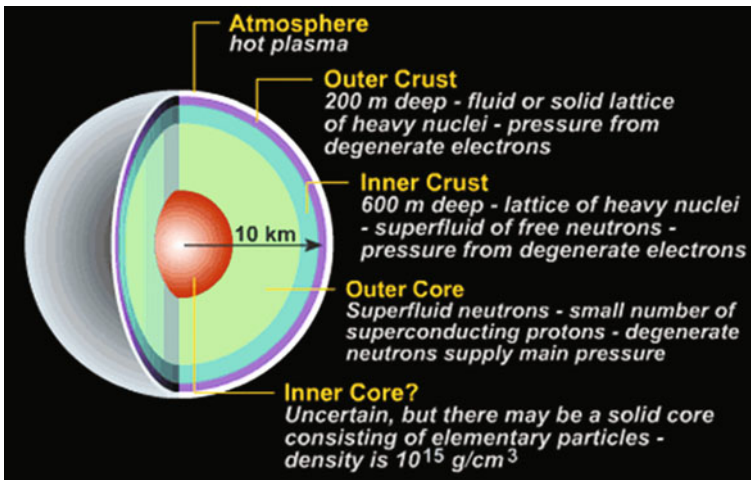
Fig. 5.4 Internal structure of an NS. Image credit: Brooks/Cole Thomson Learning

5.2.2 Classification

NSs typically have pulsations at different wavelengths, and can be classified according to the primary source of their emission and spin evolution: *Rotation-Powered Pulsars (RPPs)* derive their energy from the rotation of the pulsar, *Magnetars* from the magnetic field energy, *Isolated Neutron Stars (INSs)* from the latent heat of the NS matter, *Accretion-Powered Neutron Stars (APNSs)* from the energy released by matter accretion to the NS and finally *Compact Central Objects (CCOs)* that only manifest thermal X-ray emission (Harding 2013). A plot of the $\dot{P}$ as a function of their P for the NSs known can be seen in Fig. 5.5.

Fig. 5.5 Plot of P versus $\dot{P}$
for the currently known
rotation-powered pulsars,
INS, CCO, Rotating Radio
Transients (RRATs) and
magnetars. Lines of constant
characteristic age, $P/2\dot{P}$, and
dipole spin-down luminosity,
$\dot{E}_{sd}$, are also drawn. Plot
from (Harding 2013)
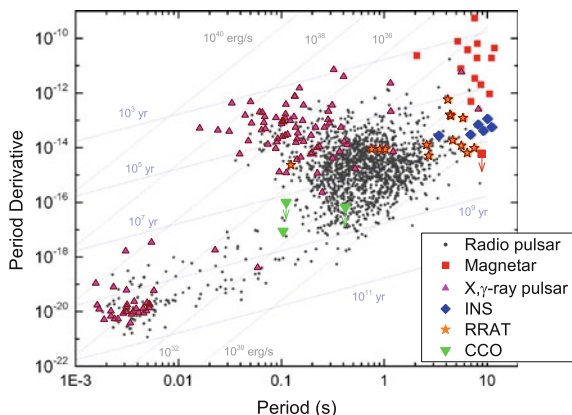
5.2.3 NS Magnetosphere

If we consider the NS as a perfect conductor, charge has to be built up in the surface
due to the law of Gauss. This surface charge induces an electric field parallel to the
magnetic field, therefore perpendicular to the NS surface. The electric field is so
strong that it tears apart some of these charged particles that initiate $e^{\pm}$ cascades and
populate with plasma the NS magnetosphere. The density of particles in the pulsar's
magnetosphere is believed to be close to the Goldreich–Julian density (Goldreich
and Julian 1969), defined as that required to screen the induced electric field (Kirk
et al. 2009):

$$\rho_{GJ} = \frac{\boldsymbol{\Omega} \cdot \boldsymbol{B}}{2\pi c} \qquad (5.1)$$

where $\boldsymbol{\Omega}$ is the angular speed, $\boldsymbol{B}$ the magnetic field and c the speed of light. A NS
can be modeled as a rotating magnetic dipole (multipole fields drop more rapidly
with the distance and become negligible at large distances). One can assume rigid
rotation of the external dipole field and the plasma until the distance R_L the rotation
velocity equals the speed of light:

$$R_L = \frac{c}{\Omega} \qquad (5.2)$$

The surface defined by the R_L is called *light cylinder*. The NS magnetosphere
is the region between the NS and the *light cylinder* and the region between the
light cylinder and the termination shock is known as the *wind zone*. Inside the light
cylinder, the magnetic field can be approximated with that of a magnetic dipole.
Inside this region magnetic field lines are closed, while magnetic field lines outside
are open. R_L separates the zones of magnetic field that are causally connected to the
rotation of the pulsar to those that are not. The particles attached to the open lines
escape the *light cylinder* region. There is a *critical open line* whose electric potential
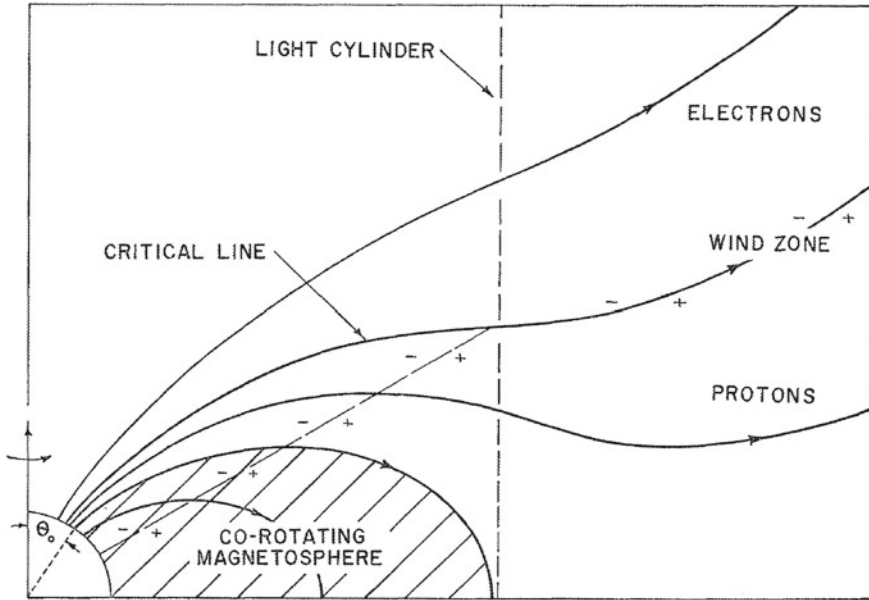
Fig. 5.6 Sketch of a pulsar, its light cylinder and wind zone. Taken from (Goldreich and Julian 1969)

is the same as in the ISM. e⁻ escape through higher-altitude lines while protons do it along lower-latitude ones (see Fig. 5.6).

5.3 Pulsars

Pulsars are rotating NSs that produce periodic radiation by spinning their powerful magnetic field through space. NSs were proposed to be the central engine powering the Crab Nebula (Pacini 1967) almost at the same time of the discovery of the first radio pulsar by Jocelyn Bell (Hewish et al. 1968). Pulsars were associated with rotating NSs (Pacini 1968) in the context of magnetic dipole moment. This association predicted a loss in the rotational energy of the pulsar and therefore a period increase that was observed by Richards and Comella (1969). An artist view of a pulsar can be seen in Fig. 5.3.

Spin-down power: Pulsars are constantly releasing their rotational energy in the form of EM emission and in the form of high-energy particles. We can compute the energy released by a pulsar as a function of P, $\dot{P}$ and I:

$$\dot{E} = -\frac{dE}{dt} = 4\pi^2 I \dot{P} P^{-3} = I \Omega \dot{\Omega} \tag{5.3}$$

where $I = 10^{38}$ kg m^2 is the moment of inertia of the pulsar and $\Omega = \frac{2\pi}{P}$ is the angular frequency of rotation of the NS. The spin-down power of all known pulsars ranges between 10^{28} and 10^{39} erg/s.

A general description of the pulsar's spin-down that takes into account energy loses is the following:

$$\dot{\Omega} = -k\Omega^n \tag{5.4}$$

where k is a constant and n the braking index that can be calculated using the second derivative of this equation:

$$n = \frac{\Omega\ddot{\Omega}}{\dot{\Omega}^2} \tag{5.5}$$

The values of n measured for the known pulsars range between 1.4 and 2.9.

Age: If we rewrite Eq. 5.4 using P and integrate it to calculate the age of the pulsar, we have (Manchester and Taylor 1977):

$$t_{age} = \int_{P_0}^{P} \frac{1}{KP'^{2-n}} dP' = \frac{P}{(n-1)\dot{P}} \left[1 - \left(\frac{P_0}{P}\right)^{n-1} \right] \tag{5.6}$$

where P_0 the initial period. If we assume $n = 3$, the one corresponding to dipole radiation and also $P_0 \ll P$, the formula can be simplified to the form:

$$\tau_c = \frac{P}{2\dot{P}} \tag{5.7}$$

that corresponds to the characteristic age of the pulsar. This value usually overestimates the real age of the pulsar, indicating that the assumptions made are not exact.

Surface magnetic field: To calculate the surface magnetic field of the NS, we assume that it is originated by a dipole. The magnetic field due to a dipole is $\sim \mu R$ (Ostriker and Gunn 1969), where μ and R are the magnetic dipole moment and the radius of the NS respectively.

$$B_s \simeq 3.2 \times 10^{19} (P\dot{P})^{1/2} \text{Gauss} \tag{5.8}$$

Temporal evolution: Assuming that the braking index n is constant, one can take Eq. 5.6 and compute the time evolution of the period P (Pacini and Salvati 1973):

$$P(t) = P_0 \left[1 - \left(\frac{n-1}{2}\right) \frac{t}{\tau_c} \right] = P_0 \left(1 + \frac{t}{\tau_0} \right)^{\frac{1}{n-1}} \tag{5.9}$$

where $\tau_0 = 2\tau_c/(n-1) - t$ represents the time-scale of the spin-down process. Similarly, one can compute the magnetic field and spin-down power evolution:

$$B(t) = B_0 \left(1 + \frac{t}{\tau_0}\right)^{\frac{n-1}{2n-2}} \tag{5.10}$$

$$\dot{E}(t) = \dot{E}_0 \left(1 + \frac{t}{\tau_0}\right)^{-\frac{n+1}{n-1}} \tag{5.11}$$

where B_0 and $\dot{E}_0$ are the initial magnetic field and the initial spin-down power respectively. The NS magnetosphere is the region between the NS and the *light cylinder*.

5.3.1 Models for the Pulsar γ-Ray Emission

Three scenarios have been proposed for the production of pulsed gamma rays, depending on the location of the emission region.

- **Polar Cap (PC)**: They predict emission near the surface of the NS, in the magnetosphere at a distance of $\sim$30 km from the pulsar (Sturrock 1971; Daugherty and Harding 1982; Arons and Scharlemann 1979). Gamma rays are emitted by curvature radiation from $e^\pm$ moving along the curved magnetic field lines above the polar cap of the pulsar. They predict a sharp super-exponential cut-off in the γ-ray spectrum.
- **Slot Gap (SG)** and **Outer Gap (OG)**: The emission region is placed farther out in the magnetosphere and extends up to the light cylinder. The SG was originally represented as an extension of the PC model. In the framework of the PC, Scharlemann et al. (1978) found that the potential gap above the pole increases when approaching to the last closed field line. Arons (1983) used this to propose that EM cascades could develop in this region, reaching higher energies due to their larger distance to the NS. Radiation from the SG produces a wider cone of emission than in the PC scenario (Harding and Muslimov 2005).

  The OG succeeds to explain most of the observational results from young, large-spin-down power pulsars. It was proposed by Cheng et al. (1986) and is based on the existence of a charge-depleted volume that can form at low latitude. This gap is contained within the last closed field line, the null surface (defined as $\mathbf{\Omega} \cdot \mathbf{B} = 0$), the light cylinder, and an open magnetic field line which is limited by pair creation. The OG model was extended to explain the VHE γ-ray emission from the Crab pulsar (Hirotani 2011, 2013). The TeV emission is explained in terms of IC scattering of secondary and tertiary $e^\pm$ pairs created in the collision of primary gamma rays emitted by curvature radiation and Ultraviolet (UV)–Infrared (IR) photons. Figure 5.7 shows a picture of a pulsar illustrating the location of the PC, SG and OG regions drawn.
- **Wind zone**: They place the emitting region of pulsed photons outside the magnetosphere, in the wind zone (Lyubarskii 1996; Kirk et al. 2002; Pétri 2011). There is
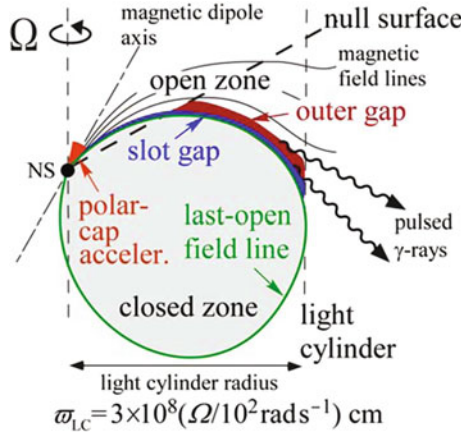
Fig. 5.7 Sketch of the pulsar magnetosphere pointing the PC, SG and OG acceleration regions. Image from Hirotani (2008)
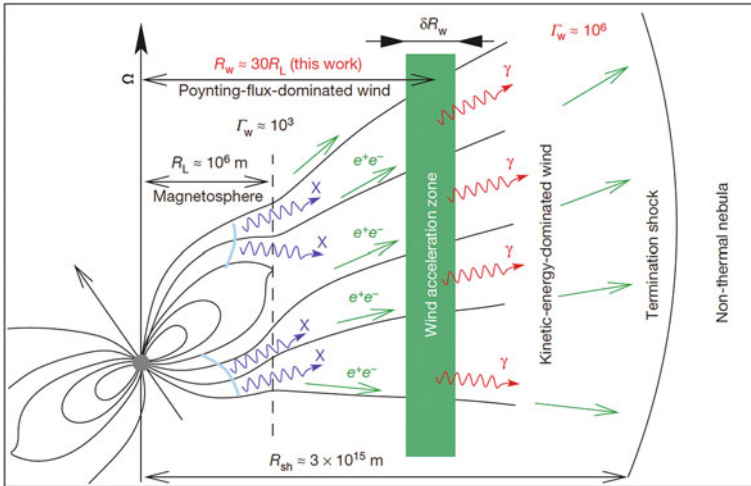
Fig. 5.8 Sketch of the wind zone model. $e^{\pm}$ pairs are accelerated in the region tagged as wind acceleration zone, at a distance of several R_L from the pulsar. Image from Aharonian et al. (2012)

also a model predicting VHE γ-ray emission by IC upscattering of photons from the wind (Aharonian et al. 2012). Emission at these energies is due to IC scattering of the X-ray photons produced in the magnetosphere or in the pulsar surface by the e^- or e^+ existing in the wind. According to Aharonian et al. (2012), acceleration takes place in a region between $20 - 50$ R_L, but this would imply a very sharp cut-off at 500 GeV. In order to match the maximum pulsed energy given by the recent observations (Zanin 2014), one has to extend the region where the X-rays interact with the wind to 70 R_L.

Due to the recent reports on pulsed emission up to TeV energies with very sharp pulse profiles (Zanin 2014), one finds that none of the proposed models is able to reproduce the broadband spectrum of the Crab pulsar giving at the same time a good description of the spin-phase folded light curve (Fig. 5.8).

5.3.2 Observational Signatures of Pulsars at VHE Gamma Rays

There are only two pulsars detected at VHE to date: the Crab and Vela pulsars (Zanin 2014; Brun 2014). Crab shows pulsed emission up to TeV, while for Vela no energy spectrum has been reported so far. In the case of Crab's light curve, two peaks can be significantly distinguished above the background, although for Vela only one is detected (see Fig. 5.9).

The peaks at TeV energies are much narrower in both cases than those reported at GeV energies. The region between P_1 and P_2 is known as the bridge region. MAGIC recently reported the detection of VHE γ-ray emission up to 400 GeV from the bridge region (Aleksić et al. 2014c).

In Fig. 5.10 we show the Crab pulsar spectrum up to 400 GeV reported by MAGIC, since the spectrum up to TeV energies is not public yet. The pulsed spectrum of both peaks is fit by a power-law with photon spectral index $\Gamma = 3.57 \pm 0.27$ and differential flux at 100 GeV 13.0 ± 1.6 TeV^{-1} cm^{-2} s^{-1} (Aleksić et al. 2012). The bridge emission is fit with a power-law with photon spectral index $\Gamma = 3.35 \pm 0.79$ and differential flux at 100 GeV 12.2 ± 3.3 TeV^{-1} cm^{-2} s^{-1} (Aleksić et al. 2014c).

5.4 Pulsar Wind Nebulae

If the SNR is centrally filled at all wavelengths, magnetic energy and relativistic particles are constantly being injected by a pulsar situated at its center and it is known as PWN (Weiler and Panagia 1978). PWNe are usually found embedded in the shell of SNRs larger than the PWN, but one can also find them entangled without the possibility of distinguishing one from the other.

The region between the light cylinder and the termination shock is known as the *wind zone*. The pulsar wind is generated in the acceleration of e$^\pm$ pairs that happens in the collapse of charge-separated gaps either near the pulsar polar caps or in outer regions that extend to the light cylinder. In practically all PWN models, the wind leaving the pulsar is Poynting flux dominated. In order to quantify this, we define a *magnetization parameter* σ as a ratio of the energy going out as EM radiation and the energy going out as kinetic energy of particles:

$$\sigma \equiv \frac{F_{E \times B}}{F_{\text{particle}}} = \frac{B^2}{4\pi\rho\gamma c^2} \tag{5.12}$$
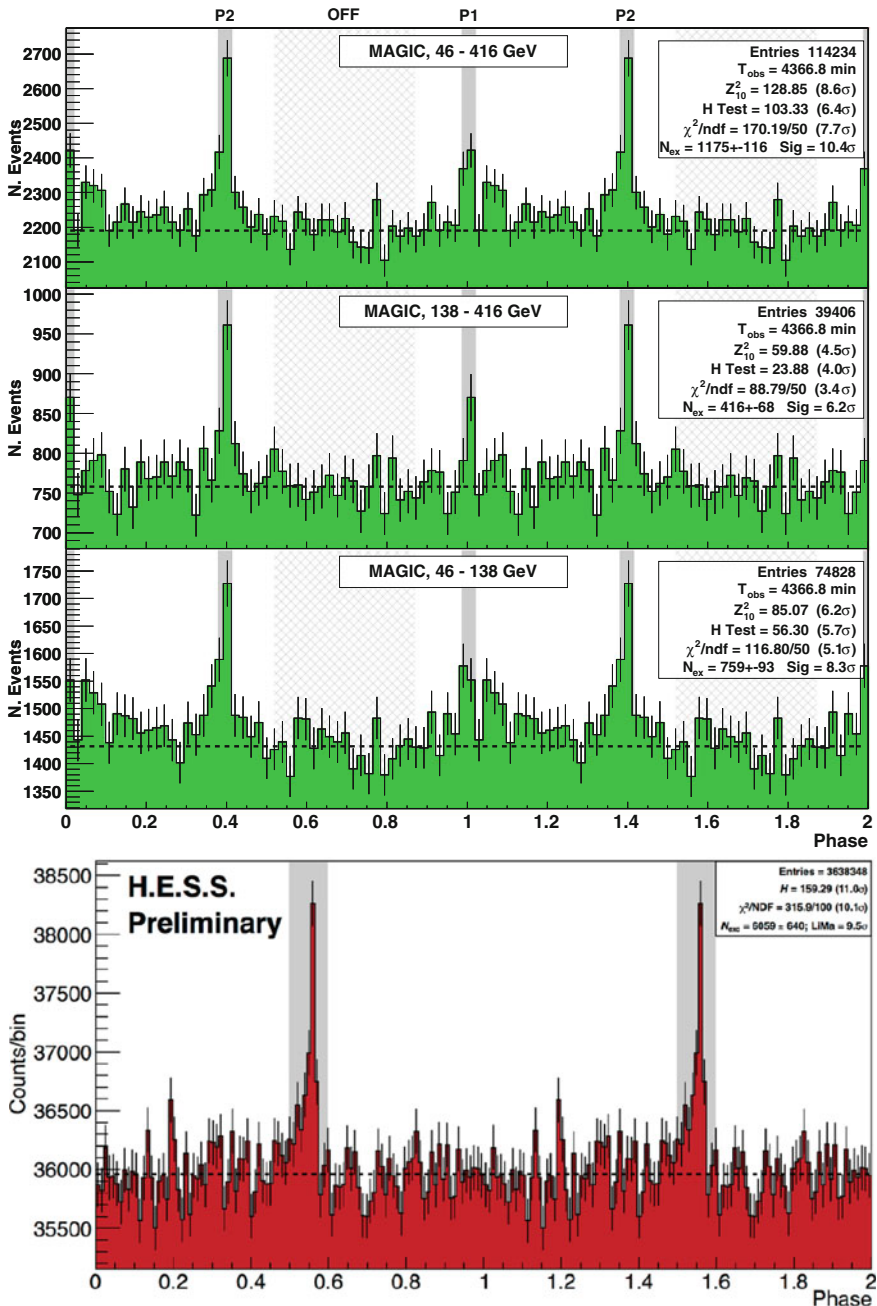
Fig. 5.9 Crab (*top panels*, filled in *green*, from Aleksić et al. (2012)) and Vela (*bottom panel*, filled in *red*, from Brun (2014)) pulsars' light curves. Two phases are shown for clarity. The peak positions are marked by the *solid shadowed areas*, while the OFF position in the Crab light curve is marked by a *dashed shadow area*. Crab light curves are shown in several energy ranges (color figure online)

Fig. 5.10 MAGIC Crab pulsar spectrum up to 400 GeV. Plot from Aleksić et al. (2012)
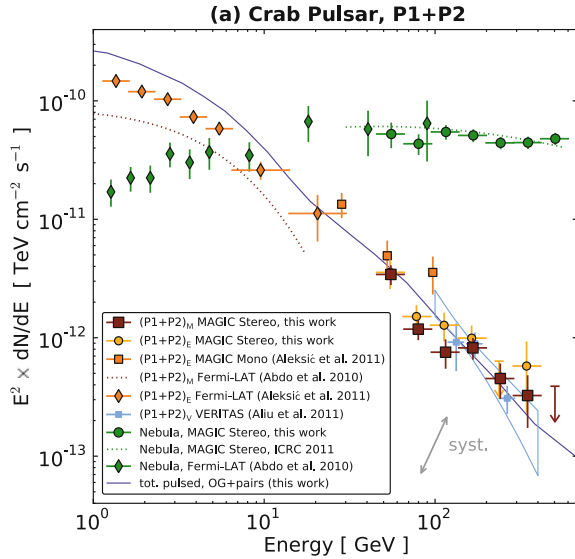
where $F_{E \times B}$ is the Poynting flux, F_{particle} the particle flux and B, ρ, γ and c the magnetic field, mass density of particles, Lorentz factor and speed of light, respectively. The parameter σ typically has a large value as the wind leaves the pulsar ($\sigma > 10^4$) and all the models require a small value right behind the termination shock ($\sigma < 0.01$) in order to compensate flow and pressure. The ratio between the synchrotron luminosity and the total spin-down luminosity also requires a particle dominated wind at the termination shock, with a Lorentz factor of $\gamma \sim 10^6$, much larger than the one expected from a freely expanding wind. And here is where the famous σ-*problem* in PWNe pops-up: the change of nature of the wind is widely assumed in all the models explaining VHE emission from PWNe, but the mechanism behind this change is still unclear (Arons 2009). Nevertheless, some solutions have been proposed along the years and the magnetic reconnection seems to be the key of this acceleration (Porth et al. 2013).

As the wind slows down to compensate the pressure applied to the PWN by the ISM, a *termination shock* is formed. It is situated at a distance R_s, given by:

$$R_s = \sqrt{\frac{\dot{E}}{4\pi \omega c P_{\text{PWN}}}} \tag{5.13}$$

where ω is the equivalent filling factor for an isotropic wind and P_{PWN} is the pressure in the nebula. An usual assumption to estimate P_{PWN} is to consider equipartition between magnetic field and particles inside the PWN. This assumption, although widely extended, leads to higher magnetic fields than the ones derived from VHE γ-ray observations by different models (see for instance Table 3 of Torres et al. 2014).

Fig. 5.11 *Chandra* X-ray
image of the Crab Nebula.
One can see the internal
structures of the pulsar as the
jet-torus and the inner ring.
Credit: NASA/CXC/ASU/J.
Hester et al.
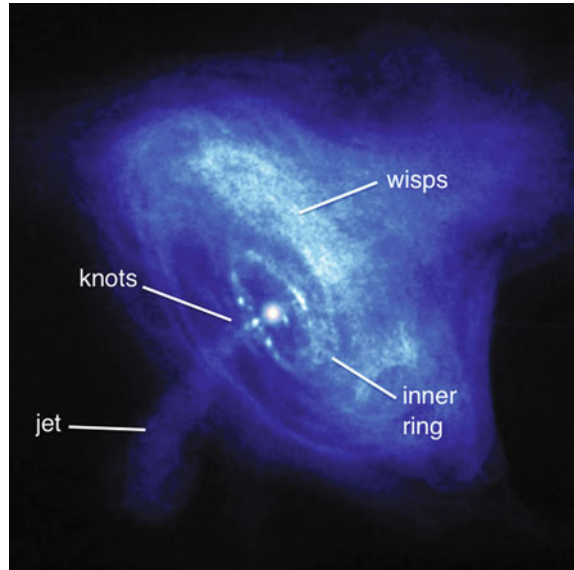
We can observe several structures inside the PWNe, all of them originated by
different phenomena. They are marked in the Crab Nebula *Chandra* image shown in
Fig. 5.11.

Jet-Torus PWNe usually show a toroidal structure brighter on one of its sides,
accompanied by a bright jet and a weaker counter-jet (due to Doppler effects) that
extend along the toroidal axis. This structure cannot be explained by an isotropic
energy flux inside the PWN proposed by the models (Kennel and Coroniti 1984), but
it may be described by an equatorial flux. The torus may actually correspond to the
pulsar's termination shock (Bucciantini et al. 2006).

Wisps They are ripples formed in the synchrotron nebula with variability in
timescales down to days. Although the exact nature of these structures is not fully
understood, they may be formed by synchrotron instabilities (Hester et al. 2002)
or may be places where the $e^\pm$ plasma is compressed (Gallant and Arons 1994;
Spitkovsky and Arons 2004).

Filamentary structures In PWNe as the Crab, a network of filaments surrounds the
non-thermal optical emission. They are explained as Rayleigh–Taylor instabilities
when the expanding relativistic bubble sweeps up and accelerates slower moving
ejecta (Hester et al. 1996).

The PWN formation can be divided in several phases: first of all, the SNR shell
moves forward freely. A shock, known as *forward shock* is formed by the interaction
of the SNR material and the ISM (Gaensler and Slane 2006). At the beginning, the
PWN is placed at the center of the SNR. Second, the shell enters the so-called "Taylor–
Sedov" phase, where the unshocked ejecta starts to decelerate due to the mass of the
ISM and a *reverse shock* is formed. It keeps advancing outwards the remnant at

Fig. 5.12 Schematic diagram of a composite SNR. In the expanded PWN view we can see the wind termination shock. Picture from Gaensler and Slane (2006)
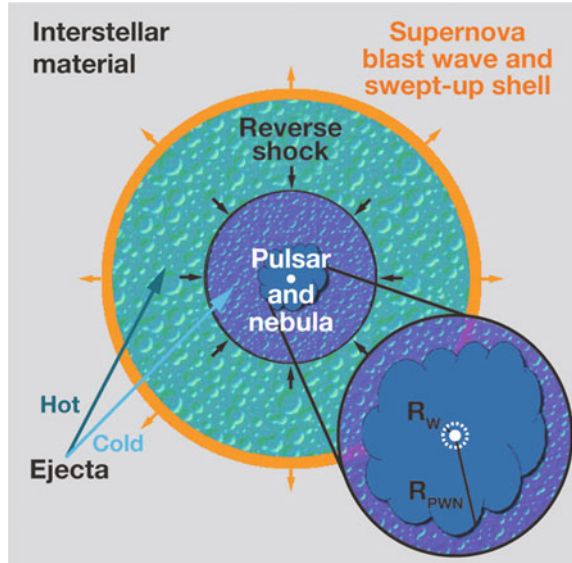
the beginning, but turns inwards eventually. The forward shock still compresses and heats material, but the reverse one decelerates and cools it, compressing the central PWN as well (see Fig. 5.12). Once the reverse shock stops compressing the PWN, the latter expands again, but this time into the hot ejecta that surrounds it. At the beginning the pulsar escapes from its original position, leaving a relic PWN. Later, the PWN motion becomes supersonic and it forms a bow shock along the SNR. Finally, the pulsar escapes from its surrounding SNR being able to form a bow shock nebula if its movement is still supersonic, but most probably ends up in a low density region where it cannot be detected.

5.4.1 Broadband Emission of PWNe

Although the pulsar wind is radiationless, one can study its properties by observing the *termination shock* formed when it is stopped by its interaction with the ISM Sect. 5.2.3. When the particles move along the magnetic field lines compressed at the *termination shock*, they produce synchrotron radiation ranging from radio to soft γ-ray energies and produce the so-called *synchrotron nebula*, situated right after the termination shock. The emission in the region ranging from soft gamma rays to VHE gamma rays is produced by IC up-scattering of low-energy photons inside the PWN. The IC scattering is produced all over the PWN. A sketch of the zones of synchrotron and IC emission can be seen in Fig. 5.13.

Fig. 5.13 Sketch of the acceleration mechanisms inside a PWN and regions where they take place. Image from Aharonian (2004)
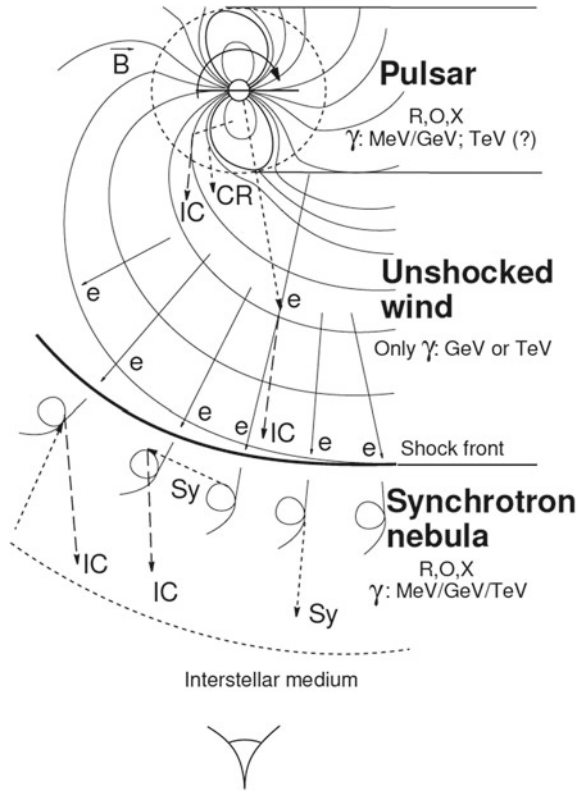
5.4.1.1 Synchrotron Emission

The synchrotron nebula extension depends on the magnetic field and lifetime of the particles. According to Ginzburg and Syrovatskii (1965), the cut-off frequency of the cooling spectrum is given by:

$$\nu_b = 10^{21} \left(\frac{B_{\text{PWN}}}{10^{-6}\text{G}} \right)^{-3} \left(\frac{t}{1\text{kyr}} \right) \text{Hz} \tag{5.14}$$

If we use a δ-approximation for the synchrotron cross-section, we can relate the energy of the synchrotron photons to the energy of the electrons (Ginzburg 1979):

$$E_{\text{syn}} = \frac{h\nu_c}{3} \tag{5.15}$$

where h is the Planck constant and ν_c the critical frequency:

$$\nu_c = \frac{3eB(t)E_e^2}{4\pi m_e^3 c^5} \tag{5.16}$$
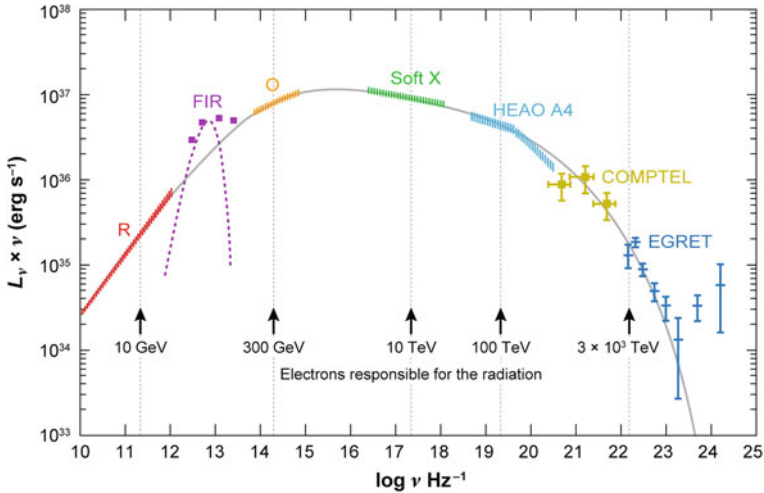
Fig. 5.14 Synchrotron spectrum of the Crab Nebula. The *grey solid line* corresponds to the synchrotron emission of the nebula. The *magenta dotted line* represents the additional component produced by dust. Figure taken from (Gaensler and Slane 2006) (color figure online)

that is dependent of the magnetic field and the energy of the electrons. The size of the nebula is inversely proportional to the frequency, although this effect is significant only in PWNe with high magnetic fields like the Crab.

The synchrotron emission from a PWN comes from the region after the *termination shock*. Radio emission is characterized by a "flat" power-law distribution such that $S_\nu \propto \nu^\alpha$, being S_ν the flux density at a frequency ν and α the spectral index of the source, which takes values between $-0.3 < \alpha < 0$. There is an intrinsic spectral break at IR-to-optical frequencies, although an extra spectral component at these energies may be generated by dust emission, as can be seen in the Far Infrared (FIR) emission of the Crab Nebula shown in Fig. 5.14. At X-ray frequencies, the emission is well-described by a power-law with a flux $F \propto E^{-\Gamma}$ with $\Gamma \sim 2$. An example of the broadband synchrotron emission of a PWN can be seen in Fig. 5.14.

5.4.1.2 Inverse Compton Emission

IC up-scattering of Cosmic Microwave Background (CMB), IR, optical-to-UV and X-ray photons can in principle happen all over the extension of the nebula (including *shocked and unshocked wind*). The IC emission of a PWN can be modeled using mainly three photon fields: the synchrotron radiation, that generates the Synchrotron Self Compton (SSC) process, dominant in young PWNe; the CMB, uniformly distributed in the whole nebula; and the FIR from galactic dust. A plot of the Crab Nebula IC emission of the Crab Nebula is shown in Fig. 6.4.

IC emission becomes important for middle-age PWNe. Since high-energy synchrotron e$^-$ lose their energies faster than those at lower energies, the population of the lower energies increases. TeV γ-ray photons require lower energy synchrotron e$^-$, therefore one expects to observe more radiation originated by IC for this type of sources.

VHE γ-ray emission from PWNe The VHE γ-ray emission of PWNe has its origin in the non-thermal IC scattering of the aforementioned photon fields present in the nebula. The first PWN discovered at VHE gamma rays was the Crab Nebula (Weekes et al. 1989) back in 1989. 26 years later there are more than 20 PWNe and PWN candidates detected at VHE (see Table B.9 in Appendix B.5).

These detections usually coincide with the falling part of the IC spectrum, so the emission is well-described by a single power-law with spectral indices between 1.3 $< \Gamma < 2.8$. This is not the case for Crab, detected by MAGIC down to ~50 GeV and whose spectrum has a more complex shape, such as a log-parabola (Aleksić et al. 2014b), or a different function as proposed in Aleksić et al. (2014a). At the highest energies the spectrum should curve due to the transition to the Klein–Nishina regime, but we need strong sources as the Crab to be able to measure this curvature.

5.4.2 Models

There have classically been two different approaches for modeling the emission of PWNe. On one hand, Magnetohydrodynamic (MHD) simulations succeed on explaining the morphological properties of PWNe. On the other hand, spherically symmetric one-dimensional PWNe spectral models do not take into account the energy-dependent morphology of the PWN, but successfully explain the spectrum. We will briefly describe both approaches.

5.4.2.1 MHD Models

Kennel and Coroniti (1984) were the first presenting a model that reproduced the morphological and spectral properties of PWNe through MHD simulations. The model consisted on solving the analytical equations for the pulsar wind in the simplified case of a symmetrically spherical MHD flow. The solution depends on the magnetization parameter σ, the spin-down power and the radius of the termination shock. The injection spectrum considered is a power-law with a cut-off that fits the observed spectrum. To calculate the synchrotron emission electron adiabatic and synchrotron losses are taken into account. The photon fields used as targets to calculate IC emission are synchrotron photons and dust IR emission. Several variations of the model using the same approach were later proposed (de Jager and Harding 1992; Atoyan and Aharonian 1996; de Jager et al. 1996; Hillas et al. 1998; Meyer et al. 2010) to account for different phenomena inside the nebula.

5.4.2.2   One-Dimensional Spectral Models

There are also several models that make a one-dimensional approach without taking into account any energy dependence in the PWN morphology. Aharonian et al. (1997) applied the diffusion-loss equation (solved for the first time by Syrovatskii 1959) to study the IC emission from PWNe. To correctly account for the evolution of the lepton population inside the nebula, one has to introduce a time parameter in the equation. Some time-dependent models apply different approximates such as neglecting the escape term (Tanaka and Takahara 2010), or substituting the energy losses by the particle's escape time (Zhang et al. 2008), while others make no approximations (Martín et al. 2012). The photon contributions considered to calculate the broadband spectrum are also diverse, although Martín et al. (2012) considers all of them: synchrotron emission, synchrotron self-Compton, IC, and bremsstrahlung. A more detail explanation about several of the time-dependent models is given in Sect. 7.3.1.

References

Aharonian F (2004) Very high energy cosmic gamma radiation : a crucial window on the extreme Universe. World Scientific
Aharonian F et al (1997) MNRAS 291:162
Aharonian F et al (2012) Nature 482:507
Aleksić J et al (2012) A&A 540:A69
Aleksić J et al (2014a). arXiv:1406.6892
Aleksić J et al (2014b). arXiv:1409.5594
Aleksić J et al (2014c) A&A 565:L12
Arons J (1983) ApJ 266:215
Arons J (2009) In: Becker W (ed) Astrophysics and Space Science Library, vol 357, p 373
Arons J et al (1979) ApJ 231:854
Atoyan AM et al (1996) MNRAS 278:525
Baade W et al (1934) Phys Rev 46:76
Brun P (2014) In: Very high energy phenomena in the universe
Bucciantini N et al (2006) MNRAS 368:1717
Chandrasekhar S (1931) ApJ 74:81
Cheng KS et al (1986) ApJ 300:500
Daugherty JK et al (1982) ApJ 252:337
de Jager OC et al (1992) ApJ 396:161
de Jager OC et al (1996) ApJ 457:253
Gaensler BM et al (2006) ARA&A 44:17
Gallant YA et al (1994) ApJ 435:230
Ginzburg VL (1979) Theoretical physics and astrophysics. Pergamon Press
Ginzburg VL et al (1965) ARA&A 3:297
Goldreich P et al (1969) ApJ 157:869
Grupen C (2005) Astroparticle physics. Springer, Berlin
Harding A et al (2005) Ap&SS 297:63
Harding AK (2013) Front Phys 8:679
Heger A et al (2003) ApJ 591:288
Hester JJ et al (1996) ApJ 456:225

Hester JJ et al (2002) ApJ 577:L49
Hewish A et al (1968) Nature 217:709
Hillas AM et al (1998) ApJ 503:744
Hirotani K (2008). arXiv:1409.6073
Hirotani K (2011) ApJ 733:L49
Hirotani K (2013) ApJ 766:98
Kennel CF et al (1984) ApJ 283:710
Kirk JG et al (2002) A&A 388:L29
Kirk JG et al (2009) In: Becker W (ed) Astrophysics and space science library, vol 357. p 421
Lyubarskii YE (1996) A&A 311:172
Manchester RN et al (1977) Pulsars. W. H. Freeman and Co
Martín J et al (2012) MNRAS 427:415
Meyer M et al (2010) A&A 523:A2
Ostriker JP et al (1969) ApJ 157:1395
Pacini F (1967) Nature 216:567
Pacini F (1968) Nature 219:145
Pacini F et al (1973) ApJ 186:249
Pétri J (2011) MNRAS 412:1870
Porth O et al (2013) MNRAS 431:L48
Reynolds SP (2008) ARA&A 46:89
Richards DW et al (1969) Nature 222:551
Scharlemann ET et al (1978) ApJ 222:297
Spitkovsky A et al (2004) ApJ 603:669
Sturrock PA (1971) ApJ 164:529
Syrovatskii SI (1959) Sov Ast 3:22
Tanaka SJ et al (2010) ApJ 715:1248
Torres DF et al (2014) J High Energy Astrophys 1:31
Weekes TC et al (1989) ApJ 342:379
Weiler KW et al (1978) A&A 70:419
Zanin R (2014) V Fermi symposium proceedings
Zhang L et al (2008) ApJ 676:1210

Chapter 6
The Crab Nebula: A Gamma-Ray Factory in Our Backyard

6.1 Introduction

The Crab Nebula is the remnant of the SN explosion in 1054 AD reported by Japanese and Chinese astrologers (Ho and Ho Ping-Yü 1962). The "new star" was visible during daytime for several weeks, and in the night sky for 22 months (Clark and Stephenson 1977). The remnant was discovered by the English astronomer John Bevis in 1731 and became the first object in Charles Messier's catalog of nebulae and star clusters. The name of the nebula was given by William Parson, third Earl of Rosse in 1850, who found the similarity with the crustacean the first time he looked at the nebula as it can be seen in the drawing he made in Fig. 6.1. Lundmark (1921) and Hubble (1928) proposed that the Crab Nebula was associated with the SN explosion in 1054, but it was not until 1941 when the Crab was unambiguously established as the remnant of the SN 1054 (Duyvendak 1942; Mayall and Oort 1942) (an optical image of the Crab can be seen in Fig. 6.2). The Crab is placed at a distance of $\sim$2 kpc (Trimble 1973) and its composition can be divided in several observables. Let us go in detail over its different components:

- **The Crab pulsar**

  The Crab pulsar (also known as PSR J0534+2200), located at the center of the SNR, is the engine that powers the nebula. It was discovered in radio by the Arecibo telescope (Staelin and Reifenstein 1968; Comella et al. 1969). It has a period $P = 33$ ms and its first derivative is $\dot{P} = 4.21 \times 10^{-13}$ s s^{-1}. If we assume that the radius of the neutron star is $\sim$10 km and its mass 1.4 $M_\odot$, the pulsar's spin-down power is $L_{\text{spin-down}} = 4\pi^2 I \frac{\dot{P}}{P^3} = 5 \times 10^{38}$ erg s^{-1}. Lyne et al. (1988) assumed a breaking index $n = 2.51$ and calculated that the initial period of the pulsar was $\sim$19 ms, meaning that it has lost 3.6×10^{49} erg since its origin, which is less than 10 % of the energy of the SN explosion that gave birth to the pulsar (assuming the fiducial value of 10^{51} erg). One has to mention that most of the rotational energy lost by the neutron star is not emitted in the form of pulsed emission, but it is carried

Fig. 6.1 Lord Rosse's
drawing of the Crab Nebula
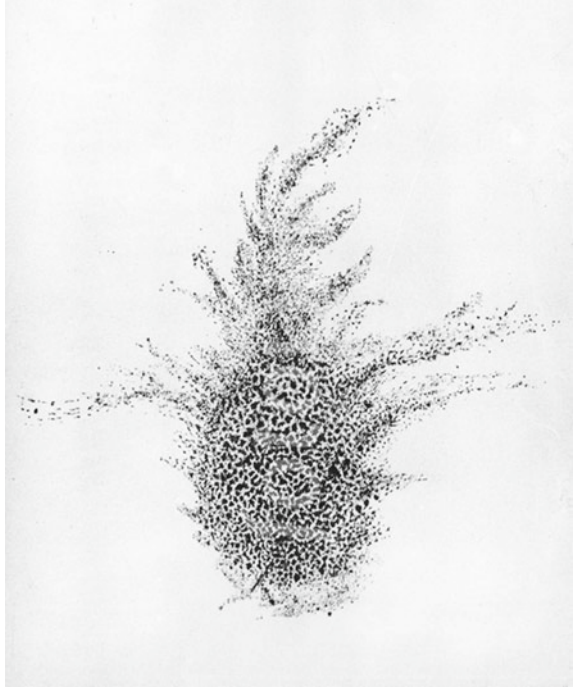
Fig. 6.2 Optical image of
the Crab Nebula by the
Hubble telescope. Image
from Hester (2008)
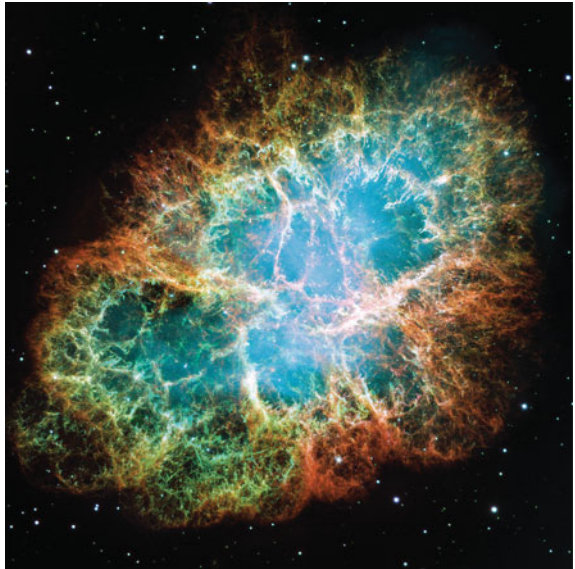
away by a highly magnetized plasma. The Crab pulsar is detected at wavelengths ranging from radio to VHE gamma rays. It is characterized by a two-peaked light-curve with peaks varying across the electromagnetic spectrum in relative height but not in phase. After the aforementioned radio detection, pulsed emission was discovered from the Crab in optical (Cocke et al. 1969), X-ray (Fritz et al. 1969; Floyd et al. 1969) and γ-ray (Browning et al. 1971; Kurfess 1971; Albats et al. 1972) wavelengths (see Fig. 6.3 for a broadband spectrum). At VHE gamma rays the detection of pulsed emission from the Crab turned out to be more difficult, and it was not until 2008 when MAGIC discovered it (Aliu et al. 2008). The detection of pulsed emission at such energies ruled out pulsed emission models as the polar-cap where the production of the pulsed radiation is too close to the pulsar to achieve the energies measured. The VHE spectrum was first extended by VERITAS and MAGIC up to 400 GeV (Aliu et al. 2011; Aleksić et al. 2012) and very recently, up to TeV energies by MAGIC (Zanin 2014). To achieve such high energies on the pulsed emission constrains the emission region to be at a larger distance than the predicted by most of the models. The MAGIC collaboration has also reported VHE γ-ray emission from the so-called *bridge* region, or region between the two peaks of the light-curve (Aleksić et al. 2014b).
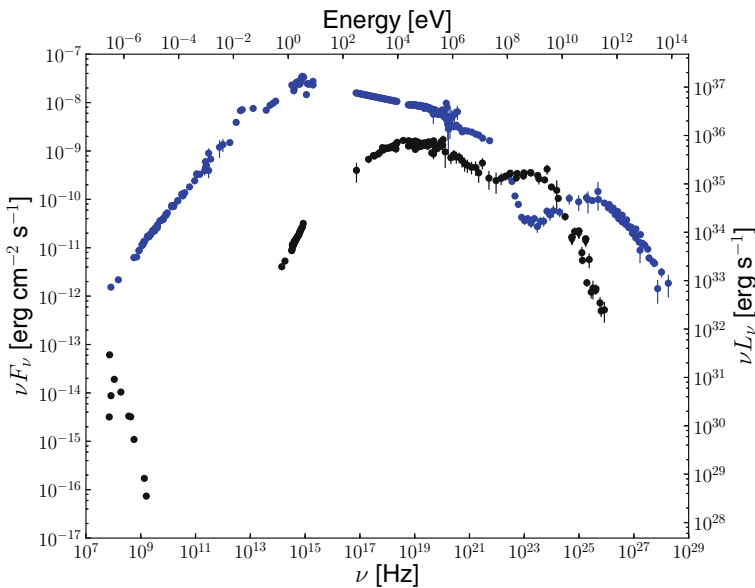
Fig. 6.3 Broadband spectral energy distribution of the Crab Nebula (*blue points*) and the phase averaged emission of the Crab pulsar (*black points*). Plot taken from Bühler and Blandford (2014) (color figure online)

- **The Crab Nebula**

  The PWNconfined by the thermal ejecta from the SN is known as the Crab Nebula. It will be described in more detail in Sect. 6.2.

- **The filaments and the shell**

  A third component of the SNR are the filaments that are visible in the outer ring of the nebula of Fig. 6.2. They form a cage where the PWN is confined. The last component consists of freely expanding ejecta beyond the visible edge of the nebula. It has been a crucial part of all theoretical models for several years, but it has only recently been observed (Sollerman et al. 2000).

6.2 The Crab PWN

The pulsar wind is radiationless ("cold wind") until it interacts with the ambient medium in a shock, situated at a distance of about 3×10^{17} cm from the pulsar. As the wind does not emit radiation, the only way to study it is the synchrotron nebula surrounding it. As mentioned in Sect. 5.2.3, (Kennel and Coroniti 1984a) derived a MHD model of the Crab where they could explain its synchrotron emission only in the case that the magnetization of the wind was very low ($\sigma = 0.003$) in the moment of the shock. They assumed an equipartition value between the magnetic field and the particle energy, deriving a magnetic field of $B = 300\,\mu\mathrm{G}$. In newer models explaining the broadband emission of the nebula, the magnetic field is between 100 and $300\,\mu\mathrm{G}$ (de Jager and Harding 1992; Atoyan and Aharonian 1996; Hillas et al. 1998; Meyer et al. 2010; Martín et al. 2012), values lower than the equipartition, but in agreement with those inferred by interpreting the hardening of the integrated spectrum of the nebula between the radio and the optical band and electron cooling (Marsden et al. 1984). At the outer edge of the synchrotron nebula, there is a second shock driven by the pressure of the synchrotron nebula into the thermal gas surrounding it.

The size of the synchrotron nebula is smaller for larger frequencies. This is interpreted as due to a cooling of the high-energy electrons. Features where the emission of the nebula increases are known as *wisps*. They vary in timescales of days and can be seen in radio, optical and X-rays, but their positions vary with frequency.

6.2.1 The Broadband Spectrum of the Crab Nebula

Two spectral components are observed in the Crab Nebula: the *synchrotron* part and the *inverse Compton* one as it was described in Sect. 5.4.1. A broadband spectrum

of the Crab Nebula and its pulsar is shown in Fig. 6.3.[1] We will have a dedicated description of the IC part of the spectrum in Sect. 6.2.1.1

6.2.1.1 The IC Part of the Spectrum

The Crab Nebula was discovered at VHE gamma rays (above 700 GeV) by the Whipple telescope, making it the first source detected by an IACT (Weekes et al. 1989). Since then, it is the standard candle in this energy band, having the highest flux amongst the steady VHE γ-ray sources. After Whipple discovery, the Crab has been used as a calibration source for the different telescopes using a similar technique. If we consider the latest MAGIC results on the Crab, its flux above 200 GeV is 2.3×10^{-10} cm^{-2} s^{-1}. This means that the γ-ray flux that current IACTs with typical collection areas of the order of 10^9 cm^2 can detect is ~4 gamma rays/minute (Aleksić et al. 2014c). With the current sensitivity of the MAGIC telescope and its low energy threshold, the Crab Nebula can be detected in less than a minute.

In the case of Crab, the emission measured by MAGIC overlaps with that measured by the *Fermi*-LAT satellite at MeV–GeV energies. One can clearly see the transition from the synchrotron-dominated emission (below 1 GeV) to the IC-dominated one (above 1 GeV) in Fig. 6.4. Using MAGIC and *Fermi* data together, the energy of the IC peak can be determined. In Aleksić et al. (2014a), the IC peak was fit using several functions. For the fit using a log-parabola, the peak is at 53 GeV, although the range of the fit and the data used (MAGIC, *Fermi* or both), strongly influences its position. On the other hand, the fit does not have a high probability. This leads to the conclusion that the IC peak is not a well-defined feature of the Crab spectrum.

6.2.1.2 Spectra

In fact, the VHE spectrum measured by different IACTs show discrepancies at the highest energies:

1. The HEGRA collaboration used a **single power-law** to describe the spectrum between 500 GeV and 80 TeV (Aharonian et al. 2004):

$$\frac{\mathrm{d}\phi}{\mathrm{d}E} = f_0 \left(\frac{E}{1\,\mathrm{TeV}}\right)^{-\alpha} \qquad [\mathrm{TeV}^{-1}\mathrm{cm}^{-2}\mathrm{s}^{-1}]$$

2. The HESS collaboration used a **power-law with an exponential cut-off**, as in Aharonian et al. (2006) for energies between 440 GeV and 40 TeV:

$$\frac{\mathrm{d}\phi}{\mathrm{d}E} = f_0 \left(\frac{E}{1\,\mathrm{TeV}}\right)^{-\alpha} \exp\left(\frac{-E}{E_c}\right) \qquad [\mathrm{TeV}^{-1}\mathrm{cm}^{-2}\mathrm{s}^{-1}]$$

where E$_c$ is the cut-off energy.

---

[1]A movie where you can see the dynamic of the synchrotron nebula in X-rays can be seen in http://chandra.harvard.edu/photo/2002/0052/animations.html.
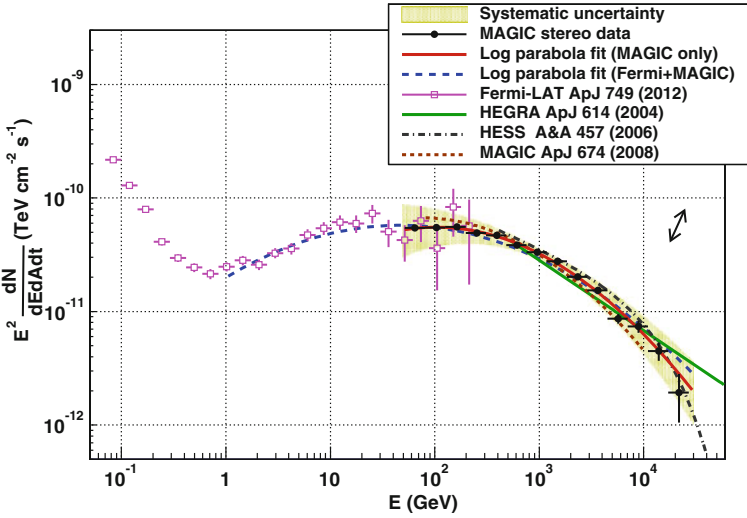
Fig. 6.4 The IC part of the spectrum of the Crab Nebula (from Aleksić et al. 2014a). *Magenta points* are the results from *Fermi*-LAT analysis and black points the ones from MAGIC. The *red solid line* shows the fit of the MAGIC data by a log-parabola, while the *blue dashed line*, the fit of MAGIC and *Fermi*-LAT data together by a log parabola as well. The *green dashed-tripple-dotted*, *black dashed-dotted* and *red-dotted lines* show HEGRA, HESS and MAGIC previous fits respectively (color figure online)

3. The MAGIC collaboration used a **variable/curved power-law function** which is the best function that fits MAGIC data between 50 GeV and 30 TeV, due to the hardening at low energies (Aleksić et al. 2014a):

$$\frac{\mathrm{d}\phi}{\mathrm{d}E} = f_0 \left(\frac{E}{1\,\mathrm{TeV}} \right)^{-\alpha + \beta \mathrm{Log}_{10}(E/1\mathrm{TeV})} \qquad [\mathrm{TeV}^{-1}\mathrm{cm}^{-2}\mathrm{s}^{-1}]$$

where β is the curvature of the function.

The parameters of each fit can be found in Table 6.1. A plot with the spectral points measured by the experiments, together with the spectral fit can be found in Fig. 6.5.

Table 6.1 Different functions used to fit the VHE γ-ray spectrum of the Crab Nebula

Function	$\phi_0 \times 10^{-11}$ [$\mathrm{TeV}^{-1}\,\mathrm{cm}^{-2}\,\mathrm{s}^{-1}$]	α	E_{cut} [TeV]	β
Power-law	2.83 ± 0.04	2.62 ± 0.02	–	–
Power-law + exp. cut-off	2.26 ± 0.08	2.39 ± 0.03	14.3 ± 2.1	–
Log-parabola	3.23 ± 0.03	2.47 ± 0.01	–	-0.24 ± 0.01
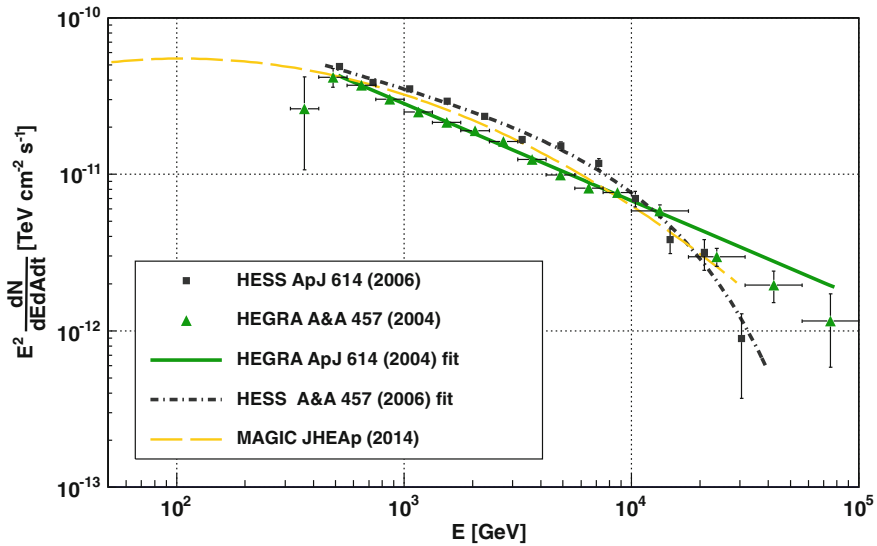
Fig. 6.5 Spectral energy distribution of the Crab Nebula from the HESS, HEGRA and MAGIC telescopes

As it will be discussed in Sect. 6.2.1.3, a spectral softening at energies >10 TeV is expected due to the transition of the IC emission to the Klein–Nishina regime. Due to this transition, a power-law cannot be a suitable function to fit the VHE γ-ray spectrum of the Crab. In fact, if we take HEGRA data with their statistical errors only, fit them using the different functions and compare the goodness of the fits, we find that for a power-law (χ^2/Ndf = 22.27/12), a power-law with a cut-off (χ^2/Ndf = 13.47/11) and a log-parabola (χ^2/Ndf = 12.23/11), the lowest fit probability is given by the power-law function.

6.2.1.3 Importance of the Observation of the VHE Tail of the Nebula

The Thomson scattering is the elastic scattering of electromagnetic radiation by a free charged particle, as described by classical electromagnetism. It is just the low-energy limit of the Compton scattering: the particle kinetic energy and photon frequency are the same before and after the scattering. This limit is valid as long as the photon energy is much less than the mass energy of the particle: $\nu \ll mc^2/h$ where ν is the frequency of the scattered photon, m the mass of the scattering particle, c the speed of light and h the Planck constant. IC here is equally treated as the Compton scattering. If we reach higher energies, quantum effects have to be taken into account using the Klein–Nishina formula, which gives the differential cross section of photons scattered from a free electron in lowest order of Quantum Electrodynamics (QED).

The motivation of the work presented here is to study the transition from the regime where the IC scattering of electrons with synchrotron photons is still classical (Thomson regime) to the regime where one has to take into account the QED effects

(Klein–Nishina regime, Klein and Nishina 1929). Since the energy of the synchrotron electrons producing the IC scattering observed at VHE gamma rays can be of several hundred of TeV (see Fig. 5.14), according to the aforementioned condition to be in the Thomson regime, we should start to measure effects on the spectrum due to the transition to the Klein–Nishina regime for energies above $\sim$10 TeV. The measurement of this transition is very important to unveil the energy up to which the electrons are accelerated inside the nebula. As a final remark, the detection of persistent emission above a few tens of TeV might be caused by efficient acceleration of hadrons in the nebula, expected to be emitting gamma rays with energies $>$10 TeV as it was proposed in Bednarek and Bartosik (2003), Horns et al. (2006), Amato et al. (2003).

6.2.1.4   Models

As we said in Sect. 5.4.2, there are two main approximations for modeling PWN-broadband emission: On one hand we have models based on MHD simulations that reproduce the morphology and spectrum of the PWNe, and on the other hand we have symmetric one-dimensional models for the evolution of PWN. The models explaining the emission from PWNe usually use the Crab to calibrate their parameters, so we refer the reader to Sect. 5.4.2 for further information about these approaches and some of the models derived from them. For the purpose of this work, we will extend the interpretation of MAGIC data in Aleksić et al. (2014a) in the framework of Meyer et al. (2010), Martín et al. (2012) models.

6.2.2   Variability

Optical variability from the Crab Nebula on monthly time scales has been known for long time (Lampland 1921). The integrated flux of the nebula varies by only $\sim$1 % per year in the radio, optical and X-ray ranges (Vinyaikin 2007; Smith 2003; Wilson-Hodge et al. 2011). The cooling time of $e^{\pm}$ emitting at higher than X-ray energies is of the order of years. The emission at these energies is therefore subject to a larger variability.

The discovery by *Fermi*-LAT and AGILE of enhanced emission from the Crab Nebula at relatively low energies $>$100 MeV (Tavani et al. 2010; Buehler et al. 2010) and time scales of the order of hours was unexpected. This emission reaches up to 30 times the steady unpulsed flux of the Crab Nebula above 100 MeV on time scales down to 6 h (Abdo et al. 2011; Tavani et al. 2011), meaning that the emission region should be smaller than 10^{-4} pc. Unfortunately, due to the angular resolution of the *Fermi*-LAT satellite at these energies, the Crab Nebula cannot be resolved, therefore the region of emission of the flares remains unknown. As of November 2014, nine flares have already been reported (Buehler et al. 2012; Ojha et al. 2012; Mayer et al. 2013; Striani et al. 2013; Buson et al. 2013; Gasparrini and Buehl 2014; Becerra et al. 2014). No enhancement of the emission has been detected at other wavelengths

than HE gamma rays and no enhancement on the pulsed γ-ray emission of the Crab has been found either.

Observation of previous flares by IACTs did not produce any report of enhanced emission (Mariotti 2010; Ong 2010). Moreover, HESS and VERITAS also observed the Crab during the March 2013 flare that will be discussed in this chapter and did not find any flux enhancement (Abramowski et al. 2014; Aliu et al. 2014). ARGO-YBJ collaboration reported several enhancements of emission at TeV energies coincident with flaring periods at HE (Aielli et al. 2010; Bartoli et al. 2012; Vernetto 2013), but they reanalyzed their data samples very recently and did not find any significant flux variability (Bartoli et al. 2015).

6.2.2.1   Models

The origin of the flares is still a mystery, although it seems that synchrotron emission is the only process that can account for the flaring emission. IC and bremsstrahlung electron cooling times are much longer than the duration of the flares, but the synchrotron cooling time of the electrons in the Crab can be of the order of the duration of the emission (Abdo et al. 2011). Particles accelerated in MHD flows can only reach maximum energies of $\sim$160 MeV, so the only explanation is that either MHD conditions are not valid in the flaring region or that the emission is boosted toward us. MHD conditions are broken in magnetic reconnection events and beaming of particles occurs in the reconnection layer (Zweibel and Yamada 2009; Cerutti et al. 2012; Uzdensky et al. 2011; Sturrock and Aschwanden 2012). Diffusive shock acceleration does not produce the hard spectra observed and acceleration due to absorption of ion cyclotron waves is expected to act on long time scales. Magnetic reconnection was studied in the context of the flares and the spectra and evolution could be reproduced by Cerutti et al. (2013), being therefore the favored mechanism responsible for the particle acceleration during Crab Nebula flares. If the origin of the HE flares is due to variations in the electric and magnetic field of the PWN, this would have no effect in the IC component of the Crab, but if the flares are caused by an increase in the lepton population, one would also expect a variation at the corresponding IC energies. This increase can go from 1 % (Lobanov et al. 2011) to values larger than 100 % depending on the model (Bednarek and Idec 2011; Kohri et al. 2012).

Since γ-ray flares from the Crab Nebula were discovered in September 2010, several models have tried to explain the emission enhancement at GeV energies, some of them also predicting a significant increase of the emission at TeV energies, in principle measurable by the current generation of IACTs. Bednarek and Idec (2011) presented a model that explains the flare emission as a new population of electrons accelerated in the region behind the shock as a result of the reconnection of the magnetic field. They assume that the flaring region is moving relativistically towards the observer to account for the short time scales measured. The target photon fields for IC they consider are only the CMB and the synchrotron photons from the nebula. They assume different parameters for the spectrum of the injected electrons and a magnetic field of 2 mG. If only the break energy in the electron spectrum changes,

the enhancement of the emission at TeV energies is very low and out of the reach of current IACTs due to the large systematic errors that affect the measurements. On the other hand, they predict a measurable increase in the TeV emission in the case that the break energy in the electron spectrum changes together with a flattening of the electron spectrum. This extra component has a $\sim$25 % larger flux at 1 TeV than the quiescence one if the magnetic field in the flaring region is 40 mG. This difference increases with the energy and reaches $\sim$4 times the quiescence Crab flux at 10 TeV. Finally, they also propose that the difference between the Crab Nebula spectra measured by the different experiments (HESS and HEGRA) might come from different stages of electron acceleration in the nebula.

Kohri et al. (2012) consider that the flare is produced in a small blob of the synchrotron nebula that is Lorentz boosted towards us. The maximum energy of the synchrotron e^- is not violated due to the mentioned Lorentz boosting. They predict an increase in the IC component a factor Γ^2 ($\Gamma \equiv$ Lorentz factor) larger than the synchrotron one due to the boosting of the target photon field. They considered a "fiducial" model with a magnetic field $B = 223\,\mu G$ and $\Gamma = 100$ and predict an enhancement of the VHE γ-ray emission above 10 TeV of $\gtrsim$ twice its quiescence value.

6.3 Observations with MAGIC

The study of the Crab Nebula performed in this work seeks a twofold objective: on one hand, study the spectral shape at energies >10 TeV and on the other hand, study the variability of the Crab Nebula during the flare that took place in March 2013.

6.3.1 Crab at High Zd

To achieve a better performance at higher energies it is essential to have the largest possible collection area. MAGIC with two telescopes cannot compete with four or five-telescope arrays such as VERITAS or HESS at energies above 1 TeV observing at low Zd. What one can do is to increase the collection area by observing at high Zd, by paying the price of increasing the energy threshold as we can see in Fig. 6.6.

If we are interested in TeV energies, we can point the telescopes to high Zd to increase the collection area at the studied energies (see Fig. 6.7). This increase translates on a better performance of the telescope at Zd > 50° for energies larger than 5 TeV with respect to the performance at lower Zd, as it can be seen in Fig. 6.8.

6.3.2 Data Sample and Analysis Procedure

MAGIC observed the Crab Nebula at high Zd (Zd > 50) in the period between November 2012 and April 2014. A summary of the observations can be found in
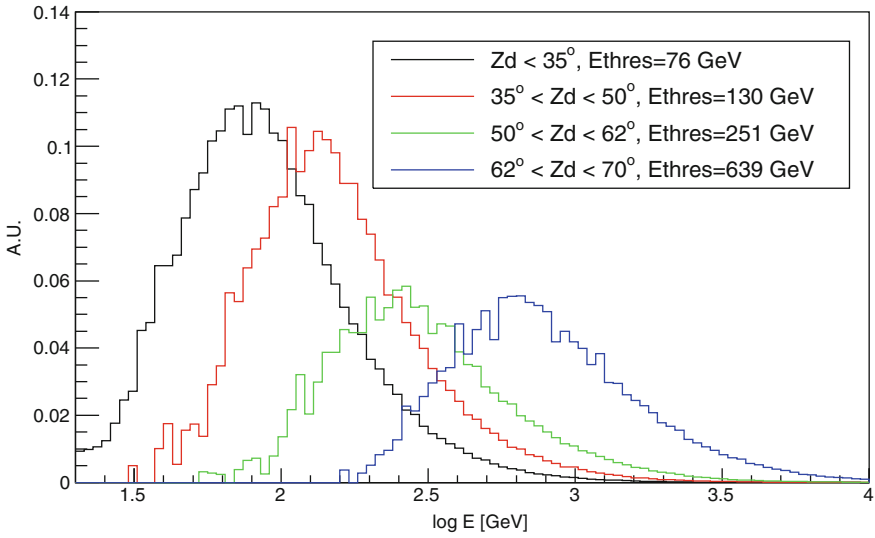
Fig. 6.6 True energy distribution of MAGIC MC γ-ray events for different ranges of Zd. The energy threshold is conventionally defined as the energy of the peak of the distribution
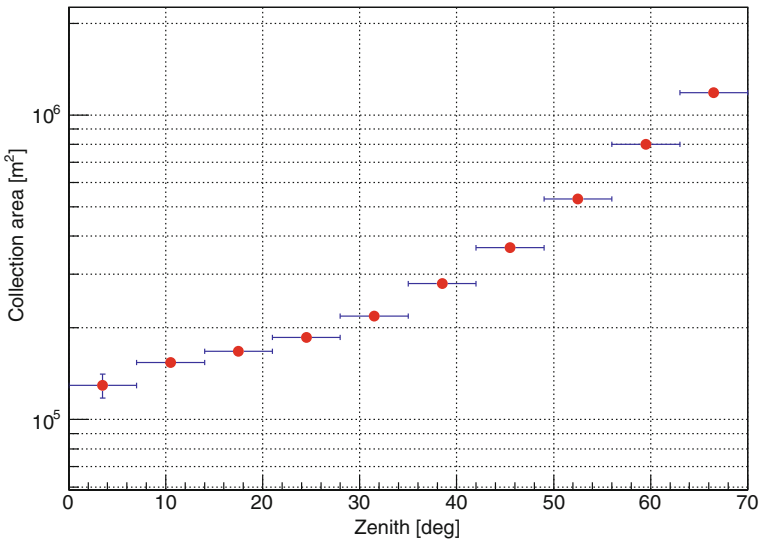
Fig. 6.7 Collection area as a function of the Zd at 10 TeV

Table B.4. For the observations at high Zd, we observed a total of 68.94 h, but only 39.6 h were left after data quality selection based on atmospheric conditions and technical problems.
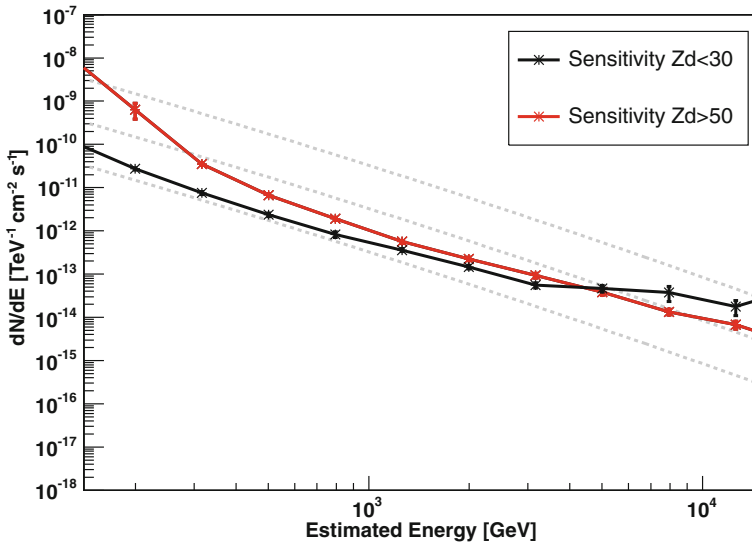
Fig. 6.8 MAGIC differential sensitivity for Zd > 50° (*red points*) and Zd < 30° (*black points*)
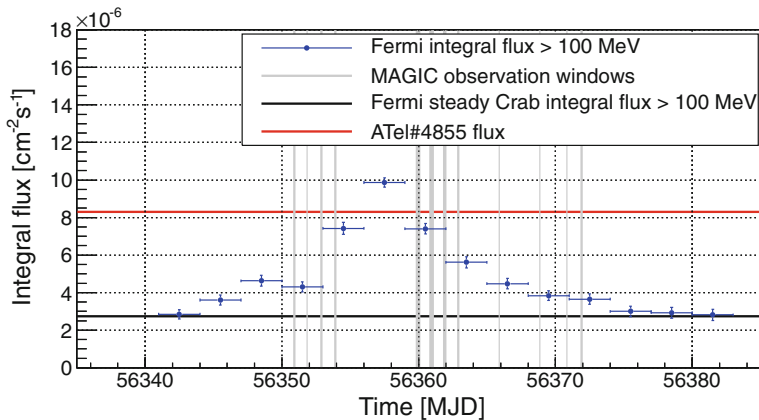
Fig. 6.9 *Fermi*-LAT light curve above 100 MeV (*blue points*) of the Crab flare in March 2013 including MAGIC observation windows (*grey lines*). The *black line points* the *Fermi*-LAT steady flux above 100 MeV and the *red* one the flux reported in the ATel#4855 by the *Fermi* collaboration Ojha et al. (2013) (color figure online)

We observed the Crab during the March 2013 flare for a total of 23.27 h at Zd ranging from 5.9° to 70.3°. Unfortunately, due to very bad weather conditions those days at the telescope site, only 3.79 h from 11 and 12 of March were left after data quality selection. A breakdown of the of the observations during the March 2013 Crab flare at all Zd can be found in Table B.5. We compare this flaring data sample with that of data previously taken under the same Zd conditions. A plot with the flux

detected by Fermi above 100 MeV, together with the MAGIC observation windows is shown in Fig. 6.9.

The data were analyzed using the standard MAGIC analysis (see Sect. 2.2.3). The data sample used to calculate the Crab spectrum presented in this work expands over 3 observation periods with slightly different performance of the telescope. For each of the observation periods a different MC simulation matching the telescope performance is used.

6.3.3 Energy Spectrum

The MC simulations reach an energy of 80 TeV. To take into account the effect of the bins with energies >80 TeV due to the energy bias, we extrapolated the migration matrix and the collection area of the last bin where we have MC data. (see Figs. 6.10 and 6.11). We checked the effect of applying this estimation by computing the dif-
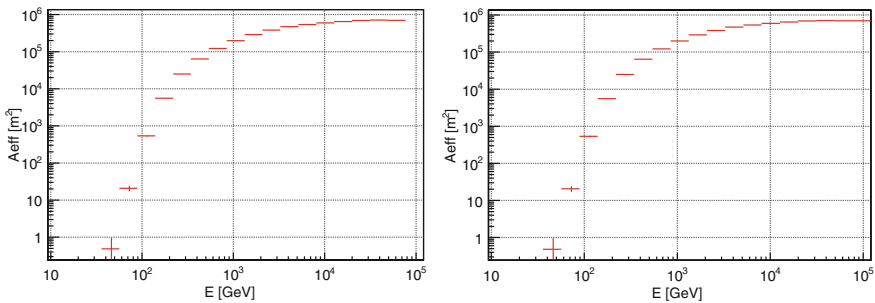
Fig. 6.10 Non-extrapolated (*left panel*) and extrapolated (*right panel*) collection area for MC gamma rays

Fig. 6.11 Migration matrix for the Crab Nebula observations at Zd > 50°
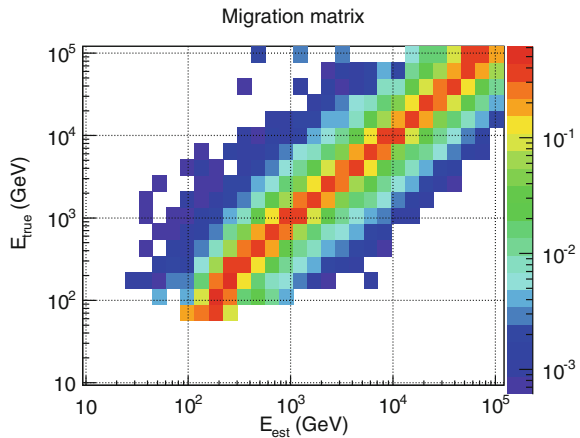
ferent spectra without extrapolating the migration matrix and the collection area and the effect was negligible.

To take into account the energy resolution and energy bias of the telescope, the spectrum was unfolded using different algorithms (Bertero, Tikhonov and Schmelling, see Albert et al. 2007). Since a single power-law, as expected, is not giving a good fit to the data (χ^2/NDF = 31.86/9), in this work we show the fit of the unfolded spectrum using a log-parabola and a power-law with a cut-off. The unfolded spectra with the different fits are shown in Fig. 6.12. The best-fit parameters, together with the goodness of the fit for the different unfolding methods and the two functions considered can be seen in Table 6.2. As we can see, all the unfolding methods agree within statistical errors.

Although the log-parabola (with probability $\sim$90 %) gives a better fit than the power-law with a cut-off (with probability $\sim$60–70 %), both functions give a good fit to the data. In addition, if we add the systematic uncertainty (Aleksić et al. 2014c), this probability increases. A plot comparing the results from the previous published experiments together with the results reported in this work for the Bertero unfolding (the one with the lowest χ^2) can be seen in Fig. 6.13.

Due to the systematic uncertainty, one cannot rule out the possibility that MAGIC data is fit either with a power-law or with a power-law with a cut-off. What we can evaluate is, given HESS and HEGRA fit functions, the probability that the number of events measured by MAGIC is compatible with one of those functions. To do it, we use a toy MC that takes the number of events in bins of estimated energy, the migration matrix between different energy bins, the collection area in bins of the true energy of the MC and the observation time. For every iteration of the toy MC, we use the collection area, time, migration matrix and assumed function to calculate the number of events that would be detected in every energy bin. We assume that the events follow a poissonian distribution and generate them using the poissonian probability. To account for the MAGIC systematic error, we assume an additional systematic uncertainty in the flux depending on the energy range where the energy bin is (18 % for $E < 100$ GeV, 11 % for 100 GeV$< E < 1$ TeV and 16 % for $E > 1$ TeV). The distribution of generated events for every energy bin is what we compare with the events measured by MAGIC and calculate the probability that this number of events measured is compatible with the assumed function. An example of the distribution of generated events together with the measured value can be seen in Fig. 6.14. In Table 6.3 we can find a summary of the results of the toy MC for energies above 34 TeV.

6.3.4 Flux Variability

As it was mentioned in Sect. 6.2.2, one could expect an increase of the TeV Crab Nebula flux during the flaring nights at GeV energies. Apart from the "flaring" sample mentioned in Sect. 6.3.2, we selected a "non-flaring" sample, taken several days before the flare under the same Zd of the flaring days. The results for the SED
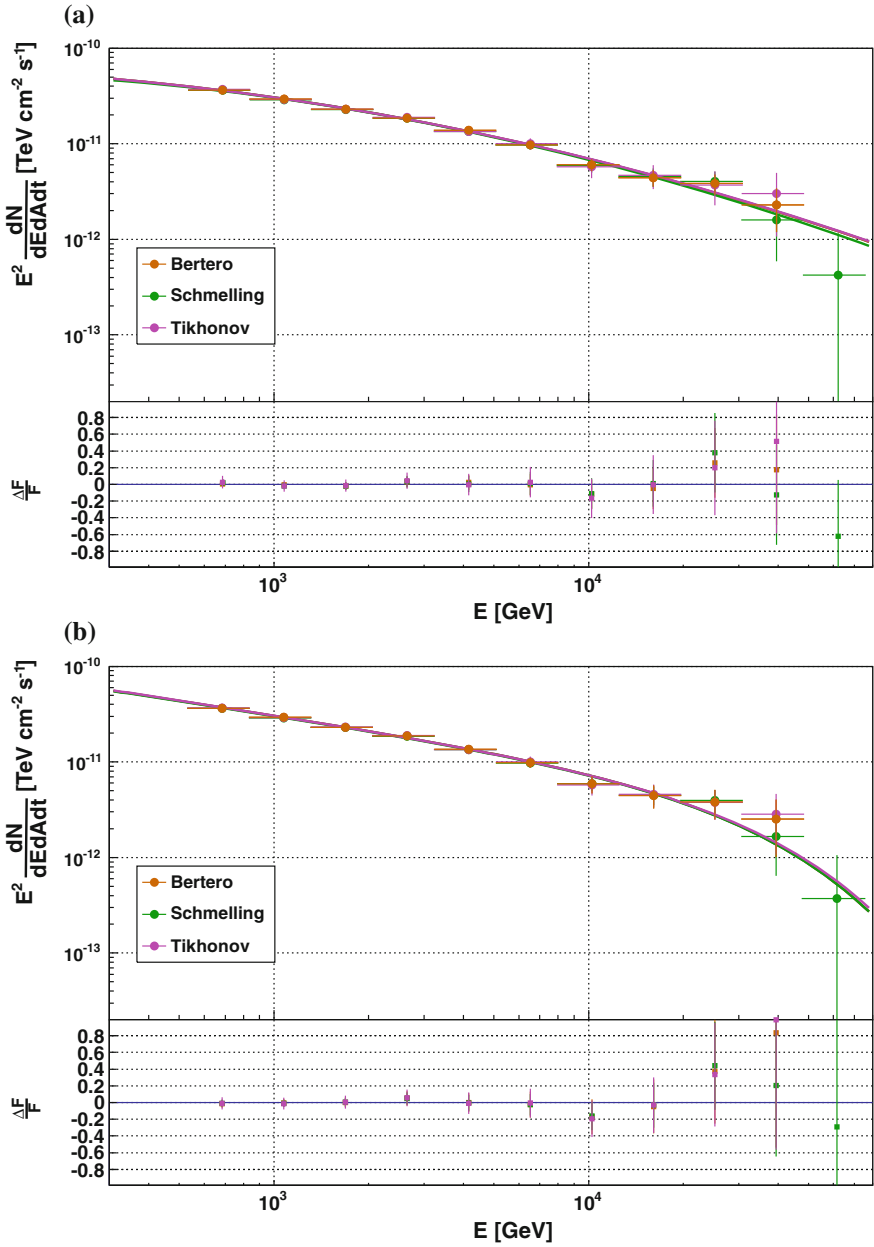
Fig. 6.12 Crab Nebula SED measured by MAGIC during observations at Zd > 50° using three different unfolding methods. Figure **a** shows the result for a log-parabola fit (*top panel*) and its residuals (*bottom panel*). Figure *b* shows the result for a power-law with a cut-off (*top panel*) and its residuals (*bottom panel*)

Table 6.2 Crab Nebula spectral fit parameters for the different unfolding methods and two different functions used to fit the results of the observations at Zd $> 50°$

Log-parabola fit					
Unfolding method	f_0 [TeV^{-1} cm^{-2} s^{-1}]	α	E_{cut} [TeV]	β	χ^2/NDF
Schmelling	$(3.03 \pm 0.04) \times 10^{-11}$	2.46 ± 0.04	–	-0.19 ± 0.04	3.52/8
Tikhonov	$(3.06 \pm 0.05) \times 10^{-11}$	2.47 ± 0.05	–	-0.17 ± 0.05	2.87/7
Bertero	$(3.06 \pm 0.04) \times 10^{-11}$	2.47 ± 0.04	–	-0.18 ± 0.04	2.38/7
Cut-off fit					
Schmelling	$(3.12 \pm 0.04) \times 10^{-11}$	2.49 ± 0.03	30 ± 8	–	5.27/8
Tikhonov	$(3.16 \pm 0.05) \times 10^{-11}$	2.50 ± 0.04	31 ± 11	–	5.69/7
Bertero	$(3.15 \pm 0.05) \times 10^{-11}$	2.49 ± 0.04	30 ± 10	–	5.54/7
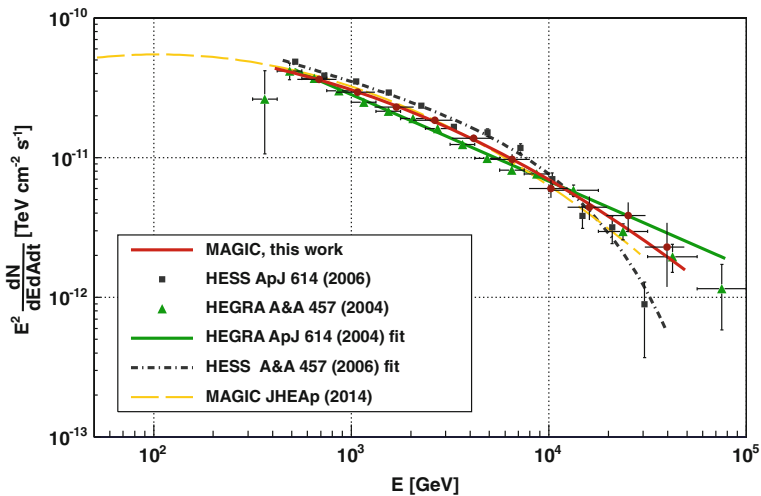
Fig. 6.13 Comparison between the published Crab Nebula SED from different experiments and the results reported in this work

of the "flaring" and "non-flaring" sample are shown in Fig. 6.15. Both curves are fit with a log-parabola function. A comparison of the fit parameters for the flaring and non-flaring days can be seen in Table 6.4. We can check that the results for all the parameters are compatible within statistical errors. The last spectral point is at ~ 15 TeV and it is also constant for both data samples.

We also studied the stability of the light curves above 1 and 10 TeV. We fit the daily integral flux of the flaring and non-flaring days. The fit above 1 TeV has a χ^2/Ndf $= 7.3/6$ and above 10 TeV has a χ^2/Ndf $= 6.7/6$, corresponding to a fit probability of 30 and 35 % respectively. The light curves above 1 and 10 TeV are shown in Fig. 6.16. The daily fluxes, the observation times and the results for the fits can be found in Table 6.5.
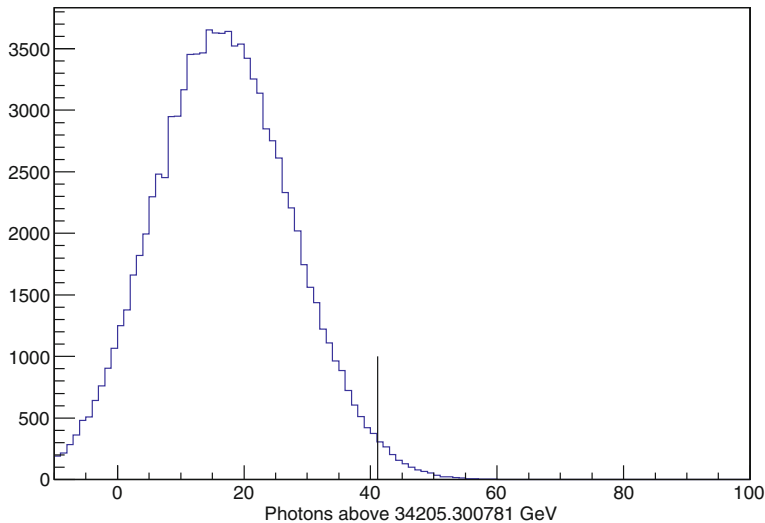
Fig. 6.14 Example of the toy MC distribution of events with energies above 34 TeV assuming the power-law with a cut-off from Aharonian et al. (2006). The *black line marks* the measured number of events on the MAGIC data. The probability of measuring this number of events, assuming that the power-law with a cut-off is the function that describes Crab Nebula data, is 1.4 % (color figure online)

Table 6.3 Results from the toy MC for $E > 34$ TeV assuming a power-law (HEGRA) and a power-law with a cut-off (HESS). We give the number of events measured by MAGIC above this energy, the mean expected number of events according to the toy MC, the probability that this measurement is compatible with the assumed function and the corresponding significance

Function assumed	$N_{\text{meas.}}$	$< N_{\text{exp.}} >$	Probability [%]	σ
HEGRA	41.1	30.94	26.5	1.12
HESS	41.1	16.84	1.4	2.45

Using the results of the fit for the flaring and non-flaring days, we compute the relative flux variation of the VHE data. Being F_{steady} the average flux for the non-flaring days and F_{flare} the average flux for the flaring days, the flux variation is given by:

$$\Delta F(E) = F_{\text{flare}}(E) - F_{\text{baseline}}(E) \tag{6.1}$$

Using the results from Table 6.5, the relative flux variation above 1 and 10 TeV is: $\Delta F/F_{\text{steady}}(E > 1 \text{ TeV}) = -0.07 \pm 0.04$ and $\Delta F/F_{\text{steady}}(E > 10 \text{ TeV}) = -0.22 \pm 0.18$. Using this relative flux variation, we can compute the UL on the flux of an additional component above 1 TeV and 10 TeV. If we assume that the relative flux change of the VHE component during flares has to be larger than 0, we can compute the 95 % C.L. Bayesian UL using the formula:
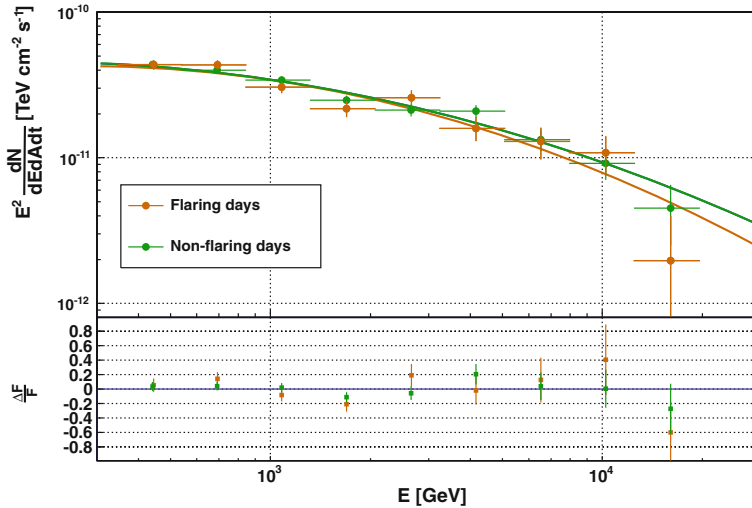
Fig. 6.15 Crab Nebula SED during flaring and non-flaring days. In *orange* we have the points and fit to the flaring days and in *green* we have the points and fit to the non-flaring ones. In the *lower panel* we find a plot of the fits residuals

Table 6.4 Crab Nebula fit parameters for flaring and non-flaring days

	f_0 [TeV^{-1} cm^{-2} s^{-1}]	α	β	χ^2/NDF
Non-flaring days	$(3.44 \pm 0.08) \times 10^{-11}$	2.34 ± 0.02	-0.23 ± 0.05	8.08/7
Flaring days	$(3.42 \pm 0.10) \times 10^{-11}$	2.34 ± 0.03	-0.30 ± 0.07	13.40/7
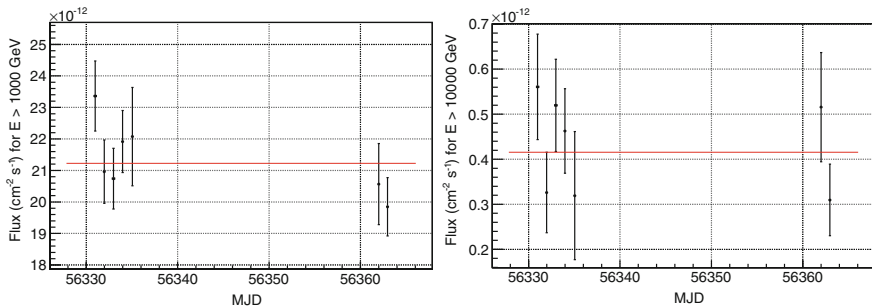
Fig. 6.16 Crab Nebula light curve for energies above 1 TeV (*left*) and 10 TeV (*right*) of the period before (MJD < 56340) and during the flaring period of March 2013 (MJD > 56360)

$$\frac{\int_0^{x_{95}} \exp\left(-\frac{(\Delta F_E/F_E - x)^2}{2\sigma^2}\right) dx}{\int_0^{\infty} \exp\left(-\frac{(\Delta F_E/F_E - x')^2}{2\sigma^2}\right) dx'} = 0.95 \qquad (6.2)$$

Table 6.5 Crab Nebula fluxes above 1 and 10 TeV for flaring and non-flaring days

State	Date	Duration of observation [s]	Flux ($E > 1$ TeV) [10^{-11} cm^{-2} s^{-1}]	Flux ($E > 10$ TeV) [10^{-13} cm^{-2} s^{-1}]
Steady	56330.99	10627.7	2.34 ± 0.11	5.6 ± 1.2
	56331.98	12179.6	2.10 ± 0.10	3.3 ± 0.9
	56332.98	12919.4	2.07 ± 0.10	5.2 ± 1.0
	56333.98	13037.0	2.19 ± 0.10	4.6 ± 0.9
	56335.05	3531.0	2.21 ± 0.16	3.2 ± 1.4
Flare	56362.00	4104.4	2.06 ± 0.13	5.2 ± 1.2
	56362.96	11154.1	1.98 ± 0.09	3.1 ± 0.8
	Fit non-flaring days		2.16 ± 0.05	4.5 ± 0.5
	Fit flaring days		2.01 ± 0.08	3.5 ± 0.7
	Fit all days		2.12 ± 0.04	4.2 ± 0.4

Table 6.6 95 % C.L. flux UL above 1 and 10 TeV for an extra component in the Crab Nebula spectrum during the March 2013 flare, expressed in absolute flux and relative to the steady Crab flux

Energy [TeV]	ΔF_E UL [%]	Flux UL [erg cm^{-2} s^{-1}]
>1	0.8	7.4×10^{-13}
>10	13.3	2.0×10^{-12}

where σ is the error in the determination of ΔF_E. x_{95} is obtained by solving Eq. 6.2 and gives the UL to the additional component above a given energy. The solving of the integrals contained in Eq. 6.2 is explained in Appendix A.3. The flux UL above an energy of 1 and 10 TeV are shown in Table 6.6.

6.4 Discussion and Conclusions

We tested different functions for the spectrum of the Crab Nebula in the energy range between 400 GeV and 80 TeV and we found that a single power-law does not provide a good description of the spectrum. Both log-parabola and power-law with a cut-off provide a good fit to the data, although the log-parabola provides a larger fit probability.

The measured spectrum is consistent with the measurement of HEGRA. The power-law with a cut-off gives a good description of MAGIC data in the energy range between 400 GeV and 80 TeV, but the cut-off energy is situated at an energy of 30 TeV, larger and not compatible within statistical errors with that measured by HESS. Using a toy MC and the MAGIC data, we can rule out HESS cut-off energy at a C.L. larger than 2σ.

If we compare this result with the models used to fit the Crab Nebula spectrum between 50 GeV and 30 TeV in Aleksić et al. (2014a), we find that both models overestimate the Crab Nebula emission at ∼TeV energies. We agree with the conclusion of the quoted paper that models have to be made more realistic to account for the broadband emission of the Crab Nebula.

Regarding the flux variability, we compare the daily light curve of the flaring days and the quasi-contemporaneous non-flaring days taken under the same conditions. We establish UL at the 95 % C.L. on the flux of an additional component at the level of $7.4 \times 10^{-13} \, \mathrm{erg} \, \mathrm{cm}^{-2} \, \mathrm{s}^{-1}$ above 1 TeV and $2.0 \times 10^{-12} \, \mathrm{erg} \, \mathrm{cm}^{-2} \, \mathrm{s}^{-1}$ above 10 TeV. A comparison of the spectra of the flaring and non-flaring days brings us to the same conclusion, having all the fit parameters the same results within the errors. If we assume that there is a linear correlation between the flare at MeV energies and a putative enhancement at TeV energies:

$$\Delta F_E \, [VHE] = C \, \Delta F_E \, [HE] \qquad (6.3)$$

where C is a constant. The combined photon flux above 100 MeV from the Crab Nebula and pulsar during the March 2013 flare is $F_{\mathrm{flare}} = (12.5 \pm 0.8) \times 10^{-6} \, \mathrm{cm}^{-2} \, \mathrm{s}^{-1}$ (Mayer et al. 2013), while the average nebula flux during the quiescence state is $F_{\mathrm{nebula}} = (6.1 \pm 0.2) \times 10^{-7} \, \mathrm{cm}^{-2} \, \mathrm{s}^{-1}$ and the average pulsar flux $F_{\mathrm{pulsar}} = (20.4 \pm 0.1) \times 10^{-7} \, \mathrm{cm}^{-2} \, \mathrm{s}^{-1}$ (Bühler and Blandford 2014). If we assume that the flare is produced by synchrotron emission in the nebula and we subtract the pulsar contribution to the nebula flare flux, we find that the relative increase of the Crab Nebula flux above 100 MeV is:

$$\Delta F_E \, [HE] = \frac{(F_{\mathrm{flare}} - F_{\mathrm{pulsar}}) - F_{\mathrm{nebula}}}{F_{\mathrm{nebula}}} = 17 \pm 3 \qquad (6.4)$$

Therefore, the UL on the linear correlation between the Crab Nebula flux above 100 MeV and above 1 TeV during flares at a 95 % C.L. is $C < 4.7 \times 10^{-4}$.

The flux UL above 1 and 10 TeV shown in Table 6.6 lead to UL on the luminosity of an extra component during the March 2013 flare above the aforementioned energies of $L_{(E > 1 \mathrm{TeV})} < 4 \times 10^{32} \, \mathrm{erg} \, \mathrm{s}^{-1}$ and $L_{(E > 10 \mathrm{TeV})} < 10^{33} \, \mathrm{erg} \, \mathrm{s}^{-1}$. Bednarek and Idec (2011) predict an increase larger than the UL reported in this work for several situations. According to their model, we can rule out magnetic fields larger than 40 mG in the flaring region because they would produce larger variations than measured. For lower magnetic fields and an injection of a new population of electrons with a change of their maximum energy together with a flattening of the spectrum, the prediction is also in conflict with the results we are reporting. We could argue that the magnetic field is significantly lower than 2 mG, although we have to note here that the magnetic field in the flaring region is given by the duration of the flare: the flaring time that an electron would emit synchrotron radiation is then:

$$t_{\mathrm{flare}} = 3 \times 10^5 \mathrm{s} \left(\frac{B}{\mathrm{mG}} \right)^{-1.5} \qquad (6.5)$$

for electrons emitting gamma rays at 200 MeV. If we consider that the duration of the flare was ∼2 weeks, then the magnetic field of the flaring region should be ∼8 mG. We can conclude that, in the framework of Bednarek and Idec (2011) model, we have to consider an injection of electrons with a change only in their maximum energy, that could account for the flaring component at HE and would not produce any measurable enhancement at TeV energies.

In the context of Kohri et al. (2012) model, as we do not detect any variability above 10 TeV, we rule out a Γ boost of the flaring blob $\gtrsim$100, which is the one they take for their fiducial model.

References

Abdo AA et al (2011) Science 331:739
Abramowski A et al (2014) A&A 562:L4
Aharonian F et al (2004) ApJ 614:897
Aharonian F et al (2006) A&A 457:899
Aielli G et al (2010) Astron Telegr 2921:1
Albats P et al (1972) Nature 240:221
Albert J et al (2007) Nucl Instrum Methods Phys Res A 583:494
Aleksić J et al (2012) A&A 540:A69
Aleksić J et al (2014a), arXiv:1406.6892
Aleksić J et al (2014b) A&A 565:L12
Aleksić J et al (2014c), arXiv:1409.5594
Aliu E et al (2008) Science 322:1221
Aliu E et al (2011) Science 334:69
Aliu E et al (2014) ApJ 781:L11
Amato E et al (2003) A&A 402:827
Atoyan AM et al (1996) MNRAS 278:525
Bartoli B et al (2012) Astron Telegr 4258:1
Bartoli B et al (2015) ApJ 798:119
Becerra J et al (2014) Astron Telegr 6401:1
Bednarek W et al (2003) A&A 405:689
Bednarek W et al (2011) MNRAS 414:2229
Browning R et al (1971) Nat Phys Sci 232:99
Buehler R et al (2010) Astron Telegr 2861:1
Buehler R et al (2012) ApJ 749:26
Bühler R et al (2014) Rep Prog Phys 77:066901
Buson S et al (2013) Astron Telegr 5485:1
Clark DH et al (1977) The historical supernovae. Pergamon Press, Oxford
Cerutti B et al (2012) ApJ 746:148
Cerutti B et al (2013) ApJ 770:147
Cocke WJ et al (1969) Nature 221:525
Comella JM et al (1969) Nature 221:453
de Jager OC et al (1992) ApJ 396:161
Duyvendak JJL (1942) PASP 54:91
Floyd FW et al (1969) Nature 224:50
Fritz G et al (1969) Science 164:709
Gasparrini D et al (2014) Astron Telegr 5971:1
Hester JJ (2008) ARA&A 46:127

Hillas AM et al (1998) ApJ 503:744
Ho PY et al (1962) Vistas Astron 5:127
Horns D et al (2006) A&A 451:L51
Hubble EP (1928) Leafl Astron Soc Pac 1:55
Kennel CF et al (1984a) ApJ 283:694
Klein O et al (1929) Z Angew Phys 52:853
Kohri K et al (2012) MNRAS 424:2249
Kurfess JD (1971) ApJ 168:L39
Lampland CO (1921) PASP 33:79
Lobanov AP et al (2011) A&A 533:A10
Lundmark K (1921) PASP 33:225
Lyne AG et al (1988) MNRAS 233:667
Mariotti M (2010) Astron Telegr 2967:1
Marsden PL et al (1984) ApJ 278:L29
Martín J et al (2012) MNRAS 427:415
Mayall NU et al (1942) PASP 54:95
Mayer M et al (2013) ApJ 775:L37
Meyer M et al (2010) A&A 523:A2
Ojha R et al (2012) Astron Telegr 4239:1
Ojha R et al (2013) Astron Telegr 4855:1
Ong RA (2010) Astron Telegr 2968:1
Smith N (2003) MNRAS 346:885
Sollerman J et al (2000) ApJ 537:861
Staelin DH et al (1968) Science 162:1481
Striani E et al (2013) ApJ 765:52
Sturrock P et al (2012) ApJ 751:L32
Tavani M et al (2010) Astron Telegr 2855:1
Tavani M et al (2011) Science 331:736
Trimble V (1973) PASP 85:579
Uzdensky DA et al (2011) ApJ 737:L40
Vernetto S (2013) arXiv:1307.7041
Vinyaikin EN (2007) Astron Rep 51:570
Weekes TC et al (1989) ApJ 342:379
Wilson-Hodge CA et al (2011) ApJ 727:L40
Zanin R (2014) V Fermi Symposium proceedings
Zweibel EG et al (2009) ARA&A 47:291

Chapter 7
The Puzzling PWN 3C 58

7.1 General Description

The SNR 3C 58 (SNR G130.7+3.1) has a flat radio spectrum and is brightest near the center, therefore it was classified as a PWN (Weiler and Panagia 1978). It is centered on PSR J0205+6449, a pulsar discovered in 2002 with the *Chandra* X-ray observatory (Murray et al. 2002). It was widely assumed that 3C 58 is located at a distance of 3.2 kpc (Roberts et al. 1993), but recent H I measurements suggest a distance of 2 kpc (Kothes 2013). The age of the system was estimated to be ∼2.5 kyr (Chevalier 2005) from the PWN evolution and energetics, however this is a matter of discussion that will be covered together with the distance estimation in Sect. 7.1.2. The pulsar has one of the highest spin-down powers known ($\dot{E} = 2.7 \times 10^{37}$ erg s^{-1}). The PWN has a size of $9' \times 6'$ in radio, infrared (IR), and X-rays (Bietenholz et al. 2001; Bocchino et al. 2001; Slane et al. 2004, 2008). Its X-ray luminosity is $L_{(0.5 - 10\,\text{keV})} = 2.4 \times 10^{34}$ erg s^{-1}, which is more than 3 orders of magnitude lower than that of the Crab Nebula (Torii et al. 2000). 3C 58 has been compared with the Crab because the jet-torus structure is similar (Slane et al. 2004). Because of these morphological similarities with the Crab Nebula and its high spin-down power (5 % of Crab), 3C 58 has historically been considered one of the PWNe most likely to emit gamma rays.

The pulsar J0205+6449 has a period $P = 65.68$ ms, a spin-down rate $\dot{P} = 1.93 \times 10^{-13}$ s s^{-1}, and a characteristic age of 5.38 kyr (Murray et al. 2002). Pulsed gamma rays where first detected by the *Fermi*-LAT. The measured energy flux is $F_{\gamma(E>0.1\,\text{GeV})} = (5.4 \pm 0.2) \times 10^{-11}$ erg cm^{-2} s^{-1} with a luminosity of $L_{\gamma(E>0.1\,\text{GeV})} = (2.4 \pm 0.1) \times 10^{34}$ erg s^{-1}, assuming a distance for the pulsar of 1.95 kpc (Xu et al. 2006). The spectrum is well described by a power-law with an exponential cutoff at $E_{\text{cutoff}} = 1.6$ GeV (Abdo et al. 2013). No pulsed emission was detected at energies above 10 GeV (Ackermann et al. 2013). In the off-peak region, defined as the region between the two γ-ray pulsed peaks (off-peak phase interval $\phi = 0.64 - 0.99$), the Fermi Collaboration reported the detection of emission from 3C 58 (Abdo et al. 2013). The reported energy flux is $(1.75 \pm 0.68) \times 10^{-11}$ erg cm^{-2} s^{-1} and the

differential energy spectrum between 100 MeV and 316 GeV is well described by a power-law with photon spectral index $\Gamma = 1.61 \pm 0.21$. No hint of spatial extension was reported at those energies. The association of the high-energy unpulsed steady emission with the PWN is favored, although an hadronic origin related to the associated SNR can not be ruled out. 3C 58 was tagged as a potential TeV γ-ray source by the Fermi Collaboration (Ackermann et al. 2013).

The PWN 3C 58 was previously observed in the VHE γ-ray range by several IACTs. The Whipple telescope reported an integral flux upper limit of $1.31 \times 10^{-11}\,\mathrm{cm}^{-2}\,\mathrm{s}^{-1}$ $\sim$19 % C.U. at an energy threshold of 500 GeV (Hall et al. 2001), and VERITAS established upper limits at the level of 2.3 % C.U. above an energy of 300 GeV (Aliu 2008). MAGIC-I observed the source in 2005 and established integral upper limits above 110 GeV at the level of $7.7 \times 10^{-12}\,\mathrm{cm}^{-2}\,\mathrm{s}^{-1}$ ($\sim$4 % C.U.) (Aliu 2007; Anderhub et al. 2010). The improved sensitivity of the MAGIC telescopes with respect to previous observations and the *Fermi*-LAT results motivated us to perform deep VHE observations of the source.

Fig. 7.1 Historical record of the SN event in 1181 AD in the *Wenxian Tongkao*. Image taken from Green and Stephenson (2003)

時虜使久在館至是乃夫

不見自去年六月己巳至是凡一百八十五日乃消伏

儀甲戌客星守傳舍第五星　九年正月癸酉客星始

奎宿爲兵姦臣僞惑天子於是金虜遣使來爭執進書

客星出紫微外座傳舍星宜備姦使邊夷侵境又云出

舍以示休咎星大者事大而禍深色白其分有兵喪今

傳舍占客星亦妖星天之使者見於天而無常所入列

八年六月己巳客星出奎宿犯

7.1.1 SN 1181 AD

The new star of AD 1181, which was extensively observed in both China and Japan, was seen for fully six months (Fig. 7.1). Such a lengthy duration of visibility in the various historical records is indicative of a SN. There are three Chinese records of the new star of AD 1181, from both the North (Jin) and South (Song) Chinese empires in existence at that time, and five Japanese accounts. None of these sources report any motion of the star. The most detailed surviving Chinese account of the guest star is found in the *Wenxian Tongkao* (Comprehensive study of civilization), an extensive work compiled around AD 1280. According to Chinese positional records, the guest star was "guarding the fifth star of the *Chuanshe* asterism". Regarding that the fifth star of the *Chuanshe* asterism is identified with SAO 12076 (Jinyu 1983, galactic coordinates $l \simeq 130°$, $b \simeq 3°$), this position is close to the position of 3C 58. Since the position of 3C 58 is situated in the same region and it hosts one of the largest spin-down power pulsars in the galaxy, it is believed to be the remnant of the SN of 1181 AD (SN 1181; Stephenson and Green 2002).

7.1.2 Distance and Age

In spite of the positional coincidence, there are several arguments against the SN 1181 and 3C 58 association, giving to the SNR an age between 2.4 to 7 kyr (Chevalier 2005; Bietenholz 2006). Chevalier (2004; 2005), calculated that the minimum energy necessary to produce the synchrotron emission is higher than the total energy released by the pulsar. The observed PWN size is larger than the expected for a PWN expanding into a normal SN for ∼800 yr. The mass ejected is also smaller than the expected from X-ray observations. All these problems were solved assuming an age of 2.4 kyr. Velocity measurements of the optical knots give an age estimation of 3–4 kyr (Fesen et al. 2008). Gotthelf et al. (2007) measured the proper motion of the pulsar and estimated an age of 3.75 kyr for a transversal velocity similar to that of Crab. According to NS cooling models, the UL to the thermal emission measured for 3C 58 is well below the expected temperature from standard cooling models and indicates an age for the system ≫5 kyr. Slane et al. (2002) proposed that the explanation for such a low surface temperature is either some exotic cooling mechanisms acting in the NS or that the object is made of exotic matter, such as quarks (Weber 2005). The measurement of the radio expansion rate suggests an age of 7 kyr (Bietenholz 2006). The peak brightness of the SN explosion and the mass ejected in it are also too low to associate the object with the SN of 1181, unless the SN explosion were much lower than the canonical 10^{51} erg (Chevalier 2004). Apart from all these estimations based on different measurements, the pulsar characteristic age τ can be calculated with Eq. 5.6, leading to a characteristic age $\tau = 5390$ yr (Murray et al. 2002). This is nevertheless not a good measurement of its real age for young pulsars because they might have not significantly spun down. To sum up, there are several evidences

based on different observations at several wavelength that point to an age for 3C 58 larger than ∼830 yr.

All these age estimations are closely associated to the estimated distance to the PWN. 3C 58 distance is widely considered to be 3.2 kpc, determined from H I measurements (Roberts et al. 1993). Nonetheless, there has recently been a deep study of newer H I data that claims a closer distance to the source. Based on H I data from the Canadian Galactic Plane Survey and recent distances measured to close objects, Kothes (2013) claims a distance of (2.0 ± 0.3) kpc to 3C 58, which is compatible with the measured distance to PSR J0205+6449. This new distance, if correct, would change all the considerations about the age previously made in this section. In Table 1 of Kothes (2013), one can find a summary of the age evaluation using the different measurements and assuming a distance of 2 kpc. From his results, the assumption of 830 yr is the most supported by the different observational results. In summary, the estimates of age and distance are entangled and the real values are controversial.

7.2 MAGIC Observations and Results

MAGIC observed 3C 58 in the period between 4 August 2013 to 5 January 2014 for 99 hours. After quality cuts, 81 hours of the data were used for the analysis. A breakdown of the MAGIC observations can be found in Appendix B.4, Table B.6. The source was observed at Zd between 36° and 52°. The data were taken in *wobble-mode* (Fomin et al. 1994) pointing at four different positions situated 0.4° away from the source to evaluate the background simultaneously with 3C 58 observations.

7.2.1 Search for Steady Emission

The analysis was performed using the analysis pipeline described in Sect. 2.2.3. As the source was weak and standard cuts are not optimized for detecting weak sources, we optimized the cut parameters for detecting a 1 % C.U. point-like source on an independent Crab Nebula data sample at the same Zd range by maximizing the Li and Ma significance shown in Eq. 2.13. The cuts selected for the analysis were: θ^2 angle $<0.01 \deg^2$, hadronness <0.18, and size in both telescopes >300 phe. The SED was finally unfolded using all the methods described in Sect. 2.2.3.10. The unfolded spectrum using all the methods was compatible within statistical errors. We give the results of the unfolded spectrum using the Schmelling method, which is the one providing the lowest χ^2.

The applied cuts and the Zd of the observations yield an energy threshold of 420 GeV. The significance of the signal, calculated with Eq. 2.13, is 5.7σ, which establishes 3C 58 as a γ-ray source. The θ^2 distribution is shown in Fig. 7.2. As the five OFF positions were taken for each of the wobble positions, the OFF histograms were re-weighted depending on the time taken on each wobble position.
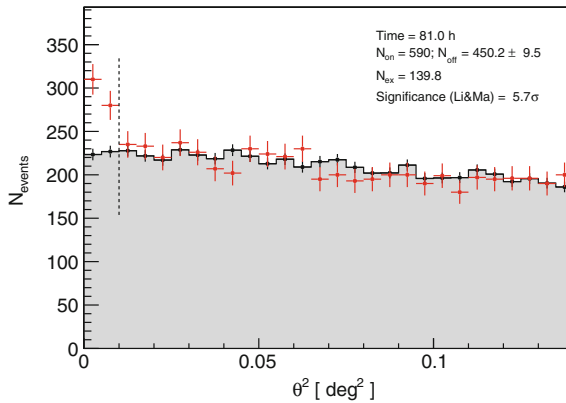
Fig. 7.2 Distribution of squared angular distance, θ^2, between the reconstructed arrival directions of gamma-ray candidate events and the position of PSR J0205+6449 (*red points*). The distribution of θ^2 for the OFF positions is also shown (*gray filled histogram*). The *vertical dashed line* defines the signal region ($\theta^2_{cut} = 0.01 \, \text{deg}^2$), N_{on} is the number of events in the source region, N_{off} is the number of background events, estimated from the background regions and $N_{ex} = N_{on} - N_{off}$ is the number of excess events. Credit: Aleksić et al. (2014b), reproduced with permission © ESO (color figure online)

We show in Fig. 7.3 the relative flux (excess/background) skymap, produced using the same cuts as for the θ^2 calculation. The TS significance, which is the Li and Ma significance applied on a smoothed and modeled background estimate, is higher than 6 at the position of the pulsar PSR J0205+6449. The excess of the VHE skymap was fit with a Gaussian function. The best-fit position is RA(J2000) = 2 h 05 m 31(09)$_{stat}$(11)$_{sys}$ s; DEC (J2000) = 64° 51′(1)$_{stat}$(1)$_{sys}$. This position is statistically deviant by 2σ from the position of the pulsar, but is compatible with it if systematic errors are taken into account. In the bottom left of the image we show the PSF of the smeared map at the corresponding energies, which is the result of the sum in quadrature of the instrumental angular resolution and the applied smearing, resulting in 4.7′ radius, at the analysis energy threshold. The extension of the signal is compatible with the instrument PSF. The VLA contours are coincident with the detected γ-ray excess.

Figure 7.4 shows the energy spectrum for the MAGIC data, together with published predictions for the gamma-ray emission from several authors, and two spectra obtained with three years of *Fermi*-LAT data, which were retrieved from the *Fermi*-LAT second pulsar-catalog (2PC, Abdo et al. 2013) and the first *Fermi*-LAT high-energy catalog (1FHL, Ackermann et al. 2013). The 1FHL catalog used events from the *Pass 7 Clean class*, which provides a substantial reduction of residual cosmic-ray background above 10 GeV, at the expense of a slightly smaller collection area, compared with the *Pass 7 Source class* that was adopted for 2PC (Ackermann et al. 2012). The two γ-ray spectra from 3C 58 reported in the 2PC and 1FHL catalogs agree within statistical uncertainties. The differential energy spectrum of the source is well fit by a single power-law function $\mathrm{d}\phi/\mathrm{d}E = f_0(E/1\,\text{TeV})^{-\Gamma}$
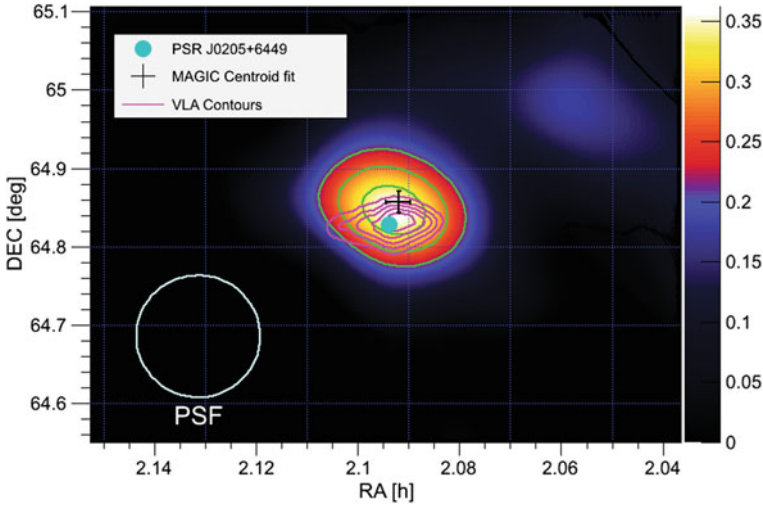
Fig. 7.3 Relative flux (excess/background) map for MAGIC observations. The *cyan circle* indicates the position of PSR J0205+6449 and the *black cross* shows the fitted centroid of the MAGIC image with its statistical uncertainty. In *green* we plot the contour levels for the TS starting at 4 and increasing in steps of 1. The *magenta contours* represent the Very Large Array (VLA) flux at 1.4 GHz (Condon et al. 1998), starting at 0.25 Jy and increasing in steps of 0.25 Jy. Credit: Aleksić et al. (2014b), reproduced with permission © ESO

with $f_0 = (2.0 \pm 0.4_{\mathrm{stat}} \pm 0.6_{\mathrm{sys}})10^{-13}$ cm^{-2}s^{-1}TeV^{-1}, $\Gamma = 2.4 \pm 0.2_{\mathrm{stat}} \pm 0.2_{\mathrm{sys}}$ and $\chi^2 = 0.04/2$. The systematic errors were estimated from the MAGIC performance paper (Aleksić et al. 2014a). The integral flux above 1 TeV is $F_{\gamma(E>1\,\mathrm{TeV})} = 1.4 \times 10^{-13}$ cm^{-2}s^{-1}. Taking into account a distance of 2 kpc, the luminosity of the source above 1 TeV is $L_{\gamma(E>1\,\mathrm{TeV})} = (3.0 \pm 1.1) \times 10^{32} d_2^2$ erg s^{-1}, where d_2 is the distance normalized to 2 kpc.

7.2.2 Search for Pulsed Emission

The search for VHE pulsed emission from PSR J0205+6449 was performed using *psearch*, a program for pulsar timing analysis that corrects the arrival times to the solar system barycenter in the framework of MARS (López 2006). The ephemeris used was provided by the *Fermi*-LAT collaboration for contemporaneous data and tested on the satellite's data to check it. The cuts applied to the data were the same as the ones mentioned in Sect. 7.2. In principle, pulsed VHE emission is not expected at energies >420 GeV according to the non-detection of pulsed γ-ray photons above 4 GeV reported by *Fermi*-LAT. Nevertheless, as it was mentioned in Sect. 5.3.1, there are models predicting a scenario with a second component due to IC in the spectrum of the pulsed signal from the Crab Nebula.
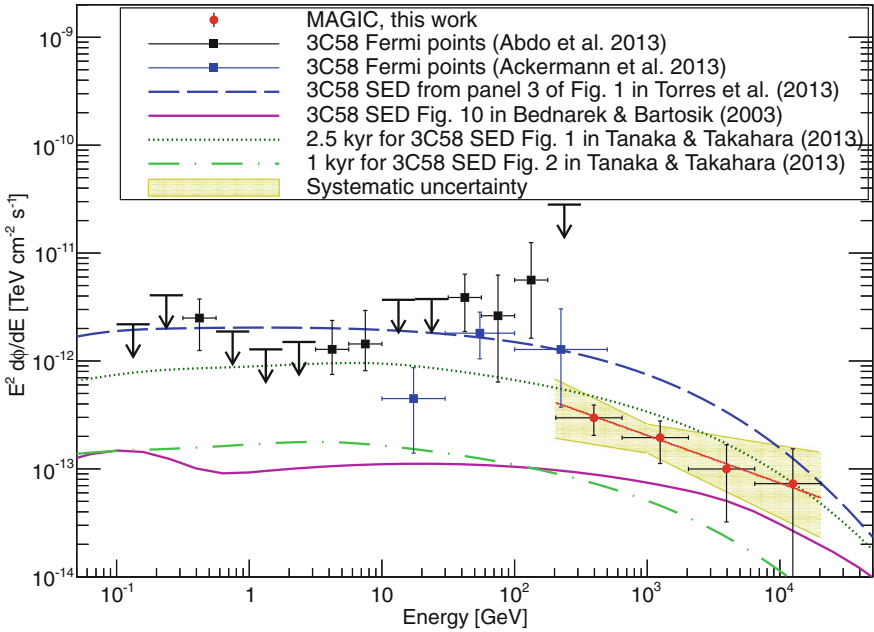
Fig. 7.4 3C 58 spectral energy distribution in the range between 0.1 GeV and 20 TeV. *Red circles* are the VHE points reported in this work. The best-fit function is drawn in red and the systematic uncertainty is represented by the *yellow shaded area*. *Black squares* and *black arrows* are taken from the 2PC (Abdo et al. 2013). *Blue squares* are taken from the 1FHL (Ackermann et al. 2013). The *magenta line* is the SED prediction for 3C 58 taken from Fig. 10 of Bednarek and Bartosik (2003). The *clear green dashed-dotted line* is the SED predicted by Tanaka and Takahara (2013), assuming an age of 1 kyr, and the *dark green dotted line* is the prediction from the same paper, assuming an age of 2.5 kyr. The *blue dashed line* represents the SED predicted by Torres et al. (2013) assuming that the Galactic FIR background is high enough to reach a flux detectable by the MAGIC sensitivity in 50 h. Credit: Aleksić et al. (2014b), reproduced with permission © ESO

Fig. 7.5 PSR J0205+6449 phaseogram above 420 GeV. Two periods are shown for clarity
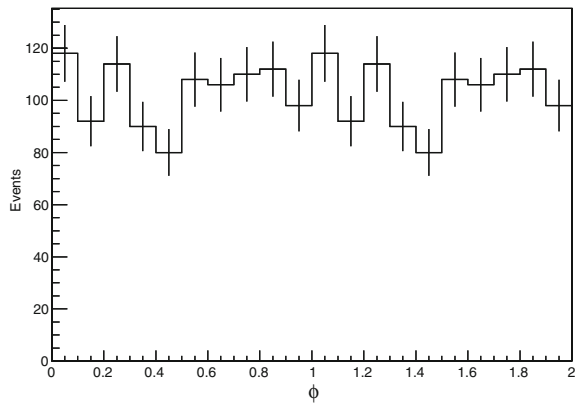
The phaseogram for the position of PSR J0205+6449 can be seen in Fig. 7.5. No significant pulsed emission was found from the whole dataset. We calculate the UL with a 95 % C.L. using the method presented in de Jager (1994). The UL for the pulsed emission above 420 GeV is $F_{\text{pulsed}} < 1.3 \times 10^{-13} \, \text{cm}^{-2} \, \text{s}^{-1}$.

7.3 Discussion

7.3.1 Comparison with Models

There are several models that predict detectable VHE γ-ray emission from PWN 3C 58. Bucciantini et al. (2011) presented a one zone model of the spectral evolution of PWNe and applied it to 3C 58 using a distance of 3.2 kpc. The VHE emission in this model is produced by IC scattering of CMB photons and optical-to-IR photons, and by pion decay. They derive a nebula in equipartition where total energy is not conserved. The flux of gamma rays above 400 GeV predicted by this model is about an order of magnitude lower than the observation.

Bednarek and Bartosik (2003) proposed a time-dependent model in which positrons gain energy in the process of resonant scattering by heavy nuclei. The VHE emission is produced by IC scattering of leptons off CMB, IR, and synchrotron photons and by the decay of pions due to the interaction of nuclei with the matter of the nebula. The age of 3C 58 is assumed to be 5 kyr, using a distance of 3.2 kpc and an expansion velocity of 1000 km s^{-1}. According to this model, the predicted integral flux above 400 GeV is $\sim 10^{-13} \, \text{cm}^{-2} \, \text{s}^{-1}$, while the integral flux above 420 GeV measured here is $5 \times 10^{-13} \, \text{cm}^{-2} \, \text{s}^{-1}$. Calculations by Bednarek and Bartosik (2005), using the same model with an initial expansion velocity of 2000 km s^{-1} and considering IC scattering only from the CMB, are consistent with the observed spectrum. However, the magnetic field derived in this case is $B \sim 14 \, \mu$G and it underestimates the radio emission of the nebula, although a more complex spectral shape might account for the radio nebula emission.

Tanaka and Takahara (2010) developed a time-dependent model of the spectral evolution of PWNe. They consider the PWN as a freely expanding sphere at a constant velocity, a reasonable assumption for a young PWN. The spectrum of the injected electrons is a broken power-law normalized using the magnetic fraction and spin-down power of the pulsar. The magnetic field is calculated using the conservation of the magnetic field energy. For the particle evolution, they solved the time-dependent diffusion-loss equation including the cooling effect of synchrotron, IC and adiabatic expansion, but ignoring particle escape. For the spectral evolution of the PWN, they considered synchrotron radiation, IC and SSC. To calculate the observability of 3C 58 at TeV energies they assumed a distance of 2 kpc and two different ages: 2.5 and 1 kyr (Tanaka and Takahara 2013). For the IC scattering they consider CMB and optical-to-IR photons as a target photon fields. The photon density for the optical and IR photons is assumed to be 0.3 eV/cm^3. For an age of 2.5 kyr, they obtained a magnetic

field $B \geq 17\,\mu G$, while for an age of 1 kyr, they obtained $B = 40\,\mu G$. The emission predicted by this model for an age of 2.5 kyr is close to the MAGIC result shown in this thesis, and the measurement of *Fermi*-LAT.

Martín et al. (2012) presented a different time-dependent leptonic model without making any approximations in the diffusion-loss equation. They include in the calculation of the emitted spectrum synchrotron, SSC, IC, and bremsstrahlung. The evolution of the magnetic field and the spectrum of the injected electrons is similar to that assumed by Tanaka and Takahara (2010). They assumed a distance of 3.2 kpc and an age of 2.5 kyr (Torres et al. 2013). The predicted emission, without considering any additional photon source other than the CMB, is more than an order of magnitude lower than the flux reported here. It can account for the VHE flux measured by MAGIC for an FIR-dominated photon background with an energy density of 5 eV/cm^3. This would be more than one order of magnitude higher than the local IR density in the Galactic background radiation model used in GALPROP ($\sim$0.2 eV cm^{-3}; Porter et al. 2006). The magnetic field derived from this model is 35 μG. To reproduce the observations, a large FIR background or a revised distance to the PWN are required. In the first case, a nearby star or the SNR itself might provide the necessary FIR targets, although there is no evidence for an enhancement in the direction of the PWN. As we mentioned in Sect. 7.1, a distance of 2 kpc has recently been proposed by Kothes (2013) based on the recent H I measurements of the Canadian Galactic Plane Survey. At this distance, a lower photon density is required to fit the VHE data (Torres et al. 2014, priv. comm.).

We have shown different time-dependent models in this section that predict the VHE emission of 3C 58. The SEDs predicted by them are shown in Fig. 7.4. They use different assumptions for the evolution of the PWN and its emission. Bucciantini et al. (2011) divided the evolution of the SNR into phases and modeled the PWN evolution inside every of them. The model fits the synchrotron part of the spectrum, but it has to assume a non-conservation of the total energy of the nebula. In Bednarek and Bartosik (2003) model, nuclei play an important role in accelerating particles inside the PWN and they also contribute to the VHE radiation through pion decay. It manages to fit the spectrum for energies higher than X-rays under certain assumptions, but they are not able to fit the synchrotron radio emission.

Tanaka and Takahara (2010) and Torres et al. (2013) modeled the evolution of the particle distribution by solving the diffusion-loss equation, but Tanaka and Takahara (2010) neglected an escape term in the equation as an approximation and Torres et al. (2013) fully solved it. Another difference between these two models is that Torres et al. (2013) included bremsstrahlung into their model, while Tanaka and Takahara (2010) did not. The differences in their predictions come mainly from the distance, target photon fields assumed and the magnetic fractions.

The models that fit the γ-ray data derive a low magnetic field, far from equipartition, very low for a young PWN, but comparable with the value derived by Slane et al. (2008) using other data. In Torres et al. (2014), they applied their model to several TeV detected PWNe. They found that all the PWNe detected at TeV energies have magnetic fields below equipartition (magnetic fraction η <0.5). This means that either only PWNe with low magnetic fraction emit in TeV at the reach of the current

IACTs and we have an observational bias, or that this is a common characteristic among all PWNe and the assumption of equipartition inside the nebula is wrong.

7.3.2 VHE Luminosity in the Context of All VHE PWNe

Mattana et al. (2009) performed a study of how the X-ray (L_X) and VHE γ-ray (L_γ) luminosities of PWNe and PWN candidates compare with parameters of the central pulsar as the spin-down luminosity ($\dot{E}$) or the characteristic age (τ). In the paper they assumed that the electrons emitting in X-rays and in gamma rays are in the cool and uncool regimes, respectively. The population of cooled and uncooled particles in this regime is given by:

$$n_{\rm c}(E, t) \propto \int_{t-t_c}^{t} \dot{E}(t') dt' = \frac{\dot{E}_0 t_{\rm dec}^2 t_{\rm c}}{(t - t_{\rm c} + t_{\rm dec})(t + t_{\rm dec})} \tag{7.1}$$

$$n_{\rm u}(E, t) \propto \int_{0}^{t} \dot{E}(t') dt' = \dot{E}_0 t_{\rm dec} \left(\frac{t}{t + t_{\rm dec}} \right) \tag{7.2}$$

where $n_{\rm c}$ is the number of cooled particles, $n_{\rm u}$ is the number of uncooled particles, $\dot{E}_0$ is the initial spin-down luminosity of the pulsar, $t_{\rm dec} \sim 100 - 1000\,$yr is a characteristic decay time and $t_{\rm c}$ the cooling time. For $t \gg t_{\rm dec}$, the population of uncooled electrons becomes constant: $n_{\rm u} \propto \dot{E}_0 t_{\rm dec}$. If we are in this regime, the VHE γ-ray luminosity of the PWNe is constant and only depends on the initial spin-down power of the pulsar and $t_{\rm dec}$. For $t \gg max(t_{\rm dec}, t_{\rm c})$, the population of cooled electrons is: $n_{\rm c} \propto \dot{E}_0 t_{\rm dec}^2 t_{\rm c} t^{-2} \propto \dot{E} t_{\rm c}$. This means that the X-ray luminosity of PWNe in this regime should be proportional to $\dot{E}$ and inversely proportional to t^{-2}. In their phenomenological studies, Mattana et al. (2009) found a correlation between the L_X and the $\dot{E}$ and an anti-correlation of the ratio between gamma and X-ray luminosities (L_γ/L_X) and the $\dot{E}$. Comparing with the τ of the central pulsar, they found that the X-ray luminosity is anti-correlated with τ and the ratio L_γ/L_X correlated with it. They explicitly mention 3C 58 as a probable outlier from the aforementioned correlations due to its low magnetic field, that would prevent X-ray emitting electrons to reach the cooled regime.

We performed a study similar to that of Mattana et al. (2009), including the PWNe and PWN candidates detected afterwards. We have computed the L_γ in the range between 1 and 10 TeV, and L_X in the range between 2 and 10 keV. All the PWN parameters used for the study can be found in Table B.9 in Appendix B.5. In the plots, we highlight the results for the two PWNe studied in this thesis: the Crab Nebula and 3C 58.

In the top panel of Fig. 7.6, a plot of L_γ as a function of $\dot{E}$ is shown. We also show lines corresponding to a fixed $L_\gamma/\dot{E}$, which is a measure of the efficiency of the PWN to convert the rotational energy of the central pulsar into VHE γ-ray emission. We find

Fig. 7.6 VHE γ-ray
luminosity between 1 and
10 TeV (*top panel*), X-ray
luminosity between 2 and
10 keV (*middle panel*) and
ratio between luminosities
(*bottom panel*) of PWNe and
PWN candidates as a
function of the spin-down
power of the central pulsar
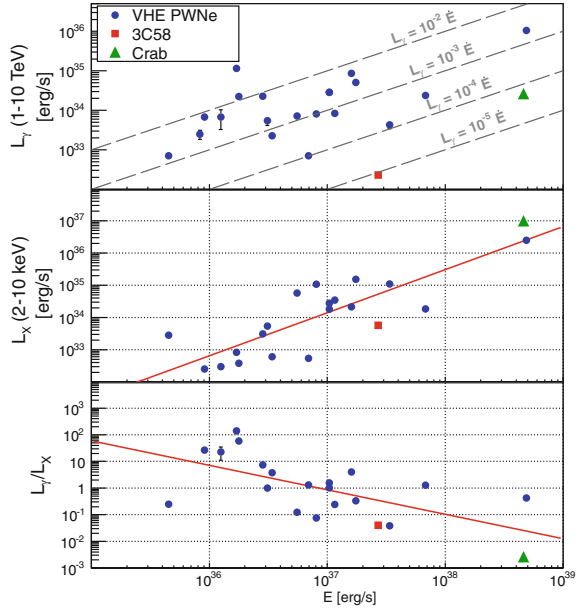
Fig. 7.7 VHE γ-ray
luminosity histogram of
PWNe and PWN candidates
detected at VHE gamma
rays. The *red line*
corresponds to a gaussian fit
to the histogram (color figure
online)
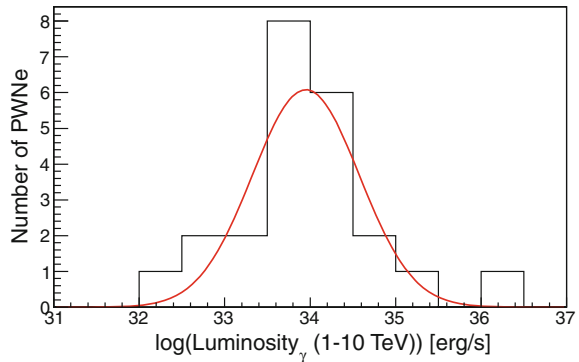
that 3C 58 is the least luminous and the most inefficient PWN converting rotational
energy into gamma rays of the detected PWNe and PWN candidates at VHE gamma
rays. The next most inefficient PWN transforming rotational energy into VHE γ-ray
emission is the Crab Nebula. Figure 7.7 shows the histogram of the logarithm of the
VHE γ-ray luminosities in the range between 1 and 10 TeV for all these PWNe.
The VHE γ-ray luminosity should be constant and only dependent on $\dot{E}_0$ and $t_{\rm dec}$
of the central pulsar. The distribution is fit by a gaussian with $\mu = 33.95 \pm 0.17$
and $\sigma = 0.6 \pm 0.3$. The luminosity of 3C 58 is deviated 2.6σ from the mean of the
distribution.

The middle and bottom plots of Fig. 7.6 represent L_X and L_γ/L_X as a function of the $\dot{E}$ respectively. We find L_X and L_γ/L_X to be correlated and anti-correlated with $\dot{E}$ respectively, similarly as in Mattana et al. (2009). The best-fit relation between L_X and $\dot{E}$ is given by:

$$\log_{10} L_X = (-15 \pm 7) + (1.33 \pm 0.19) \log_{10} \dot{E} \qquad (7.3)$$

and $\chi^2/\mathrm{Ndf} = 9.0/19$. We can compare this quantities with the ones obtained by Possenti et al. (2002) in the $0.1 - 2.4\,\mathrm{keV}$ band: $\log_{10} L_X = (-14.36 \pm 0.01) + (1.34 \pm 0.03) \log_{10} \dot{E}$, with a very similar result as the one obtained in this work. Kargaltsev and Pavlov (2008) obtained in the energy range between 0.5 and 8 keV the relation $\log_{10} L_X = (-20.00 \pm 0.05) + (1.46 \pm 0.04) \log_{10} \dot{E}$, whose slope is also compatible with the result obtained in this work. Mattana et al. (2009) obtained in the energy range between 2 and 10 keV the relation $\log_{10} L_X = (-35.39 \pm 0.04) + (1.87 \pm 0.04) \log_{10} \dot{E}$, showing a softer correlation than the one obtained in this work in the same energy range. The relation between L_γ/L_X and $\dot{E}$ is:

$$\log_{10} L_\gamma/L_X = (34 \pm 9) - (0.9 \pm 0.3) \log_{10} \dot{E} \qquad (7.4)$$

with $\chi^2/\mathrm{Ndf} = 16.3/20$. Mattana et al. (2009) derived the relation $\log_{10} L_\gamma/L_X = (69.66 \pm 0.04) - (1.87 \pm 0.07) \log_{10} \dot{E}$, using the same energy range for the X-ray analysis as mentioned before and the range between 1 and 30 TeV for the γ-ray luminosity. The relation obtained in this work is not compatible with that obtained in Eq. 7.4. The different offset might come from the different energy ranges used when deriving both relations, but the difference in slope only comes from the additional data added to the sample.

As we can check in Fig. 7.6, in spite of its low luminosity, 3C 58 does not constitute an outlier of the relation between luminosities and the $\dot{E}$, meaning the the assumption that the X-ray electrons are already cooled also applies for this nebula. In spite of not being an outlier, in the middle plot of Fig. 7.6, we can see that L_X of 3C 58 is lower than the fit, making it into an inefficient source transforming rotational energy into X-rays.

In the top panel of Fig. 7.8, we show L_γ as a function of τ, two quantities that are not correlated. In the middle and bottom panels of Fig. 7.8 we show L_X and L_γ/L_X as a function of the $\dot{E}$. We find L_X and L_γ/L_X to be anti-correlated and correlated with τ respectively, similarly as in Mattana et al. (2009). The relation between L_X and τ is given by:

$$\log_{10} L_X = (40.9 \pm 1.4) - (1.7 \pm 0.3) \log_{10} \tau \qquad (7.5)$$

with $\chi^2/\mathrm{Ndf} = 14.3/20$. Kargaltsev and Pavlov (2008) found in the energy range between 0.5 and 8 keV the relation $\log_{10} L_\gamma/L_X = (42.41 \pm 0.01) - (2.03 \pm 0.01) \log_{10} \tau$, compatible with the results derived in this work. Mattana et al. (2009) derived the relation $\log_{10} L_\gamma/L_X = (43.66 \pm 0.04) - (2.49 \pm 0.06) \log_{10} \tau$, again softer than the relation obtained in this work. The relation between L_γ/L_X and τ is:

Fig. 7.8 VHE γ-ray luminosity between 1 and 10 TeV (*top panel*), X-ray luminosity between 2 and 10 keV (*middle panel*) and ratio between them (*bottom panel*) of PWNe and PWN candidates as a function of the characteristic age of the central pulsar
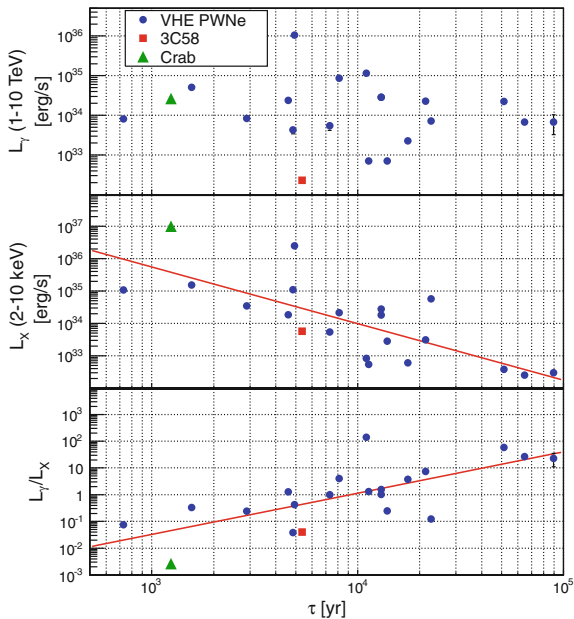
$$\log_{10} L_\gamma/L_X = (-5.9 \pm 1.4) + (1.5 \pm 0.3) \log_{10} \tau \tag{7.6}$$

with $\chi^2/\text{Ndf} = 14.4/20$. The relation in Mattana et al. (2009) is $\log_{10} L_\gamma/L_X = (-8.14 \pm 0.06) + (2.21 \pm 0.09) \log_{10} \tau$, not compatible again with that derived in this work.

3C 58 is not an outlier of the aforementioned correlations. We would like to note, however, that 3C 58 has lower L_X and lower L_γ/L_X than the one derived from the fits, meaning that its efficiency transforming rotational energy into EM emission is lower than the average.

Let us compare the results of the fit for the ratios between L_γ/L_X as a function of $\dot{E}$ and τ, as it is done in Mattana et al. (2009). From the fits shown in Eqs. 7.4 and 7.6 we derive that $L_\gamma/L_X \propto \dot{E}^{-0.9\pm0.3}$ and $L_\gamma/L_X \propto \tau^{1.5\pm0.3}$. According to Eqs. 7.1 and 7.2 where the cooled and uncooled particle populations are calculated, the theoretical ratio between luminosities, assuming that the X-ray particles are in the cooled regime and the γ-ray ones in the uncooled one, is $L_\gamma/L_X \propto t^2 \propto \dot{E}^{-1}$, very close to the relations obtained. The results obtained by Mattana et al. (2009) differ from the results drawn from the fits performed in this thesis. We note, however, that we used the same data set used by Mattana et al. (2009) adding the newly discovered PWNe and PWN candidates at VHE. On the other hand, the results drawn from the fits are in agreement with those from Kargaltsev and Pavlov (2008), obtained with a larger data sample.

7.4   Conclusions

We have detected VHE gamma rays up to TeV energies from the PWN 3C 58 for the first time. The measured luminosity and flux make 3C 58 into an exceptional object. 3C 58 is the weakest VHE PWN detected to date, a fact that attests to the sensitivity of MAGIC. According to the currently existing models predicting VHE γ-ray emission from 3C 58, only a closer distance of 2 kpc or a high local FIR photon density can qualitatively reproduce its multiwavelength data. Since the high FIR density is unexpected, the closer distance with FIR photon density comparable with the averaged value in the Galaxy is favored. The age derived by the models in both cases is 2.5 kyr. The models that fit the γ-ray data derive magnetic fields which are very far from equipartition. We did not find any significant VHE γ-ray pulsed signal and established ULs above 420 GeV.

3C 58 is the least luminous VHE PWN, far less luminous than the original expectations. Its ratio $\sim L_\gamma/\dot{E} \simeq 10^{-5}$ is the lowest measured, similar to Crab, which makes it into a very inefficient γ-ray emitter. Assuming that the X-ray and γ-ray emitting particles are in different cooling regimes, we find that, for the PWNe detected at VHE gamma rays, L_X is correlated to $\dot{E}$ and anti-correlated to τ. The ratio between L_γ/L_X is anti-correlated to $\dot{E}$ and correlated to τ. We have found that $L_\gamma/L_X \propto \tau^{1.5\pm0.3}$ and $L_\gamma/L_X \propto \dot{E}^{-0.9\pm0.3}$, close to the expected values. Contrary to what it was thought, 3C 58 is not an outlier of these relations, although it shows an L_X and a ratio L_γ/L_X lower than the fit for the rest of PWNe, making it an inefficient accelerator also in the X-ray regime. Part of the results presented in this chapter are published in Aleksić et al. (2014b).

References

Abdo AA et al (2013) ApJS 208:17
Ackermann M et al (2012) ApJS 203:4
Ackermann M et al (2013) ApJS 209:34
Aleksić J et al (2014a). arXiv:1409.5594
Aleksić J et al (2014b) A&A 567:L8
Aliu E (2007) VHE gamma-ray observations of Northern sky pulsar wind nebulae with the MAGIC telescope, Ph.D. thesis
Aliu E (2008) In: Aharonian FA, Hofmann W, Rieger F (eds) American institute of physics conference series, vol 1085, pp 324–327
Anderhub H et al (2010) ApJ 710:828
Bednarek W et al (2003) A&A 405:689
Bednarek W et al (2005) J Phys G Nucl Phys 31:1465
Bietenholz MF (2006) ApJ 645:1180
Bietenholz MF et al (2001) ApJ 560:772
Bocchino F et al (2001) A&A 369:1078
Bucciantini N et al (2011) MNRAS 410:381
Chevalier RA (2004) Adv Space Res 33:456
Chevalier RA (2005) ApJ 619:839

Condon JJ et al (1998) AJ 115:1693

de Jager OC (1994) ApJ 436:239

Fesen R et al (2008) ApJS 174:379

Fomin VP et al (1994) Astropart Phys 2:137

Gotthelf EV et al (2007) ApJ 654:267

Green DA et al (2003) In: Weiler T (ed) Supernovae and gamma-ray bursters, vol 598., Lecture notes in physicsSpringer, Berlin, pp 7–19

Hall TA et al (2001) Internationalz cosmic ray conference, vol 6, p 2485

Jinyu L (1983) Stud Hist Nat Sci 2:45

Kargaltsev O et al (2008) 40 years of pulsars: millisecond pulsars, magnetars and more. In: Bassa C, Wang Z, Cumming A, Kaspi VM (eds) American institute of physics conference series, vol 983, pp 171–185

Kothes R (2013) A&A 560:A18

López M (2006) Observaciones de la Nebulosa y Pulsar del Cangrejo, Ph.D. thesis

Martín J et al (2012) MNRAS 427:415

Mattana F et al (2009) ApJ 694:12

Murray SS et al (2002) ApJ 568:226

Porter TA et al (2006) ApJ 648:L29

Possenti A et al (2002) A&A 387:993

Roberts DA et al (1993) A&A 274:427

Slane P et al (2002) ApJ 571:L45

Slane P et al (2004) ApJ 616:403

Slane P et al (2008) ApJ 676:L33

Stephenson FR et al (2002) Historical supernovae and their remnants. In: Richard Stephenson F, Green DA (eds) International series in astronomy and astrophysics, vol 5. Clarendon Press, Oxford ISBN 0198507666, 5

Tanaka SJ et al (2010) ApJ 715:1248

Tanaka SJ et al (2013) MNRAS 429:2945

Torii K et al (2000) PASJ 52:875

Torres DF et al (2013) ApJ 763:L4

Torres DF et al (2014) J High Energy Astrophys 1:31

Weber F (2005) Prog Part Nucl Phys 54:193

Weiler KW et al (1978) A&A 70:419

Xu Y et al (2006) Science 311:54

Part IV
Cataclysmic Variable Stars
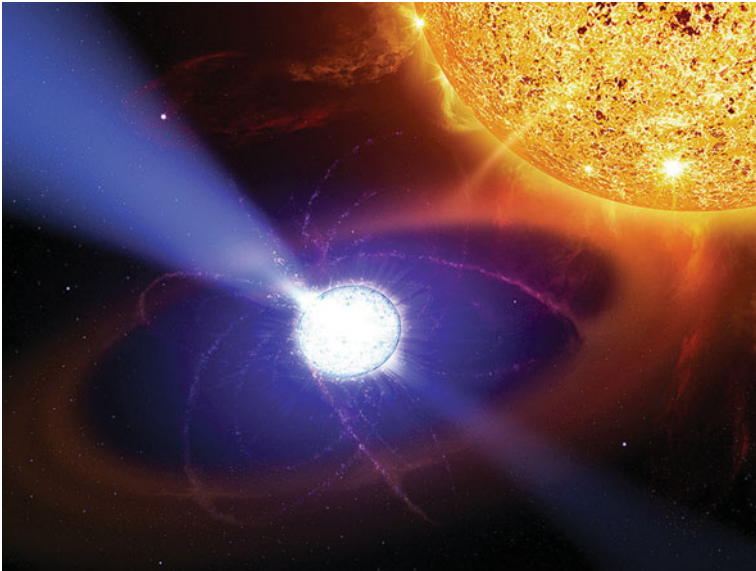
Fig. 1 Artist view of AE Aqr. Credit: Casey Reed

Chapter 8
Introduction to Cataclysmic Variable Stars

8.1 Introduction

Cataclysmic Variables (CVs) are semi-detached binaries consisting of a WD (called primary) that accretes material from a companion star (usually a Red Dwarf (RD), known as secondary) that transfers matter to the WD. The distance between them is of the order of a few solar radii. The companion is usually gravitationally distorted into a tear-drop shape. If the WD is non-magnetic, an accretion disk surrounding the WD is formed. If it is magnetized, the accretion disk is disrupted or not even formed in the case of strongly magnetized WDs (Warner 2003).

CVs show episodes when the system increases in luminosity by several orders of magnitude for a period that goes from hours to days, known as an outburst. These luminosity variations were firstly explained by a process of mass transfer in binary systems (Walker 1954). The mass transfer allows the formation of accretion disks, essential to understand planet and galaxy formation, and CV stars are an unique laboratory to test them. Accretion is the most efficient form of transforming mass into energy known. It can also be found in objects such as BHs, although the complete physical mechanisms acting in the accretion disks formed around WDs are still under debate.

8.2 Composition

As we discussed in Sect. 5.1, a massive star with initial mass $M < 9 - 10 \, M_\odot$ becomes a WD at the end of its life. On the other hand, there are smaller stars such as RDs that have masses between 0.1–0.3 $M_\odot$. They are thought to be fully convective, not building up a core and never becoming a red giant. These stars have constant brightness and a slow consumption of their fuel, resulting in long life times. They are the most common type of star in our galaxy.
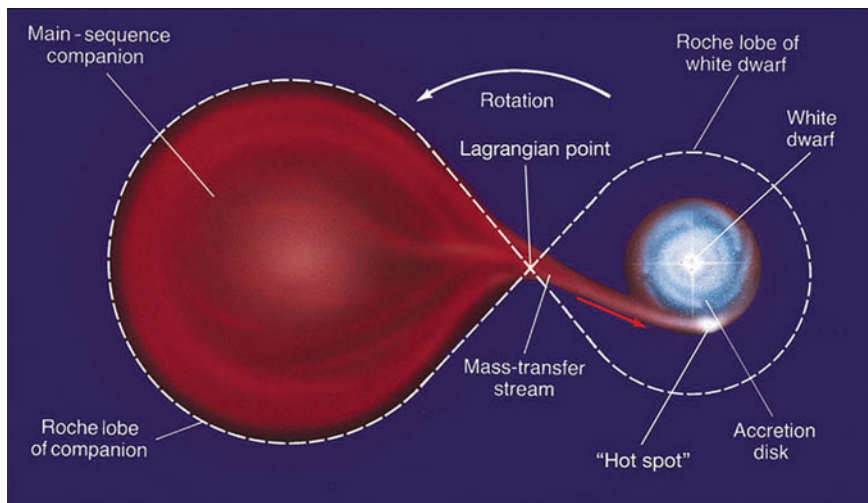
Fig. 8.1 Scheme of a CV system viewed from the pole of the orbit. Credit: Pearson Prentice Hall, Inc

In CVs, the *primary* is the WD, and the *secondary* is the star which is transferring mass to the WD. In a binary system, the *Roche lobe* of one of the stars is the region where matter is gravitationally attached to that star. In CVs, since the companion star fills its Roche lobe, the system is called semi-detached (see Fig. 8.1). The contact point of both Roche lobes, also known as Lagrangian point, is the saddle point of the potential between both Roche lobes. Matter is transferred through this point from the secondary to the primary (Connon Smith 2007). The stream of matter that crosses the Lagrangian point moves at a speed much lower than the orbital velocity, so it does not fall directly into the primary. If the magnetic field of the primary is not strong, the material starts to rotate around the WD forming an *accretion disk*. When the matter accreted from the secondary impacts the accretion disk, kinetic energy is released and the zone heated up, producing as a result a "hot spot". The whole process is illustrated in Fig. 8.1.

8.3   CV Fauna

Due to the diversity in several of their characteristics, it is difficult to place CVs in groups with common features. There are systems as AE Aqr (to which we dedicate Chap. 9) that do not fit into any of them and are proposed to constitute a class of CVs on their own (Ikhsanov and Beskrovnaya 2012). However, CVs are usually classified by the type of variation they manifest (for a review see Warner 2003) into Classical Novae (CNe), Recurrent Novae (RNe), Dwarf Novae (DNe), nova-like variables and magnetic CVs.

- **Classical Novae**

  A CV is called classical nova or just *nova* when only an outburst has been reported and its brightness has increased from 6 up to 19 magnitudes (see Appendix A.4) during this outburst. Novae explosions are caused by the accumulation of hydrogen-rich material on the surface of the WD. This results in a thermonuclear runaway that generates the nova (Bode and Evans 2012; Starrfield et al. 2012; Woudt and Ribeiro 2014). This system is illustrated in Fig. 8.1.

  There are records of *novae stellae* or "new stars" since 1500 BC by Chinese astrologers (Clark and Stephenson 1976), that might be attributed either to CN or SN events. No such reports have been found in Europe, maybe because Europeans maintained the aristotelian idea of an immutable sky until Tycho Brahe's discovery of a SN in 1572. The first true CN was discovered in Europe in 1670 and is shown in Fig. 8.2.

  Symbiotic Novae:

  Symbiotic novae, like CNe, are also initiated by a thermonuclear explosion on the surface of the WD. However, in the case of symbiotic novae, the WD is immersed in the wind of a late-type companion star and the increase of brightness ranges from 9 to 11 magnitudes (Shore et al. 2011, 2012).
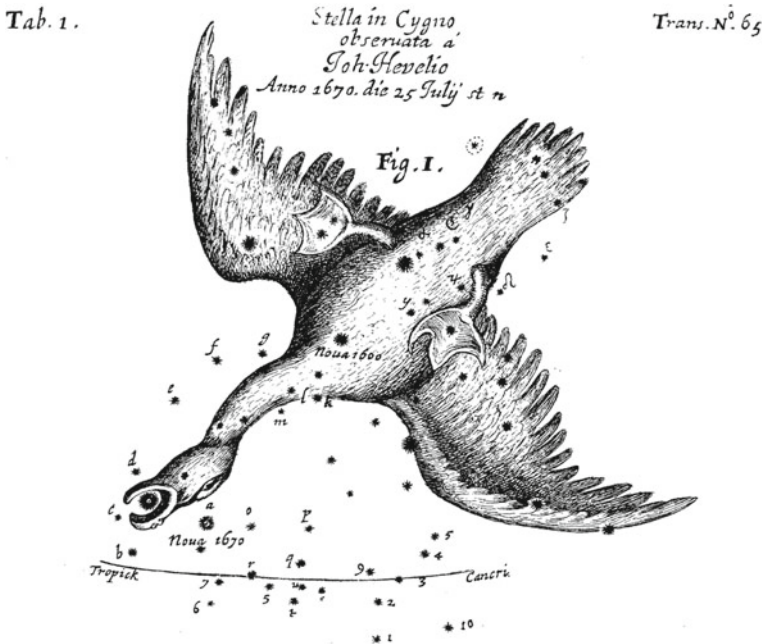
Fig. 8.2 Chart of the nova Vulpeculae (tagged as "nova 1670"), the first nova identified by European astronomers (Hevelius 1670). The star tagged as "Nova 1600" was believed to be a nova, but is currently known as P Cygni, an hypergiant luminous blue variable whose brightness variations are attributed to the ejection of its outer layers

- **Recurrent Novae**
  They are previously identified CNe that repeat their emission.
- **Dwarf Novae**
  They show outbursts of 2–8 magnitudes caused by a release of gravitational energy
  due to the increase in the rate of mass transfer from the companion. They differen-
  tiate from CNe, apart from the mechanism generating the increase of emission, in
  the fact that there is no shell ejection, while in CNe part of the shell is lost during
  the outburst.
- **Nova-like variables**
  They are CVs that do not show outbursts. They can be systems that are in pre-nova
  or post-nova phases and have shown no outbursts during the last hundreds of years.
  Some of the nova-like systems show small flux increases in their light curve, but
  unlike other types of novae, they show them all the time.
- **Magnetic CVs**
  The sources included in this group have a WD with magnetic fields typically larger
  than 10^5 G
  Intermediate Polar:
  Also known as DQ Her type, they show an accretion disk disrupted due to the
  magnetic field of the WD. At the innermost part of the disk, the falling matter
  follows the magnetic field lines forming accretion streams before reaching the WD
  surface. They are expected to show lower accretion rates than polars. A sketch of
  an intermediate polar is shown on the right panel of Fig. 8.3.
  Polar:
  No accretion disk is formed because of the strong magnetic field. Matter transferred
  from the secondary forms an accretion stream that falls directly into the WD. A
  sketch of a polar is shown on the left panel of Fig. 8.3.
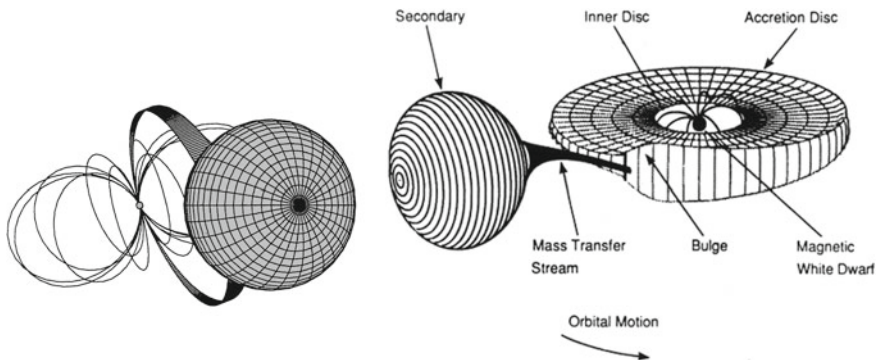
Fig. 8.3 Sketch of a polar (*left panel*) and an intermediate polar (*right panel*) CVs. Credit for the
left panel image: Schmidt, G.D., 1999, ASP Conf, 157 207

Out of this classification, we have observed with the MAGIC telescope one classical nova (V339 Del), one symbiotic nova (YY Her), one dwarf nova (ASASSN-13ax) and one nova-like variable (AE Aqr).

8.4 Spectral Characteristics

CVs emit from radio to HE gamma rays. Nevertheless, most of the observations are concentrated in the optical, where even amateur astronomers are able to measure their variability. Spectroscopy is used to measure the composition of the accretion disk and the orbital parameters of the system. Radio emission from CVs is usually weak, although it can be detected from novae in outburst or magnetic CVs. It is produced in large scale structures in the binary system (Drechsel et al. 1987). Observations in the IR allow the discovery of faint red secondary companions. UV observations are used to study the primary, although it might be obscured by the accretion disc depending on the observation angle. A thermal X-ray continuum is often detected by X-ray satellites in CN and magnetic CVs.

CVs have been proposed as candidates for non-thermal γ-ray emission. In AE Aqr a propeller model has been used to predict detectable VHE γ-ray emission under determined circumstances (Meintjes and de Jager 2000). The problem of this model is that makes assumptions that are not based on observations, such as the presence of a disk. Nevertheless, there are claims of VHE γ-ray emission from this source that are explained in detail in Sect. 9.1.

Since the discovery of transient γ-ray emission from the symbiotic nova V407 Cygni by *Fermi*-LAT (Abdo et al. 2010) and the subsequent report of transient emission from six additional novae (Cheung et al. 2013, 2014; Ackermann et al. 2014a; Cheung et al. 2015), CVs have been included among HE γ-ray emitters ($E > 100$ MeV). Several models explain the HE γ-ray emission of novae in terms of leptonic or hadronic acceleration. According to these models, there is the possibility that particles are accelerated to TeV energies and produce VHE γ-ray emission. We describe the models explaining the HE γ-ray emission and predicting a VHE component in Sect. 10.1.

References

Abdo AA et al (2010) Science 329:817
Ackermann M et al (2014a) Science 345:554
Bode MF et al (2012) Classical novae. Cambridge University Press, Cambridge
Cheung CC et al (2013) Astron Telegr 5653:1
Cheung CC et al (2014) Astron Telegr 5879:1
Cheung CC et al (2015) Astron Telegr 7283:1
Clark DH et al (1976) QJRAS 17:290
Connon Smith R (2007) arXiv:astro-ph/0701654

Drechsel H et al (1987) Ap&SS 130
Hevelius M (1670) R Soc Philos Trans 5:2087
Ikhsanov NR et al (2012) Astron Rep 56:595
Meintjes PJ et al (2000) MNRAS 311:611
Shore SN et al (2011) A&A 527:A98
Shore SN et al (2012) A&A 540:A55
Starrfield S et al (2012) Bull Astron Soc India 40:419
Walker MF (1954) PASP 66:230
Warner B (2003) Cataclysmic variable stars. Cambridge University Press, Cambridge
Woudt PA et al (eds) (2014) Astronomical society of the pacific conference series, vol 490. Stella
    Novae: past and future lcades

Chapter 9
Multiwavelength Campaign on AE Aquarii

9.1 Introduction

AE Aquarii (AE Aqr) is a bright nova-like CV consisting of a magnetic WD and a K4-5 V secondary. The orbital period of the system is $T_o = 9.88$ h, and the spin period of the WD is $T_s = 33.08$ s (Patterson 1979), which is the shortest known for a WD. The system is located at a distance of 102^{+42}_{-23} pc (Friedjung 1997), and the spin-down power of the WD is 6×10^{33} erg s^{-1} (de Jager et al. 1994). It was originally classified as a DQ Her star (Patterson 1994), but it shows features that do not fit such a classification, e.g., violent variability at multiple wavelengths, Doppler tomograms that are not consistent with those of an accretion disk (Welsh et al. 1998), and the fast spin-down rate of the WD ($\dot{P} = 5.64 \times 10^{-14}$ s^{-1}, de Jager et al. 1994). Recent X-ray measurements show that the spin-down rate is slightly higher, which is compatible with an additional term $\ddot{P} = 3.46 \times 10^{-19}$ d^{-1} (Mauche 2006). AE Aqr is considered to be in a magnetic propeller phase, ejecting most of the material transferred from the secondary by the magnetic field of the WD (Wynn et al. 1997). It exhibits flares 50 % of the time, varying in the optical band from $B = 12.5$ mag (during the low state) to $B = 10$ mag (during flares). Bastian et al. (1988) observed radio flares with fluxes in the range 1–12 mJy at 15 GHz. They show that the radio flares may be produced by relativistic electrons, which provides evidence of accelerated particles that radiate synchrotron emission in magnetized clouds. The time of both the optical and radio flares is random. Soft (0.5–10 keV) and hard (10–30 keV) X-rays have also been detected with a 33 s modulation (Patterson et al. 1980; Mauche 2006; Terada et al. 2008). A non-thermal origin of the hard X-rays is favored by Terada et al. (2008), who report an X-ray luminosity of $L_{\text{Hard X-rays}} \simeq 5 \times 10^{30}$ erg s^{-1} for the isotropic emission. They also report a sharp feature in the hard X-ray pulse profile that has not been confirmed by subsequent observations (Kitaguchi et al. 2014). Because of the large magnetic field and the fast rotating period of the WD, AE Aqr has been compared to pulsars (Ikhsanov 1998) and has been proposed as a source of cosmic ray electrons (Terada 2013).

The groups operating the Nooitgedacht Mk I Cherenkov telescope (de Jager et al. 1986) and the University of Durham VHE γ-ray telescopes (Brazier et al. 1990) reported TeV γ-ray emission from AE Aqr using the imaging atmospheric Cherenkov technique. The Durham group claimed that they detected gamma rays of energies above 350 GeV pulsed at the second harmonic of the optical period (60.46 mHz), as well as two bursts of TeV gamma rays (Bowden et al. 1992; Chadwick et al. 1995) lasting for 60 and 4200 s with 4.5 σ and 5.3 σ significance, respectively. The Nooitgedacht group, using the Mk I telescope, reported pulsed signals above energies of a few TeV at frequencies close to the spin frequency of the WD (30.23 mHz), with significances varying from 3 σ to 4 σ. Meintjes et al. (2012) claim that the duty cycle of the occurrence of TeV periodic signals above 95 % significance level is $\sim$30 %. They find coincidence in the orbital phase of their detections with the time of superior conjunction of the WD (orbital phase 0), but the burst reported by the Durham group is not coincident with this orbital phase. In the reports made by the two groups, the fluxes measured for the pulsed emission and burst episodes are at 10^{-9}–10^{-10} cm^{-2} s^{-1} for $E >$350 GeV for the Durham group and $E >$2.4 TeV for the Nooitgedacht group.

The luminosity corresponding to these fluxes is in the range 10^{32}–10^{34} erg s^{-1}, where the latter is at the level of the spin-down power of the WD. After the reports of TeV emission of such extraordinary luminosities, models were proposed to explain the fluxes measured (Meintjes and de Jager 2000), as well as others predicting lower levels of emission (Ikhsanov and Biermann 2006). According to classical models of particle emission, the magnetic moment of some WDs in binaries might provide enough energy to accelerate particles to VHE (Chanmugam and Brecher 1985). The flux levels reported by the Durham and Nooitgedacht groups is measurable in less than one hour of observations with the current generation of IACTs. AE Aqr has been observed by different generations of IACTs since the detection claims were reported, but none have confirmed them. The Whipple telescope observed the source for 68.7 h and did not find any evidence of emission (Lang et al. 1998). They reported flux ULs at 4×10^{-12} cm^{-2} s^{-1} for the steady emission and 1.5×10^{-12} cm^{-2} s^{-1} for the pulsed emission above 900 GeV. Later attempts by MAGIC and HESS did not lead to conclusive results (Sidro et al. 2008; Mauche et al. 2012).

The purpose of this campaign was to perform VHE observations of AE Aqr with MAGIC in a multiwavelength context, and hence confirm or rule out previous claims of γ-ray emission. We present in this work the results of the campaign, with emphasis on the search for signals in the VHE γ-ray range.

9.2 Observations

During the period between May 15 (MJD 56062) and June 19, 2012 (MJD 56097), we carried out a multiwavelength campaign on AE Aqr. The purpose of this campaign was to look for γ-ray emission during the different states of the source at

other wavelengths. The log of the observation times during the campaign for all the instruments is shown in Table B.7 in Appendix B.4.

9.2.1 Optical Facilities

We used data from three optical telescopes for the campaign. The observations are described in the following:

KVA

The KVA optical telescope is located on La Palma, but is operated remotely from Finland. It has a mirror diameter of 35 cm. The effective aperture ratio of the system is f/11 with a SBIG ST-8 CCD camera (0.98 arcsec/pix) (Takalo et al. 2008).

The AE Aqr observations were performed in the *B* band using 20-s exposures extending to about two hours of data per night during 19 nights. The magnitude of the source was measured from CCD images using differential photometry with 5″ radius aperture, and the data were reduced using the standard analysis software to analyze KVA data (Nilsson 2014). The seeing during the observations was 1″ FWHM. The typical error in the magnitude measurement is ∼0.04 mag. The comparison star used to calibrate the AE Aqr flux was the star 122 of the AAVSO AE Aqr finder chart.

Skinakas

The data from the Skinakas Observatory[1] in Crete (Greece) were obtained with the 1.3-m Ritchey-Chrétien telescope located on the Skinakas mountain at an altitude of 1750 meters. The telescope has a focal ratio of f/7.6. The data were acquired with an Andor Tech DZ436 2048 × 2048 water cooled CCD. The physical pixel size is 13.5 microns resulting in 0.28 arcsec on the sky. The camera was used in the 2-µs-per-pixel readout mode. The observations were taken with a Bessel *B* filter using 10-s exposures, while the cycle time from the start of one exposure to the next was 14 s.

The data from Skinakas were taken during about one hour for four nights, and they were reduced using IRAF routines. Differential photometry was performed using the photometry package DAOPHOT using 25 pixel (7″) radius apertures. The seeing conditions during the observations were 2″ FWHM. The typical error in the magnitude measurement is ∼0.005 mag. The AE Aqr data were flux-calibrated using stars 122 and 124 in the AAVSO AE Aqr finder chart.

Vidojevica

The Astronomical Station Vidojevica is located on Mt. Vidojevica (Serbia),[2] at an elevation of 1150 m. The data were obtained with the 60-cm Cassegrain telescope. The telescope was used in the f/10 configuration with the Apogee Alta U42 CCD camera (2048 × 2048 array, with 13.5-micron pixels providing a 0.46 arcsec/pix plate scale). The *B* filter from Optec Inc. (Stock No. 17446) was used for all observations.

---

[1]http://skinakas.physics.uoc.gr/en/.

[2]http://belissima.aob.rs/.

The field centered on the target AE Aqr was observed with ten seconds of exposure time. Only a fraction of the full CCD chip FoV, roughly 5 arcmin on a side, was read out in approximately four seconds, resulting in 14 s of total cycle time between exposures.

The data were taken for periods between one and two hours for five nights and they were reduced using standard procedures in IRAF. The photometry was performed with Source Extractor, using five-pixel (2.3″) radius circular apertures. Typical seeing conditions during the observations were 2″ FWHM. The typical error in the magnitude measurement is ~0.015 mag. The AE Aqr flux was calibrated using the same comparison stars as for Skinakas.

AAVSO

A number of AAVSO observers provided us with additional observations. However, due to the low time resolution of these observations and the lack of time coincidence with γ-ray observations, we did not include the AAVSO data into our timing analysis.

9.2.2 Swift

Swift (Gehrels et al. 2004) target-of-opportunity observations of AE Aqr were scheduled during 25 orbits from MJD 56062 to 56079 and from MJD 56091 to 56094. Data were obtained with the X-ray Telescope (XRT, sensitive over the energy range 0.3–10 keV Burrows et al. 2005), the Ultraviolet/Optical Telescope (UVOT), and the Burst Alert Telescope (BAT), although only the XRT data have been analyzed to support the MAGIC observations. The screened and calibrated XRT CCD/PC event data for ObsIDs 00030295011–00030295035 were downloaded from the HEASARC data archive.[3] The data were processed using the XRTDAS software package (v.2.9.3) developed at the ASDC and distributed by HEASARC within the HEASoft package (v. 6.15.1). On-source events were selected within a circle of a 30-pixel (69 arcsec) radius. The background was evaluated in an adjacent 60-pixel radius off-source region. Event energies were restricted to the 0.5–10 keV bandpass, and all event times were corrected to the solar system barycenter. The 25 ObsIDs consisted of 29 good-time intervals, which were combined into 25 satellite orbits, although one orbit was rejected because the exposure was too short (20 s), and three orbits were rejected because the source image fell on one of the dead strips on the detector. The net exposure during the remaining orbits ranged from 559 to 1178 s, with ~950 s being typical, and the total exposure was 19.94 ks. The analysis was crosschecked using a flexible IDL script developed by C.W. Mauche to deal with event data from instruments on numerous science satellites including *ROSAT*, *ASCA*, *EUVE*, *Chandra*, *XMM-Newton* and adapted to Swift for this study.

---

[3]http://HEASARC.gsfc.nasa.gov/docs/archive.html.

9.2.3 MAGIC

MAGIC observed AE Aqr during 14 non-consecutive nights during the period between MJD 56073 and 56097. The observations were performed with a single telescope owing to a hardware failure in the M I camera. This worsened the sensitivity to ~1.5% of the Crab Nebula flux above 300 GeV in 50 h (Aleksić et al. 2012). The source was observed at Zd ranging between 28° and 50°, and after quality cuts, 9.5 h of data were obtained. The data were taken in *wobble mode*, as explained in Sect. 2.2.2.1). They were analyzed following the usual procedure in MAGIC, as explained in Sect. 2.2.3.

To search for pulsed emission, the arrival times of the events were corrected to the solar system barycenter using the software package TEMPO2 (Hobbs et al. 2006). To calculate the phases of the events, we used the ephemeris presented in de Jager et al. (1994) using the second-order correction proposed by Mauche (2006). We corrected the times for the orbital motion of the system using TEMPO2 as well. The ephemeris, particularly the phase of spin-pulse maximum, was checked using the Swift data (see Sect. 9.3.2). The U.L. for the pulsed emission were calculated with a 95% C.L. following the method described in de Jager (1994) that makes use of the H-test for the significance of weak periodic signals (de Jager et al. 1989). The simultaneity of the optical and MAGIC observations allows us to investigate the TeV flux of the source for different optical emission levels.

9.3 Results

The measured optical magnitudes are presented in Sect. 9.3.1. In Sect. 9.3.2 the results obtained with Swift are discussed. In Sect. 9.3.3, we present the results of the search for a steady and pulsed γ-ray signal. The light curves of the multiwavelength campaign are shown in Fig. 9.1.

9.3.1 Optical Results

We present the results of all the optical observations together to check for consistency between the magnitudes measured by the different telescopes (top panel of Fig. 9.1). We find that the measurements performed by the different optical telescope lead to similar results. The highest optical state was measured on MJD 56080, reaching $B = 11.08$ mag. The short time exposures (~10 s) mean that it is not possible to produce the optical spin-phase-folded light curve.
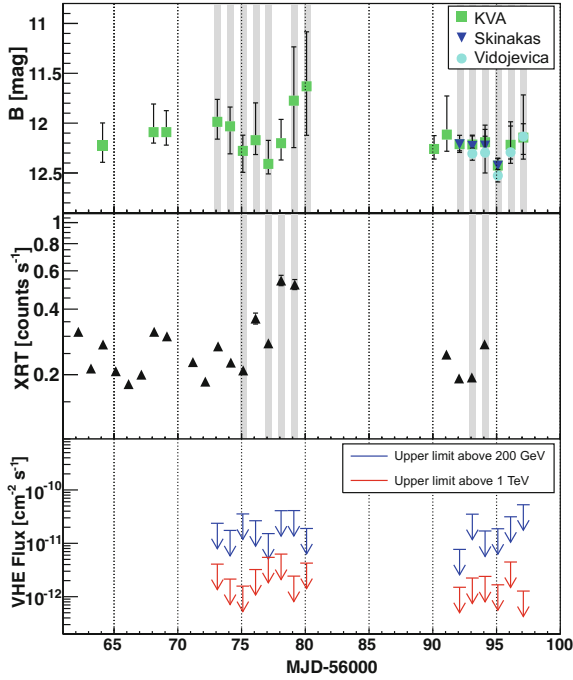
Fig. 9.1 Light curves of the multiwavelength campaign. The plot includes *B* magnitudes measured by the optical telescopes (*top panel*), XRT count rate in the energy range 0.5–10 keV (*middle panel*) and MAGIC daily integral ULs assuming a power-law spectrum with a 2.6 photon spectral index above 200 GeV and 1 TeV (*bottom panel*). *Vertical dotted lines* every 5 days are plotted across all the panels for reference. For the optical data, since the source variability is very large, the *point plotted* is the average magnitude of the night and the *error bars* indicate the maximum and minimum magnitude reached during that observation night. The *shaded areas* indicate the X-ray and optical observations with simultaneous data with MAGIC. Credit: Aleksić et al. (2014), reproduced with permission © ESO

9.3.2 Swift Results

The *Swift*/XRT event data were used to compute the X-ray light curve (Fig. 9.1, middle panel) and the spin-phase-folded light curve (Fig. 9.2). The background-subtracted XRT count rate varied by a factor of three, from 0.18 counts s^{-1} to 0.53 counts s^{-1}, with a mean of 0.27 counts s^{-1}. A similar ratio of mean-to-base and peak-to-base count rate ratios and a similar light curve morphology were observed during the long *Chandra* observation of AE Aqr in 2005 (Mauche 2009). The spin-phase-folded light curve was calculated using the ephemeris provided by Mauche (2006), with parameters:
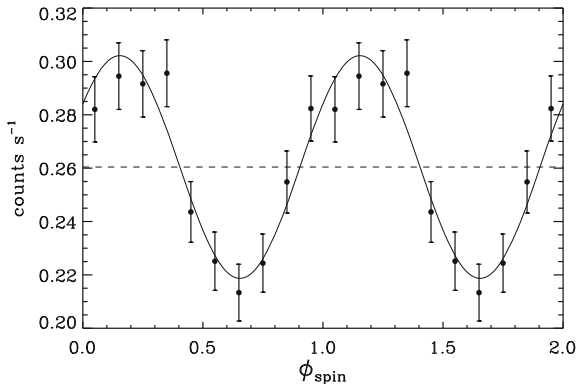
Fig. 9.2 XRT spin-phase-folded light curve in the energy range 0.5–10 keV. Two cycles are shown for clarity. The errors quoted are the square root of number of counts in the source region plus the area-scaled number of counts in the background region, divided by the exposure. The *continuous black line* shows the best fit using Eq. 9.1. The *dashed line* represents the mean value $A_0 = 0.260$ counts s^{-1} obtained from the fit. Credit: Aleksić et al. (2014), reproduced with permission © ESO

Orbital period	$P_{orb} = 0.411655610$ d
Time of superior conjunction	$T_0 = 2445172.2784$ BJD
Spin period	$P_s = 0.00038283263840$ d
Spin period derivative	$\dot{P}_s = 5.642 \times 10^{-14}$ d d^{-1}
Spin period second derivative	$\ddot{P}_s = 3.46 \times 10^{-19}$ d^{-1}
Projected semi-amplitude	$a_{WD} \sin i = 2.04$ s.

The points were fit with a cosine function:

$$A(\phi_{spin}) = A_0 + A_1 \cos[2\pi(\phi_{spin} - \phi_{off})] \tag{9.1}$$

with parameters

$$A_0 = 0.260 \pm 0.004 \text{ counts s}^{-1}$$
$$A_1 = 0.042 \pm 0.005 \text{ counts s}^{-1}$$
$$\phi_{off} = 0.15 \pm 0.02$$

and $\chi^2/\text{dof} = 5.90/7 = 0.84$. The fit function is shown in Fig. 9.2.

As a result, the relative pulse amplitude is $A_1/A_0 = 16\% \pm 2\%$, which is slightly higher than previously measured by *ASCA*, *XMM-Newton*, and *Chandra*, which are 13 %, 10 %, and 15 %, respectively (see Table 2 of Mauche 2006). A shift of $\phi_{off} = 0.15 \pm 0.02$, which is not compatible with $\phi_{off} = 0$, is observed. That is an indication of the inaccuracy of the ephemeris used or a drastic variation in either $\dot{P}$ or $\ddot{P}$. Nevertheless, we use this result for the time of the maximum of the pulsed X-ray emission to look for pulsed gamma-ray signals.

9.3.3 MAGIC Results

The energy threshold achieved for these observations, defined as in Sect. 2.2.3.6, for a power-law with a 2.6 photon spectral index is 250 GeV, although the number of events surviving the gamma/hadron separation cuts is still high below this energy, down to 200 GeV, where it falls rapidly. This result is obtained from MC simulations without applying any cut in reconstructed energy. We searched for steady and periodic emission in the MAGIC dataset. We computed ULs to the integral flux above two values of energy; namely, above 200 GeV, as the lowest energy with sufficient gamma-ray detection efficiency (for this observation); and above 1 TeV, to compare our results with the previous claims. Most of those observations were simultaneous with optical and X-ray ones. Therefore, we also study the correlation of optical/X-ray flux with the possible γ-ray emission.

9.3.3.1 Search for Steady TeV Emission

The total dataset did not show any significant steady signal. For the U.L. calculation, we assumed power-law functions with different photon spectral indices (2.0, 2.6, and 3.0). The results are listed in Table 9.1. We also computed integral ULs (95 % C.L.) for the single-night observations, assuming a source steady emission with a power-law function with photon spectral index 2.6. These ULs can be found in Table 9.2 and are plotted in Fig. 9.1 (bottom panel). The single-night ULs for TeV emission coincident with the highest states of the source in X-rays (MJD 56078 and 56079) and in the optical (MJD 56079 and 56080) are at the same level as the ULs for the remaining days.

We also studied the behavior of the source during different bright optical states. Based on the optical states observed during the multiwavelength campaign, we selected γ-ray events during times when $B < 12$ mag (1.22 h) and $B < 11.5$ mag (0.34 h). The integral ULs for those states are shown in Table 9.3.

Table 9.1 MAGIC integral ULs to steady flux assuming a power-law spectrum with different photon spectral indices Γ above 200 GeV and 1 TeV. Credit: Aleksić et al. (2014), reproduced with permission © ESO

Γ	U.L. (95 % C.L.) (cm^{-2} s^{-1})	
	>200 GeV	>1 TeV
2.0	4.2×10^{-12}	7.6×10^{-13}
2.6	6.4×10^{-12}	7.4×10^{-13}
3.0	8.0×10^{-12}	7.4×10^{-13}

Table 9.2 MAGIC daily integral ULs to steady flux assuming a power-law spectrum with photon spectral index 2.6 above 200 GeV and 1 TeV. Credit: Aleksić et al. (2014), reproduced with permission © ESO

Date [MJD]	U.L. (95 % C.L.) (cm^{-2} s^{-1})	
	>200 GeV	>1 TeV
56073	2.4×10^{-11}	4.0×10^{-12}
56074	1.7×10^{-11}	2.1×10^{-12}
56075	3.6×10^{-11}	1.6×10^{-12}
56076	2.7×10^{-11}	3.2×10^{-12}
56077	1.5×10^{-11}	5.5×10^{-12}
56078	4.1×10^{-11}	6.3×10^{-12}
56079	4.1×10^{-11}	2.4×10^{-12}
56080	1.9×10^{-11}	4.3×10^{-12}
56092	0.8×10^{-11}	1.5×10^{-12}
56093	3.5×10^{-11}	2.2×10^{-12}
56094	1.7×10^{-11}	2.4×10^{-12}
56095	1.9×10^{-11}	1.7×10^{-12}
56096	3.1×10^{-11}	4.5×10^{-12}
56097	5.3×10^{-11}	1.3×10^{-12}

Table 9.3 MAGIC integral ULs to steady flux for different optical states above 200 GeV and 1 TeV and for a photon spectral index 2.6. Credit: Aleksić et al. (2014), reproduced with permission © ESO

B [mag]	U.L. (95 % C.L.) (cm^{-2} s^{-1})	
	>200 GeV	>1 TeV
<11.5	2.1×10^{-11}	1.6×10^{-12}
<12	7.3×10^{-12}	1.2×10^{-12}

9.3.3.2 Search for Pulsed TeV Emission

We searched for pulsed TeV emission at the rotation frequency of the WD (30.23 mHz) and its first harmonic (60.46 mHz). We did not find any hint of periodic signal for any of the two frequencies. For the U.L. calculation, we limited the signal region to 30 % of the pulsar phaseogram, centered on the bin corresponding to the maximum of the XRT spin-phase-folded light curve (see Fig. 9.2). The phaseograms for data above 200 GeV are shown in Fig. 9.3. These ULs, calculated as explained in Sect. 9.2.3, can be found in Table 9.4.

We also searched for periodic emission at different frequencies using the Rayleigh test (Mardia 1972). We scanned the complete dataset for periodic signals in the range between 20.0 and 70.0 mHz in steps of 0.5 mHz (101 frequencies). This range is selected in order to cover the whole range of interest in the frequencies. For all the
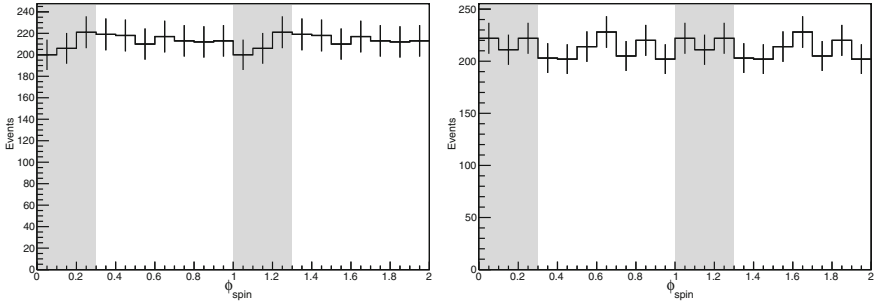
Fig. 9.3 Phaseogram for the MAGIC data above 200 GeV for a frequency of 30.23 mHz (*left panel*) and 60.46 mHz (*right panel*). The *shaded area* corresponds to the region where the signal is expected assuming a duty cycle of 30 %. Credit: Aleksić et al. (2014), reproduced with permission © ESO

Table 9.4 MAGIC integral ULs for the pulsed emission at the spin frequency and its first harmonic above 200 GeV and 1 TeV for a photon spectral index of 2.6. Credit: Aleksić et al. (2014), reproduced with permission © ESO

Frequency	U.L. (95 % C.L.) (cm^{-2} s^{-1})	
	>200 GeV	>1 TeV
30.23 mHz	2.6×10^{-12}	2.6×10^{-12}
60.46 mHz	2.1×10^{-12}	3.7×10^{-12}

frequencies, we calculated the Rayleigh power z and the chance probability of getting that value or higher from pure white noise as $P = \exp(-z)$. The histogram of z values is fit with an exponential function $f(z) = A \exp(-bz)$. In case of purely white noise, we expect $b = 1$ and $A = b \times N$, where N is the number of scanned frequencies. The result of the fit is $A = 115 \pm 22$ and $b = 1.17 \pm 0.17$. The complete dataset scan for significant periodic signals is shown in Fig. 9.4. The result of the fit of the histogram in the inset of Fig. 9.4 is compatible with white noise. The minimum pretrial chance probability obtained is 3.5×10^{-3} for a frequency of 23.0 mHz, which corrected after trials (101 frequencies) gives a post-trial probability of 3.0×10^{-1}. Hence, no significant signal of periodic/variable behavior was found.

We applied the Rayleigh test to the daily datasets as well. The range of frequencies is the same as the one used for the complete dataset. The minimum pre-trial chance probability obtained for all the scans is 1.5×10^{-4} for a frequency of 54.0 mHz, achieved on MJD 56094. This probability, corrected after trials (101 frequencies × 14 observations), gives a 1.9×10^{-1} post-trial chance probability. The histogram with the distribution of Rayleigh power for all scanned frequencies and days is shown in Fig. 9.5. The result of the fit of the histogram $f(z)$ is $A = 1450 \pm 60$ and $b = 0.99 \pm 0.03$, which is compatible with white noise.

Fig. 9.4 Periodogram of the frequencies in the range between 20.0 and 70.0 mHz in steps of 0.5 mHz for the complete MAGIC dataset. The selected events have energies above 200 GeV. The plot in the *inset* represents the histogram of the Rayleigh power z for the complete MAGIC dataset. Credit: Aleksić et al. (2014), reproduced with permission © ESO
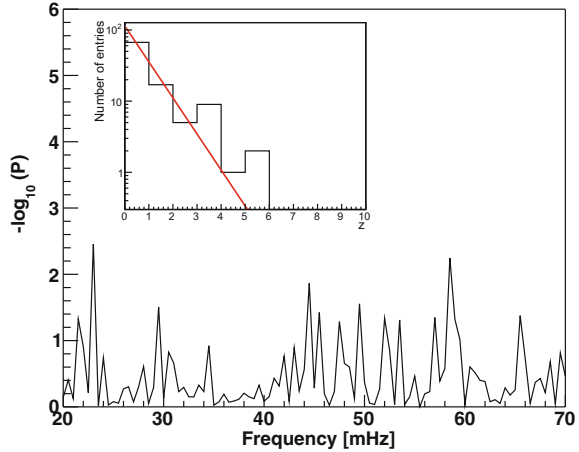
Fig. 9.5 Histogram of the Rayleigh power z for events above 200 GeV for all frequencies and individual MAGIC observations. Credit: Aleksić et al. (2014), reproduced with permission © ESO
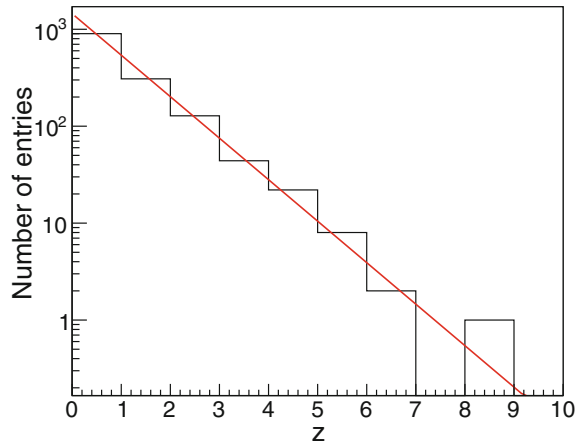
9.4 Discussion

MAGIC observations did not confirm the previous reports of emission from AE Aqr. We report flux ULs from two to three orders of magnitude below the fluxes previously reported. Specifically, Meintjes et al. (2012), using the Nooitgedacht telescope, reported the detection of periodic signals with 95 % C.L. significance in 30 % of the observation time. Assuming that this is the typical behavior of the source and thanks to the higher sensitivity of MAGIC with respect to the Nooitgedacht telescopes, our observations should have produced signals with a large significance. We do not find any hint of a periodic signal. Regarding the reports of random VHE bursts from the Narrabri telescope (Bowden et al. 1992; Chadwick et al. 1995), because they do not

follow any periodicity, they cannot be excluded by the results presented in this work. On the other hand, if one of such events had happened during our observations, we would have detected it.

There are several days when the source is at a state in the optical and X-rays higher than the baseline. In the *B* band, the source reached a state up to 1.5 magnitudes brighter than the quiescence state at magnitude 12.5. In X-rays, the highest state is about three times brighter than the baseline. This eruptive behavior is normal for this source. We searched for a correlation between the optical/X-ray emission and the γ-ray ULs. As shown in Sect. 9.3.3.1, flux ULs for the γ-ray emission are at the same level for all days, independently of the state of the source in the optical or X-rays.

If we take the U.L. on the integral flux of Tables 9.1 and 9.4, we can calculate the U.L. of the γ-ray luminosity of AE Aqr. The U.L. on the luminosity for the steady emission of AE Aqr, considering a power-law function with photon spectral index 2.6, above 200 GeV is $L_{\gamma, E>200\text{GeV}} < 6.8 \times 10^{30} \, d_{100}^2$ erg s^{-1}, where d_{100}^2 is the distance normalized to 100 pc and above 1 TeV is $L_{\gamma, E>1\text{TeV}} < 3.9 \times 10^{30} \, d_{100}^2$ erg s^{-1}. The U.L. on the luminosity for the pulsed emission at 30.23 and 60.46 mHz, considering a power-law with photon spectral index 2.6, above 200 GeV, are $L_{\gamma, E>200\text{GeV}}$ [30.23 mHz] $< 2.8 \times 10^{30} \, d_{100}^2$ erg s^{-1} and $L_{\gamma, E>200\text{GeV}}$ [60.46 mHz] $< 2.2 \times 10^{30} \, d_{100}^2$ erg s^{-1}.

To explain the large γ-ray fluxes measured in the past, Meintjes and de Jager (2000) proposed a model based on the propeller emission of particles that predicts large γ-ray fluxes, which are easily detected with the current generation of IACTs. The generation of VHE particles is based on the idea that a very high potential difference can be generated thanks to differences in the density of the gas present in a clumpy ring surrounding the WD. This model predicts luminosities of up to $L_\gamma \sim 10^{34}$ erg s^{-1} during the largest bursts of the source, which would be able to explain the fluxes observed at $F > 10^{-10}$cm^{-2} s^{-1} by Meintjes et al. (1994) and Chadwick et al. (1995). To explain these luminosities, the model makes assumptions that do not match the observations, like the presence of an accretion disk. We present in this work ULs on the pulsed/steady γ-ray luminosities measured by MAGIC on the order of 10^{30} erg s^{-1}, which is several orders of magnitude below the prediction of the model.

Since there is evidence of non-thermal emission in the system, there has to be a mechanism that converts a fraction of the spin-down power into particle acceleration. To explain this non-thermal emission, there are mechanisms like the magnetic pumping in the magnetosphere (Kuijpers et al. 1997), which explains the radio outbursts as eruptions of bubbles of fast particles from the magnetosphere surrounding the WD, and the Ejector White Dwarf (EWD) model (Ikhsanov 1998), which describes a pulsar-like acceleration mechanism for AE Aqr and predicts the γ-ray emission of the system as well (Ikhsanov and Biermann 2006). Following the EWD model, the source emits TeV gamma rays during the optical highest state of the source ($B = 10$ mag) with a luminosity lower than 4×10^{29} erg s^{-1}. The U.L. for higher optical magnitudes derived in this work are one order of magnitude higher, therefore they do not conflict with our results. The future CTA (Acharya et al. 2013) will have

a sensitivity that is roughly one order of magnitude better than the current sensitivity of MAGIC (Bernlöhr et al. 2013). The flux prediction for the high-level optical state is expected to be detectable by CTA.

9.5 Summary

We have observed AE Aqr simultaneously in VHE, optical and X-rays. This allows us to characterize the behavior of the source in different states. During our observations, the source displayed a level of brightness and type of variability that was consistent with previous observations in the optical and X-ray wavebands. We found a shift in the maximum of the spin-phase-folded X-ray light curve respect to the phase calculated with the most recent ephemeris of the source. We searched for steady γ-ray emission during the whole observation period, for enhanced emission coincident with different optical states and for pulsed γ-ray emission. We did not find any significant γ-ray signal from AE Aqr in any of the searches performed. We have established the most restrictive ULs so far for VHE emission (above 200 GeV and above 1 TeV) of this source, and of any other CV in general. The corresponding ULs are up to three orders of magnitude lower than some of the emission reports by the Nooitgedacht and Durham groups about two decades ago. The propeller model is a good candidate for explaining the emission from radio to X-ray energies. However, it is very unlikely to be responsible for the production of γ-ray photons in the way described in Meintjes and de Jager (2000), unless the probability of flaring events is less than reported. Finally, we note that the level of γ-ray emission predicted by the EWD model is consistent with our ULs, and it could be detected with CTA. Part of the results presented in this chapter are published in Aleksić et al. (2014).

References

Acharya BS et al (2013) Astropart Phys 43:3
Aleksić J et al (2012) Astropart Phys 35:435
Aleksić J et al (2014) A&A 568:A109
Bastian TS et al (1988) ApJ 324:431
Bernlöhr K et al (2013) In: Proceedings of the 33rd ICRC. arXiv:1307.2773
Bowden CCG et al (1992) Astropart Phys 1:47
Brazier SKT et al (1990) Int Cosm Ray Conf 4:270
Burrows DN et al (2005) Space Sci Rev 120:165
Chadwick PM et al (1995) Astropart Phys 4:99
Chanmugam G et al (1985) Nature 313:767
de Jager HI et al (1986) S Afr J Phys 9:107
de Jager OC (1994) ApJ 436:239
de Jager OC et al (1989) A&A 221:180
de Jager OC et al (1994) MNRAS 267:577
Friedjung M (1997) New A 2:319

Gehrels N et al (2004) ApJ 611:1005
Hobbs GB et al (2006) MNRAS 369:655
Ikhsanov NR (1998) A&A 338:521
Ikhsanov NR et al (2006) A&A 445:305
Kitaguchi T et al (2014) ApJ 782:3
Kuijpers J et al (1997) A&A 322:242
Lang MJ et al (1998) Astropart Phys 9:203
Mardia KV (1972) Statistics of directional data. Academic Press, New York
Mauche CW (2006) MNRAS 369:1983
Mauche CW (2009) ApJ 706:130
Mauche CW et al (2012) Mem Soc Astron Ital 83:651
Meintjes PJ et al (1994) ApJ 434:292
Meintjes PJ et al (2000) MNRAS 311:611
Meintjes PJ et al (2012) Mem Soc Astron Ital 83:643
Nilsson K (2014) in preparation
Patterson J (1979) ApJ 234:978
Patterson J et al (1980) ApJ 240:L133
Patterson J (1994) PASP 106:209
Sidro N et al (2008) Int Cosm Ray Conf 2:715–718
Takalo LO et al (2008) In: Aharonian F, Hofmann W, Rieger F (eds) American Institute of Physics
    Conference Series. Vol 1085, pp 705–707
Terada Y (2013) Thirteenth marcel grossmann meeting. arXiv:1306.4053
Terada Y et al (2008) PASJ 60:387
Welsh WF et al (1998) MNRAS 298:285
Wynn GA et al (1997) MNRAS 286:436

Chapter 10
Nova and Dwarf Nova Observations with MAGIC

Starting in fall 2012, the MAGIC collaboration conducts a nova follow-up program in order to detect a possible VHEγ-ray component. The program responded to *Fermi*-LAT detections of different types of novae at GeV energies: it initially focussed on symbiotic novae and later extended to bright CNe and additional outbursts from other CVs. I will report on the observations performed with the MAGIC telescopes of the symbiotic nova YY Her, the DN ASASSN-13ax, and the CN V339 Del and present the contemporaneous updated analysis of *Fermi*-LAT data.

10.1 Introduction

As introduced in Chap. 8, novae are thermonuclear explosions where the envelope of a WD is ejected. The diffusive shock acceleration at the blast wave of symbiotic novae was expected to accelerate particles up to energies of a few TeVs (Tatischeff and Hernanz 2007). In 2010 the first GeV γ-ray emission was detected by *Fermi*-LAT from the symbiotic nova V407 Cyg (Abdo et al. 2010). The γ-ray emission has been subsequently explained in terms of leptonic or hadronic models (Abdo et al. 2010; Ackermann et al. 2014). Local radiation fields create a target for the IC scattering of the electrons. Protons accelerated in the same conditions can interact with matter producing gamma rays via proton-proton interactions. For instance, Sitarek and Bednarek (2012) attribute the GeV γ-ray emission to the IC process on the strong radiation field of the red giant. The same model predicts a second component in the TeV range due to proton-proton interactions with the wind of the red giant. Also Martin and Dubus (2013) consider acceleration of leptons and hadrons in the nova shock. In that model the magnetic field, which determines the acceleration efficiency,

is obtained assuming equipartition with the thermal energy density upstream of the shock. The GeV γ-ray emission is then a product of IC scattering of the nova light by the electrons.

In the last few years *Fermi*-LAT has discovered GeV γ-ray emission from a few more novae: V1324 Sco, V959 Mon, V339 Del, V1369 Cen, V745 Sco and the very recent Nova Sagittarii 2015 (Cheung et al. 2013, 2014; Ackermann et al. 2014; Cheung et al. 2015). Most of these sources are CNe. Contrary to the symbiotic ones, the wind of the companion star is not strong, but they all show similar spectral properties. In CNe the particle acceleration can occur e.g. on a bow shock between the nova ejecta and the interstellar medium or in weaker internal shocks due to inhomogeneity of the nova ejecta (Ackermann et al. 2014). In particular, orbital motion of the system can shape the nova ejecta into a faster polar wind and a denser material expanding on the equatorial plane (Chomiuk et al. 2014). Metzger et al. (2015) suggest that the γ-ray emission might come from hadronic interactions in clumps of ejected material.

So far no VHEγ-ray emission has been detected from any nova event. VERI-TAS observations of V407 Cyg starting 10 days after the nova explosion yielded a differential UL on the flux of $2.3 \times 10^{-12} \, \mathrm{erg \, cm^{-2} \, s^{-1}}$ at 1.6 TeV(Aliu et al. 2012).

10.2 Instruments

V339 Del and the other outbursts were first detected by optical instruments. The results of the MAGIC observations were supported by the analysis of quasi-simultaneous *Fermi*-LAT observations.

10.2.1 *MAGIC Telescopes*

The telescope and data analysis description can be found in Sect. 2.2.

10.2.2 **Fermi-*LAT***

Fermi-LAT is a pair-conversion telescope launched in 2008 that detects photons with energies from 20 MeV to > 300 GeV (Atwood et al. 2009). Thanks to a large FoV ($\sim$2.4 sr), the *Fermi*-LAT observatory, operated in scanning mode, provides coverage of the full sky every three hours enabling searches for transient sources and overlap with ground-based observatories. The LAT data were analyzed in the energy range 100 MeV–300 GeV using an unbinned maximum likelihood method (Mattox et al. 1996) as implemented in the *Fermi* Science Tools v9r32p5, the P7REP_SOURCE_V15 LAT Instrument Response Functions (IRF), and associated

standard Galactic and isotropic diffuse emission models.[1] We selected events within a RoI of 15° centered on the LAT best position reported by Ackermann et al. (2014) for V339 Del and required a maximum Zd of 100° in order to avoid contamination from Earth limb photons. Additionally, we applied a gtmktime filter (no.3) recommended for combined survey and pointed mode observations,[2] selecting good quality data at times when either the rocking angle was less than 52° or the edge of the analysis region did not exceed the maximum Zd at 100°. Sources from the 2FGL catalogue (Nolan et al. 2012) located within 20° the RoI were included in the model used to perform the fitting procedure. The ULs were calculated at 95 % C.L. using the Bayesian method provided with the *Fermi* Science Tools.[3]

10.3 Observations and Results

During the first year of MAGIC novae follow-up program three sources were observed: YY Her, ASASSN-13ax and V339 Del (Fig. 10.1).

10.3.1 YY Her

YY Her is a symbiotic star with an M2 companion (Herbig 1950). In the 20th century it exhibited four long outbursts (Munari et al. 1997). It recently underwent an outburst phase that finished in 2006. It lasted several years and was characterized by a ∼500 days separation between brightness maxima. On MJD 56397 the maximum in a new outburst was observed in optical (Munari et al. 2013). This outburst is the second in a new outburst phase that started in December 2011. The optical observations around this time are shown in Fig. 10.2. Even while symbiotic novae are much more rare than classical ones, the very first nova detected in the GeV energy range was of symbiotic type. This, and the fact that the dense wind and strong radiation field of the red giant in symbiotic novae produce favorable conditions for production of GeV-TeV gamma rays by hadrons and electrons (Sitarek and Bednarek 2012) encouraged MAGIC to follow all the observable symbiotic novae. The MAGIC observations were performed on MJD 56404 and could not be continued due to the Full Moon. The total observation time was 0.9 h, out of which 0.7 h survived data quality selection and were used for analysis. The source was observed at low Zd (<11°).

No significant excess of γ-ray events was detected in the MAGIC observations. The energy threshold of this analysis computed as in Sect. 2.2.3.6 is ∼70 GeV.

---

[1]The P7REP data, IRFs, and diffuse models (gll_iem_v05.fit and iso_source_v05.txt) are available at http://fermi.gsfc.nasa.gov/ssc.

[2]http://fermi.gsfc.nasa.gov/ssc/data/analysis/documentation/Cicerone/Cicerone_Likelihood/Exposure.html.

[3]http://fermi.gsfc.nasa.gov/ssc/data/analysis/scitools/python_tutorial.html.
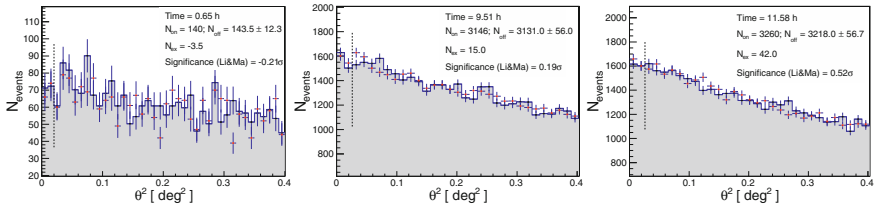
Fig. 10.1 Distribution of the squared distance between the nominal and reconstructed source position (*red points*) and the background estimation (*shaded* region) in the MAGIC observations of the three objects: YY Her (*left panel*, $E \gtrsim 70\,\text{GeV}$), ASASSN-13ax (*middle panel*, $E \gtrsim 110\,\text{GeV}$) and V339 Del (*right panel*, $E \gtrsim 80\,\text{GeV}$)

Fig. 10.2 Optical observations of YY Her during the outburst in April 2013. The data points in V (filled circles) and Tri-G (empty squares) range are obtained from AAVSO-LCG service. The *grey vertical line* shows the observation night with MAGIC
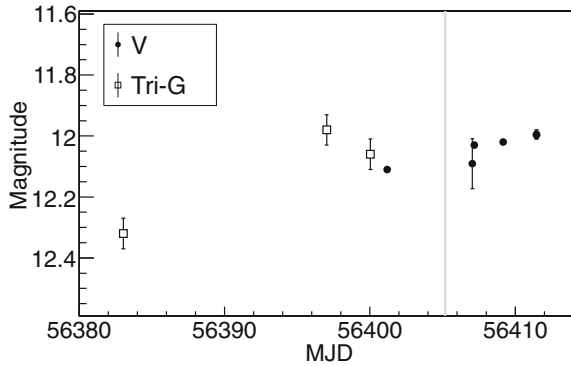
Fig. 10.3 Differential ULs on the flux from YY Her measured by MAGIC (filled circles) and *Fermi*-LAT (empty squares). For comparison, a spectrum of Crab Nebula is shown with a *grey* curve
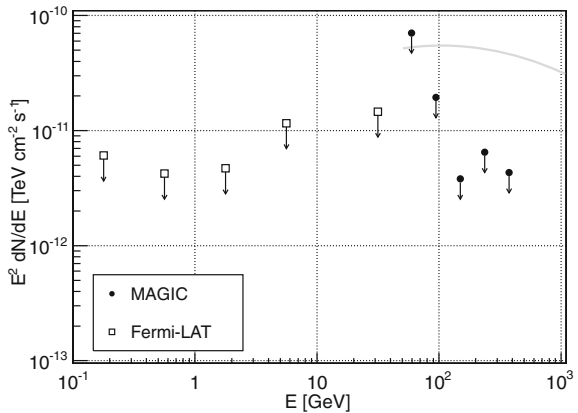
Assuming a photon spectral index of 2.6 we obtain a 95 % C.L. ULs of $5.0 \times 10^{-12}\,\text{cm}^{-2}\text{s}^{-1}$ above 300 GeV, which corresponds to 4 % C.U. Differential ULs in bins of energy are shown in Fig. 10.3. The values can be found in Table 10.1.

Also at GeV energies no emission was detected from YY Her. Observations of this source with *Fermi*-LAT led to a 95 % C.L. UL on the flux above 100 MeV

Table 10.1 Differential ULs on the flux from YY Her measured by *Fermi*-LAT and MAGIC. The bins spans from E_{min} to E_{max}, while the UL value is computed at the energy of E_{UL}. Credit: Ahnen et al. (2015), reproduced with permission © ESO

E_{min} [GeV]	E_{max} [GeV]	E_{UL} [GeV]	F_{UL} [TeV cm^{-2}s^{-1}]
Fermi-LAT, MJD 56392.5-56412.5			
0.100	0.316	0.178	6.1×10^{-12}
0.316	1.00	0.562	4.2×10^{-12}
1.00	3.16	1.78	4.7×10^{-12}
3.16	10.0	5.62	1.2×10^{-11}
10.0	100.0	31.6	1.5×10^{-11}
MAGIC, MJD 56405			
50.0	79.2	59.4	7.1×10^{-11}
79.2	125.6	94.2	1.9×10^{-11}
125.6	199.1	149.3	3.8×10^{-12}
199.1	315.4	236.6	6.5×10^{-12}
315.4	500.0	375.1	4.3×10^{-12}

of 2.8×10^{-8} ph cm^{-2} s^{-1} in the time period between MJD 56392.5 and 56412.5 assuming a spectral index of 2.2. The differential UL, computed between 100 MeV and 100 GeV are shown in Table 10.1.

10.3.2 ASASSN-13ax

ASASSN-13ax is a CV star which underwent a very strong ∼7.7 mag outburst on MJD 56474 (Stanek et al. 2013). The optical spectrum seems to be disk-dominated with features suggesting a hydrogen-rich DN (Copperwheat et al. 2013). The large outburst amplitude suggests that ASASSN-13ax is a WZ Sge-type. This object has a counterpart called SDSS J180005.88+525632.6.

The origin of outbursts in DN is different than the one in classical and symbiotic novae, so as it is not certain if GeV and TeV emission can occur in them, MAGIC in its novae observation program does not normally follow DN. However the very strong optical outburst and uncertain classification just after the outburst encouraged MAGIC to observe this source (Fig. 10.4).

The MAGIC observations were performed on two consecutive nights starting MJD 56478.

Good weather conditions allowed to observe for a total time of 9.5 h. No significant γ-ray excess was found. Due to higher Zd range than in the case of Her YY (24°–39°) the energy threshold of this analysis of the above plot is also higher. Assuming a spectral index of 2.6 we obtain a 95 % C.L. UL of 1.5×10^{-12} cm^{-2}s^{-1} above 300 GeV, which corresponds to 1.2 % of Crab Nebula flux. The corresponding differential ULs in bins of energy can be found in Table 10.2 (Fig. 10.5).
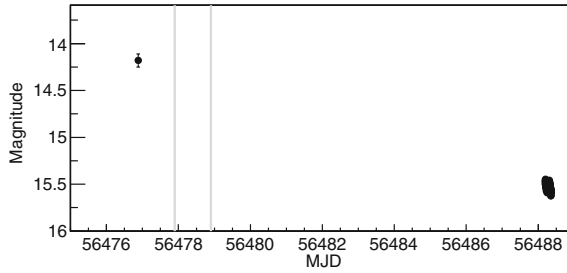
Fig. 10.4 Optical observations in V band of ASASSN-13ax during the outburst in July 2013. The data points are obtained from AAVSO-LCG service. The *grey* vertical line shows the two observation nights with MAGIC

Table 10.2 Differential ULs on the flux from ASASSN-13ax measured by *Fermi*-LAT and MAGIC (see text for details). Columns as in Table 10.1. Credit: Ahnen et al. (2015), reproduced with permission © ESO

E_{min} [GeV]	E_{max} [GeV]	E_{UL} [GeV]	F_{UL} [TeV cm^{-2}s^{-1}]
Fermi-LAT, MJD 56468.5–56488.5			
0.100	0.316	0.178	3.3×10^{-12}
0.316	1.00	0.562	3.7×10^{-12}
1.00	3.16	1.78	2.6×10^{-12}
3.16	10.0	5.62	1.4×10^{-11}
10.0	100.0	31.6	1.5×10^{-11}
MAGIC, MJD 56478–56479			
79.2	125.6	94.2	1.2×10^{-11}
125.6	199.1	149.3	1.2×10^{-12}
199.1	315.4	236.6	1.7×10^{-12}
315.4	500.0	375.1	7.3×10^{-13}
500.0	792.4	594.4	1.1×10^{-12}
792.4	1255.9	942.1	7.9×10^{-13}
1255.9	1990.5	1493.1	9.1×10^{-13}
1990.5	3154.7	2366.4	1.7×10^{-12}
3154.7	5000.0	3750.5	9.3×10^{-13}

No GeV emission was observed from the direction of ASASSN-13ax. *Fermi*-LAT observations put a 95 % C.L. UL on the flux of the source above 100 MeV at the level of 1.6×10^{-8}cm^{-2} s^{-1} in the time period MJD 56468.5 to 56488.5. The differential ULs between 100 MeV and 100 GeV can be found in Table 10.2.

Fig. 10.5 Differential ULs on the flux from ASASSN-13ax measured by MAGIC (filled circles) and *Fermi*-LAT (empty squares). For comparison a spectrum of Crab Nebula is shown with a *grey* curve
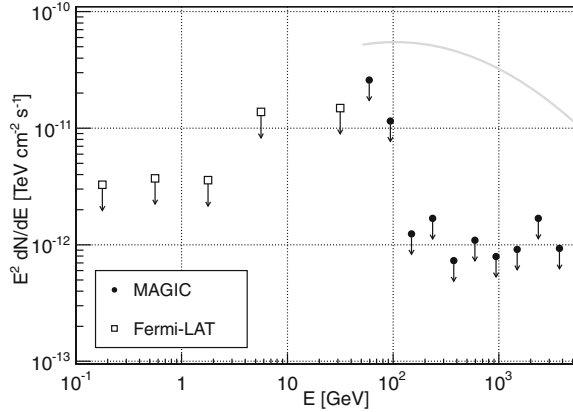
10.3.3 V339 Del

V339 Del was a fast, CN detected by optical observations on MJD 56520 (CBET #3628). The nova was exceptionally bright reaching a magnitude of V∼ 5 mag (see top panel of Fig. 10.6), and it triggered follow-up observations at frequencies ranging from radio to VHEgamma rays. Photometric measurements suggest a distance for V339 Del of 4.5 ± 0.6 kpc Schaefer et al. (2014). Nearly a month after the optical detection, X-ray emission was detected in the 1–10 keV energy band by *Swift*/XRT (Page et al. 2013). Afterwards, the object became a super-soft X-ray source, with most of the photons detected in the 0.3–1 keV energy range (Osborne et al. 2013). The object shows large amplitude variations and a 54 s quasi-periodic oscillation in the soft X-ray energy band. They are possibly explained by the spin of the WD or an oscillation in the nuclear burning rate (Beardmore et al. 2013; Ness et al. 2013). The spectroscopic observations performed on MJD 56522.1 revealed emission wings extending to about ± 2000 km/s and a Balmer absorption component at a velocity of 600 ± 50 km/s (Shore et al. 2013a). The pre-outburst optical images revealed the progenitor of nova V339 Del to be a blue star (Denisenko et al. 2013).

Originally MAGIC observations of V339 Del were motivated by its extreme optical outburst. Soon after MAGIC started observations they were additionally supported by the detection of GeV emission by *Fermi*-LAT from the direction of V339 Del. The MAGIC observations started on the night of MJD 56520, however they were marred by bad weather conditions. The good quality data used for most of the analysis span 8 nights between MJD 56529 and 56537. The total effective time was 11.6 h. In addition to the nightly ULs we performed a dedicated analysis of the poor quality (affected by calima, a dust layer originating from Sahara) night of MJD 56520. We applied an estimated energy and collection area correction based on LIDAR measurements (Fruck et al. 2014). No VHEγ-ray signal was found from

Fig. 10.6 Multiwavelength light curve of V339 Del during the outburst in August 2013. *Top panel* optical observations in the V band obtained from AAVSO-LCG (http://www.aavso.org/lcg) service. *Middle panel Fermi*-LAT flux (filled symbols) and ULs (empty symbols) above 100 MeV in 1-day (circles, thin red lines) or 3-day (squares, thick *blue lines*). A 95 % C.L. flux UL is shown for time bins with TS<4. *Bottom panel* UL on the flux above 300 GeV observed with MAGIC telescopes. The *grey* bands show the observation nights with MAGIC
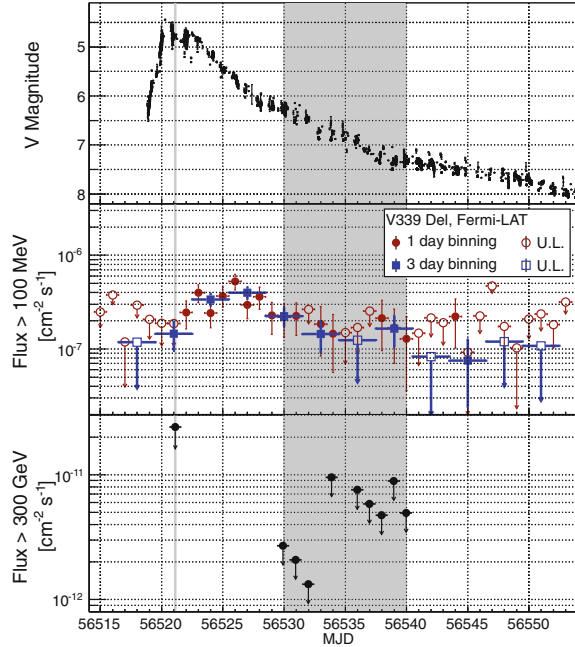
the direction of V339 Del. We computed a nightly integral ULs above 300 GeV (see bottom panel of Fig. 10.6) and differential ULs for the whole good quality data set in bins of energy (see Sect. 10.4).

Nova V339 Del was the subject of a *Fermi*-LAT Target of Opportunity (ToO) observation (Hays et al. 2013) triggered by the optical discovery (CBET #3628); the ToO started on MJD 56520 and lasted for six days. The γ-ray emission from V339 Del was first detected by *Fermi*-LAT in 1-day bins on MJD 56522 (Ackermann et al. 2014). The emission peaked on MJD 56526 and entered a slow decay phase afterwards (Fig. 10.6). For the light curves, the data were fitted using a power-law spectral model initially leaving the spectral index and the normalization free to vary. We then fixed the spectral index at the average value of 2.3 calculated over the most significant detections (TS > 9) to generate the plots shown in the middle panel of Fig. 10.6. The LAT SED of V339 Del shown in Fig. 10.8 was extracted in five logarithmically spaced energy bins from 100 MeV to 100 GeV. Similarly to the light curves, energy binned data shown in Fig. 10.8 were fitted using a simple power-law and showing a 95 % C.L. ULs for TS < 9. In the period coincident with the MAGIC observations (MJD 56529 to 56539) the *Fermi*-LAT spectrum can be described by an effective power-law with a spectral index of 2.37 ± 0.17 and flux above 100 MeV of $(0.15 \pm 0.04) \times 10^{-6} \mathrm{cm}^{-2}\,\mathrm{s}^{-1}$. The rather low statistical significance (TS = 49) does not constrain the value of an exponential cut-off of the emission in this period. Note, however, that the most energetic photon, with $E = 5.9$ GeV was recorded on MJD 56534, i.e. within the time period covered by MAGIC. The *Fermi*-LAT

analysis for a broader time range, MJD 56526–56547, covering the whole decay phase of the *Fermi*-LAT light curve allowed us to obtain a more significant signal with a TS of 121. Nevertheless we obtain a similar value of flux above 100 MeV, $(0.13 \pm 0.03) \times 10^{-6} \text{cm}^{-2} \text{s}^{-1}$, for this broader period. The spectrum in this case can be described, with a 3.3σ significance higher with respect to the simple power-law, by an exponentially cut-off power-law with a spectral index of 1.44 ± 0.29 and a cut-off energy of $1.6 \pm 0.8\,\text{GeV}$.

10.4 Modeling of Gamma-Rays from Nova V339 Del

Out of the three objects observed by MAGIC and discussed in this chapter, V339 Del is the only one detected by *Fermi*-LAT. Moreover, it was also extensively observed in the optical band which sheds some light on both the companion star and the photosphere of the nova. Therefore, it has the highest potential for constraining the leptonic and hadronic processes in novae, and we concentrate the modeling efforts on it.

In order to understand the physical implications of this observation, I will describe the model that is used in Ahnen et al. (2015) in preparation. This model follows the original one in Sitarek et al. (2012) which was originally applied to the symbiotic nova V407 Cyg. In that case, the GeV γ-ray emission was attributed to IC up-scattering of the electrons on the strong radiation field in the vicinity of the red giant companion star. On the contrary, the radiation field of the companion star is not as strong for V339 Del. Instead, the photosphere of the nova provides a dominant target for the IC process. Moreover, the wind of the companion star is not as dense as in the V407 Cyg symbiotic system. Nevertheless, if protons of sufficient energy are accelerated in the nova shock, they can still interact with the ejecta of the nova producing pions. As in Sitarek et al. (2012) the GeV γ-ray emission can be used for constraining the parameters describing the acceleration of the electrons, which are otherwise poorly known. Protons will be then accelerated in the same conditions, however up to much higher energies due to lower energy losses.

In order to apply the above model we need to evaluate the radiation field which is encountered by electrons at the time of the observations by MAGIC and *Fermi*-LAT. Therefore we need to estimate first the parameters of the nova photosphere about 10 days after the optical detection. The spectral evolution of V339 Del was studied by Metzger et al. (2015). During the time of the observations by MAGIC the reported temperature of the photosphere was $\sim$7000 K. With a reported optical luminosity of $\sim$$6 \times 10^4 L_\odot$ this corresponds to a radius of the photosphere of 1.2×10^{13} cm (see Table 10.3). The solution describes roughly the optical continuum emission observed by NOT (see Fig. 10.7).

As there are no UV measurements available in this late stage of the V339 Del outburst we also use another approach for obtaining the photosphere parameters. We use NOT optical observations of V339 Del combined with UV observations of a similar CO nova, OS And, performed in the same optically thick stage at the

Table 10.3 Parameters characterizing the optical emission of the V339 Del nova according to the two scenarios (see Fig. 10.7) assumed in the modeling of the GeV and TeV emission

	T (K)	R_{ph} (cm)	$L/L_\odot$
Metzger et al. (2015)	0.7×10^4	1.2×10^{13}	6×10^4
optical+UV	1.3×10^4	0.4×10^{13}	8×10^4

Fig. 10.7 *Thin black lines* optical spectrum of V339 obtained by NOT on MJD 56532 (above 3500 Å) and scaled UV spectrum of OS And nova in SWP and LWP ranges (points obtained from Shore, S. N. 2015, in preparation). *Thick lines* the spectra are overlaid with simple black-body photosphere modelings of Metzger et al. (2015) (*blue dashed line*) and one taking into account also SWP and LWP ranges (*red solid line*). The assumed distance of V339 Del is 4.5 kpc

time of the MAGIC and *Fermi*-LAT observations. Such stacking of two sources is possible because the STIS UV spectra of V339 Del (taken about a month after the outburst) follow closely the shape of the OS And observations with the IUE obtained between 12 and 21 days after optical discovery (Shore et al. 2013b). The similarity of the two sources is further supported by the fact that the distance estimation of V339 Del obtained from spectral comparison with OS And (Shore 2013) is in line with the estimation from expansion parallax (Schaefer et al. 2014). The OS And spectral points are available in two UV ranges: Short Wavelength Primary (SWP) (1150–2000 Å) and Long Wavelength Primary (LWP) (2000–3200 Å). The OS And UV spectra are calibrated, corrected for extinction and scaled due to the different distance to the ones of V339 Del using UV measurements performed at a later time with the STIS (Shore, S.N. 2015, in preparation, Shore et al. 2013b). The resulting spectrum can be roughly fit with a black body with a temperature 13000 K and a radius 4×10^{12} cm. Due to the uncertainty in the radiation field of the photosphere, mostly in the UV band, we use both sets of parameters, which bracket the possible range of the temperature and the luminosity.

Let us consider a photosphere of radius $R_{ph} = 10^{13} R_{ph,13}$ cm and temperature $T_{ph} = 10^4 T_4$ K. Leptons and hadrons are accelerated at a distance $R_{sh} = 10^{13} R_{sh,13}$ cm from the photosphere. Assuming that the velocity of the shock is

~1000 km/s, similar to the one observed in another GeV-emitting nova (Chomiuk et al. 2014), we estimate that during the MAGIC observations the distance to the shock was $R_{sh} \sim 10^{14}$ cm. The gamma rays with energy $E_\gamma = 10E_{10}$ GeV can be produced via IC scattering in the Thomson regime of thermal photons by electrons with energy of:

$$E_e = 22 \times E_{10}^{1/2}/(T_4(1 + \cos\beta))^{1/2} \text{ [GeV]}, \tag{10.1}$$

where β is the angle between the electron and the direction to the point on the photosphere where the thermal photon was emitted. On the other hand, by comparing the energy losses on the IC scattering with the acceleration rate we obtain that the maximum energies of electrons are (see e.g. Sitarek et al. (2012)):

$$E_{e,\max} = 13(\xi_{-4}B)^{1/2}R_{sh}/(T_4^2 R_{ph}) \text{ [GeV]}, \tag{10.2}$$

where B is the magnetic field at the shock (measured in Gauss), and $\xi = 10^{-4}\xi_{-4}$ is the acceleration coefficient. By comparing the above two formulae we obtain:

$$\xi_{-4}B = 2.9E_{10}T_4^3 R_{ph}^2/(R_{sh}^2(1 + \cos\beta)), \tag{10.3}$$

In the same conditions protons with energy E_p (measured in units of GeV) can be accelerated with a time scale of:

$$\tau_{acc,p} = 1E_p/(\xi_{-4}B) = 0.34\frac{E_p R_{sh}^2(1 + \cos\beta)}{E_{10}T_4^3 R_{ph}^2} \text{ [s].} \tag{10.4}$$

The acceleration can be limited both by the dynamic time scale of $t_d \sim 10$ days (after which time most of the MAGIC observations were performed), or by the energy losses of protons from the pp collisions. The time scale of the latter can be computed as:

$$\tau_{pp} = (\sigma_{pp}n_H kc)^{-1}, \tag{10.5}$$

where $\sigma_{pp} \approx 3 \times 10^{-26} \text{cm}^2$ is the interaction cross section, n_H is the density of the nova ejecta, the inelasticity coefficient, $k \approx 0.5$, is the fraction of energy lost in each interaction, and c is the speed of light. The density of the ejecta will be decreasing as the nova shock progresses with the speed of $v = 10^3 v_3$ km s^{-1} following:

$$n_H = 4.4 \times 10^{12} M_{-5}/(v_3^3 t_d^3) \text{ [cm}^{-3}], \tag{10.6}$$

where $10^{-5}M_{-5}M_\odot$ is the total mass ejected during the outburst. Thus:

$$\tau_{pp} = 500(v_3^3 t_d^3)/M_{-5} = 780R_{sh,13}^3/M_{-5} \text{ [s]}, \tag{10.7}$$

where we used that $R_{sh} = v(86400\,t_d)$.

By comparing the acceleration and cooling time scales we obtain:

$$E_p = 2300 \frac{E_{10} T_4^3 R_{ph,13}^2 R_{sh,13}}{(1 + \cos \beta) M_{-5}} \, [\text{GeV}]. \tag{10.8}$$

Therefore, using the parameters of the photosphere obtained by Metzger et al. (2015) (see Table 10.3) a fortnight after the peak and taking into account the break in the GeV spectrum at $\sim$1.6 GeV, it is plausible to expect protons being accelerated at least up to energies of $\sim$1.6 TeV. Smaller maximum energy of protons, 1.1 TeV is expected in the case of the second set of photosphere parameters computed from the optical+UV fit.

The acceleration can be also limited by the dynamic time scale rather than hadronic interaction losses. By comparing the dynamic time scale with the proton cooling time scale we obtain that the former starts to dominate only after $13 M_{-5}^{1/2} v_3^{-3/2}$ days. Therefore the accelerated protons will mostly cool down on the time scale of the MAGIC

Fig. 10.8 Differential ULs on the flux from V339 Del measured by MAGIC (filled squares) and the flux measured by *Fermi*-LAT (empty crosses) in the period between MJD 56529 and 56539. The thin *solid line* shows the IC scattering of thermal photons of the nova's photosphere. The *dashed line* shows the gamma rays coming from the decay of π^0 from hadronic interactions of the relativistic protons with the nova ejecta. The *dotted line* shows the contribution of gamma rays coming from IC of e^+e^- originating from $\pi^+\pi^-$ decays. *Thick solid lines* show the total predicted spectrum. Electrons and protons are injected with a power-law with a spectral index of 1.5 and the cut-offs reported in the figures. Photosphere parameters (see Table 10.3) by Metzger et al. (2015) (*left panels*) or from optical+UV fit (*right panels*). *Top panels* $L_p = L_e$, bottom panels for obtained L_p/L_e limits, i.e. $L_p = 0.1L_e$ or $L_p = 0.15L_e$ (see top right corner of panels)

observations. The normalization of both components is determined by L_p/L_e, i.e. the ratio of total power of accelerated protons to the one of electrons.

The modified version of Sitarek et al. (2012) is used to adjust the *Fermi*-LAT GeV spectrum and constrain the maximum proton luminosity compared to that of electrons using MAGIC observations. We consider that the electrons and protons accelerated in Fermi-like acceleration obtain a power-law energy spectrum with a spectral index of 1.5. The cut-off energies in the spectra of electrons and protons can be determined by Eqs. 10.2 and 10.8 respectively. In Fig. 10.8 we show the predictions for lepton/hadron spectrum compared with *Fermi*-LAT and MAGIC measurements.

The *Fermi*-LAT spectrum can be described mostly by IC scattering of the photosphere thermal photons by electrons. In the case of equal power of accelerated protons and electrons (i.e. $L_p = L_e$), the expected hadronic component predicts a flux higher than the MAGIC ULs at ~ 100 GeV by a factor of a few. Using the ULs from the MAGIC observations we can place a limit on $L_p \lesssim 0.1 - 0.15 L_e$ depending on the assumed parameters of the photosphere (see bottom panels of Fig. 10.8).

10.5 Conclusions

We performed observations of three CVs during a period of enhanced emission: the symbiotic nova YY Her, the DN ASASSN-13ax and the CN V339 Del. No VHEγ-ray emission was found. Contemporaneous *Fermi*-LAT observations revealed GeV emission from V339 Del. We modeled this GeV emission as due to IC of thermal photons from the photosphere by the GeV electrons accelerated in the nova shock. We used the *Fermi*-LAT and MAGIC observations of V339 Del to constrain the amount of protons accelerated in the same conditions as the electrons in the nova shock. The modeling shows that the total power of the accelerated protons must be much smaller ($\lesssim 15\%$) than that of electrons for two sets of plausible photosphere parameters. MAGIC will continue follow-up observations of promising nova candidates in the following years. Part of the results presented in this chapter are published in Ahnen et al. (2015).

References

Abdo AA et al (2010) Science 329:817
Ackermann M et al (2014) Science 345:554
Ahnen ML et al (2015) A&A 582:A67
Aliu E et al (2012) Apj 754:77
Atwood WB et al (2009) Apj 697:1071
Beardmore AP et al (2013) Astron Telegr 5573:1
Cheung CC et al (2013) Astron Telegr 5653:1
Cheung CC et al (2014) Astron Telegr 5879:1
Cheung CC et al (2015) Astron Telegr 7283:1

Chomiuk L et al (2014) Nature 514:339
Copperwheat CM et al (2013) Astron Telegr 5195:1
Denisenko D et al (2013) IAU Circ 9258:2
Fruck, C., et al. 2014, arXiv:1403.3591
Hays E et al (2013) Astron Telegr 5302:1
Herbig GH (1950) PASP 62:211
Martin P et al (2013) A& A 551:A37
Mattox JR et al (1996) Apj 461:396
Metzger, B. D., et al. 2015, arXiv:1501.05308
Munari U et al (1997) A&A 323:113
Munari U et al (2013) Astron Telegr 4996:1
Ness JU et al (2013) Astron Telegr 5626:1
Nolan PL et al (2012) ApJS 199:31
Osborne JP et al (2013) Astron Telegr 5505:1
Page KL et al (2013) Astron Telegr 5429:1
Schaefer GH et al (2014) Nature 515:234
Shore SN et al (2013a) Astron. Telegr. 5312:1
Shore SN et al (2013b) Astron Telegr 5409:1
Shore SN (2013) Astron Telegr 5410:1
Sitarek J et al (2012) Phys Rev D 86:063011
Stanek KZ et al (2013) Astron Telegr 5186:1
Tatischeff V et al (2007) Apj 663:L101

Chapter 11
Summary and Concluding Remarks

During the period of my thesis, I have worked on the development of an analog trigger system to be used in the analog cameras of LSTs and MSTs of CTA. The final hardware option selected for the L0 trigger is the ASIC trigger. I participated in the preparation of the setup for the quality control that is currently taking place and developed the software to analyze the results automatically. We have already fully characterized 30 chips and are currently characterizing the rest of the L0 ASICs to be installed in 2016 in the LST prototype camera in La Palma. We performed simulations of the different implementations of the analog trigger in the LST and MST cameras. We found that the trigger option that achieves the lowest energy threshold is the sum trigger. Using this option and triggering in stereo with the LSTs, we can achieve a trigger energy threshold of $\mathcal{O}(10)$ GeV. We showed that the collection area of the telescope significancy worsens for the most aggressive scenarios if the FWHM of the PMTs is larger than 3.0 ns.

We developed a new trigger system for the MAGIC telescope that uses the spatial information of the triggers issued in both MAGIC cameras to reduce the energy threshold. Using this information we manage to eliminate 85 % of the triggers due to accidental events, which allows us to decrease the DT while keeping the same global trigger rate of the original trigger system. The DT reduction translates into an 8 % improvement in the analysis energy threshold of the telescopes. The improvement in collection area is ∼60 % at the lowest energies and between 10 and 20 % at the energy threshold, where most of the events are recorded. We also showed, using telescope's data recorded with the original trigger but filtered through the Topo-trigger algorithm, that the sensitivity and γ-ray rate are not affected. A full implementation of the Topo-trigger in the MAGIC telescope is currently taking place.

Regarding the study of PWNe, I worked in this thesis with the most and the least luminous PWNe in the VHE γ-ray regime: the Crab Nebula and 3C 58. We tested different functions to fit the Crab Nebula spectrum between 400 GeV and 80 TeV. We found that a single power-law does not provide a good fit to the spectrum. A log-parabola and a power-law with a cut-off provide a good fit to the data, although the fit probability for a log-parabola is higher. The cut-off energy obtained for the

power-law with a cut-off is $\sim$30 TeV, more than double the energy reported by HESS in the past. Using a toy MC, we showed that the measurement presented in this thesis deviates from HESS fit to the Crab Nebula spectrum with a significance larger than 2σ. We also studied the VHE γ-ray flux variability of the Crab Nebula during flaring episodes at MeV energies, but we did not find any significant enhanced emission at TeV energies. We established that the linear correlation between the Crab Nebula flux above 100 MeV and above 1 TeV during flares is $<4.7 \times 10^{-4}$ at a 95 % C.L. We established ULs on the integral flux for an additional component in the spectrum $F < 7.4 \times 10^{-13}$ cm^{-2} s^{-1} above 1 TeV and $F < 2.0 \times 10^{-12}$ cm^{-2} s^{-1} above 10 TeV. In the context of Bednarek and Idec (2011) model, the only possibility to explain the MeV enhancement and the flux ULs measured at TeV is that it is produced by an injection of a new population of electrons with a change only in their maximum energy. In the framework of Kohri et al. (2012), a $\Gamma \gtrsim 100$ in the flaring region is also ruled out.

We discovered VHE γ-ray emission from 3C 58 and put it into context with the rest of PWNe and PWN candidates detected at TeV energies. We showed that 3C 58 is the less efficient PWN in this energy regime, making it closer to the Crab Nebula, which is the second. We compared the results obtained with the state of the art PWN models predicting emission for 3C 58. The broadband spectrum of the source can be explained if we assume a distance of 2 kpc or an unexpectedly high local FIR component, both of them assuming an age of 2.5 kyr. We favor the explanation of a 2 kpc distance to the PWN. The magnetic field derived by all the models is below equipartition, as for the rest of PWNe detected at TeV energies. We did not find any significant VHE γ-ray pulsed signal from PSR J0205+6449, the pulsar powering 3C 58. We established relations between the X-ray (L_X) and γ-ray (L_γ) luminosities of PWNe and PWN candidates detected at VHE and the properties of their central pulsar. We found that L_γ is not dependent on $\dot{E}$ or τ and L_X is correlated with $\dot{E}$ and anti-correlated with τ. As expected, the ratio L_γ/L_X is anti-correlated with $\dot{E}$ and correlated to τ. We found that $L_\gamma/L_X \propto \tau^{1.5\pm0.3}$ and $L_\gamma/L_X \propto \dot{E}^{-0.9\pm0.3}$, close to the values expected assuming that the X-ray emitting electrons are in the cooled regime and the γ-ray emitting ones are in the uncooled regime. In spite of being a young and low magnetic field PWN, 3C 58 is not an outlier of these relations.

We observed the CV AE Aqr in a multiwavelength campaign including X-ray and optical observations. We did not detect any significant VHE γ-ray steady emission during the whole observation period, neither during high optical or X-ray states. We searched for pulsed emission at the rotation frequency of the WD, its first harmonic and at different frequencies using the Rayleigh test. We did not find any significant signal in any of these searches either. We established the most restrictive ULs for the steady and pulsed VHE γ-ray emission of AE Aqr reported so far, up to three orders of magnitude lower than some of the signals claimed by the Nooitgedacht and Durham groups about two decades ago. We conclude that the model presented in Meintjes and de Jager (2000) is not suitable to predict the γ-ray emission for AE Aqr.

We observed three additional CVs during a period of enhanced emission: the symbiotic nova YY Her, the DN ASASSN-13ax and the CN V339 Del. We did not

find any hint of VHE emission in any of the searches performed. Out of the three CVs observed, only V339 Del showed GeV emission detected by *Fermi*-LAT. We used the model in Sitarek and Bednarek (2012) to constrain the amount of protons accelerated in the nova shock. According to the model, the total power of the accelerated protons must be $\lesssim 15\%$ that of the electrons accelerated in the shock.

References

Bednarek W et al (2011) MNRAS 414:2229
Kohri K et al (2012) MNRAS 424:2249
Meintjes PJ et al (2000) MNRAS 311:611
Sitarek J et al (2012) Phys. Rev. D 86:063011

Appendix A
Mathematical Calculations

A.1 Weighting the MC

MC gamma rays are simulated with a given function $f(E)$ dependent of the energy. Usually this function is a power law with spectra index Γ_{sim}:

$$f_{\text{sim}}(E) \propto E^{-\Gamma_{\text{sim}}} \tag{A.1}$$

The spectral index Γ_{sim} is chosen in a way that the simulation will provide good statistics at any simulated energy range. In MAGIC or CTA simulations shown in this thesis, the Γ chosen for the MC production is $\Gamma_{\text{sim}} = 2.0$ or $\Gamma_{\text{sim}} = 1.6$ respectively. When one wants to measure physical properties of a given source, the simulated spectrum needs to be weighted to match the spectrum of the source we are trying to analyze. The total number of events after weighting N_{weighted} is given by:

$$N_{\text{weighted}} = \sum_{n=0}^{N \text{sim}} \frac{f_{\text{source}}(E_n)}{f_{\text{sim}}(E_n)} \tag{A.2}$$

where E_n is the energy of the event n, N_{sim} the total number of events simulated and $f_{\text{source}}(E)$ the spectrum assumed for the source. In the case of the energy threshold, we weight the spectrum to match a power-law with spectral index $\Gamma_{\text{source}} = 2.6$.

A.2 Calculation of Stereo NSB Rate from Single-Telescope NSB Rate

We would like to calculate the stereo rate due to NSB for an array of telescopes. This rate is theoretically independent on the position of the telescopes, so the probability of having a stereo trigger is the addition of the probabilities of having trigger in two

or more telescopes. We will show here the calculations in the case of the LST array, composed by four telescopes.

If the single-telescope NSB rate R is already known, the probability P of having a trigger is $P = R \times$ Coincidence window. The Coincidence window we have used is 100 ns. As $(1-P)$ is the probability of not having a trigger in a telescope, the probability of having a trigger (P_2) in two or more telescopes is given by:

$$P_2 = PPPP + PPP(1-P) \times 4 + PP(1-P)^2 \times 6$$

as we have one scenario where the four telescopes trigger, four where three telescopes trigger and one not, and six where two telescopes trigger and the others two not. Finally, the probability of having stereo trigger due to NSB is:

$$P_2 = 3P^4 - 8P^3 + 6P^2.$$

A.3 Solving Gaussian Integrals

A Gaussian distribution with mean μ and standard deviation σ is given by:

$$P(x) = \frac{1}{\sigma\sqrt{2\pi}} \exp\left\{ -\frac{(x-\mu)^2}{2\sigma^2} \right\} dx \qquad (A.3)$$

Since this probability is normalized, it means that the integral for the x domain is:

$$\int_{-\infty}^{\infty} \frac{1}{\sigma\sqrt{2\pi}} \exp\left\{ -\frac{(x-\mu)^2}{2\sigma^2} \right\} dx = 1 \qquad (A.4)$$

As $P(x)$ is an even function, the integral:

$$\int_{0}^{\infty} \frac{1}{\sigma\sqrt{2\pi}} \exp\left\{ -\frac{(x-\mu)^2}{2\sigma^2} \right\} dx = \frac{1}{2} \qquad (A.5)$$

If we wish to compute the integral up to a given number a different from infinity, we have to make a variable change $z \equiv (x-\mu)/\sigma$:

$$\int_{0}^{a} \frac{1}{\sigma\sqrt{2\pi}} \exp\left\{ -\frac{(x-\mu)^2}{2\sigma^2} \right\} dx = \int_{0}^{(a-\mu)/\sigma} \frac{1}{\sqrt{2\pi}} \exp\left\{ -\frac{z^2}{2} \right\} dz = \frac{1}{2}\mathrm{erf}\left(\frac{a-\mu}{\sigma\sqrt{2}} \right) \qquad (A.6)$$

A.4 Measurement of the Magnitude of a Star

The magnitude of a star is the measurement of the brightness of the object for a given range of wavelengths. It is usually used in the optical or near-IR. It is measured with respect to the brightness of a known star using the following equation:

$$m_x - m_{ref} = -2.5 \log_{10} \left(\frac{F_x}{F_{ref}} \right) \tag{A.7}$$

where m_{ref} and F_{ref} are the magnitude and flux of the reference star respectively, and m_x and F_x the magnitude and flux of the star we are measuring respectively. According to this formula, the brighter the object, the lower the magnitude. Some magnitude examples in the visible band are Sirius ($m = -1.46$) or the Sun ($m = -27$).

Appendix B
Additional Tables

B.1 Requirements and Measurements for the L0 Trigger ASICs

See Table B.1.

Table B.1 Requirements and measurements for the L0 trigger ASICs

	Requirement	Measurement
Comparator efficiency at 1phe	>95 %	Not measured
Comparator purity at 1phe	>99.99 %	∼6 σ
Linearity comparator	±5 % or 0.25 phe	<10 %
Width output comparator	ToT ±5 %	Checked
Output noise	<1 phe or	500 μV (Sum)
	20 % at comparator level	500 μV (Maj.)
Latency	<10 ns	<6 ns (Sum); 10.3 ns (Maj.)
Power consumption	<150 mW/channel	86 mW/channel
Cost	<10 euros/channel	5 euros/channel (for 8 LSTs)
Failure rate	0.1 %/year	Cannot be measured

B.2 DTs and Operation Points Assuming Different FWHMs for the PMT Signals

See Table B.2.

Table B.2 DTs for the different clipping levels, scenarios considered and for several FWHMs

FWHM (ns)	DT [phe]					
	Sum Clip 8			Sum Clip 6		
	Safe	Aggressive	$1\times$ NSB	Safe	Aggressive	$1\times$ NSB
2.0	32.6	30.0	25.3	32.7	29.9	23.7
2.2	34.6	31.0	25.3	33.8	30.7	24.8
2.4	34.6	32.6	25.7	33.8	32.4	25.4
2.6	35.6	33.6	26.6	34.7	33.2	26.4
2.8	36.7	33.8	27.4	34.7	33.4	27.5
3.0	37.7	33.9	27.8	34.7	33.0	27.7
3.2	37.7	34.9	28.4	34.8	33.9	28.5
3.4	37.7	35.7	29.4	35.7	34.7	29.5
3.6	38.7	36.4	29.7	35.8	34.9	29.7
3.8	39.0	37.6	30.5	37.7	36.4	30.5
4.0	39.0	36.7	31.7	38.1	35.6	31.8

B.3 Topo-Trigger Selection Tables Depending on the Azimuth

See Table B.3.

Table B.3 Topo-trigger macrocells selected depending on the Azimuth

	Macrocells selected in M2					
Az cuts	19–49	49–79	79–109	109–139	139–169	169–199
M1 Macr.						
0	0, 1, 2	0, 1, 2, 6	0, 1, 6	0, 1, 5, 6	0, 5, 6	0, 5, 6
1	1, 7, 8	1, 7, 8, 18	1, 7, 18	1, 7, 18	1, 6, 18	1, 6, 18
2	2, 8, 9	1, 2, 8, 9	1, 2, 8	0, 1, 2, 8	0, 1, 2	0, 1, 2, 3
3	2, 3, 10	0, 2, 3, 10	0, 2, 3	0, 2, 3, 4	0, 3, 4, 12	0, 3, 4, 12
4	0, 3, 4	0, 3, 4, 5	0, 4, 5	0, 4, 5	4, 5, 14	4, 5, 14
5	0, 5, 6	0, 5, 6, 16	5, 6, 16	5, 6, 15, 16	5, 6, 15, 16	5, 14, 15, 16
6	1, 6, 18	1, 6, 17, 18	6, 17, 18	6, 17, 18	6, 16, 17	5, 6, 16, 17
7	7, 8	7	7	7, 18	7, 18	7, 18
8	8, 9	7, 8	7, 8	7, 8	1, 7, 8	1, 2, 7, 8

(continued)

Table B.3 (continued)

	Macrocells selected in M2					
Az cuts	19–49	49–79	79–109	109–139	139–169	169–199
M1 Macr.						
9	8	8, 9	8, 9	8, 9	2, 8, 9	2, 8, 9, 10
10	9, 10	9, 10	2, 9, 10	2, 9, 10	2, 3, 9, 10	2, 3, 10, 11
11	10, 11	10, 11	3, 10, 11	2, 3, 10, 11	3, 11, 12	3, 11, 12
12	3, 11, 12	3, 4, 11, 12	3, 4, 11, 12	3, 4, 11, 12, 13	4, 12, 13	4, 12, 13
13	4, 12, 13	4, 12, 13, 14	4, 13, 14	4, 13, 14	13, 14	13, 14
14	4, 5, 13, 14	4, 5, 14, 15	5, 14, 15	14, 15	14, 15	14, 15
15	5, 15, 16	5, 15, 16	15, 16	15, 16	15, 16	15
16	6, 16, 17	6, 16, 17	16, 17	16, 17	16, 17	15, 16
17	17, 18	17, 18	17, 18	17	17	16, 17
18	7, 18	7, 18	7, 18	17, 18	17, 18	17, 18
	Macrocells selected in M2					
Az cuts	199–229	229–259	259–289	289–319	319–349	349–19
M1 Macr.						
0	0, 4, 5	0, 3, 4, 5	0, 3, 4	0, 2, 3, 4	0, 2, 3	0, 2, 3
1	0, 1, 6	0, 1, 2, 6	0, 1, 2	0, 1, 2	1, 2, 8	1, 2, 8
2	0, 2, 3	0, 2, 3, 10	2, 3, 10	2, 3, 9, 10	2, 9, 10	2, 8, 9, 10
3	3, 4, 12	3, 4, 11, 12	3, 11, 12	3, 10, 11, 12	2, 3, 10, 11	2, 3, 10, 11
4	4, 13, 14	4, 12, 13, 14	4, 12, 13	4, 12, 13	3, 4, 12	3, 4, 12
5	5, 14, 15	4, 5, 14, 15	4, 5, 14	0, 4, 5, 14	0, 4, 5, 14	0, 4, 5, 6
6	5, 6, 16	0, 5, 6, 16	0, 5, 6	0, 5, 6	0, 1, 6	0, 1, 6, 18
7	1, 7, 18	1, 7, 8, 18	1, 7, 8	1, 7, 8	7, 8	7, 8
8	1, 2, 7, 8	1, 2, 8, 9	2, 8, 9	8, 9	8, 9	8, 9
9	2, 9, 10	2, 9, 10	9, 10	9, 10	9, 10	9
10	3, 10, 11	3, 10, 11	10, 11	10, 11	10, 11	9, 10
11	11, 12	11, 12	11, 12	11	11	10, 11
12	12, 13	12, 13	12, 13	11, 12	11, 12	11, 12
13	13, 14	13	13	12, 13	12, 13	12, 13
14	14, 15	13, 14	13, 14	13, 14	4, 13, 14	4, 5, 13, 14
15	15	14, 15	14, 15	14, 15	5, 14, 15	5, 14, 15, 16
16	15, 16	15, 16	5, 15, 16	5, 15, 16	5, 6, 15, 16	5, 6, 16, 17
17	16, 17	16, 17	6, 16, 17	6, 16, 17, 18	6, 17, 18	6, 17, 18
18	6, 17, 18	1, 6, 17, 18	1, 6, 7, 17, 18	1, 6, 17, 18	1, 7, 18	1, 7, 18

B.4   Observation Summaries

See Tables B.4, B.5, B.6, B.7 and B.8.

Table B.4 Summary of Crab Nebula observations at Zd > 50 during cycles VIII and IX without including the data from the March 2013 flare

Period	Dates	Time observed [h]
122	October–November 2012	0.82
123	November–December 2012	10.68
124	December 2012–January 2013	13.31
125	January–February 2013	16.08
126	February–March 2013	–
127	March–April 2013	–
128	April–May 2013	0.83
132	August–September 2013	3.50
133	September–October 2013	0.82
134	October–November 2013	0.65
135	November–December 2013	0.90
136	December 2013–January 2014	8.25
137	January–February 2014	4.37
138	February–March 2014	1.98
139	March–April 2014	4.83
140	April–May 2014	1.92
Total		68.94

Table B.5 Observation start and stop UT times for every night of Crab Nebula observations of the February–March 2013 flare

Starting date [MJD]	Observation interval	Time observed [h]	Zd
56350	2.22	20:15–23:48	6.7–47.9
56351	0.33	20:28–20:48	6.5–10.4
56351	0.93	22:20–23:36	30.6–46.2
56352	1.42	20:57–22:31	12.9–34.2
56353	1.71	20:06–21:59	5.9–25.6
56359	4.22	20:14–00:50	10.2–69.7
56360	3.99	20:13–00:50	11.7–69.8
56361	0.44	05:40–06:07	62.2–65.1
56361	0.24	20:18–20:33	12.3–14.6

(continued)

Table B.5 (continued)

Starting date [MJD]	Observation interval	Time observed [h]	Zd
56361	1.64	22:57–00:45	47.1–70.3
56362	3.09	21:22–00:41	27.2–69.5
56365	0.48	21:59–22:29	37.1–44.2
56368	0.15	22:17–22:27	43.7–45.6
56368	0.15	22:54–23:04	52.6–54.5
56370	0.25	22:41–22:56	51.7–54.2
56371	2.01	20:28–22:49	22.7–53.5
Total		23.27 h	

Table B.6 Summary of 3 C 58 observations with MAGIC on the cycles VIII and IX of observations

Period	Dates	Time observed [h]
131	July–August 2013	11.57
132	August–September 2013	10.35
133	September–October 2013	30.19
134	October–November 2013	13.86
135	November–December 2013	17.50
136	December 2013–January 2014	15.75
Total		99.32

Table B.7 Observation start and stop UT times for every night and every facility involved in the AE Aqr multiwavelength campaign. The number of minutes simultaneous to the MAGIC observations is included in brackets for each facility. Credit: (Aleksić et al. 2014a), reproduced with permission © ESO

Date [MJD]	KVA	Skinakas	Vidojevica	*Swift*	MAGIC
56062	–	–	–	04:35–04:54	–
56063	–	–	–	04:15–04:49	–
56064	03:39–05:07	–	–	03:04–03:24	–
56065	–	–	–	03:04–03:22	–
56066	–	–	–	03:10–03:28	–
56067	–	–	–	03:15–03:33	–
56068	03:20–04:18	–	–	03:19–03:37	–
56069	03:13–04:14	–	–	03:23–03:41	–
56071	–	–	–	03:30–03:49	–

(continued)

Table B.7 (continued)

Date [MJD]	KVA	Skinakas	Vidojevica	*Swif*	MAGIC
56072	–	–	–	03:33–03:54	–
56073	02:50–03:51 [43]	–	–	03:37–03:55	02:47–03:33
56074	02:47–03:54 [38]	–	–	03:40–03:57	02:40–03:25
56075	02:38–03:39 [43]	–	–	02:11–03:55 [43]	02:40–03:23
56076	02:48–03:55 [29]	–	–	02:06–02:26	02:34–03:17
56077	02:51–03:52 [23]	–	–	02:17–02:36 [8]	02:28–03:14
56078	03:21–04:22	–	–	02:17–02:36 [19]	02:15–03:09
56079	03:24–04:50 [73]	–	–	03:56–04:15 [19]	03:37–04:57
56080	03:57–04:59 [57]	–	–	–	03:42–04:54
56090	01:47–02:30	–	–	–	–
56091	01:49–02:25	–	–	01:28–01:47	–
56092	01:33–02:34 [61]	–	–	01:13–01:32	01:32–02:34
56093	01:27–02:16 [39]	01:17–02:18 [39]	01:13–01:58 [27]	01:15–01:34 [3]	01:31–02:10
56094	01:25–02:07 [41]	01:03–02:11 [43]	00:21–02:00 [37]	01:15–01:35 [12]	01:23–02:06
56095	01:20–02:03 [38]	01:19–02:18 [39]	01:00–02:00 [40]	–	01:18–01:58
56096	01:15–01:54 [39]	01:11–02:12 [51]	00:35–02:00 [47]	–	01:13–02:04
56097	01:11–02:00 [33]	–	01:02–01:47 [25]	–	01:22–01:55

Table B.8 Summary of CV objects in flaring state observations with MAGIC on cycle VIII

Period	Dates	Time observed [h]
YY Her		
127	March–April 2013	1.07
ASASSN-13ax		
130	June–July 2013	9.52
Nova Del 2013		
131	July–August 2013	1.63
132	August–September 2013	16.10

B.5   PWNe Detected at VHE

See Table B.9.

Table B.9 (a) Distance d, characteristic age τ and spin-down power $\dot{E}$ of the central pulsar associated to the PWNe and PWN candidates. (b) Size in x and y-axes (Size$_X$, Size$_Y$ respectively) of the PWNe at TeV energies. Normalization f_0 and spectral index Γ of the γ-ray differential energy spectrum[a]. Cut-off energy E_{cut}, in case it applies[b]. L_γ is the γ-ray luminosity between 1 and 10 TeV and L_X the X-ray luminosity between 2 and 10 keV of the PWNe

(a)

#	Name	Associated pulsar	d [kpc]	τ [kyr]	$\dot{E}$ 10^{36}[erg/s]	References
(1)	3C58	PSR J0205+6449	2	5.4	27.0	Aleksić et al. (2014b), Torii et al. (2000)
(2)	Crab	PSR J0534+2200	2	1.2	461.0	Aharonian et al. (2004), Willingale et al. (2001)
(3)	CTA1	PSR J0007+7303	1.4	13.9	0.5	Aliu et al. (2013), Slane et al. (1997)
(4)	LHA-120-N-N157B	PSR J0537-0710	48	4.9	488.0	Abramowski et al. (2015), Chen et al. (2006)
(5)	Vela-X	PSR B0833-45	0.29	11.3	6.9	Aharonian et al. (2006b), Manzali et al. (2007)
(6)	HESS-J1026-582	PSR J1028-5819	2.3	90.0	0.8	Abramowski et al. (2011b)
(7)	HESS-J1303-631	PSR J1301-6305	6.6	11.0	1.7	Abramowski et al. (2012)
(8)	HESS-J1356-645	PSR J1357-6429	2.4	7.3	3.1	Abramowski et al. (2011a), Izawa et al. (2015)
(9)	Kookaburra (Rabbit)	PSR J1420-6049	5.6	13.0	10.4	Aharonian et al. (2006a), Roberts et al. (2001)
(10)	Kookaburra (K3)	PSR J14206049	5.6	13.0	10.4	Aharonian et al. (2006a), Roberts et al. (2001)
(11)	HESS-J1458-608	PSR J1459-60	4	64.7	0.9	de los Reyes et al. (2012), Kanai (2010)
(12)	MSH-15-52	PSR B1509-58	5.2	1.6	17.5	Aharonian et al. (2005b), Mineo et al. (2001)

Table B.9 (continued)

#	Name	Associated pulsar	d [kpc]	τ [kyr]	$\dot{E}$ 10^{36}[erg/s]	References
(13)	HESS-J1616-508	PSR J1617-5055	6.5	8.1	16.0	Aharonian et al. (2006c), Kargaltsev et al. (2009)
(14)	HESS-J1708-443	PSR B1706-44	2.3	17.5	3.4	Aharonian et al. (2006c), Roberts et al. (2001)
(15)	HESS-J1718-385	PSR J1718-3825	4.2	89.5	1.2	Aharonian et al. (2007), Hinton et al. (2007)
(16)	HESS-J1809-193	PSR J1809-1917	3.7	51.3	1.8	Aharonian et al. (2007), Kargaltsev and Pavlov (2007)
(17)	HESS-J1813-178	PSR J1813-1749	4.7	4.6	68.0	Aharonian et al. (2006c), Funk et al. (2007)
(18)	HESS-J1825-137	PSR B1823-13	3.9	21.4	2.8	Aharonian et al. (2005a), Uchiyama et al. (2009)
(19)	G21.5-0.9	PSR J1833-1034	4.8	4.8	33.7	Djannati-Atai et al. 2007, Slane et al. (2000)
(20)	HESS-J1837-069	PSR J1838-0655	6.6	22.7	5.5	Aharonian et al. (2006c), Anada et al. (2009)
(21)	Kes75	PSR J1846-0258	6.3	0.7	8.1	Djannati-Atai et al. (2007), Helfand et al. (2003)
(22)	G54.1+0.3	PSR J1930+1852	6.2	2.9	11.6	Acciari et al. (2010), Bocchino et al. (2010)

(b)

#	Size$_X$ [deg]	Size$_Y$ [deg]	f_0 10^{-13}[TeV^{-1}cm^{-2}s^{-1}]	Γ	E_{cut} [TeV]	L_γ 10^{32}[erg/s]	L_X 10^{32}[erg/s]
(1)	0.1	0.1	2.0 ± 0.4	2.4 ± 0.2	–	2.3 ± 0.4	57.6
(2)	0.05	0.05	283 ± 4	2.62 ± 0.02	–	266 ± 6	101000
(3)	0.3	0.24	10.2 ± 1.5	2.2 ± 0.2	–	7.1 ± 0.6	28.2
(4)	0.05	0.05	8.2 ± 0.8	1.8 ± 0.2	–	10600 ± 1700	24900
(5)	0.48	0.36	116 ± 6	1.36 ± 0.06	13.9 ± 1.6	7.0 ± 0.4	5.4
(6)	0.14	0.14	10 ± 3	1.9 ± 0.2	–	25 ± 6	–
(7)	0.14	0.19	56 ± 5	1.5 ± 0.2	7.7 ± 2.2	1160 ± 210	8.4
(8)	0.2	0.2	27 ± 9	2.2 ± 0.2	–	55 ± 14	54.6
(9)	0.08	0.06	24.8 ± 2.0	2.17 ± 0.06	–	284 ± 19	276
(10)	0.06	0.06	26.4 ± 2.0	2.22 ± 0.08	–	287 ± 21	181
(11)	0.17	0.17	21 ± 4	2.8 ± 0.2	–	68 ± 11	2.6
(12)	0.11	0.04	57.0 ± 2.0	2.27 ± 0.03	–	506 ± 16	1520
(13)	0.14	0.14	67 ± 5	2.35 ± 0.06	–	860 ± 50	213
(14)	0.29	0.29	14.0 ± 2.0	2.34 ± 0.11	–	23 ± 3	6.0
(15)	0.15	0.07	3.0 ± 1.9	0.7 ± 0.3	7 ± 3	70 ± 40	3.0
(16)	0.53	0.25	46 ± 9	2.2 ± 0.1	–	220 ± 30	3.8
(17)	0.04	0.04	27 ± 3	2.09 ± 0.08	–	238 ± 21	186
(18)	0.13	0.12	55 ± 5	2.46 ± 0.08	–	228 ± 17	31.2
(19)	0.05	0.05	4.6 ± 1.0	2.08 ± 0.22	–	43 ± 9	1100

(continued)

Table B.9 (continued)

(b)

#	$Size_X$ [deg]	$Size_Y$ [deg]	f_0 10^{-13}[TeV^{-1}cm^{-2}s^{-1}] Γ E_{cut} [TeV]			L_γ 10^{32}[erg/s]	L_X 10^{32}[erg/s]
(20)	0.12	0.05	5.0 ± 0.4	2.27 ± 0.06	–	72 ± 5	575
(21)	0.05	0.05	6.2 ± 0.9	2.26 ± 0.15	–	82 ± 11	1080
(22)	0.05	0.05	7.5 ± 1.2	2.39 ± 0.23	–	84 ± 15	346

[a]$dN/dE = f_0 E^{-\Gamma}\,dE$

[b]If the differential energy spectrum is described by a power-law with a cut-off $dN/dE = f_0 E^{-\Gamma}\exp(E/E_{cut})\,dE$

References

Abramowski A et al (2011a) A&A 533:A103
Abramowski A et al (2011b) A&A 525:A46
Abramowski A et al (2012) A&A 548:A46
Abramowski A et al (2015) Science 347:406
Acciari VA et al (2010) ApJ 719:L69
Aharonian F et al (2004b) ApJ 614:897
Aharonian F et al (2005a) A&A 442:L25
Aharonian F et al (2005b) A&A 435:L17
Aharonian F et al (2006a) A&A 456:245
Aharonian F et al (2006b) A&A 448:L43
Aharonian F et al (2006c) ApJ 636:777
Aharonian F et al (2007) A&A 472:489
Aleksić J et al (2014a) A&A 568:A109
Aleksić J et al (2014b) A&A 567:L8
Aliu E et al (2013) ApJ 764:38
Anada T et al (2009) PASJ 61:183
Bocchino F et al (2010) A&A 520:A71
Chen Y et al (2006) ApJ 651:237
de los Reyes R et al. (2012) arXiv:1205.0719
Djannati-Atai A et al. (2007) arXiv:0710.2247
Funk S et al (2007) A&A 470:249
Helfand DJ et al (2003) ApJ 582:783
Hinton JA et al (2007) A&A 476:L25
Izawa M et al. (2015) arXiv:1502.03893
Kanai Y (2010) X-ray and Gamma-ray Emission Properties of Pulsars Detected by the Fermi Gamma-ray Space Telescopee, PhD thesis
Kargaltsev O et al (2007) ApJ 670:655
Kargaltsev O et al (2009) ApJ 690:891
Manzali A et al (2007) ApJ 669:570
Mineo T et al (2001) A&A 380:695
Roberts MSE et al (2001) ApJS 133:451
Slane P et al (1997) ApJ 485:221
Slane P et al (2000) ApJ 533:L29
Torii K et al (2000) PASJ 52:875
Uchiyama H et al (2009) PASJ 61:189
Willingale R et al (2001) A&A 365:L212